

# Modeling the dynamics of barrier coasts and ebb-tidal deltas

Het modelleren van de dynamica van waddenkusten  
en buitendelta's

(met een samenvatting in het Nederlands)

PROEFSCHRIFT

ter verkrijging van de graad van doctor aan de Universiteit Utrecht  
op gezag van de Rector Magnificus, Prof. dr. W.H. Gispen,  
ingevolge het besluit van het College voor Promoties  
in het openbaar te verdedigen op

maandag 20 maart 2006 des middags om 2.30 uur

door

**Maarten van der Vegt**

geboren op 17 september 1977 te Hattem

**Promotor:** Prof. dr. H.E. de Swart

**Promotor:** Prof. dr. W.P.M. de Ruijter

Instituut voor Marien en Atmosferisch onderzoek Utrecht (IMAU),  
Faculteit Bètawetenschappen, Universiteit Utrecht

**Copromotor:** Dr. H.M. Schuttelaars

Delft institute for applied mathematics, Technische Universiteit Delft

This work has been conducted in the framework of the NWO-ALW 'Outer Delta Dynamics' programme and was supported by NWO-ALW grant no. 810.63.12 and 810.63.15.

Cover: Design by Hilde van der Vegt-Beugelink. Figure is based on bathymetric map of the coast of Georgia and South Carolina, USA. It shows the presence of inlets, barrier islands and ebb-tidal deltas. Light parts are deep, dark parts shallow.

ISBN 90-393-4197-4

# Contents

<b>1</b>	<b>Introduction</b>	<b>1</b>
1.1	Sequences of barrier islands and ebb-tidal deltas . . . . .	1
1.2	Focus of this thesis . . . . .	4
1.3	Georgia Bight . . . . .	5
1.3.1	Barrier Islands . . . . .	5
1.3.2	Ebb-tidal delta of Beaufort Inlet . . . . .	5
1.4	Wadden coast . . . . .	7
1.4.1	Barrier islands . . . . .	7
1.4.2	Ebb-tidal delta of Ameland Inlet . . . . .	8
1.5	Present-day knowledge . . . . .	8
1.6	Research questions . . . . .	12
1.7	Research approach . . . . .	12
<b>2</b>	<b>A potential mechanism for the initial formation of sequences of barrier islands</b>	<b>15</b>
2.1	Introduction . . . . .	16
2.2	Model formulation . . . . .	17
2.2.1	Hydrodynamics . . . . .	18
2.2.2	Volumetric sediment transport . . . . .	20
2.2.3	Evolution of the coastline . . . . .	21
2.3	Basic state and linear stability analysis . . . . .	22
2.3.1	Basic state . . . . .	22
2.3.2	Stability analysis . . . . .	24
2.3.3	Solution procedure . . . . .	25
2.3.4	Numerical implementation . . . . .	26
2.4	Results . . . . .	26
2.4.1	Reference case . . . . .	26
2.4.2	Sensitivity of results to tidal current amplitude . . . . .	29
2.4.3	Sensitivity of results to bathymetric parameters . . . . .	31
2.4.4	Influence of waves on the instability mechanism . . . . .	33
2.5	Comparison model results with observations . . . . .	33
2.6	Physical interpretation . . . . .	36
2.6.1	Growth and migration of perturbations . . . . .	36
2.6.2	Magnitude of growth rate for large wave numbers . . . . .	39
2.6.3	Sensitivity of model results to bathymetry . . . . .	41

2.6.4	Sensitivity of model results to forcing conditions . . . . .	41
2.6.5	Fastest growing mode when wave flux is included . . . . .	42
2.7	Discussion and conclusions . . . . .	42
	Appendix . . . . .	44
<b>3</b>	<b>Modeling of equilibrium tide-dominated ebb-tidal deltas</b>	<b>45</b>
3.1	Introduction . . . . .	46
3.2	Model . . . . .	48
3.2.1	Domain . . . . .	48
3.2.2	Hydrodynamics . . . . .	48
3.2.3	Sediment transport . . . . .	51
3.2.4	Sediment mass balance . . . . .	52
3.2.5	Morphodynamic equilibrium condition . . . . .	53
3.2.6	Reference equilibrium . . . . .	53
3.3	Methods . . . . .	53
3.3.1	Finding morphodynamic equilibria . . . . .	53
3.3.2	Numerical method to solve the hydrodynamic equations . . . . .	54
3.3.3	Method to solve the Poisson problem . . . . .	55
3.4	Results . . . . .	56
3.4.1	Default case . . . . .	56
3.4.2	Sensitivity to width of the inlet . . . . .	58
3.4.3	Influence of waves . . . . .	58
3.5	Comparison of model results with observations . . . . .	58
3.5.1	Beaufort Inlet . . . . .	58
3.5.2	Observed and modeled sand volumes . . . . .	61
3.6	Physical interpretation . . . . .	63
3.6.1	Hydrodynamics . . . . .	63
3.6.2	Equilibrium bathymetry . . . . .	64
3.6.3	Relation between ESV and TP . . . . .	66
3.7	Discussion and conclusions . . . . .	67
	Appendix . . . . .	69
<b>4</b>	<b>Physical processes causing asymmetry of tide-dominated ebb-tidal deltas</b>	<b>71</b>
4.1	Introduction . . . . .	72
4.2	Model description . . . . .	75
4.2.1	Domain . . . . .	75
4.2.2	Currents . . . . .	76
4.2.3	Sediment transport . . . . .	77
4.2.4	Sediment mass conservation and morphodynamic equilibrium . . . . .	77
4.3	Reference state and inlet state . . . . .	78
4.3.1	Reference state morphodynamic equilibrium . . . . .	78
4.3.2	Morphodynamic equilibrium due to presence of tidal inlet . . . . .	80
4.4	Methods . . . . .	82
4.4.1	Finding morphodynamic equilibria . . . . .	82
4.4.2	Method to solve hydrodynamic equations . . . . .	82

4.4.3	Numerical Method to Solve the Poisson Problem . . . . .	83
4.5	Results . . . . .	83
4.5.1	Coriolis force . . . . .	83
4.5.2	Shore-parallel currents . . . . .	85
4.5.3	Residual currents at sea . . . . .	90
4.6	Discussion and conclusions . . . . .	92
4.6.1	Coriolis force . . . . .	93
4.6.2	Shore-parallel tidal currents . . . . .	94
4.6.3	Residual currents at sea . . . . .	96
4.6.4	Suggestions for further research . . . . .	97
<b>5</b>	<b>Numerical modeling of ebb-tidal deltas</b>	<b>99</b>
5.1	Introduction . . . . .	100
5.2	Model formulation . . . . .	101
5.2.1	Domain . . . . .	102
5.2.2	Hydrodynamics . . . . .	102
5.2.3	Sediment transport . . . . .	106
5.2.4	Sediment mass balance . . . . .	107
5.2.5	Morphodynamic equilibrium . . . . .	108
5.3	Methods . . . . .	108
5.3.1	Domain . . . . .	108
5.3.2	Hydrodynamics . . . . .	108
5.3.3	Sediment transport . . . . .	109
5.3.4	Morphodynamic equilibria . . . . .	109
5.4	Results . . . . .	110
5.4.1	Set-up of the experiments . . . . .	110
5.4.2	Results for default case . . . . .	111
5.4.3	Sensitivity of model results to tidal velocity amplitude in the inlet . . . . .	115
5.4.4	Sensitivity of results to tidal asymmetry . . . . .	115
5.4.5	Sensitivity of results to quadratic bottom stress . . . . .	119
5.4.6	Sensitivity of results to waves . . . . .	119
5.5	Comparison of model results with observations and idealized model . . . . .	125
5.5.1	Comparison with field data . . . . .	125
5.5.2	Comparison with idealized model . . . . .	127
5.6	Discussion . . . . .	131
5.7	Conclusions . . . . .	135
<b>6</b>	<b>Discussion and conclusions</b>	<b>137</b>
6.1	Length scale of barrier islands . . . . .	137
6.2	Symmetric tide-dominated ebb-tidal deltas . . . . .	138
6.3	Asymmetric tide-dominated ebb-tidal deltas . . . . .	140
6.4	Suggestions for further research . . . . .	142
6.4.1	Modeling the dynamics of barrier coasts . . . . .	142
6.4.2	Modeling the dynamics of ebb-tidal deltas . . . . .	142

<b>Bibliography</b>	<b>145</b>
<b>Samenvatting</b>	<b>151</b>
<b>Dankwoord</b>	<b>157</b>
<b>Curriculum Vitae</b>	<b>159</b>

# Chapter 1

## Introduction

This thesis discusses the physics of morphologic features in shallow seas that are formed by stirring and transport of sediment by tides and waves. Two main topics are investigated. The first one concerns systems of barrier islands and inlets with a distinct alongshore rhythmicity (length scale from a few km to tens of km). The second topic concerns the dynamics of ebb-tidal deltas, which are shallow sandy areas that are located seaward of these inlets. In section 1.1 general observational evidence of sequences of barrier islands and of ebb-tidal deltas is given. Section 1.2 motivates the choice and relevance of these topics. Two examples of sequences of barrier islands are presented that have a different hydrodynamic setting: The barrier islands of the Georgia Bight (Section 1.3) and of the Dutch and German Frisian Islands (Section 1.4). In section 1.5 the present-day knowledge with regard to the modeling and understanding of the dynamics of barrier coasts and ebb-tidal deltas is briefly discussed. Based on this information, in section 1.6 the research questions are formulated. Finally, in section 1.7 the methodology and approach that are used in this thesis are discussed.

### 1.1 Sequences of barrier islands and ebb-tidal deltas

A significant fraction (about 12%) of the world's coasts are sandy and are characterized by barrier islands separated by tidal inlets (*Glaesser, 1978*). Examples are the Dutch and German Wadden coast (*Ehlers, 1988*), the Atlantic coast of the United States (*FitzGerald, 1996; Davis, 1997*) and the barrier coast of New Zealand (*Hicks et al., 1999*). The typical length of the barrier islands ranges between a few kilometers (Florida coast; *Davis (1997)*) to tens of kilometers (e.g. Wadden Sea, North Carolina and Virginia coast). An example of a chain of barrier island is presented in Figure 1.1. It shows the barrier islands located along the coast of Georgia and South Carolina (USA). The light parts are shallow and the dark parts are deep. The black line represents the zero meter contour line and indicates the transition from land to water. White parts represent land.

The water motion observed in the region of barrier islands comprises many components with different length and time scales which, mutually affect each other. The tidal wave traveling along the coast induces both variations in sea level and currents. For most coastal regions the semi-diurnal lunar tide (also called  $M_2$  tide, period 12 h 25 m) is the dominant tidal constituent. The typical amplitudes of the sea surface variation is  $\sim 1$  m

and of the tidal currents  $\sim 1 \text{ ms}^{-1}$ . The wind blowing over the water generates surface waves (periods in order of seconds and heights in the order of 1-2 m) and wind-driven currents (magnitudes of order  $0.1 \text{ ms}^{-1}$ ). In shallow areas these waves break and induce wave-driven currents (order  $1 \text{ ms}^{-1}$ ) and set-up of the sea level (order of 1 m). River outflow induces density differences which drive estuarine circulations (order of  $0.1 \text{ ms}^{-1}$ ).

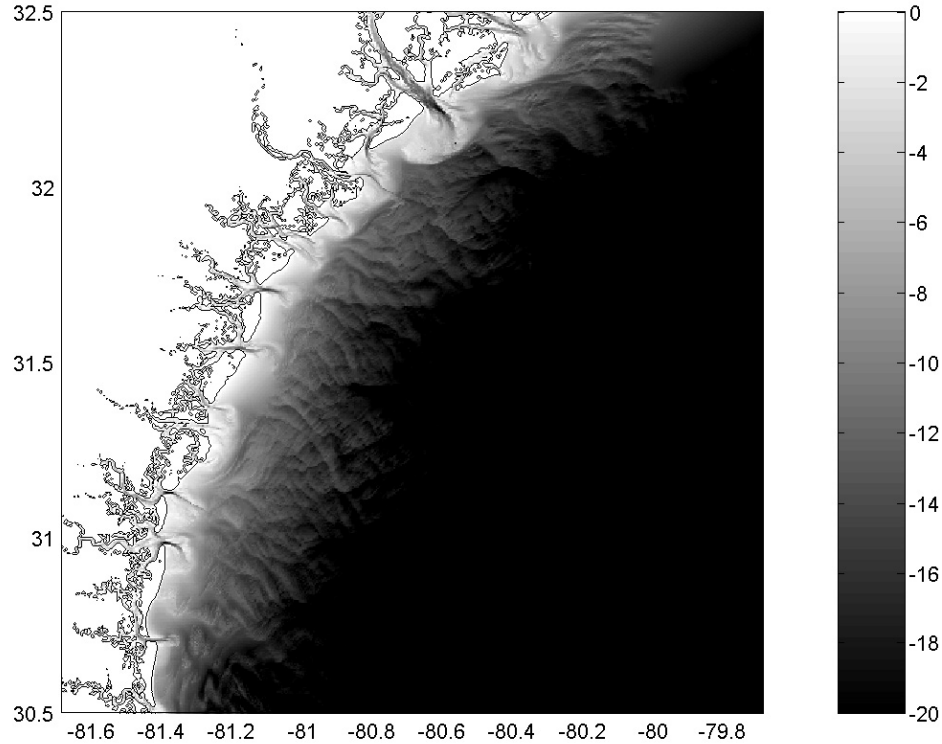


Figure 1.1: Barrier islands along the coast of Georgia and south Carolina. Dark parts are deep, light parts are shallow. Black line is zero meter contour line. Data obtained from NOAA's coastal relief model (<http://www.ngdc.noaa.gov/mgg/gdas>).

In between the barrier islands the tidal inlets are located. They connect a backbarrier basin to the sea. The bathymetry in the area seaward of the inlet is in general characterized by a deep ebb-dominated channel (meaning that peak currents during the ebb phase are stronger than during the flood phase) and two adjacent flood-dominated channels (Figure 1.2). The ebb-tidal delta is located at the end of the ebb-dominated channel. Spatial extents (alongshore and cross-shore) of the ebb-tidal delta vary from several hundreds of meters observed for tidal inlets along the Florida coast (*FitzGerald, 1996; Davis, 1997*) up to 10 kilometer for the Texel inlet (the Netherlands). The maximum depth of the ebb-dominated channel ranges between several meters for small tidal inlets (*FitzGerald, 1996*) and  $\sim 50 \text{ m}$  for Texel inlet (*Sha, 1989b*). The region of the ebb-tidal delta is shallow, with depths in the order of several meters, while some parts can be above mean sea level. Furthermore, smaller-scale channels and shoals repetitively form in the region



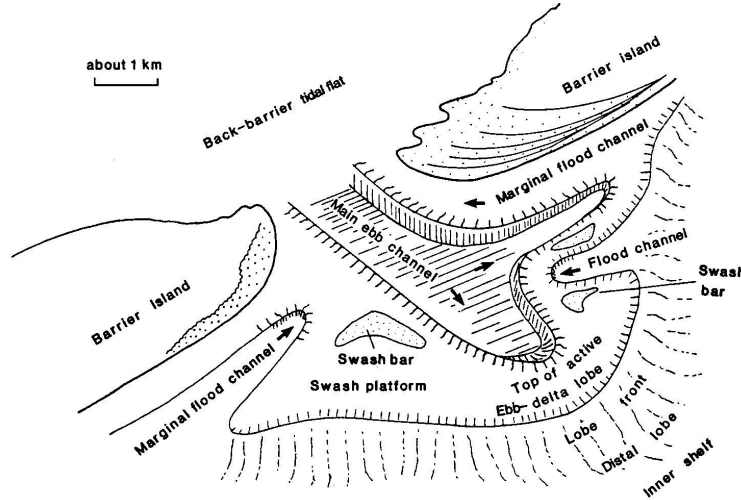


Figure 1.2: Typical spatial configuration of ebb-tidal deltas (Hayes, 1975). The ebb-tidal delta is the large shallow area at the seaward side of the tidal inlet. In the center it is intersected by a deep ebb-dominated channel. At both sides of the ebb-tidal delta two flood-dominated channels are seen.

of the ebb-tidal delta and subsequently migrate from one side of the inlet to the other side (Sha, 1989b; Oost and de Boer, 1994; FitzGerald, 1996); the ebb-tidal delta exhibits cyclic behavior. Typical time scale of this cycle ranges between decades (Ameland Inlet, the Netherlands) to centuries (Texel Inlet, the Netherlands).

In many tidal inlets the cross-shore tidal currents are in the order of  $\sim 1 \text{ ms}^{-1}$ . The transport of water by these currents causes the basin to fill and empty with water during one tidal cycle. The tidal prism (TP) is defined as the volume of water that enters and leaves the tidal basin during one tidal cycle and is a function of the tidal range and of the characteristics of the backbarrier basin. The tidal prism ranges from  $1 \cdot 10^6 \text{ m}^3$  (Walton and Adams, 1976) to  $10^9 \text{ m}^3$  for Texel Inlet (Sha, 1989a; Gibeaut and Davis Jr., 1993). The characteristics of the morphology in the area seaward of the tidal inlets strongly depend on the magnitude of the tidal prism. Based on data of ebb-tidal deltas along the Atlantic US-coast, Walton and Adams (1976) concluded that there is a power-law relationship between the ebb-tidal sand volume (ESV) and the tidal prism (Figure 1.3). The ebb-tidal sand volume is defined as the amount of sediment that is stored in the ebb-tidal delta. Only the areas which are shallower than a reference bathymetry (defined as the bathymetry that would be obtained when no tidal inlet is present) are considered as a part of the ebb-tidal sand volume. Walton and Adams (1976) found that

$$\text{ESV} = c_1 \text{TP}^{c_2} \quad (1.1)$$

When making ESV and TP dimensionless by dividing them through a unit volume of  $1 \text{ m}^3$ , a best fit of the data is obtained for  $c_1 = 0.0066$  and  $c_2 = 1.23$ . The islands along the Dutch and German Wadden coast show an almost linear relation between TP and the depth of the ebb-dominated channel (Sha, 1990).

Field observations indicate that the overall orientation of ebb-dominated channels is quite different for different barrier coasts. The channels located seaward of the inlets along

the Atlantic coast of the USA often have a shore-normal orientation (see Figure 1.1). In contrast, the ebb-dominated channels observed off the Dutch Wadden coast bend to the left, when viewing from the inlet in the seaward direction, and those observed off the German coast bend to the right. In the rest of this thesis they will be referred to as left- (or right-) oriented channels. Since the ebb-tidal deltas are located at the end of the ebb-dominated channels the deltas of the Dutch and German Wadden coast are asymmetric with respect to reflection about the mid-axis of the inlet. Analysis and interpretation of data suggest that the orientation of the channels is controlled by three factors, viz. the tidal prism, the magnitude of shore-parallel tidal currents and the intensity of the wave-driven alongshore currents *Sha* (1989a).

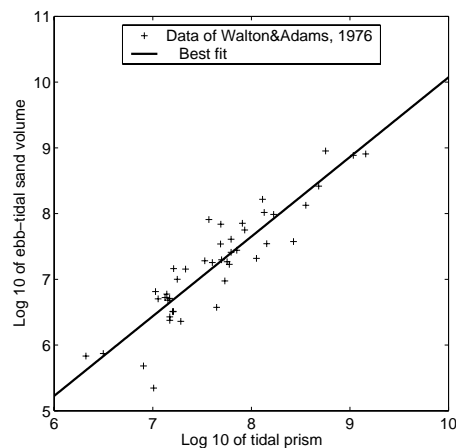


Figure 1.3: Data of ebb-tidal sand volumes and tidal prisms of tidal inlets along the Atlantic US-coast obtained by *Walton and Adams* (1976).

## 1.2 Focus of this thesis

Apart from being scientifically interesting features, barrier coasts and the tidal inlets with their adjacent ebb-tidal deltas are important for economic reasons. Often a harbor is situated at the landward side of the tidal inlet. Furthermore, these areas are densely populated, they are attractive for recreation and they are also important from an ecological point of view since they serve as nurseries for fish larvae and as feeding grounds for e.g. migrating birds. In addition, human interferences in the backbarrier basin take place, which influence the dynamics of both the backbarrier basin and the the ebb-tidal delta (e.g. the closure of the Zuiderzee by the construction of the Afsluitdijk in 1927-1932, see *Sha* (1990) for a discussion). It is thus important to gain more understanding of the natural behavior of the tidal inlet and the ebb-tidal delta. In spite of the important function of ebb-tidal deltas and tidal inlets, they belong to the least studied coastal environments. This is mainly due to the complex hydro- and morphodynamics.

The general aim of this thesis is to obtain fundamental knowledge about processes that are important for the morphodynamics of (i) barrier coasts and (ii) ebb-tidal deltas. More specific, the physical mechanisms that determine the length of barrier islands and

the physical mechanisms that generate and maintain ebb-tidal deltas are studied. A model approach is used. One of the problems with formulating models for the barrier coasts and ebb-tidal deltas is the difficulty in devising a model that is representative for a large population of the ebb-tidal deltas, while at the same time making the model sufficiently accurate to study the fundamental physical processes. This makes it inevitable to limit the scope of this study. This thesis focuses on barrier coasts and ebb-tidal deltas of which the morphological developments are largely induced by tides and to a lesser extent by waves.

In the following section the hydrodynamics and morphodynamics of two chains of barrier islands are discussed. Furthermore, for each case the hydrodynamics and morphodynamics of the ebb-tidal delta of one specific inlet is discussed in more detail. The first chain of barrier islands that is discussed is found along the Georgia Bight (USA). The ebb-tidal delta of Beaufort Inlet is discussed in more detail and serves as an example of an (almost) symmetric ebb-tidal delta. The second chain of barrier islands are the barrier islands of the Dutch, German and Danish Wadden Sea (Frisian Islands). The ebb-tidal delta of the Ameland inlet is discussed in more detail and serves as an example of a spatially asymmetric ebb-tidal delta.

## 1.3 Georgia Bight

### 1.3.1 Barrier Islands

The Georgia Bight stretches over 1200 km from Cape Hatteras (North Carolina) down to Cape Canaveral (Florida). Typical tidal range of the  $M_2$  tide is 1 – 2 m. It is maximum along Georgia and minimum along Florida and North Carolina. The tidal currents in the inlets are up to  $1 \text{ ms}^{-1}$ . The shore-parallel currents are typically one order of magnitude smaller and range between  $0.05 \text{ ms}^{-1}$  along the shelf of North Carolina to a maximum of  $0.11 \text{ ms}^{-1}$  along the shelf of Georgia (*Blanton et al.*, 2004). The deepwater average wave height is 1 – 2 m and the waves approach from the north-east (*Davis and FitzGerald*, 2004). The bottom consists of fine to coarse sand (grain size 100 – 1000  $\mu\text{m}$ ) with a median grain size of 500  $\mu\text{m}$ . At large time and space scales the sediment transport is predominantly to the south. The inner shelf, which is the area just seaward of the surf zone (where the waves break), is steep near both edges of this coast and wider and less steep in the middle (Figure 1.4). A sequence of barrier islands is present with a typical distance between successive inlets that varies between a few up to tens of kilometers. The length of the barrier islands seems to be inversely related to the magnitude of the tide (Figure 1.4). In regions with small tidal range the average length of the barrier islands is larger and the number of inlets per length scale is smaller. This is typically the case in the region along the North Carolina coast. When tidal range is larger the length of the barrier islands is smaller and the number of inlets is larger.

### 1.3.2 Ebb-tidal delta of Beaufort Inlet

Many ebb-tidal deltas along the Georgia Bight have almost symmetric ebb-tidal deltas. One inlet is studied in more detail: Beaufort Inlet. This choice is motivated by the avail-

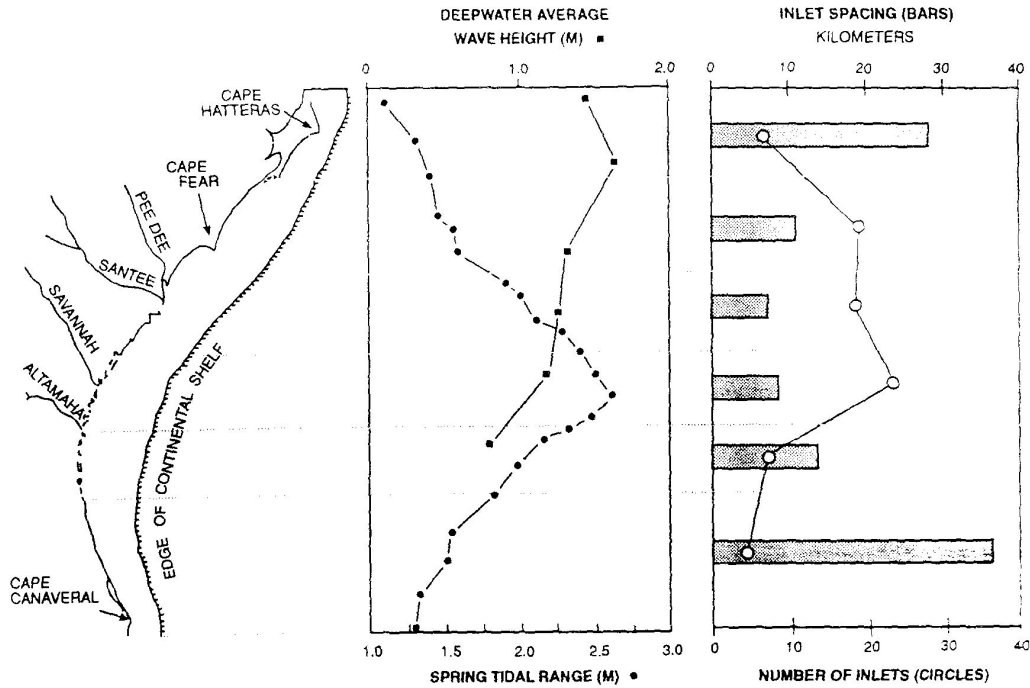


Figure 1.4: Length of barrier islands and number of tidal inlets as a function of inner shelf width, tidal range and wave amplitude for the Georgia Bight (*FitzGerald, 1996*). The left panel shows the Georgia Bight and the edge of the inner shelf. The middle panels shows the local tidal range and significant wave height. The right panel shows the number of tidal inlets and average inlet spacing.

ability of many observations and by previous modeling studies (e.g., *Hench and Luetlich (2003)*). Beaufort Inlet is located at the east coast of the US with the center of the inlet at  $34.7^{\circ}N$ ,  $76.6^{\circ}W$  and it has a width of 1 km. The Beaufort inlet is characterized by a small tidal range ( $\sim 1$  m) and the maximum tidal currents in the tidal inlet are up to  $\sim 1 \text{ ms}^{-1}$  (*Hench and Luetlich, 2003*). The tidal prism is  $2.8 \cdot 10^7 \text{ m}^3$ . Beaufort inlet is sheltered from (storm) waves from northwest by the presence of a cape. The mean off-shore significant wave height is about 1 m and the mean significant wave period is about 6 s. The ebb-tidal delta is almost spatially symmetric. The spatial extent of the ebb-tidal delta is several kilometers (Figure 1.5). There is one elongated ebb-channel. This channel is maintained at 10-15 m depth and has a shore-normal orientation. The flood-dominated channels, which are often observed for ebb-tidal deltas, seem to be absent. This is probably due to fact that the tidal inlet is maintained by man. Depths of the ebb-tidal tidal delta range from 2 to 10 m. The total volume of sand stored in the ebb-tidal delta is  $2.4 \cdot 10^7 \text{ m}^3$ .

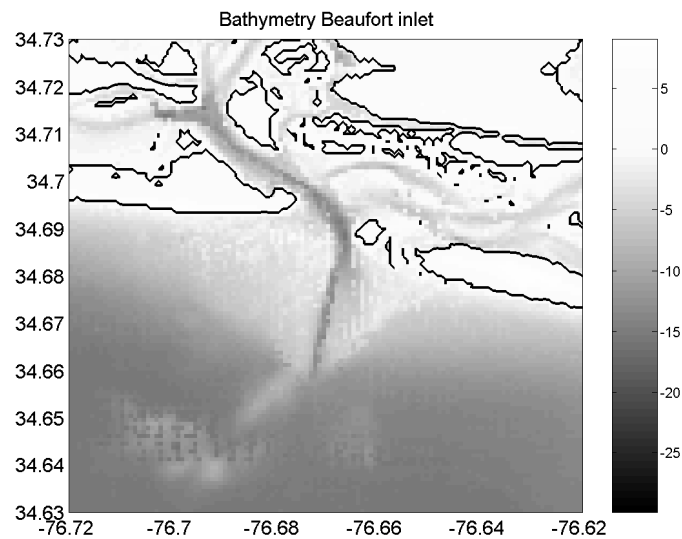


Figure 1.5: Bathymetry of Beaufort Inlet, North Carolina, USA. Data obtained from NOAA's coastal relief model (<http://www.ngdc.noaa.gov/mgg/gdas>).

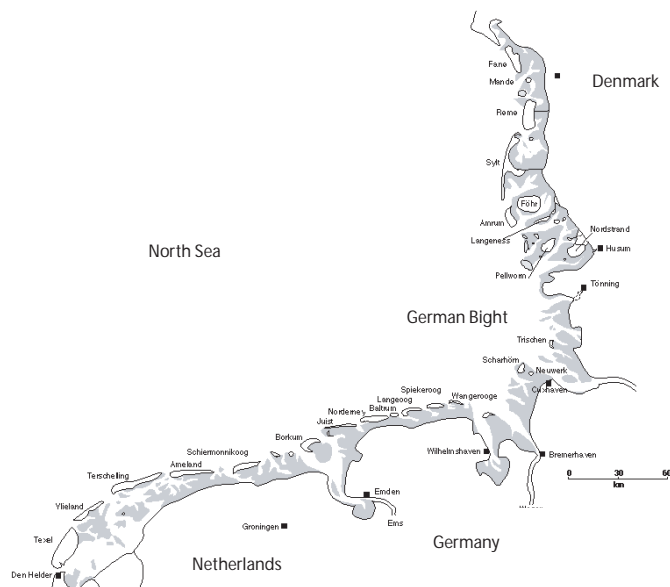


Figure 1.6: Barrier islands (Frisian Islands) and tidal inlets along the Dutch, German and Danish coast.

## 1.4 Wadden coast

### 1.4.1 Barrier islands

The second sequence of barrier islands that is discussed, is that along the Dutch, German and Danish coast (Figure 1.6). Both tides and waves are important constituents of the water motion in this area. The tidal range is minimum near the island of Texel of  $\sim 1.5$

m and increases when moving to the German Bight, where it reaches its maximum of 3 – 4 m. From thereon the tidal range decreases to  $\sim 2$  m for the island of Sylt. The cross-shore tidal currents through the tidal inlets are in the order of  $1 \text{ ms}^{-1}$  while the tide-induced shore-parallel currents are also significant with magnitudes of  $0.5 \text{ ms}^{-1}$ . The mean significant wave height in the area of the Frisian Islands is  $\sim 1.2$  m and is almost uniform (*Sha*, 1989a). The mean significant wave period is 6 s. On average, the waves approach from the north-west and at large time and space scales they transport sediment from west to east. The length of the so-called Frisian Islands is not constant. The islands of Texel and Terschelling are the longest ones (20 – 30 km). The length of the barrier islands gradually decreases up to the German Bight, where the barrier islands are even absent. From thereon the length of the islands increases again. Also in this area the length of the barrier islands is inversely related to the tidal range (*Oost and de Boer*, 1994).

### 1.4.2 Ebb-tidal delta of Ameland Inlet

The ebb-tidal deltas along the Frisian islands are asymmetric with respect to reflection about the mid-axis of the inlet. A typical example of an asymmetric ebb-tidal delta is the one that is located seaward of the Ameland Inlet (Figure 1.7). This inlet has been selected because this is one of the most natural tidal inlet systems along the Dutch coast. It is located between the islands of Terschelling and Ameland (Figure 1.6). The width of the inlet is 2 km. The mean tidal range is 2.30 m and the tidal prism is  $4 \cdot 10^8 \text{ m}^3$ . Maximum cross-shore tidal currents are in the order of  $1 \text{ ms}^{-1}$  and the shore-parallel tidal currents outside the region of the ebb-tidal delta are  $0.3 \text{ ms}^{-1}$ . The significant wave height is 1.10 m and waves approach from the north-west (*Israel and Dunsbergen*, 1999). The deep channel that is seen in Figure 1.7 is ebb-dominated and the ebb-tidal delta is left-oriented. The depth in the main channel is about 30 m. The typical depth of the ebb-tidal delta is several meters.

## 1.5 Present-day knowledge

Modeling the dynamics of barrier coast and ebb-tidal deltas is a necessary way to interpret the field data and to obtain fundamental understanding about the dominant physical processes. There are several types of models (*de Vriend*, 1996; *de Vriend and Ribberink*, 1996) and in this section the present-day knowledge based on these different model concepts will be discussed.

Till 1990 most models that were used to understand the dynamics of barrier coasts and ebb-tidal deltas had a conceptual character. The aim of these models is to describe certain physical mechanisms without using equations that are based on first principles. Concerning the dynamics of barrier coasts, *FitzGerald* (1996) formulated a conceptual model for the dependence of the length of the barrier islands on tidal range. He argues that when the tidal range increases, more inlets are needed to drain the backbarrier basins. His underlying assumption is that a larger tidal range causes a larger tidal prism, which requires more openings exchange water through the tidal inlets. However, a small tidal

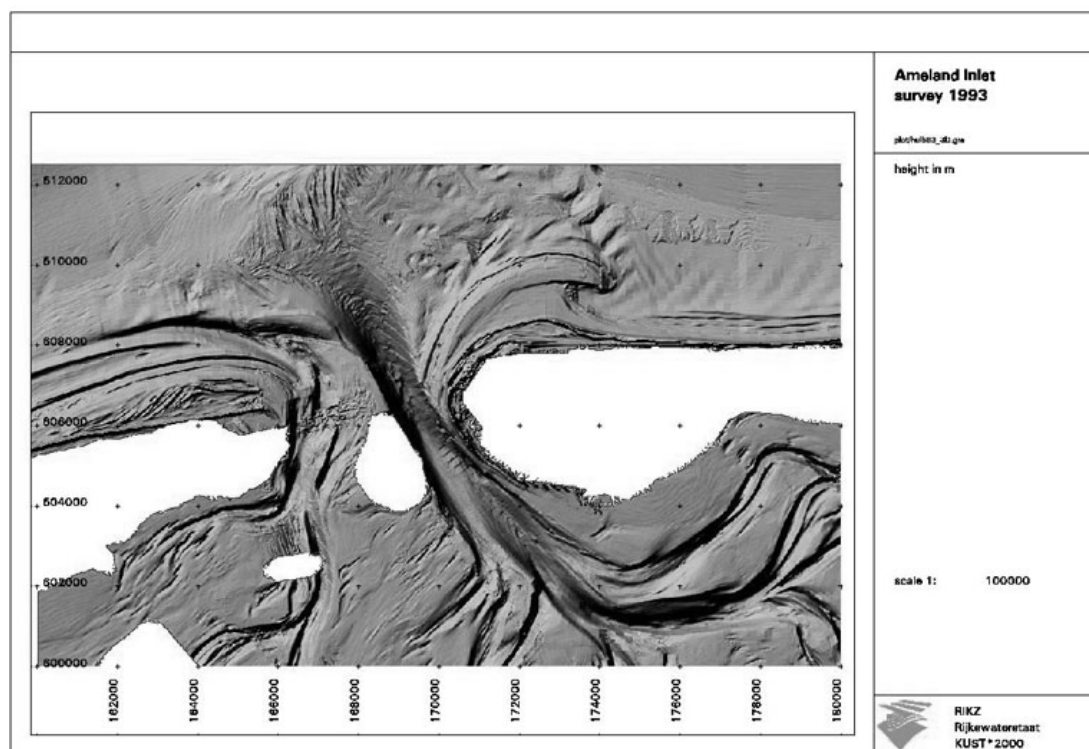


Figure 1.7: Bathymetry of Ameland Inlet in 1993. Dark parts are deep part. Light parts are shallow. White parts are above mean sea level. Barrier island on the left-hand side is the island of Terschelling, the one on the right-hand side is the island of Ameland. Source: RIKZ The Haque.

range does not automatically imply that the tidal prism is small, since the latter also depends on the size of the backbarrier basin and its resonance characteristics. Texel Inlet, for instance, has a small tidal range, but it is the inlet with the largest tidal prism of all inlets located along the Wadden coasts.

Concerning ebb-tidal deltas, *Stommel and Farmer* (1952) were the first to identify the different nature of the tidal currents during ebb and flood. During ebb, the currents are directed from the tidal inlet to the sea and are characterized by a small alongshore and a large cross-shore velocity component. Hence, the flow behaves like a jet, called the ebb-jet. During flood the inflow pattern is radial. These flow pattern have also been observed in laboratory experiments (*Wells and Van Heyst*, 2003). The different nature of the flow during ebb and flood has a strong influence on the morphology of the area seaward of the tidal inlet. During ebb sand is removed from the entrance of the tidal inlet, subsequently transported with the ebb-jet, and deposited at the seaward end of the jet (*Oertel*, 1972, 1988). During flood sand is transported from all sides towards the inlet. As a result, not all sand that is transported during ebb, is reworked during flood. On average, the sediment is removed from the tidal inlet and deposited further seaward. This gives a conceptual explanation why in the center of the inlet the ebb-dominated channel and further offshore the ebb-tidal delta are formed.

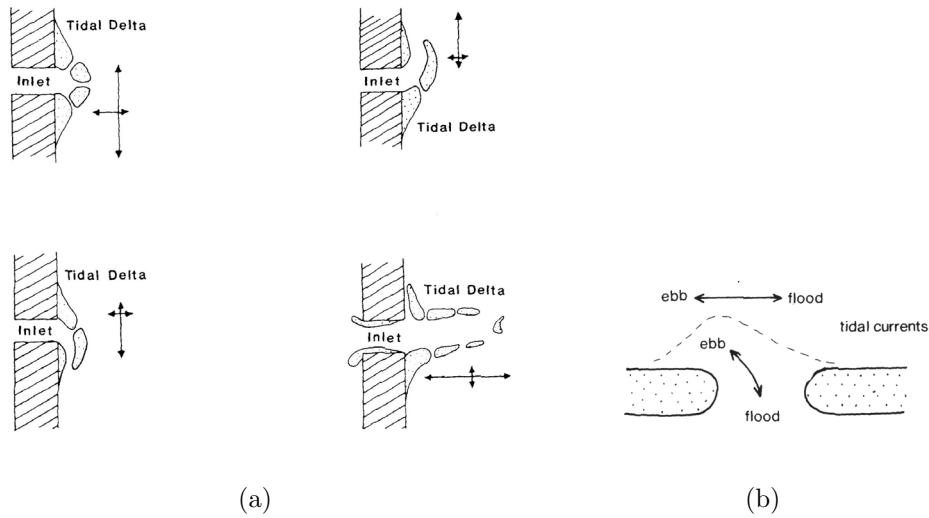


Figure 1.8: (a) Conceptual model of *Oertel* (1975) to explain (a)symmetry of ebb-tidal deltas. Cross-shore arrows indicate strength of cross-shore tidal currents and alongshore arrows indicate strength and direction of wave-induced currents. (b) Conceptual model of *Sha* (1989a) to explain the asymmetry of ebb-tidal deltas along the Dutch Wadden Sea. Due to interaction of shore-parallel tidal currents and cross-shore tidal currents are maximum ebb-currents oriented to the left of the inlet.

Several processes related to the influence of waves and tides can render the ebb-tidal delta asymmetric. In the conceptual model of *Oertel* (1975) it is argued that the asymmetry of the ebb-tidal delta is caused by processes related to waves. Obliquely incident waves refract and break in the surf zone and this results in a wave-driven current. Assume that far away from the tidal inlet the wave-drive currents are from left to right and transport sediment. The presence of the tidal inlet causes an interruption of the wave-driven currents, because the waves do not break in the inlet where the depths are large. This interruption causes deposition at the left-hand side of the tidal inlet and erosion of sediment at the right-hand side. Hence, the ebb-dominated channel will be right-oriented (Figure 1.8(a)).

The influence of the interaction of the shore-parallel and cross-shore tidal currents on the asymmetry of the ebb-tidal delta was first noted by *Sha* (1989a). His conceptual model can be applied to the tidal inlet systems of the of the Dutch Wadden Sea. The interaction of the shore-parallel and cross-shore tidal currents leads to strong bi-directional tidal currents at the left-hand side of a tidal inlet (viewing from the inlet in seaward direction) and smaller, rotary, currents at the righthand side (Figure 1.8(b)). Furthermore, he argued that the strong bi-directional currents will result in erosion of sediment and that this sediment is deposited in the area where the currents are weak and rotary. Hence, the ebb-dominated channel is left-oriented.

The conceptual models are not based on an explicit description of the physical processes. The concepts have to be tested by using process-based models that are based on physical first principles. The objective is to gain physical insight in the dominant physical processes that are important for the morphodynamics of barrier coasts and ebb-



tidal deltas. In principle, process-based morphodynamic models consist of three separated modules. In the first module the water motion (tides, waves and density-driven currents and their interaction) is calculated for a specific bathymetry. In the next module these currents are used to calculate the sediment transport. In the last module the new bottom is calculated from the divergence of the sediment transport. When the sediment transport is divergent, sediment is removed from the bed; when the sediment transport is convergent, sediment is deposited at the bed.

Before 1990 only process-based models have been developed that describe the hydrodynamics in the area seaward of the tidal inlet (e.g., *Awaji et al.* (1980); *Ridderinkhof* (1989)). Together with more recent studies of *van Leeuwen and de Swart* (2002); *Hench and Luettich* (2003), these studies identified, explained and analyzed important aspects of the currents in the seaward region of a tidal inlet. An important aspect is the presence of residual circulation cells, as was already discussed by *Stommel and Farmer* (1952). The cells can be symmetric in the case of a model for the Beaufort Inlet (*Hench and Luettich*, 2003) or they can have asymmetric properties in the case of models based on the Dutch Wadden Sea (*Ridderinkhof*, 1989; *van Leeuwen and de Swart*, 2002).

After 1990 computers became powerful enough to study the morphodynamic evolution of ebb-tidal deltas by direct simulation. In *Wang* (1991); *Wang et al.* (1995) the Delft2D-MOR model was used to study the long-term evolution of the backbarrier basin of the Frisian Inlet. Wave effects were modeled in a heuristic manner by assuming that they cause a spatially uniform stirring of sediment from the bed. The simulations reproduced some observed gross features of the Frisian Inlet, such as the presence of channels and shoals. The results for the evolution of the ebb-tidal delta were less satisfactory. *Cayocca* (2001) used a two-dimensional horizontal model to study several stages of the evolution of the Arcachon inlet (France). Both waves, tidal currents and their interaction were modeled for a realistic geometry. The model reproduced several observed features such as the opening of a new channel. A detailed study for the sediment transport patterns in the Teignmouth estuary was carried out by *Siegle et al.* (2004). They showed that waves are important for the migration of shoals.

In *van Leeuwen et al.* (2003) the evolution of the asymmetric ebb-tidal delta of the Frisian Inlet was modeled, starting from a situation without an ebb-tidal delta. The model was only forced by  $M_2$  tidal currents. After a long simulation time (hundreds of years) the system evolved to a configuration that compared reasonably well with the Frisian Inlet system. Furthermore, at the end of the simulation the evolution of the ebb-tidal delta was slowing down. This suggested that an equilibrium configuration was achieved. However, due to numerical problems a real equilibrium (no evolving bathymetry) was not reached.

A drawback of the complex process-based morphodynamic models is the difficulty to analyze the results. The models are too complicated to study fundamental processes in isolation and to perform a large number of sensitivity experiments. Therefore it is hard to reveal which processes are causing the observed phenomena. These models are not very suitable to test the ideas that are obtained from the conceptual models.

Idealized process-based models are more suitable to test conceptual ideas and to obtain fundamental physical understanding about the dynamics of barrier coasts and ebb-tidal deltas. In these kind of models simplified equations are derived from first principles in which only processes are retained that are believed to be important for the specific

phenomena studied. They allow for a systematic analysis of the basic mechanisms. The fundamental knowledge that is obtained by these kind of models can be used to validate the conceptual models and to interpret the results obtained with complex process-based models. Idealized process-based models have mainly been used to study the channel-shoal dynamics in tidal basins and estuaries (*Schuttelaars and de Swart (2000); Schramkowski et al. (2004)*) and the morphodynamics of tidal sand ridges, shoreface-connected ridges and sand waves (e.g., *Huthnance (1982); Hulscher et al. (1993); Calvete et al. (2001); Roos et al. (2004)*).

## 1.6 Research questions

From the previous sections it follows that there is still a lack in our understanding of barrier coast and ebb-tidal deltas. Concerning the morphodynamics of barrier island sequences, there is no satisfactory explanation for the observed length of the barrier islands. Concerning the morphodynamics of ebb-tidal deltas, observations by *Hayes (1975)* and *Walton and Adams (1976)* and the results described in *van Leeuwen et al. (2003)* suggest that the ebb-tidal delta is a part of the equilibrium morphology at the seaward side of the tidal inlet, but this has never been proved. Furthermore, many conceptual models for the dynamics of ebb-tidal deltas as discussed by *Oertel (1972, 1988); Sha (1989a)* have not been tested with process-based models. Therefore, in this thesis the following research questions are addressed:

1. Which physical mechanisms can cause an initial straight coastline to develop into an undulating one, with spacing between successive undulations in the order 1-30 km, thereby crudely mimicking the initial formation of a barrier coast? Can such mechanisms be modeled and does the model explain why the length of barrier islands is inversely related to the tidal range, as observations suggest?
2. Which physical processes are required to model the presence of a spatially symmetric ebb-tidal delta as a part of a morphodynamic equilibrium bathymetry at the seaward side of a tidal inlet? Can such a model quantitatively explain observed empirical relationships between e.g. ebb-tidal sand volume and tidal prism?
3. Which physical mechanisms cause the spatial asymmetry of ebb-tidal deltas with respect to their mid-axis through the tidal inlet and can this be simulated by a process-based model?

## 1.7 Research approach

To find answers to the research questions 1,2 and 3, both idealized and complex process-based models are used. In Chapter 2, the first question is addressed. An idealized model is developed to study the stability of a straight coastline under influence of tides and waves. It describes the feedback between tides, waves and the small-amplitude undulations of a sandy coastline. The model employs a so-called linear stability analysis, i.e., the evolution of small perturbations evolving on a known equilibrium state of the system

is studied. Because the perturbations are small the equations can be linearized. The small perturbations can grow or decay and migrate. The main assumption in Chapter 2 is that the joint action of tidal currents and waves cause growing initial undulations of the coastline. Spots where the coastline has retreated are more vulnerable to breaching during storms and are the spots where tidal inlets may form.

In Chapter 3 and 4 and 5 the focus is on the dynamics of ebb-tidal deltas. One of the key issues addressed is whether the ebb-tidal delta can be modeled as a part of the morphodynamic equilibrium (a state characterized by a steady bottom pattern) in the area seaward of the tidal inlet. A continuation technique is used. This technique requires the knowledge of one morphodynamic equilibrium for a certain choice of parameter values. Next, a parameter is slightly changed. It is assumed that the previous equilibrium is a good estimate of the equilibrium state for the new parameter setting. This estimate is used to calculate the hydrodynamics, the sediment transport and its divergence and convergence for the new parameter setting. From this a new estimate of the morphodynamic equilibrium state for the parameter setting is obtained. If the difference with the previous estimate of the equilibrium is small the equilibrium state for the new parameter setting is reached and a parameter can be changed again. The success of this technique for morphodynamic problems was already demonstrated in the context of models that calculated the morphodynamic equilibrium states of the backbarrier basin (*Schuttelaars and de Swart, 2000; Schramkowski et al., 2004*).

In Chapter 3 and 5 the dynamics of the symmetric ebb-tidal delta is studied. First, in Chapter 3 an idealized process-based model is developed and analyzed. Many assumptions and limitations in the description of the hydrodynamics are introduced. These concern the adoption of a rigid-lid approximation, the use of a linearized bed shear-stress formulation, the neglect of higher harmonics of the tide in computing the net sediment transport and the use of a heuristic wave model. The model described in Chapter 3 is used to quantify the concepts of *Stommel and Farmer (1952)* and *Oertel (1972, 1988)*. Second, in Chapter 5 a complex process-based numerical model is developed to validate the idealizations that were used in the idealized model of Chapter 3. The results obtained with the idealized and the numerical model are compared. Furthermore, the sensitivity of the results to aspects that could not be studied with the idealized model (such as a quadratic bed shear-stress formulation, higher harmonics of the tide and waves calculated with a sophisticated wave model) are studied.

In Chapter 4 the focus is on the processes that cause spatially asymmetric ebb-tidal deltas. The idealized model of Chapter 3 is extended with tide-related processes that lead to asymmetry. In Chapter 6 the results of this thesis are summarized and discussed and a perspective on new ways to study the morphodynamics of ebb-tidal deltas is presented.



## Chapter 2

# A potential mechanism for the initial formation of sequences of barrier islands

### Abstract

An idealized model is developed and analyzed to demonstrate the potential relevance of tidal motion for the emergence of undulations of a sandy coastline. These undulations might trigger the formation of inlets and barrier islands. The model describes the feedback between depth-averaged tidal and steady flow on the inner shelf, sediment transport in the nearshore zone and an irregular coastline. It is demonstrated that an initially straight coastline can become unstable with respect to perturbations with a rhythmic structure in the alongshore direction. Using parameter values that are representative for the Dutch coast, it is found that perturbations with a length scale smaller than 8 km will grow. The time scale of the evolution is in the order of hundred years and perturbations typically migrate in the order of 10 meters per year. The mechanism responsible for the growth of perturbations is explained in terms of vorticity concepts. The alongshore gradient in the transfer of vorticity in the alongshore direction generates residual circulation cells that cause a growth of the perturbation. The cross-shore gradient in the transfer of vorticity in the cross-shore direction induces residual circulation cells that cause a decay of the perturbations. If the influence of waves on the net sediment transport is ignored, there is no fastest growing mode. When the wave-induced sediment transport is accounted for, the model predicts a fastest growing mode with wavelengths that can be in the order of observed length scales of barrier islands. The model predicts that the wavelength of the preferred mode decreases with increasing amplitude of the tidal currents and increases with increasing wave height. This is in gross correspondence with observed behavior of the lengths of barrier islands that are located along the Dutch and German Wadden coast and of those located in the Georgia Bight.

## 2.1 Introduction

A large part of the world's sandy coastlines show alongshore rhythmic variations on a wide range of length and time scales (*Ehlers, 1988; Komar, 1998; Ruessink and Jeuken, 2002*). This chapter focuses on rhythmic mesoscale variations of sandy coasts, i.e., with a characteristic length scale in the alongshore direction of a few kilometers to tens of kilometers. Such mesoscale variations are e.g. observed along the Dutch, German and Danish Wadden coast. This coast is characterized by a sequence of barrier islands and inlets. The typical length of the barrier islands decreases from a maximum length of 30 km for the island of Texel to an absence of barrier island in the German Bight (see Figure 1.6). It has been noted that the typical length of the barrier islands is inversely related to the tidal range (*Oost and de Boer, 1994*). The tidal range increases when moving from the Dutch part of the Wadden Sea to the Danish part, as has been discussed in Chapter 1. This behavior of the length of barrier islands along the Dutch and German Wadden Sea is not unique. In the Georgia Bight a similar relation between tidal range and the length of the barrier islands is observed (*FitzGerald, 1996*). In addition, the length of the barrier islands in this region is also linearly related to the mean height of the waves (see Chapter 1 for more details).

The general objectives of the present study are twofold. The first is to gain fundamental knowledge about the origin of the observed rhythmic mesoscale variations of the coastline using a model. The second is to derive a qualitative relationship between the characteristic length of these undulations and physical control parameters (like tidal, wave and shelf characteristics). In the past, several models were developed to study the dynamics of coastlines which are influenced by waves. They are all one-line models, i.e., the complex three-dimensional dynamics is parameterized, resulting in an equation for the coastline position only. A simple, widely used one-line model that simulates the initial evolution of rhythmic alongshore perturbations of a straight coastline, is that described by *Komar (1998)* (originally from *Pelnaud-Considère (1956)*). In this model it is assumed that the width of the surf zone (the area where the waves are breaking) is constant. The conceptual idea is that obliquely incident waves refract and break in the surf zone and drive a current which transports sediment. Alongshore variations in this sediment transport result in changes of the position of the coastline. Under the aforementioned assumptions, and by only considering the dynamics due to a small rhythmic perturbation of the coastline, the *Komar (1998)* model boils down to a diffusion equation for the position of the coastline. The diffusion parameter is a function of the wave characteristics at the breaker line and the angle between the direction of the wave rays at breaking and the normal of the local (perturbed) coastline. A positive diffusion parameter implies that a small initial perturbation of the coastline will decay and a negative diffusion parameter results in growth. A negative diffusion parameter is obtained when the angle between wave rays at breaking and the normal of the local coastline is more than 45 degrees.

The one-line model of *Komar (1998)* was extended by *Ashton et al. (2001); Falqués (2003)*. They assumed that a change in the position of the coastline also results in a change of the bathymetry outside the surf zone. The bathymetric contour lines are kept parallel. Hence, a change in the position of the coastline results in a shift of the entire bathymetric profile. Already far offshore the waves are influenced by the change in the coastline

position because the bottom has changed. The diffusion parameter is now calculated as a function of the wave characteristics far offshore. The model results of *Falqués* (2003) show that the diffusion parameter in the model of *Komar* (1998) is always positive because the waves refract such that the wave rays at breaking will always have an angle of less than 45 degrees with respect to the normal of the local coastline. This does not imply that in the model of *Falqués* (2003) the perturbations of the coastline always decay. The model also takes into account the influence of alongshore variations in the wave height at the breaker line due to focusing of wave energy. Adding this effect leads to the so-called high-angle wave instability. Wave rays at deep water which have an angle of more than  $42^\circ$  with respect to the normal of the local coastline can lead to a growth of the perturbation of the position of the coastline.

Although interesting results are obtained with the models of *Ashton et al.* (2001) and *Falqués* (2003), there are problems with the physical interpretation. The main problem is that in these models sediment mass is not conserved. In *Falqués and Calvete* (2005) this problem was solved. They assumed that a perturbation in the position of the coastline results in a perturbation of the bottom profile with finite cross-shore extent. Hence, the bathymetric contours far offshore are not parallel anymore to the bathymetric contour lines in the nearshore zone. The model results show that fastest growing modes emerge which have typical time scales of years and wavelengths of the order of 10 km. The model was applied to the Dutch coastline, where a sequence of barrier islands is observed. Using their model, the Dutch coastline was found to be stable, i.e., no growing rhythmic coastline undulations were found (*Ashton et al.*, 2003; *Falqués and Calvete*, 2005; *Falqués*, 2005).

Since the action of waves in itself is not sufficient to trigger the evolution of an undulating coastline along the Dutch and German Wadden coast, tidal motions might be important as well. The observation that the barrier length increases with decreasing tidal range seems to support the importance of tidal motion for understanding the emergence of coastline undulations. Therefore, in this study a process-based one-line model is developed and analyzed to study whether the feedback between the coastline and tidal currents can cause the initial formation of an undulating coastline with length scales ranging between a few and tens of kilometers. In section 2.2 a model is formulated in which coastline undulations develop as free instabilities of an alongshore uniform coastline. The new aspect of this model is that it explicitly accounts for the influence of tidal currents on the stability of the coastline. In section 2.3 the basic state is described and the linear stability analysis is discussed. The model calculates the growth rate and phase speed of the coastline perturbation for different alongshore wavelengths of the perturbation. The results of this linear stability analysis are presented in section 2.4. In section 2.5 the results are compared with observations. Section 2.6 gives the physical interpretation of the results, and in section 2.7 the results are discussed and the main conclusions are given.

## 2.2 Model formulation

In this study a Cartesian coordinate system is adopted with the  $x$ -axis pointing in the cross-shore direction, the  $y$ -axis coinciding with the alongshore mean position of the coast-

line and the  $z$ -axis pointing in the upward vertical direction. The domain of the model consists of three regions: the surf zone, the nearshore zone and the inner shelf (Figure 2.1(a)). The surf zone is the area where the waves break and is located between the coastline  $x = x_c$  and the breaker line  $x = x_b$ . The nearshore zone is also called the active zone and is the area where bottom changes occur due to changes in the position of the coastline. The nearshore zone is located between the coastline  $x = x_c$  and the transition line  $x = x_t$ , with  $x_t > x_b$ . Here, the transition from the nearshore zone to the inner shelf occurs. The inner shelf is the region that is located between the nearshore region and the outer shelf. Sediment transport is small and the time scale of bathymetric changes is large compared to that of the nearshore zone.

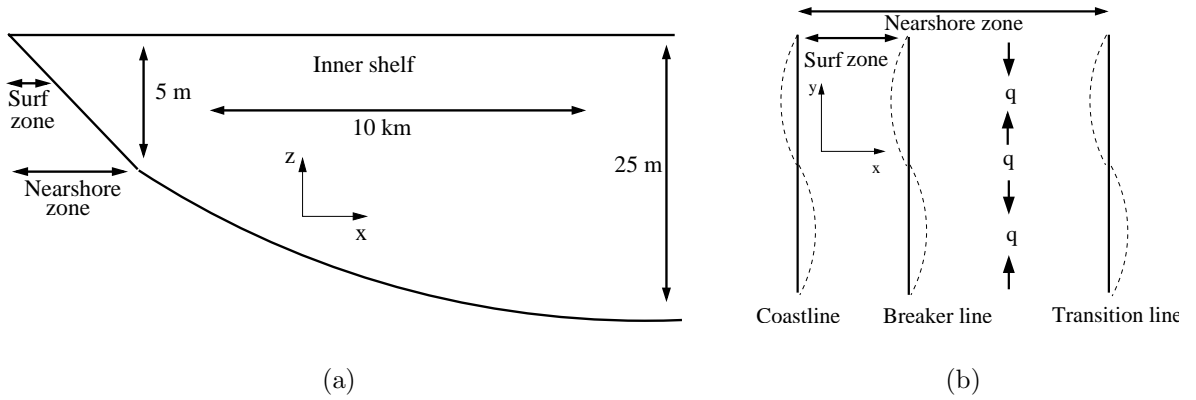


Figure 2.1: (a) Sideview of the geometry of the model. The nearshore zone is the area from the coastline to the transition line. The width of the nearshore zone is approximately 500 m. The surf zone is the area from the coastline to the breaker line. It has a width of typically 100 m. The transition between nearshore zone and inner shelf takes place at a typical depth of 5 m. The typical width of the inner shelf is 10 km. At the position where the inner shelf connects to the outer shelf the typical depth is 25 m. For more information see the text.

(b) Top view of the model. The position of the coastline is perturbed rhythmically and is denoted by the dashed variations. It is assumed that the width of the surf zone and the nearshore zone is constant. Therefore, the position of the breaker line and the position of the transition line are also perturbed when the coastline is perturbed. The typical length of the rhythmic variations of the position of the coastline is 1 – 10 km. The volumetric sediment flux in the alongshore direction is denoted by  $q$  and takes place in the whole nearshore zone.

### 2.2.1 Hydrodynamics

The tidal hydrodynamics at the inner shelf are governed by the depth-averaged, shallow water equations. The water motion is forced by the semi-diurnal lunar ( $M_2$ ) tide, which has frequency  $\sigma \sim 1.4 \times 10^{-4} \text{ s}^{-1}$ . The characteristic tidal wavelength is  $L_g \sim 2\pi\sqrt{gH_*}/\sigma \sim 450 \text{ km}$ , where  $g$  is the acceleration due to gravity and a  $H_* = 10 \text{ m}$  a characteristic water depth. The spatial scales of the phenomena that are the focus of this study (typically  $L_{\text{barrier}} \sim 10 \text{ km}$ ) are small compared to the wavelength of the tidal wave. Hence, the Froude number ( $\text{Fr} \sim L_{\text{barrier}}/L_g$ ) is very small. This allows for a rigid



lid approximation: The sea level variations themselves can be neglected, but their spatial gradients are important and result in pressure gradients in the momentum equations (see e.g., *Huthnance (1982); Calvete et al. (2001)*). The hydrodynamic equations are

$$\frac{\partial \vec{u}}{\partial t} + (\vec{u} \cdot \vec{\nabla})\vec{u} + f\vec{e}_z \times \vec{u} = -g\vec{\nabla}\zeta - \frac{\vec{\tau}_b}{\rho H} \quad (2.1a)$$

$$\vec{\nabla} \cdot (H\vec{u}) = 0 \quad (2.1b)$$

Here  $\vec{u}$  is the horizontal velocity vector,  $t$  is time,  $\vec{\nabla}$  the horizontal gradient operator,  $f$  the Coriolis parameter,  $\vec{e}_z$  the unity vector in vertical direction,  $\zeta$  the elevation of the free surface,  $H$  the water depth with respect to  $z = 0$  and  $\vec{\tau}_b$  the bed shear-stress. Usually, the bed shear-stress is taken to depend quadratically on the local velocity. In this study a linearized bed shear-stress formulation is used. Hence, instead of using

$$\vec{\tau}_b = \rho C_d |\vec{u}| \vec{u} \quad (2.2)$$

the bed shear-stress is approximated by

$$\vec{\tau}_b = \rho r \vec{u} \quad (2.3)$$

The friction factor  $r$  is taken such that the tidally averaged dissipation due to the linearized bottom stress equals that of the quadratic bottom stress. A discussion on the derivation of the linearized bed shear-stress can be found in *Zimmerman (1992)*. In this study we choose the friction parameter to be

$$r = \frac{8}{3\pi} C_d U \quad (2.4)$$

with  $U$  the mean tidal velocity amplitude at the transition line. This implies that the friction parameter  $r$  is constant in the domain.

In this model tidal motion is due to a prescribed alongshore pressure gradient. As boundary conditions in the alongshore direction periodic conditions (with an as yet unspecified length scale) are imposed, at the transition line the shore-normal velocity component must vanish and far offshore the velocity is required to have no cross-shore component:

$$x = x_t : \quad u = v \frac{\partial x_t}{\partial y} \quad (2.5a)$$

$$x \rightarrow \infty : \quad u \rightarrow 0 \quad (2.5b)$$

where  $u, v$  are the cross-shore and alongshore component of the velocity vector  $\vec{u}$ , respectively.

## 2.2.2 Volumetric sediment transport

The tidal hydrodynamics and sediment transport in the nearshore zone are not explicitly calculated in the model. Instead, the tidal currents are calculated on the inner shelf and the velocities at the transition line are taken as representative for the whole nearshore zone. They are used to calculate the volumetric sediment flux  $q$  in the nearshore zone (Figure 2.1(b)). In general, the sediment flux has a component due to waves and due to tides,

$$q = q_{(\text{wave})} + q_{(\text{curr})} \quad (2.6)$$

where  $q_{(\text{wave})}$  is the part due to waves only and  $q_{(\text{curr})}$  due to the joint action of tides and waves. It is assumed that  $q_{(\text{curr})}$  involves the stirring of sediment from the bed by waves, which is subsequently transported by a tide-driven residual current. This is parameterized as

$$q_{(\text{curr})} = \beta \langle v_{\parallel} \rangle \quad (2.7)$$

Here  $\beta$  is a constant and  $\langle v_{\parallel} \rangle$  is the tidally averaged shore-parallel component of the velocity at the transition line,

$$\langle v_{\parallel} \rangle = \frac{1}{T} \int_0^T v_{\parallel} dt \quad (2.8)$$

where  $T$  is the tidal period. The constant  $\beta$  in equation (2.7) accounts for the fact that the sediment is transported in the complete nearshore zone and has the unit of  $\text{m}^2$ . A physical interpretation of  $\beta$  is the available volume of sediment in the nearshore zone per unit length,

$$\beta = \int \int \frac{c}{\rho_s} dz dx \quad (2.9)$$

In this expression is  $c$  the tidally averaged sediment mass concentration and  $\rho_s$  the density of the sediment. The mean wave height along the Dutch and German Wadden coast is in the order of 1 m *Sha* (1989a). Using observations performed by *Grasmeijer and Kleinhans* (2004) of sediment concentrations at different levels in the vertical in the nearshore zone near Egmond aan Zee (the Netherlands) yields an estimate of  $\int \frac{c}{\rho} dz = \mathcal{O}(5 \cdot 10^{-5} - 1 \cdot 10^{-3}) \text{ m}^3/\text{m}^2$ . Assuming that the width of the nearshore zone is in the order of 500 m, this yields that  $\beta = \mathcal{O}(2.5 \cdot 10^{-2} - 5 \cdot 10^{-1}) \text{ m}^2$ .

Although the focus in this study is on the sediment transport due to tidal currents, some experiments have been performed in which both sediment transport due to waves only and tidal currents are accounted for (section 2.4.4). The expressions of *Pelnaud-Considère* (1956); *Komar* (1998) are used to parameterize wave-driven sediment transport,

$$q_{(\text{wave})} = \mu H_b^{2.5} \sin 2(\theta_b - \phi) \quad (2.10)$$

where  $\mu \sim 0.1 - 0.2 \text{ m}^{\frac{1}{2}}\text{s}^{-1}$  is a constant of proportionality,  $H_b$  is the (rms) wave height of the waves at the breaker line and  $\theta_b - \phi$  (see Figure 2.2) is the angle between the wave fronts at breaking and the local coastline. In the present model both  $H_b$  and  $\theta_b$  are input parameters. The local angle between the coastline and the  $y$ -axis is defined as

$$\phi = \arctan \left[ \frac{\partial x_t / \partial y}{(1 + |\partial x_t / \partial y|^2)^{1/2}} \right] \quad (2.11)$$

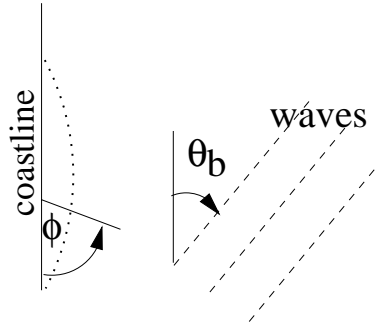


Figure 2.2: Definition of angle between wave rays at breaking and the local coastline. Dashed lines represent wave rays. Dotted line is coastline perturbation. The angle between  $y$ -axis and local normal to the coastline is  $\phi$  and  $\theta$  is the angle between the wave rays and the local unperturbed coastline.

### 2.2.3 Evolution of the coastline

When the position of the coastline changes, it can be expected that the bathymetry further offshore also changes. Hence, a change in the position of the coastline results in change of the position of breaker line and of the transition line. The most simple approach is to assume that variations in the coastline results in variations of the position of transition line of the same amplitude and vice versa,  $x_t - x_c = \text{constant}$ . In this section the sediment mass balance is used to derive an evolution equation for the location of the transition line ( $x_t$ ). Assume that the location of the coastline is shifted in time  $\Delta t$  over a small distance  $\Delta x_t$  (Figure 2.3). In the present model it is assumed that entire bathymetric profile in the nearshore zone shifts over a distance  $\Delta x_t$ . Therefore, the volume of sediment per unit length necessary for the displacement equals  $\Delta x_t H(x = x_t) + \mathcal{O}(\Delta x_t^2)$ . Here  $H(x = x_t)$  is the depth at the transition line  $x = x_t$ . The change in the volume of sediment results from the convergence of the sediment transport in the alongshore direction,  $\Delta q / \Delta y$ . Taking the limit  $\Delta q, \Delta x_t, \Delta y \rightarrow 0$ , it follows that

$$\frac{\partial x_t}{\partial t} = - \frac{1}{H} \frac{\partial q}{\partial y} \Big|_{x=x_t} \quad (2.12)$$

The evolution of the transition line (and hence the coastline) takes place on a long morphological time scale  $T_m$ . Applying a scaling analysis and calculating the influence of alongshore variations in  $q_{(\text{curr})}$  (Equation (2.7)) on the evolution of the coastline (defined

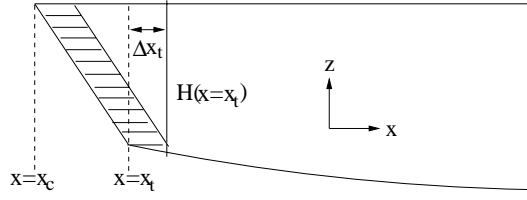


Figure 2.3: Sediment conservation in the present model. The coastline is at  $x = x_c$  and the transition line at  $x = x_t$ . The coastline is shifted in seaward direction with  $\Delta x_t$  while  $x_t - x_c$  is constant. The shaded area is the volume of sediment per unit length that is added to this coastal section.

by Equation (2.12)) and using boundary condition (2.5a) to obtain an estimate of  $v_{\parallel}$  yields

$$T_m = \frac{[H(x = x_t)][\lambda]^2}{\beta[v]} \quad (2.13)$$

where the typical value of the alongshore tidal currents is  $[v] = 1 \text{ ms}^{-1}$ , the typical value of the alongshore wavelength of the perturbation is  $[\lambda] = 10 \text{ km}$ , the typical depth at the transition line is  $[H(x = x_t)] = 5 \text{ m}$  and typically  $\beta = 10^{-1} \text{ m}^2$ . Using these values, the morphological time scale is approximately 150 years. Physically this means that the coastline is not changing on the tidal time scale, but only on a very long time scale. Therefore, the position of the coastline can be considered as constant during one tidal cycle.

## 2.3 Basic state and linear stability analysis

### 2.3.1 Basic state

The model solutions are denoted by a state vector  $\Psi = (\vec{u}, \vec{\nabla}\zeta, q, q_{(\text{curr})}, q_{(\text{wave})}, x_t)^T$ . This state vector can be split into a part which describes a basic state with alongshore uniform conditions and a part which describes deviations from this basic state,  $\Psi = \Psi_{\text{eq}} + \Psi'$ . Here,  $\Psi_{\text{eq}} = (\vec{U}, \vec{\nabla}Z, Q, Q_{(\text{curr})}, Q_{(\text{wave})}, X_t)^T$  with  $\vec{U} = (U, V)$  the basic state velocity vector with components  $U$  and  $V$  in the  $x$ - and  $y$ -direction, respectively, and  $\vec{\nabla}Z$  the basic state gradient of the sea surface. Furthermore,  $Q$  is the basic state volumetric sediment flux in the nearshore zone,  $Q_{(\text{curr})}$  and  $Q_{(\text{wave})}$  are the basic state volumetric sediment flux in the nearshore zone due to joint action of waves and tides and due to waves only, respectively, and  $X_t = \text{constant}$  is the position of the transition line in the basic state (straight coast).

In the basic state a spatially uniform alongshore pressure gradient is prescribed that consists of a residual component ( $S_0$ ) and the main tidal ( $M_2$ ) component with amplitude  $S_2$  and frequency  $\sigma$ ,

$$\frac{\partial Z}{\partial y} = -S_2 \cos \sigma t + S_0 \quad (2.14a)$$

$$\frac{\partial Z}{\partial x} = \frac{f}{g} V(x, t) \quad (2.14b)$$

No higher harmonics of the tide are taken into account. The free surface elevation  $Z$  is linear in the alongshore direction. In the cross-shore direction the gradient in the free surface elevation follows from geostrophic balance. The basic state velocity has an alongshore component that varies only in the cross-shore direction, i.e.,  $\vec{U} = (0, V(x, t))$ . This velocity component is determined by a balance between inertia, alongshore sea surface gradient and depth-dependent friction,

$$\frac{\partial V}{\partial t} = -g \frac{\partial Z}{\partial y} - r \frac{V}{H} \quad (2.15)$$

The solution for the basic state velocity is

$$V(x, t) = V_2(x) \cos(\sigma t + \Phi(x)) + V_0(x) \quad (2.16)$$

with

$$V_2(x) = \frac{HS_2g}{\sqrt{\sigma^2 H^2 + r^2}} \quad (2.17a)$$

$$V_0(x) = \frac{-gS_0}{r} H \quad (2.17b)$$

$$\Phi(x) = \arctan\left(\frac{r}{\sigma H}\right) \quad (2.17c)$$

The depth-dependent friction term in the alongshore momentum balance causes a phase lag between currents and sea surface gradient (in case of time dependent pressure gradient). It also results in an increasing magnitude of the alongshore velocity with increasing depth, i.e., cross-shore distance. Hence, the basic state velocity contains vorticity, defined by  $\Omega(x, t) = \partial V(x, t)/\partial x$ . Furthermore, the magnitude of  $U$  can be defined

$$U = V_2(x = X_t) \quad (2.18)$$

The basic state sediment transport due to tides is

$$Q_{(\text{curr})} = \beta V_0 \quad (2.19)$$

Following *Komar (1998)*, the basic state sediment transport that is solely due to waves reads

$$Q_{(\text{wave})} = \mu H_b^{2.5} \sin(2\theta_b) \quad (2.20)$$

### 2.3.2 Stability analysis

The stability of the alongshore uniform coastline is studied by considering the dynamics of alongshore rhythmic perturbations. Hence, in Equations (2.1) and (2.4)-(2.12)  $\Psi = \Psi_{eq} + \Psi'$  is substituted, with  $\Psi_{eq}$  as defined in Equations (2.14), (2.16), (2.19), (2.20), and  $\Psi' = (\vec{u}', \vec{\nabla}\zeta', q', q'_{(curr)}, q'_{(wave)}, x'_t)^T$  denotes the state vector with the perturbed variables, which are assumed to be small compared to their values in the equilibrium state.

Linearizing the equations with respect to the small variables results in the following equations that describe the perturbed hydrodynamics,

$$\frac{\partial u'}{\partial t} + V \frac{\partial u'}{\partial y} - f v' = -g \frac{\partial \zeta'}{\partial x} - \frac{r u'}{H} \quad (2.21a)$$

$$\frac{\partial v'}{\partial t} + \left( u' \frac{\partial V}{\partial x} + V \frac{\partial v'}{\partial y} \right) + f u' = -g \frac{\partial \zeta'}{\partial y} - \frac{r v'}{H} \quad (2.21b)$$

$$u' \frac{dH}{dx} + H \frac{\partial u'}{\partial x} + H \frac{\partial v'}{\partial y} = 0 \quad (2.21c)$$

The linearized boundary conditions (2.5) read

$$u' \Big|_{x=X_t+x'_t} = V \frac{\partial x'_t}{\partial y} \Big|_{x=X_t} \quad (2.22a)$$

$$u' = 0 \Big|_{x \rightarrow \infty} \quad (2.22b)$$

The next step is to find  $q'_{(curr)}$  and  $q'_{(wave)}$ . Using (2.7) and the definition  $v_{\parallel} = \vec{u} \cdot \vec{s}$ , with  $\vec{s}$  the tangent of the transition line, the tidally induced sediment transport at the undulating transition line becomes

$$Q_{(curr)} + q'_{(curr)} = \frac{\beta \langle V + v' \rangle}{\left[ 1 + \left( \frac{\partial x'_t}{\partial y} \right)^2 \right]^{1/2}} \Big|_{x=X_t+x'_t} \quad (2.23)$$

To evaluate this expression at location  $x = X_t + x'_t$  (which is unknown), a Taylor expansion of the various variables is made, resulting in

$$Q_{(curr)} + q'_{(curr)} = \frac{\beta \langle V + v' \rangle \Big|_{x=X_t} + \beta x'_t \frac{\partial \langle V + v' \rangle}{\partial x} \Big|_{x=X_t} + \dots}{1 + \frac{1}{2} \left( \frac{\partial x'_t}{\partial y} \right)^2 + \dots} \quad (2.24)$$

Keeping only contributions that are linear in the perturbed quantities results in

$$q'_{(curr)} = \beta \left[ \langle v' \rangle + x'_t \frac{d \langle V_0 \rangle}{dx} \right]_{x=X_t} \quad (2.25)$$

For the perturbed wave-induced volumetric sediment flux  $q'_{(wave)}$  the expression of *Komar* (1998) is used,

$$q'_{(wave)} = \mu H_b^{2.5} \cos(2\theta_b) \frac{\partial x'_t}{\partial y} \quad (2.26)$$

The last step is to obtain the evolution equation for the perturbed position of the transition line. The spatial variations in the sediment transport result in changes in the position of the coastline and the transition line. The linearized evolution equation for the position of the transition line becomes

$$\frac{\partial x'_t}{\partial t} = -\frac{\beta}{H} \frac{\partial}{\partial y} \left[ \langle v' \rangle + x'_t \frac{d}{dx} \langle V_0 \rangle \right] \Big|_{x=X_t} + \gamma \frac{\partial^2 x'_t}{\partial y^2} \quad (2.27)$$

Equation (2.27) clearly shows that the waves cause diffusion of the coastline perturbation with the diffusion parameter  $\gamma$  defined by

$$\gamma = \frac{2\mu H_b^{2.5}}{H(x = X_t)} \cos(2\theta_b) \quad (2.28)$$

### 2.3.3 Solution procedure

The model equations have solutions of the form

$$\Psi' = \Re \left[ \left( \hat{u}(x, t), \hat{v}(x, t), \vec{\nabla} \hat{\zeta}(x, t), \hat{q}, \hat{q}_{(\text{curr})}, \hat{q}_{(\text{wave})}, \hat{x}_t \right) e^{iky} e^{\Gamma t} \right]^T \quad (2.29)$$

Note that all variables behave exponentially in time. Besides, the hydrodynamic variables also show oscillatory behaviour on the tidal time scale which is much smaller than the time scale on which the transition line is evolving. The alongshore wave number is denoted by  $k$  and can be chosen arbitrarily. Furthermore,  $\Gamma = \Gamma_{\text{re}} + i\Gamma_{\text{im}}$  is the complex growth rate, with a real part ( $\Gamma_{\text{re}}$ ) that describes the growth of the perturbations, and an imaginary part ( $\Gamma_{\text{im}}$ ) that determines the phase speed,  $c = -\Gamma_{\text{im}}/k$ .

The aim is to determine  $\hat{u}(x, t)$ ,  $\hat{v}(x, t)$ ,  $\vec{\nabla} \hat{\zeta}(x, t)$ ,  $\hat{q}$ ,  $\hat{q}_{(\text{curr})}$ ,  $\hat{q}_{(\text{wave})}$ ,  $\hat{x}_t$  and  $\Gamma$  as a function of wave number  $k$  and model parameters. The interest is in perturbations that have positive growth rates ( $\Gamma_{\text{re}} > 0$ ). The mode with wave number  $k = k_p$  that has the largest growth rate will dominate the dynamics after some time. Therefore, it is called the most preferred mode. The growth rate is calculated as follows. First, the perturbation  $x'_t$  with given wave number  $k$  is chosen. The hydrodynamic problem, described by Equations (2.21a), (2.21b), (2.21c) and boundary conditions (2.22), has to be solved. Because the alongshore dependence of the variables is known a priori,  $\hat{v}$  is known as a function of  $\hat{u}$  (Equation (2.21c)), and reads

$$\hat{v} = -\frac{\hat{u} \frac{dH}{dx} + H \frac{\partial \hat{u}}{\partial x}}{ikH} \quad (2.30)$$

The two momentum equations (2.21a) and (2.21b) are combined into a vorticity equation. This is done by taking the  $x$ -derivative of Equation (2.21b) and subtracting the  $y$ -derivative of Equation (2.21a). When substituting for  $\hat{v}$ , one equation for the complex cross-shore velocity  $\hat{u}$  is found,

$$U_{12} \frac{\partial^3 \hat{u}}{\partial t \partial x^2} + U_{11} \frac{\partial^2 \hat{u}}{\partial t \partial x} + U_{10} \frac{\partial \hat{u}}{\partial t} + U_{02} \frac{\partial^2 \hat{u}}{\partial x^2} + U_{01} \frac{\partial \hat{u}}{\partial x} + U_{00} \hat{u} = 0 \quad (2.31)$$

The coefficient  $U_{ij}$  are given in the appendix. As boundary conditions at  $x = X_t$   $\hat{u}$  is prescribed and for  $x \rightarrow \infty$  it is required that  $\hat{u} \rightarrow 0$ . Solving Equation (2.31) together

with the boundary conditions yields  $\hat{u}$ , and using Equation (2.30) yields  $\hat{v}$ . Now, the perturbed sediment transport  $\hat{q}_{(\text{curr})}$  is known. For given wave conditions also  $\hat{q}_{(\text{wave})}$  can be calculated. Substituting Equation (2.29) into Equation (2.27) yields an expression for  $\Gamma$ ,

$$\Gamma \hat{x}_t = -\frac{\beta}{H} \left( ik \langle \hat{v} \rangle + \hat{x}_t \frac{dV_0}{dx} \right) \Big|_{x=X_t} - \gamma k^2 \hat{x}_t \quad (2.32)$$

### 2.3.4 Numerical implementation

Equation (2.31) is solved using a pseudospectral method. The spatial variables are expanded in Chebyshev polynomials (see *Boyd (2001)* for details). In previous morphodynamic modeling studies these Chebyshev polynomials have been successfully used in resolving spatial patterns (*Falqués et al., 1996*). Employing the method discussed *Calvete et al. (2001)*, for the time-dependent part a Galerkin approach is adopted. The velocity component  $\hat{u}$  and  $\hat{v}$  are expanded in their harmonic agents  $M_0$ ,  $M_2$ ,  $M_4$  and so on. In this study the series is truncated after the  $M_2$  components, so nonlinear tides are not accounted for. Hence, the variables are expanded as

$$\hat{u}(x, t) = \sum_{p=1}^N \left[ u_p^0 + u_p^{-1} e^{-i\sigma t} + u_p^1 e^{i\sigma t} \right] T_i(\tilde{x}) \quad (2.33a)$$

$$\hat{v}(x, t) = \sum_{p=1}^N \left[ v_p^0 + v_p^{-1} e^{-i\sigma t} + v_p^1 e^{i\sigma t} \right] T_i(\tilde{x}) \quad (2.33b)$$

$$(2.33c)$$

where  $x = L_x \frac{1+\tilde{x}}{1-\tilde{x}}$  with  $L_x$  is a stretching parameter and  $T_i$  are Chebyshev polynomials. Furthermore,  $N$  is the number of collocation points in the  $x$ -direction and  $u_p^0$ ,  $u_p^{-1}$ ,  $u_p^1$  are the Chebyshev coefficients of the residual component, the  $e^{-i\sigma t}$  Fourier component and the  $e^{i\sigma t}$  Fourier component of the cross-shore velocity, respectively. The expansions of Equation (2.33) are substituted into Equation (2.31) and are evaluated at  $N$  collocation points in the  $x$ -direction. This results in a system of  $3N$  by  $3N$  linear algebraic equations with  $3N$  variables of the form  $Ax = B$ , which is solved by standard numerical techniques. Here,  $A$  is a complex  $3N$  by  $3N$  matrix describing the model equations. The vector  $x$  describes the coefficients of the expansions of Equation (2.33). The complex vector  $B$  is zero for all  $3N$  components, except for the collocation points at the transition line. In those points the magnitude of  $\hat{u}$  is prescribed (boundary condition (2.22)).

## 2.4 Results

### 2.4.1 Reference case

In the first experiments the focus is on the influence of tidal currents on the stability of the equilibrium state with respect to perturbations in the position of the coastline.



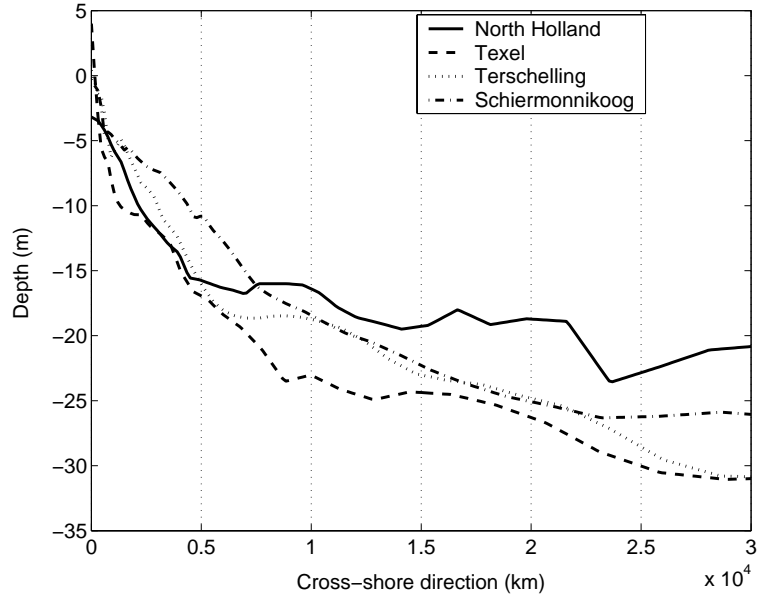


Figure 2.4: Four cross-shore profiles along the Frisian Islands. The profile of 'North Holland' is taken 20 km south of Den Helder. For other positions of cross-shore transects, see Figure 1.6.

Thus,  $\gamma = 0$  is assumed in Equations (2.27) and (2.32). Within the present model this situation occurs when the angle of wave incidence  $\theta_b = 45^\circ$ . The meaning of this choice will be discussed later on. Experiments are performed for parameter values which are representative for the Dutch coastal area. The following profile has been used to represent the depth profile of the inner shelf,

$$H(x) = H_0 + (H_s - H_0)(1 - e^{-(x-X_t)/L}) \quad (2.34)$$

Here,  $H_0 = H(x = x_t)$  and far offshore, where the inner shelf connects to the outer shelf, the depth is  $H_s$ . Parameter  $L$  is an  $e$ -folding length scale which is a measure of the width of the inner shelf. Typical values have been determined by fitting this expression to observed profiles along the Dutch coast. This yields estimates of  $H_0 \sim \mathcal{O}(1 - 10)$  m,  $H_s \sim \mathcal{O}(15 - 25)$  m and  $L \sim \mathcal{O}(8 - 15)$  km. In the reference experiment  $H_0 = 5$  m,  $H_s = 20$  m and  $L = 10$  km. The alongshore sea surface gradient is chosen such that the maximum velocity amplitude at the transition line is  $V_2(x = X_t) = U = 0.5 \text{ ms}^{-1}$ . No net flow is considered in the basic state ( $S_0 = 0$ ). The Coriolis parameter  $f = 1.14 \cdot 10^{-4} \text{ s}^{-1}$  and the drag coefficient  $C_d = 2.5 \cdot 10^{-3}$ . Furthermore, it has been used that  $\beta = 10^{-1} \text{ m}^2$ . The number of collocation points is  $N = 100$  and the stretching parameter  $L_x = 10$  km.

The dependence of the growth rate on the alongshore wave number is shown in Figure 2.5(a). The growth rate is scaled with  $T_m$ , so a growth rate of 1 corresponds to an  $e$ -folding time scale of 150 years. The variable along the horizontal axis of Figure 2.5(a) is the non-dimensional alongshore wave number  $kL = 2\pi L/\lambda$ , where  $\lambda$  is the wavelength and  $L = 10$  km is the width of the inner shelf. The basic state is stable with respect to perturbations having small values of the dimensionless wave number, corresponding to wavelengths which are long compared to the width of the inner shelf. Perturbations with these wavelengths have negative growth rates and hence decay exponentially. For  $kL > 3$

the growth rate increases with increasing  $kL$  and for  $kL \sim 8$  the growth rate is zero. The wavelength of the perturbation with zero growth rate is called  $\lambda_0$ . In this case  $\lambda_0 = 7.9$  km. For  $kL > 8$  the growth rate is positive. Hence, there is a positive feedback between the coastline perturbation and the tidal flow. The growth rate curve does not show a maximum, so there is no fastest growing mode. For large wave numbers the growth rate tends to a constant.

The model also yields the phase speed of the perturbations. This phase speed is shown as a function of the dimensionless alongshore wave number in Figure 2.5(b). It has a minimum for  $kL \sim 5$  and decreases for larger  $kL$ . A nondimensional phase speed of  $-0.3$  is in dimensional values  $-20$  m/yr. A negative sign means that the perturbation is migrating in the negative  $y$ -direction, that is to the right when viewing in the seaward direction.

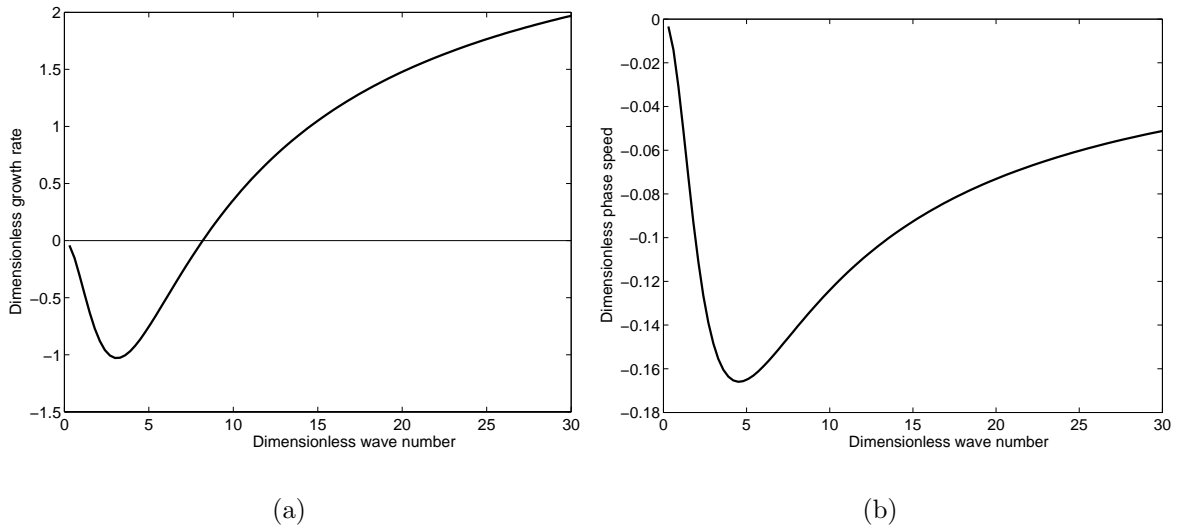


Figure 2.5: (a) Growth rate as a function of wave number for the reference case. A growth rate of 1 corresponds to an  $e$ -folding time scale of 150 years. Wave numbers are scaled with the width of the inner shelf, 10 km. (b) Phase speed as a function of wave number for the reference case. A phase speed of  $-0.3$  corresponds to a dimensional phase speed of  $-20$  m/yr.

The sediment transport  $q'_{(\text{curr})}$  is linear in the residual currents (Equation (2.25)). Figure 2.6(a) shows a vector plot of the residual currents on the inner shelf. Because the model does not yield a fastest growing mode, a wavelength is chosen that has a positive growth rate,  $\lambda = 3$  km ( $kL = 20.9$ ). Furthermore, because the model is linear in  $x'_t$  an amplitude is chosen of  $[x'_t] = 500$  m. Two residual circulation cells per alongshore wavelength appear. The structure of the residual circulation cells is such that the maximum convergence of the velocity at the transition line (and hence the convergence of the net sediment flux) is slightly out of phase (to the right when viewing in the seaward direction) with the coastline perturbation. The perturbation will therefore grow and migrate. The migration is forced by the Coriolis force. When  $f = 0$ , there is no phase difference between the residual velocities at the transition line and the coastline perturbation (Figure 2.6(b)). Hence, the perturbation does not migrate. The magnitude of the velocities is determined

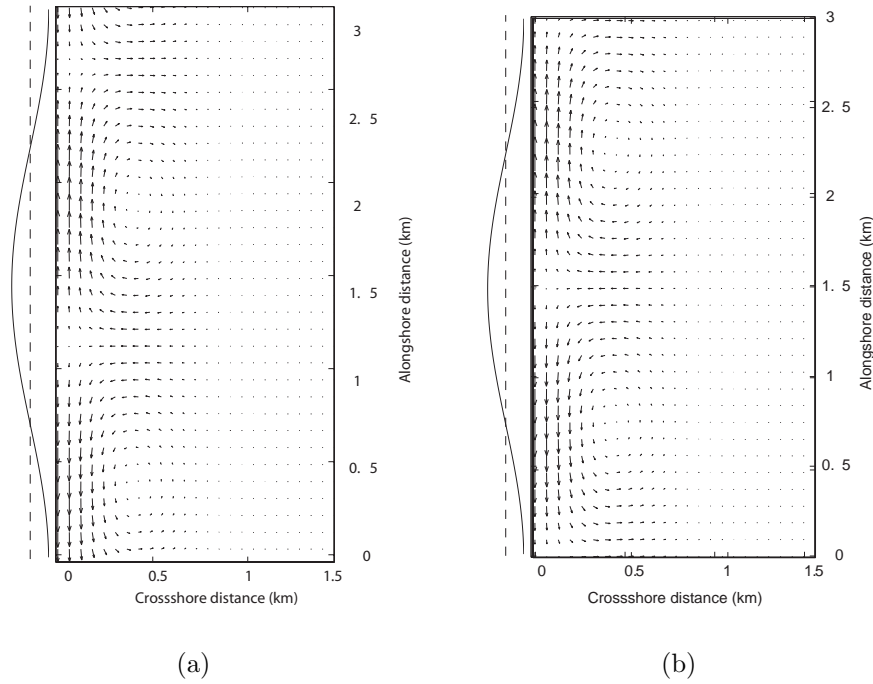


Figure 2.6: (a) Vector plot of residual currents for a perturbation of the coastline with alongshore wavelength  $\lambda = 3$  km ;reference case. The coastline perturbation is shown at the left-hand side. An amplitude of the coastline perturbation of  $[x'_t] = 500$  m has been chosen. This yields that  $\langle u' \rangle \sim \langle v' \rangle = 10^{-2} \text{ ms}^{-1}$ . The residual flow is such that the perturbation is amplified. In addition, the Coriolis force induces a migration of the perturbation.(b) Same as (a), but now the residual currents in the case of no Coriolis. In this case the coastline perturbation only grows and is not migrating.

by the amplitude of the coastline perturbation. This amplitude can be chosen arbitrarily.

### 2.4.2 Sensitivity of results to tidal current amplitude

Observations show that the shore-parallel tidal current amplitudes on the transition line vary between approximately  $0.1 \text{ ms}^{-1}$  and  $\sim 1 \text{ ms}^{-1}$  in regions where barrier islands are observed. In the reference case the maximum tidal velocity at the transition line was  $0.5 \text{ ms}^{-1}$ . In the next experiment the magnitude of the basic state tidal velocity at the transition line is varied between  $0.1$  and  $1.0 \text{ ms}^{-1}$ . A change in the magnitude of the basic state velocity causes a change of the magnitude of the friction parameter  $r$ , defined in Equation (2.4). The friction parameter scales linearly in the magnitude of the tidal velocity. All other parameters have the same values as in the reference experiment.

The influence of the magnitude of the tidal currents at the transition line ( $U$ ) on the growth rate is shown in Figure 2.7(a). Larger values of  $U$  result in larger growth rates for large  $kL$ . Furthermore, a larger velocity magnitude results in a larger  $\lambda_0$ . Hence, coastline perturbations with larger length scales grow exponentially in time. For  $U = 0.1 \text{ ms}^{-1}$   $\lambda_0 = 4.6$  km, while for  $U = 1 \text{ ms}^{-1}$   $\lambda_0 = 10.3$  km.

A change the magnitude of the tidal currents at the transition line ( $U$ ) leads to only

a moderate change of the phase speed (Figure 2.7(b)). The plot reveals that a change in  $U$  will not influence the phase speed of the coastline perturbation for small wavelengths. For larger wavelengths the tidal current amplitude does influence the phase speed. A smaller tidal current results in a smaller phase speed. However, a doubling of the tidal current amplitude with respect to the reference experiment hardly affects the phase speed for small  $kL$ .

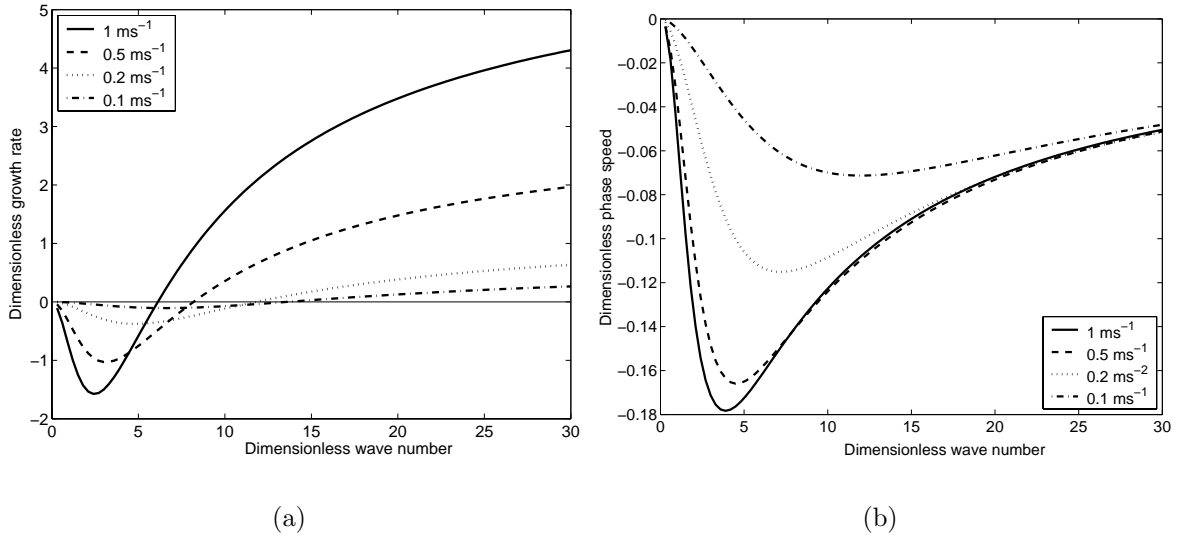


Figure 2.7: (a) Growth rate curves for different values of the magnitude of the basic state tidal  $M_2$  flow at the transition line. The magnitude of  $U$  is 0.1, 0.2, 0.5 and  $1.0 \text{ ms}^{-1}$ , respectively. A dimensionless growth rate of 1 corresponds to time scale of 150 years and alongshore wave number is scaled with 10 km. (b) Same as (a), but now the phase speed as a function of the wave number. A non-dimensional phase speed of  $-0.3$  is in dimensional values  $-20 \text{ m/yr}$ .

In a second series of experiment, a time-invariant pressure gradient  $S_0$  was prescribed. Hence, the basic state velocity has a residual component on top of the tidal component. The profile is described by Equation (2.17b). The residual pressure gradient is chosen such that  $V_0(x = X_t)$  is varied between  $0.02$  and  $-0.02 \text{ ms}^{-1}$ . This implies that the residual currents far offshore are varied between  $-0.1$  and  $0.1 \text{ ms}^{-1}$  for the reference bathymetry. All other parameters have their reference values. Results are shown in Figure 2.8. Growth rates of perturbations of the coastline are hardly affected by this small basic state residual current. The phase speed, however, is strongly influenced by the basic state residual current. For  $V_0(x = X_t) = -0.02 \text{ ms}^{-1}$  all perturbations are migrating to the right (when viewing in seaward direction). For smaller wavelengths (larger  $kL$ ) the phase speed is larger. For  $V_0(x = X_t) = 0.02 \text{ ms}^{-1}$  the perturbations are migrating to the right for  $\lambda > 9.5 \text{ km}$  ( $kL < 6.6$ ) and for  $\lambda < 9.5 \text{ km}$  ( $kL > 6.6$ ) the perturbations are migrating to the left.

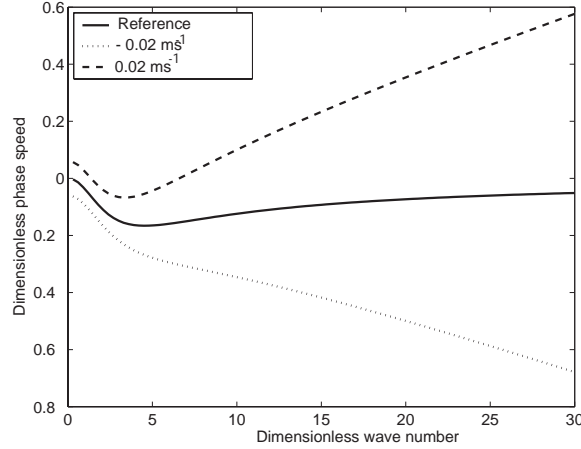


Figure 2.8: Phase speed as a function of the wave number for different values of the residual current amplitude at the transition line ( $V_0(x = X_t)$ ). Non-dimensional phase speed of  $-0.3$  is  $-20$  m/yr in dimensional values. Alongshore wave number is scaled with a length of 10 km.

### 2.4.3 Sensitivity of results to bathymetric parameters

The bathymetry of the inner shelf influences the basic state velocity profile. Therefore, in this section the sensitivity of the results to the bathymetric parameters (in particular  $L$  and  $H_0$ ) is studied. In the first experiment the length of the inner shelf is varied with all other parameters having their reference values. Experiments show that a steeper profile results in smaller values of  $\lambda_0$  (Figure 2.9(a)). The dependence of  $\lambda_0$  on  $L$  is almost linear. Not only  $\lambda_0$  changes, but also the growth rate. For small values of  $L$ , growth rates are larger for small wavelengths compared to the reference case. For relatively large values of  $L$ , growth rates are smaller for small wavelengths compared to the reference case. The sensitivity of the phase speed to  $L$  is shown in Figure 2.9(b). The magnitude of the phase speed is larger when  $L$  is smaller. For  $L = 5$  km the phase speed has a maximum of 16 m/yr for  $\lambda = 12.6$  km ( $kL = 5$ ).

In another series of experiments the value of  $H_0$  was changed. When  $H_0$  is changed the value of  $\beta$  has to be changed as well. Parameter  $\beta$  can be interpreted as the volume per unit length in the alongshore direction of sediment that is in suspension in the nearshore zone (see Equation (2.9)). It is assumed that the steepness of the nearshore zone is constant and that the average concentration in the nearshore zone does not change with changing  $H_0$ . From this it follows that  $\beta \sim H_0^2$ . Furthermore, when  $H_0$  is changed and the alongshore sea surface gradient  $S_2$  is kept fixed, the magnitude of the friction parameter  $r$  should be changed as well. However, it is assumed that the profile of the basic state velocity is not changed, which implies that the velocity profile is such that the tidal current amplitude is  $0.5 \text{ ms}^{-1}$  at 5 meters depth. The friction parameter  $r$  and the amplitude of the  $M_2$  pressure gradient  $S_2$  keep their reference values.

The results of Figure 2.10(a) show that a smaller  $H_0$  results in a shift of  $\lambda_0$  to smaller wavelengths. For small wavelengths a smaller  $H_0$  results in larger growth rates, compared to the reference case (Figure 2.10(a)). The influence of  $H_0$  on the phase speed is shown in Figure 2.10(b). An increase of  $H_0$  with respect to the reference experiment results in

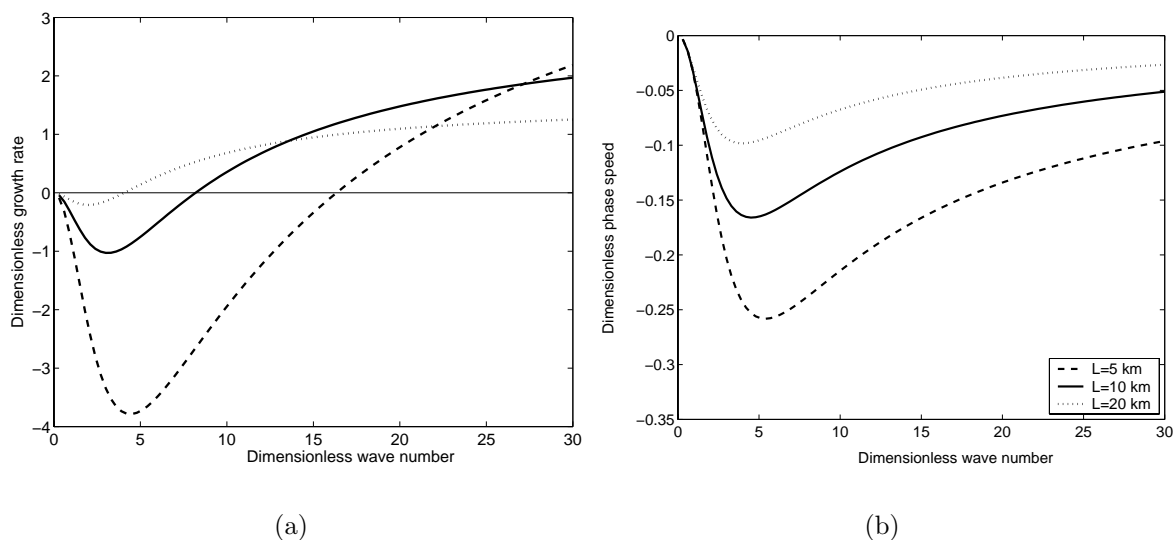


Figure 2.9: (a) Growth rate curves for  $L = 5$  km (dashed line),  $L = 10$  km (solid line) and  $L = 20$  km (dotted line). A dimensionless growth rate of 1 corresponds to time scale of 150 years and alongshore wave number is scaled with 10 km. (b) Same as (a), but now the phase speed as a function of the wave number. A dimensionless phase speed of  $-0.3$  corresponds to a dimensional phase speed of  $-20$  m/yr.

an increase of the phase speed. A decrease of  $H_0$  results in a decrease of the phase speed. The phase speed is in the order of 10 m/yr.

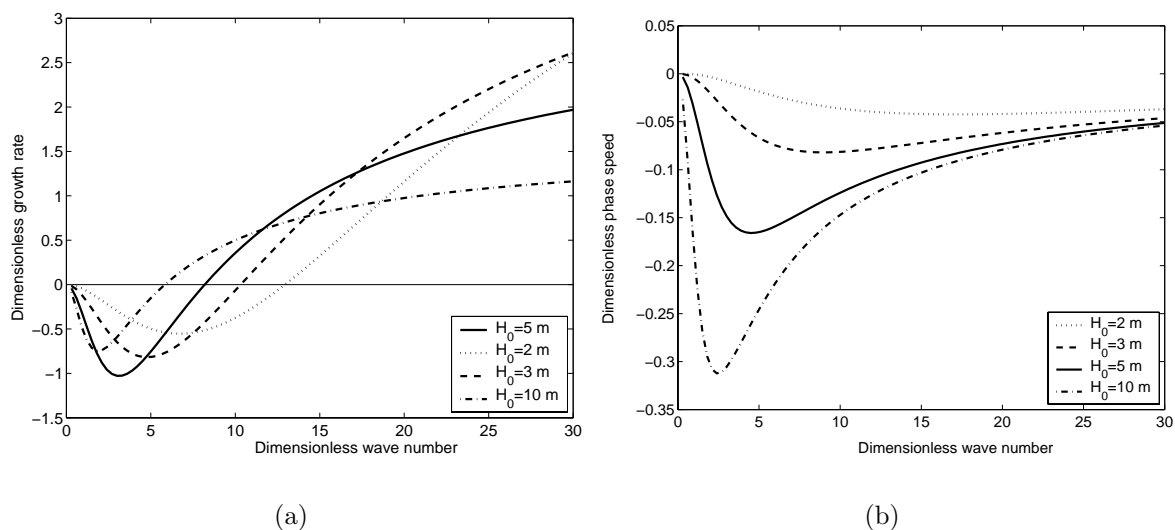


Figure 2.10: (a) Growth rate curves for different values of  $H_0$ . A dimensionless growth rate of 1 corresponds to time scale of 150 years and alongshore wave number is scaled with 10 km. (b) Same as (a), but now the phase speed as a function of the wave number. A dimensionless phase speed of  $-0.3$  is in dimensional values  $-20$  m/yr.

### 2.4.4 Influence of waves on the instability mechanism

In all the previous experiments, i.e. with significant tidal currents and  $\gamma = 0$ , no fastest growing mode was obtained. Hence, the model can not explain why undulations of the coastline have preferred length scales, as field data indicate. Furthermore, the growth rates are largest for the smallest wavelengths, which implies that perturbations with an infinitesimal small length scale will grow fastest. Hence, the model is missing a mechanism that results in decay of the perturbations with the smallest length scale. By accounting for a net volumetric sand flux due to obliquely incident waves ( $q'_{(\text{wave})}$ ), a selection mechanism for the growing perturbations is introduced. In the model of *Komar* (1998) the divergence the sediment transport due to waves is modeled as a diffusive term and it causes a decay of the perturbations. This decay is fastest for the smallest length scales. In the next experiment the diffusivity of coastline perturbations due to waves is included. Two types of experiments are presented. In the first experiment the diffusion coefficient  $\gamma$  due to waves is constant while the magnitude of the alongshore tidal currents is varied. In the second experiment the magnitude of the alongshore tidal currents is constant and the value of  $\theta_b$  is varied, thereby causing a change of diffusion coefficient  $\gamma$  (Equations (2.12) and (2.28)).

In all the previous experiments  $\theta_b$  was  $45^\circ$ . This yielded that  $q'_{(\text{wave})} = 0$ . In the following experiments  $H_b = 1$  m is taken and a different value for  $\theta_b$  is assumed. In the first experiment the diffusion parameter is  $\gamma = 2 \cdot 10^{-5} \text{ m}^2\text{s}^{-1}$ , while other parameters settings are as in the reference experiment. This diffusion parameter is obtained for  $H_b = 1$  m and  $\theta_b = 44.94^\circ$ . Results show that a fastest growing mode occurs (Figure 2.11). For  $U = 0.5 \text{ ms}^{-1}$  this occurs for  $\lambda = 2.6$  km. The time scale on which these perturbation grow is 130 years. The perturbation migrates 5 meters per year. For  $U = 0.8 \text{ ms}^{-1}$  a fastest growing mode is obtained at  $\lambda = 2.26$  km, with a typical  $e$ -folding growth rate of 60 years. The phase speed is again 5 meters per year. For  $U = 0.3 \text{ ms}^{-1}$  a fastest growing mode is obtained at  $\lambda = 2.94$  km, with a typical  $e$ -folding growth rate of 470 years.

In the second experiment the shore-parallel tidal currents at the transition line are  $U = 0.5 \text{ ms}^{-1}$ . All other parameters have their reference magnitude. The wave influence is varied by changing the magnitude of the diffusion parameter. The results show that for increasing wave influence and constant magnitude of the alongshore tidal currents, the preferred length scale of the undulations increases (Figure 2.12). The preferred length scale for  $\gamma = 2 \cdot 10^{-5} \text{ m}^2\text{s}^{-1}$  ( $\theta_b = 44.94^\circ$ ) is  $\lambda = 2.6$  km and the corresponding time scale is 130 years. For  $\gamma = 6 \cdot 10^{-5} \text{ m}^2\text{s}^{-1}$  ( $\theta_b = 44.83^\circ$ ) a fastest growing mode is obtained for  $\lambda = 3.6$  km, with a typical growth rate of 380 years. For  $\gamma = 1 \cdot 10^{-4} \text{ m}^2\text{s}^{-1}$  ( $\theta_b = 44.71^\circ$ ) the preferred wavelength is  $\lambda = 4.8$  km (however, the growth rate is negative).

The fastest growing mode with the largest length scale is obtained for  $H_0 = 10$  m,  $H_s = 20$  m,  $L = 20$  km,  $U = 1 \text{ ms}^{-1}$  and  $\gamma = 8 \cdot 10^{-4} \text{ m}^2\text{s}^{-1}$  ( $\theta_b = 40.42^\circ$ ). In that case a fastest growing mode is obtained for  $\lambda \sim 14$  km.

## 2.5 Comparison model results with observations

In this section the model results are compared with observations. The predicted dependence of the length scale of the fastest growing mode (FGM) on the magnitude of the tidal currents is compared with the observed trend along the Dutch and German Wadden

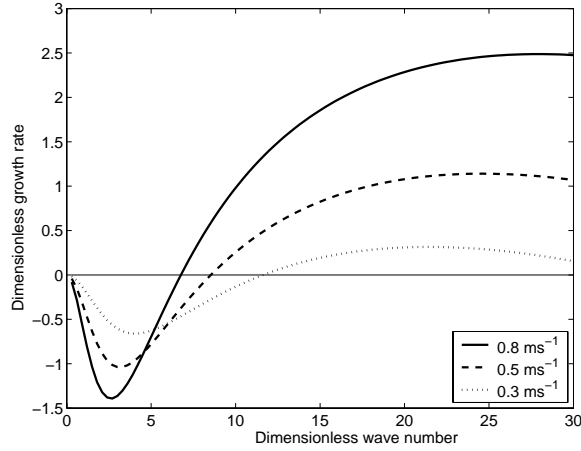


Figure 2.11: Growth rate curves for constant values of the diffusion coefficient related to waves ( $\gamma = 2 \cdot 10^{-5} \text{ m}^2\text{s}^{-1}$ ) and varying the magnitude of  $U$ .

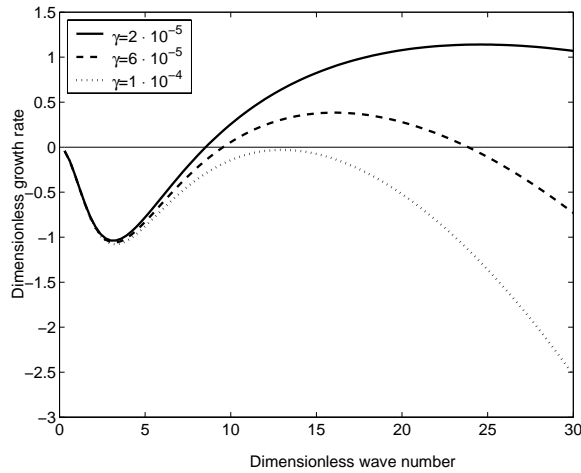


Figure 2.12: Growth rate curves for different values of diffusion coefficient  $\gamma$  caused by waves and constant strength of tidal currents ( $U = 0.5 \text{ ms}^{-1}$ ).

coast and in the Georgia Bight.

The length of the barrier islands along the Dutch and German Wadden Sea varies between a few kilometers (Simonszand and Rottumeroog) up to 30 kilometer (Texel) (Ehlers, 1988; Oost and de Boer, 1994). The typical migration speed of the islands is in the order of tens of meters per year and migration is from west to east Luck (1975). The length scales of the FGM obtained with the model have the correct order of magnitude. The typical length scale ranges from zero up to 15 kilometer. The predicted migration rates are also in accordance with the observed ones and vary between 5 and 24 meters per year, depending on the specific parameter values. The model also predicts that the perturbations are migrating to the east.

An important finding of the model is that the preferred length scale decreases with increasing magnitude of the tidal currents  $U$ . To test this result, observed wave and tidal characteristics along the Dutch and German Wadden coast were analyzed. It has



been argued by *Sha* (1989a) that the wave influence is constant along the Frisian Islands. Unfortunately, there are not many observations of the magnitude of the alongshore tidal currents at sea. Instead, the results of a numerical model were used. This is the ZUNO model from WL—Delft Hydraulics (*Roelvink et al.*, 2001), a model that has been developed to predict tidal heights and depth-averaged tidal currents in the southern North Sea. Figure 2.13(a) shows the major axis of the  $M_2$  tidal current ellipse in the region of the Frisian Islands. The magnitude of the major axis in the regions close to the tidal inlets are strongly influenced by the dynamical interaction between the backbarrier basin and the ebb-tidal delta. Therefore, the magnitudes of the major axis far offshore are considered. It is assumed that these are representative for the situation that the coastline is straight and no tidal inlets are present. Two transects (see the two lines in Figure 2.13(a)) of the major axis of the  $M_2$  tidal current ellipse are shown in Figure 2.13(b). These transects show that the long axis is increasing from Texel to Schiermonnikoog. Here the long axis has a maximum. From thereon it decreases when going to the island of Spiekeroog. The length of the barrier islands in this region is slightly larger than it is in the region just after Schiermonnikoog. The length scale of the barrier islands seems to be inversely related to the magnitude of the shore-parallel tidal currents. This is in agreement with model predictions.

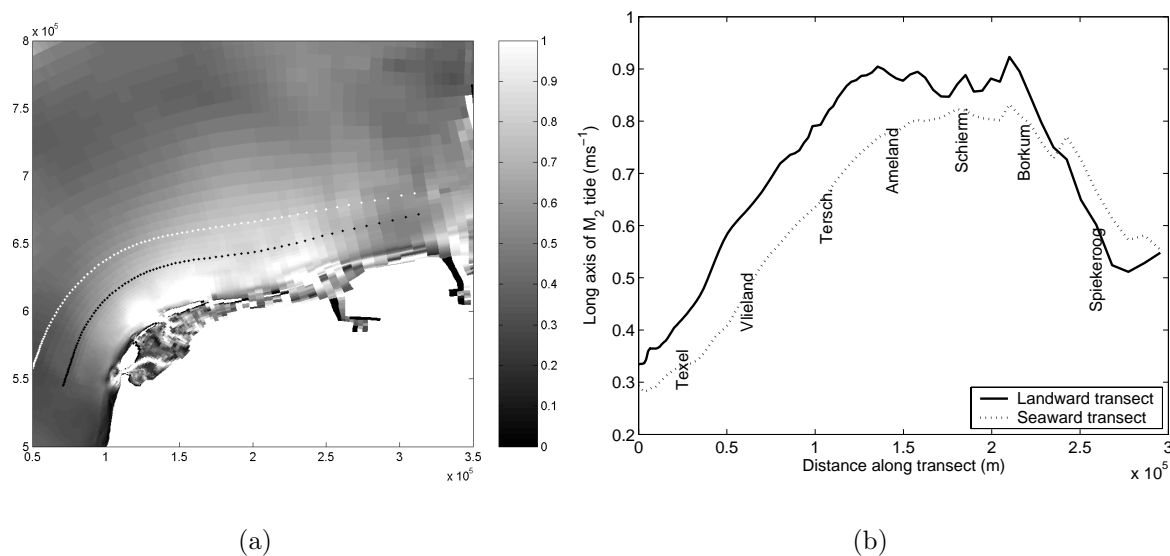


Figure 2.13: (a) Major axis of the  $M_2$  tidal current ellipse in the region of the Frisian Islands. Model results are obtained with numerical model (ZUNO). White diamonds show seaward transect while black diamond show landward transect. (b) Two transects of the major axis of the  $M_2$  tidal current ellipse in the region of the Frisian Islands. The two transects are shown in panel (a).

Finally, the model results are compared with observations in the Georgia Bight. In this area the magnitude of the tidal height and the tidal currents increases and wave influence decreases from the shelf of North Carolina towards the shelf of Georgia (*FitzGerald*, 1996; *Blanton et al.*, 2004). The model results predict that both the decreasing wave influence

and the increasing tidal current amplitude will result in smaller length scales of the barrier islands. This is in gross agreement with the observed trend in the length of the barrier islands in the Georgia Bight.

## 2.6 Physical interpretation

It was shown that for the default settings of the model parameters, perturbations with wavelengths  $\lambda > 8$  km have negative growth rates, while for  $\lambda < 8$  km the growth rate is positive. The perturbations not only grow but also migrate to the right when viewing in the seaward direction. When wave effects are included in the calculation of the alongshore sediment flux, a fastest growing mode is obtained. In this section these results are explained in terms of basic physical mechanisms. The following aspects are discussed:

- Why do perturbations decay for long wavelengths and grow for small ones?
- Why do perturbations migrate?
- Why are the growth rates small?
- What is the physical explanation behind sensitivity of the results to basic state bathymetry and velocity?

### 2.6.1 Growth and migration of perturbations

In this section the physical mechanism behind the growth and decay of the coastline perturbations is studied, with the focus on the role of tides in this process. The influence of wave-induced alongshore sediment fluxes on the evolution of perturbations of the coastline has already been discussed in *Komar* (1998).

The growth and migration of the perturbations are due to the divergence of the volumetric sediment flux  $q'_{\text{curr}}$  as defined in Equation (2.25). This flux is linearly related to the tidally averaged velocity at the transition line, which is related to circulation patterns (see Figure 2.6(a) and 2.6(b)) on the inner shelf. The physics causing the generation of residual circulation cells will be analyzed using vorticity concepts in a similar way as described in *Zimmerman* (1981). The vorticity balance for the perturbed variables, retaining only linear terms, is obtained by taking the  $x$ -derivative of Equation (2.21b) and subtracting the  $y$ -derivative of Equation (2.21a):

$$\underbrace{\frac{\partial \omega'}{\partial t}}^{(a)} + \underbrace{\frac{\partial (u' \Omega)}{\partial x}}^{(b)} + \underbrace{\frac{\partial (V \omega')}{\partial y} + \frac{\partial (v' \Omega)}{\partial y}}^{(c)} - \underbrace{\frac{r}{H^2} \frac{dH}{dx} v'}^{(d)} + \underbrace{f \left( \frac{\partial u'}{\partial x} + \frac{\partial v'}{\partial y} \right)}^{(e)} = \underbrace{\frac{-r \omega'}{H}}^{(f)} \quad (2.35)$$

Here,  $\Omega = \partial V / \partial x$  is the vorticity of the basic state flow and  $\omega' = \partial v' / \partial x - \partial u' / \partial y$  is the vorticity of the perturbed flow. In Equation (2.35), term (a) models the local time evolution of the perturbed vorticity, term (b) the cross-shore gradient of the perturbed vorticity flux in the cross-shore direction, term (c) the alongshore gradient of the perturbed vorticity flux in the alongshore direction, term (d) the generation of perturbed vorticity by the frictional torque, term (e) the generation of perturbed vorticity due to vortex stretching of the planetary vorticity and term (f) the dissipation of perturbed vorticity due to friction.

### Generation of tidally averaged vorticity

Residual currents are organized in cells with cyclonic (anticyclonic) circulation. These cells are areas where the tidally averaged perturbed vorticity is positive (negative). To obtain the relation between the perturbation of the coastline and residual current at the transition line, it is thus important to study the tidally averaged vorticity balance. The latter follows from averaging Equation (2.35) over the tidal period and reads

$$-\overbrace{\left[\frac{\partial}{\partial x}\langle u'\Omega \rangle + \frac{\partial}{\partial y}\langle V\omega' \rangle + \frac{\partial}{\partial y}\langle v'\Omega \rangle\right]}^1 + \overbrace{\frac{r}{H^2}\frac{dH}{dx}\langle v' \rangle}^2 + \overbrace{\frac{f}{H}\frac{dH}{dx}\langle u' \rangle}^3 = \overbrace{\frac{r}{H}\langle \omega' \rangle}^4 \quad (2.36)$$

Here,  $\langle \rangle$  denotes an average over the tidal cycle, see Equation (2.8) for its definition. Also, the continuity equation (2.21c) has been applied here. The three source terms of tidally averaged vorticity are on the left-hand side of Equation (2.36). Term (1) describes the convergence of the tidally averaged perturbed vorticity flux, (2) the frictional torque due to alongshore currents over cross-shore sloping bathymetry and (3) the Coriolis torque due to vortex stretching. The right-hand side of Equation (2.36), term (4), describes the dissipation of residual perturbed vorticity due to friction.

Now, the different terms are estimated for a typical coastline perturbation of  $\lambda = 3$  km, tidal currents at the transition line with a magnitude of  $U = 0.5 \text{ ms}^{-1}$ , absence of residual currents at sea ( $V_0(x = X_t) = 0 \text{ ms}^{-1}$ ) and  $f = 0$ . The perturbation was already shown in Figure 2.6(b). For this perturbation it turns out that the magnitude of term (2) is much smaller than that of term (1) because the generated residual currents are much smaller than the  $M_2$  component of  $u'$  and  $v'$ . The main balance in Equation (2.36) is between the production of tidally averaged perturbed vorticity described by term (1) and the dissipation of it described by term (4).

So, to understand the generation of residual circulation cells the focus should be on term (1), which describes the gradient of three fluxes of vorticity. The first one is  $\langle u'\Omega \rangle$  and describes the mean flux of basic state vorticity by the perturbed cross-shore currents. The second one is  $\langle \omega'V \rangle$  and represents the mean flux of perturbed vorticity by the basic state alongshore currents. The third one is  $\langle v'\Omega \rangle$  and describes the mean flux of basic state vorticity by the perturbed alongshore currents.

Let us first consider the cross-shore gradient of  $\langle u'\Omega \rangle$ . During flood the basic state tidal currents are in the negative  $y$ -direction:  $V_2$  is negative, see Figure 2.14(a). Furthermore,  $\partial V_2/\partial x < 0$  and therefore  $\Omega < 0$ . The perturbed cross-shore velocity  $u'$  during ebb is  $180^\circ$  out of phase with the alongshore gradient of the coastline perturbation (see Figure 2.14(a), which shows the perturbed velocity vector  $\vec{u}'$ ). The vorticity flux  $u'\Omega$  is therefore in phase with the alongshore gradient of the coastline perturbation. Because the magnitude of  $u'\Omega$  is decreasing in the cross-shore direction, the cross-shore gradient of  $u'\Omega$  during flood results in areas on the inner shelf where vorticity is accumulating with a same sign as that of the alongshore gradient of the coastline perturbation. During ebb the value of  $V_2, \Omega$  and  $u'$  change sign. This results in the same sign of  $u'\Omega$  and in the same cross-shore gradient of  $u'\Omega$ . Hence, the cross-shore gradient of the mean cross-shore vorticity flux results in areas on the inner shelf characterized by mean perturbed vorticity

which has the same sign as that of the alongshore gradient in the coastline perturbation. In other words, residual circulation cell as sketched in Figure 2.14(b) are generated. The mean currents transport the sediment from areas where the coastline has accreted to areas where the coastline has eroded. This results in a decay of the perturbation of the coastline.

Next, let us consider the alongshore gradient of  $\langle v'\Omega \rangle$  and  $\langle V\omega' \rangle$ . During flood  $V_2 < 0$  and  $\Omega < 0$  (see above) and the perturbed alongshore velocity  $v'$  is  $180^\circ$  out of phase with the coastline perturbation (Figure 2.14(a)). The perturbed vorticity flux is  $v'\Omega$  is therefore in phase with the coastline perturbation. The alongshore gradient of  $v'\Omega$  is  $180^\circ$  out of phase with the alongshore gradient in the coastline perturbation and therefore leads to accumulation of vorticity with a sign that is opposite to that of the gradient of the coastline perturbation. This results in residual circulation cells as sketched in Figure 2.14(c). During ebb  $V_2, \Omega$  and  $v'$  change sign. This results in the same sign of  $v'\Omega$  and in the same alongshore gradient of  $v'\Omega$ . Hence, averaged over one tidal cycle the alongshore gradient of  $v'\Omega$  results in mean perturbed vorticity with a sign opposite to that of the alongshore gradient in the coastline perturbation. The mean currents transport the sediment from areas where the coastline has eroded to areas where the coastline has accreted. This results in a growth of the perturbation of the coastline.

The last contribution to the convergence of the mean vorticity flux is the alongshore gradient of  $\langle V\omega' \rangle$ . During flood, the perturbed vorticity  $\omega'$  is in phase with the coastline perturbation of the coastline and the perturbed vorticity flux is  $180^\circ$  out of phase with the coastline perturbation because  $V_2 < 0$ . Hence, following a similar argumentation as for the alongshore gradient of  $\langle v'\Omega \rangle$ , the alongshore gradient of  $\langle V\omega' \rangle$  results in residual circulation cells that cause a growth of the perturbation of the coastline.

Whether the residual circulation cells are located along the coast in such a way that the coastline perturbation is growing or decaying depends on the magnitudes of the cross-shore gradient of  $\langle u'\Omega \rangle$  and of the alongshore gradient of  $\langle v'\Omega \rangle$  and  $\langle V\omega' \rangle$ . For small wave numbers the magnitude of the cross-shore gradient of  $\langle u'\Omega \rangle$  is larger than the alongshore gradient of  $\langle v'\Omega \rangle + \langle V\omega' \rangle$  and therefore the locations of the residual circulation cells are such that the perturbations of the coastline decay. For increasing wave numbers the magnitude of the alongshore gradient of  $\langle v'\Omega \rangle$  and  $\langle V\omega' \rangle$  increases stronger than that the cross-shore gradient of  $\langle u'\Omega \rangle$ . When the magnitude of the alongshore gradient of  $\langle v'\Omega \rangle + \langle V\omega' \rangle$  is larger than the cross-shore gradient of  $\langle u'\Omega \rangle$ , the locations of the generated residual circulation cells along the coast are such that the perturbations of the coastline grow.

When the Coriolis force is nonzero ( $f \neq 0$ ) the perturbations also migrate. The Coriolis torque (term (e) in Equation (2.35)) is a source of tidal vorticity and causes a phase shift of the tidal vorticity with respect to the coastline perturbation. While in the case that  $f = 0$  the perturbed vorticity  $\omega'$  is in phase with the coastline perturbation during flood, in the case that  $f \neq 0$  the maximum of the perturbed vorticity  $\omega'$  is shifted in the negative  $y$ -direction with respect to the coastline perturbation due to planetary vortex stretching. The perturbed vorticity is transferred by the basic state velocity and the alongshore gradient of  $V\omega'$  results in the accumulation of perturbed vorticity which is slightly shifted in the negative  $y$ -direction compared to the case that  $f = 0$ . During ebb a similar argumentation holds and residual circulation cells occur of which the centers are shifted

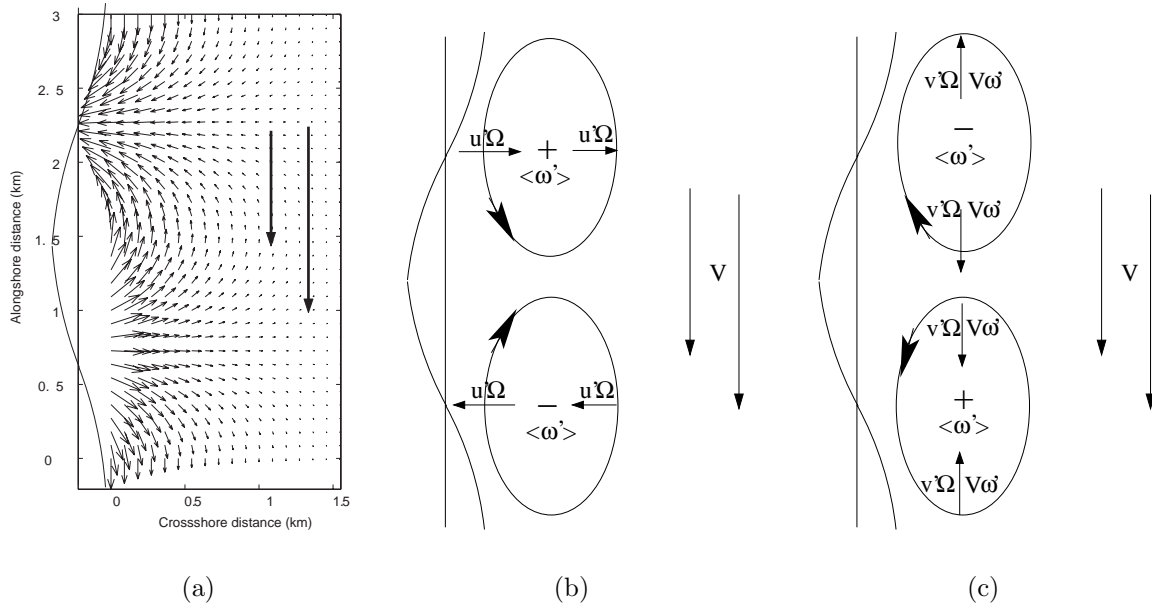


Figure 2.14: (a) Perturbed velocity induced by coastline at maximum flood. The basic tidal flow is from north to south (big arrows). The coastline perturbation has a cosine structure. (b) Small arrows represent perturbed cross-shore vorticity flux  $u\Omega$ . The cross-shore gradient of the vorticity in the cross-shore direction generates two residual circulation cells (denoted by the two counter rotating cells) that cause a decay of the coastline perturbation. (c) Same as (b), but now the alongshore gradient of the alongshore vorticity flux is visualized. Small arrows represent perturbed alongshore vorticity flux  $v\Omega$  and  $V\omega'$ . The alongshore gradient of the alongshore vorticity flux generates residual circulation cells that cause a growth of the coastline perturbation.

in the negative  $y$ -direction compared to those obtained in the case that  $f = 0$ . Hence, the residual circulation cells in the case that  $f \neq 0$  cause both growth and migration of the coastline perturbation.

## 2.6.2 Magnitude of growth rate for large wave numbers

An interesting result mentioned in the previous section is that for  $\gamma = 0$  the growth rate of perturbations with large wave numbers ( $kL \gg 1$ ) tends to a constant. In this section the physics underlying this behavior will be investigated. Starting point is Equation (2.27), which shows that for  $\gamma = 0$  the growth rate is proportional to  $\partial \langle v' \rangle / \partial y$  at the transition line. The latter term scales as  $k[V'_{res}]$ , where  $[V'_{res}]$  is the magnitude of  $\langle v' \rangle$  at the transition line. From the observed behavior of the growth rate for  $kL \gg 1$  it thus follows that

$$[V'_{res}] \sim (kL)^{-1} \quad \text{for } kL \gg 1$$

To understand this result, we next estimate for the large wave number case the scale of the residual velocity component  $\langle u' \rangle$  and from there the scale of the residual vorticity. The latter will allow a quantification of the main terms in the residual vorticity balance

(2.36).

The scale  $[u'_{res}]$  of  $\langle u' \rangle$  follows from continuity equation (2.21c). Using the observed fact that the cross-shore and longshore length scale of the perturbations are of the same order the result is

$$[U'_{res}] \sim (kL)^{-1} \quad \text{for } kL \gg 1$$

Since  $\omega' = \partial v'/\partial x - \partial u'/\partial y$  the magnitude  $[\omega'_{res}]$  of the residual vorticity obeys

$$[\omega'_{res}] \sim \text{constant} \quad \text{for } kL \gg 1$$

These results are used to analyze the residual vorticity balance (2.36). It was already argued that terms (1) and (4) are the dominant terms in this equation. Using this fact and applying the continuity equation yields the order estimate

$$\langle \omega' \rangle \sim \langle u' \frac{\partial \Omega}{\partial x} \rangle - \frac{1}{H} \frac{dH}{dx} \langle \Omega u' \rangle + \frac{\partial}{\partial y} \langle \omega' V \rangle$$

When  $kL \gg 1$  the magnitude of the first two terms on the right-hand side scale as  $kL$  because

$$[u'_{M2}] \sim kL \quad \text{for } kL \gg 1$$

due to boundary condition (2.22) and because the cross-shore length scale of the variables  $H$  and  $\Omega$  is the shelf width  $L$  rather than  $k^{-1}$ . Since  $\langle \omega' \rangle$  becomes constant in this parameter regime the last term on the right-hand side has to balance the first two terms. Consequently, the scale  $[\omega'_{M2}]$  of the perturbed vorticity  $\omega'_{M2}$  behaves as

$$[\omega'_{M2}] \sim \text{constant} \quad \text{for } kL \gg 1$$

The final point is to understand the behavior of  $[\omega'_{M2}]$  by considering the tidal vorticity balance. The latter is obtained by projecting the vorticity equation (2.35) onto the  $M_2$  tidal components. This yields

$$\frac{\partial \omega'_{M2}}{\partial t} + \langle u' \rangle \frac{\partial \Omega}{\partial x} - \frac{\Omega}{H} \frac{dH}{dx} \langle u' \rangle + V \frac{\langle \omega' \rangle}{\partial y} - \frac{r}{H^2} \frac{dH}{dx} v'_{M2} + \frac{r}{H} \omega'_{M2} = 0$$

Here,  $f = 0$  has been assumed and the continuity equation has been applied.

The magnitude  $[v'_{M2}]$  of  $v'_{M2}$  can be estimated from the continuity equation and using that boundary condition (2.22) implies that  $u'_{M2} \sim \partial x'_t / \partial y$ . The result is

$$[v'_{M2}] \sim (kL) \quad \text{for } kL \gg 1$$

Using all previous estimates of the magnitudes of the various variables in the case  $kL \gg 1$  shows that the main balance in the tidal vorticity equation is between the fourth and fifth term. This conclusion is also found if Coriolis parameter  $f$  is nonzero. The final picture is thus that the tidal frictional torque (the fifth term) generates tidal vorticity by balancing with the fourth term, which represents the alongshore gradient in the transfer of perturbed residual vorticity by the undisturbed tidal current. This residual vorticity is associated with a residual current pattern with magnitude of the velocity components that were given above and which result in the saturation of the growth rate curve (i.e.,  $\Gamma \sim \text{constant}$  for  $kL \gg 1$ ).

### 2.6.3 Sensitivity of model results to bathymetry

In Section 2.4.3 the sensitivity to the parameters  $L$  and  $H_0$  was shown. A larger  $L$  resulted in a shift of  $\lambda_0$  to larger values (Figure 2.9(a)). In addition, the growth rate and phase speed were smaller.

In the previous section it was shown that the value of  $\lambda_0$  is determined by the wave number for which the magnitude of the alongshore gradient in the mean alongshore perturbed vorticity flux equals the magnitude of the cross-shore gradient in the mean cross-shore perturbed vorticity flux. Increasing the width of the inner shelf ( $L$ ) results in a decrease of the magnitude of the cross-shore gradient of the mean cross-shore vorticity flux (both  $\Omega$  and  $\partial\Omega/\partial x$  decrease). Therefore, already for smaller values of the wave number the growth rate becomes positive. Furthermore, a larger  $L$  results in smaller growth rates because the basic state vorticity and perturbed vorticity are smaller. This results in a smaller mean perturbed vorticity flux and its convergence is also smaller. Hence, the magnitude of the residual currents, the magnitude of  $q'_{(\text{curr})}$  and the growth rate are smaller for a fixed value of the wavelength. In addition, a larger  $L$  implies that planetary vortex stretching is smaller and therefore the phase speed of the perturbations of the coastline decrease for increasing values of  $L$ .

An increase of  $H_0$  resulted in an increase of  $\lambda_0$  (Figure 2.10(a)). When varying  $H_0$ , the friction parameter  $r$  and the pressure gradient due to the gradient in the sea surface elevation  $S_2$  were not changed. When increasing  $H_0$ ,  $U$  at the transition line increases as well, while the magnitudes of  $\Omega$  and  $\partial\Omega/\partial x$  decrease. Consequently, for a fixed wavelength the magnitude of the alongshore gradient in the mean alongshore vorticity flux increases with respect to the cross-shore gradient of the mean cross-shore vorticity flux when  $H_0$  becomes larger. Therefore, already for smaller values of the wave number the growth rate becomes positive.

### 2.6.4 Sensitivity of model results to forcing conditions

The results of Section 2.4.2 show that an increase of the shore-parallel tidal currents results in an increase of  $\lambda_0$  and an increase of the growth rates (Figure 2.7(a)). This is because an increase of the basic state tidal velocity results in a linear increase of the friction parameter  $r$ . Furthermore, an increase of  $r$  results in an increase of the basic state vorticity and its gradient. Consequently, considering a perturbation with a fixed wavelength, both the cross-shore gradient of the mean perturbed vorticity flux in the cross-shore direction and the alongshore gradient of the mean perturbed vorticity flux in the alongshore direction increase when  $U$  becomes larger. This results in the generation of residual circulation cells with large magnitude of the residual currents and therefore to an increase of  $q'_{(\text{curr})}$  and the growth rate. Furthermore, because the alongshore gradient of the mean alongshore vorticity flux increases stronger than the cross-shore gradient of the mean cross-shore vorticity flux with increasing magnitude of  $U$ , also the wavelength with zero growth rate  $\lambda_0$  increases with increasing magnitude of  $U$ .

### 2.6.5 Fastest growing mode when wave flux is included

Including the influence of the volumetric sediment flux that is solely due to waves on the growth rate of the perturbations of the coastline has a considerable influence on the results. For certain parameter combinations a fastest growing mode is obtained (Figures 2.11 and 2.12). The reason why a fastest growing is obtained is straightforward. The alongshore gradient of the perturbed volumetric sediment flux  $q'_{(\text{wave})}$  cause a decay of the perturbations of the position of the coastline and this decay is quadratic in the wave number (Equation (2.27)). The tidal currents cause growth of the perturbations with wavelengths smaller than  $\lambda_0$ . The growth rate tends to a constant for decreasing wavelengths (increasing values of  $kL$ ). If the diffusion parameter due to the influence of waves (defined in Equation (2.28)) is too large, the perturbations decay for all wavelengths. When the diffusion parameter is zero no fastest growing mode is obtained. The influence of a very small diffusion parameter becomes noticeable for large wave numbers. For small wave numbers the growth rate of the perturbations is not affected by the waves and the growth rate increases for increasing wave numbers. For large wave numbers a positive value of the diffusion parameter causes the perturbations to decay and the growth rate decreases for increasing wave numbers. For moderate values of the wave number there exists a wave number for which the growth rate neither increase or decreases when the wave number is changed. This is the fastest growing mode. Increasing the wave influence causes an increase of the wavelength of the preferred mode. In a similar way it can be explained why for constant wave influence and increasing magnitude of the tidal currents the wavelength of the preferred mode decreases.

## 2.7 Discussion and conclusions

In this chapter a simplified model was developed to study and analyze the initial evolution of alongshore periodic perturbations on an otherwise alongshore uniform coastline. The aim was to study the dynamics behind the rhythmic occurrence of barrier islands and whether the dependence of the length scale could be understood in term of basic physical mechanisms. The new aspect of this study was the role of tides in the possible generation of these rhythmic coastline undulations. The model described in this study is meant as a natural extension of the one-line models of *Komar* (1998); *Falqués* (2003); *Falqués and Calvete* (2005), who only considered the influence of waves on the initial coastline development. The influence of waves on the growth rate of the alongshore rhythmic perturbation of the coastline was modeled as a diffusive process and the formulations of *Komar* (1998) are used. Since no nonlinear analysis has been carried out, no results are obtained that describe the finite-amplitude behavior of the coastline perturbations.

In the experiments described in Section 2.4.1-2.4.3 the evolution of the perturbations of the coastline under influence of tides only was studied. The results described in Section 2.4.1 show that for typical Dutch shelf conditions the growth rates are negative for long wavelengths,  $\lambda > 8$  km. For smaller wavelengths the growth rate is positive, i.e., the perturbation of the position of the coastline is amplified. Typical time scales of the growth rate are in the order of 100 years. The Coriolis force induces a migration of the perturbations in the order of 10 meter per year. The perturbations are migrating to the



right, when viewing in the seaward direction. Although the model results change qualitatively when parameters describing the bathymetry of the inner shelf and the magnitude of the basic state tidal currents are changed, the result that the growth rate is negative for large wavelengths and positive for small wavelengths is robust when varying these parameters.

The physical mechanism resulting in growth or decay of coastline perturbations and their migration rates can be understood with vorticity dynamics. There is a competition between the cross-shore gradient of the mean cross-shore vorticity flux, which acts stabilizing, and alongshore gradient of the mean alongshore vorticity flux, which acts destabilizing. The width of the inner shelf determines the cross-shore length scale over which the cross-shore vorticity fluxes vary, while the wavelength of the perturbation determines the length scale over which the alongshore vorticity fluxes vary. If the length scale in the alongshore direction is smaller than the length scale in the cross-shore direction, the growth rate is positive. When the alongshore length scale is larger than the cross-shore length scale, a negative growth rate is obtained.

When the diffusion parameter due to the influence of sediment transported by waves is zero, the model does not predict a fastest growing mode because no damping mechanism is present for the small-scale perturbations. Including the influence of waves on the stability of the coastline results in the emergence of a fastest growing mode. The model results predict that under constant wave conditions the preferred length scale is smaller in regions where the alongshore tidal currents are stronger. This is observed along the Frisian Islands (Figure 2.13(b)). Furthermore, the model predicts that an increase of the diffusion parameter due to waves, while keeping the tidal current amplitude constant, results in a fastest growing mode with a larger wavelength. Along the Georgia Bight, when moving from the shelf of North Carolina to the shelf of Georgia, wave influence decreases and the tidal current amplitude increases (Figure 1.4). The model predicts that both effects result in a decrease of the preferred length scale. This is also observed.

For a realistic range of parameter values, a wavelength of the fastest growing mode in the range of 0 to 15 kilometer is obtained. This is in the range of observed length scales of barrier islands. However, the growth rates are small, in the order of hundred years. The predicted migration rates are up to ten meters per year. When wave influence is too strong, no growing perturbations are found. When the expression of *Komar* (1998) for the diffusion parameter due to waves is used (Equation (2.28)), the results show that for waves with  $H_b$  of 1 m the maximum angle of incidence of the waves is  $40.42^\circ$ . For smaller values the diffusion parameter is too large to have coastline perturbations that grow. However, *Falqués* (2003); *Falqués and Calvete* (2005) argue that the diffusion parameter in the model of *Komar* (1998) is a strong overestimation. Furthermore, the growth rate due to tides only ( $\gamma = 0$ ) is also very small. As has been explained in Section 2.6.2, the alongshore gradient in the alongshore tidal vorticity flux counteracts the generation of tidal vorticity due to frictional torques. Therefore, for small wavelengths the generation of perturbed mean vorticity due to the perturbation of the position of the coastline is small and this results in the generation of only small residual currents. The predicted residual currents for a coastline perturbation of 500 meter and a wavelength of 3 km, are in the order of  $10^{-3} \text{ ms}^{-1}$ . The residual currents obtained with the present model seem to underestimate the magnitude of observed residual currents. Because the sediment flux

due to the influence of tides is linear in the mean alongshore velocity also the sediment flux due to tides is small and the evolution of the position of the coastline is small. Initial results suggest that adding horizontal turbulent mixing terms in the momentum equations increases the growth rate of coastline perturbations with at least a factor 10. In that case, the perturbations also grow when the diffusion parameter due to waves is much larger. Hence, a much smaller angle of incidence of the waves is possible. Still it is found that perturbations with small wavelengths grow and perturbations with long wavelengths decay.

## Appendix

### 2.A Parameters in the flow over topography problem

The parameters  $U_{ij}$  in Equation (2.31) read

$$U_{12} = 1 \quad (2.A-1a)$$

$$U_{11} = \frac{1}{H} \frac{dH}{dx} \quad (2.A-1b)$$

$$U_{10} = -k^2 + \frac{1}{H} \frac{d^2H}{dx^2} - \frac{1}{H^2} \left( \frac{dH}{dx} \right)^2 \quad (2.A-1c)$$

$$U_{02} = ikV + \frac{r}{H} \quad (2.A-1d)$$

$$U_{01} = \frac{ikV}{H} \frac{dH}{dx} \quad (2.A-1e)$$

$$\begin{aligned} U_{00} = & -ik^3V + \frac{ikV}{H} \frac{d^2H}{dx^2} - \frac{ikV}{H^2} \left( \frac{dH}{dx} \right)^2 \\ & + \frac{ik\hat{f}}{H} \frac{dH}{dx} + \frac{ik}{H} \frac{\partial V}{\partial x} \frac{dH}{dx} - ik \frac{\partial^2 V}{\partial x^2} \\ & - \frac{k^2r}{H} + \frac{r}{H^2} \frac{d^2H}{dx^2} - \frac{2r}{H^3} \left( \frac{dH}{dx} \right)^2 \end{aligned} \quad (2.A-1f)$$

# Chapter 3

## Modeling of equilibrium tide-dominated ebb-tidal deltas

### Abstract

This study focuses on identifying physical mechanisms that lead to symmetric, tide-dominated ebb-tidal deltas. An idealized morphodynamic model is developed and analyzed to demonstrate that these deltas can be modeled as morphodynamic equilibria (no evolving bathymetry). It is assumed that the large-scale alongshore tidal currents are small compared to the cross-shore tidal currents, waves have shore-normal incidence, the tidal velocity profile over the inlet is symmetric with respect to the mid-axis and that Coriolis force can be ignored. The modeled tidal hydrodynamics are characterized by an ebb-jet during the ebb-phase of the tide and a radial inflow pattern during flood. Two residual eddies are formed. The mechanism behind these current patterns is explained with vorticity concepts. The modeled bottom patterns are similar to those of observed symmetric tide-dominated ebb-tidal deltas. In the center of the tidal inlet an ebb-dominated channel is observed that branches further off-shore into two flood-dominated channels. At the end of the ebb-dominated channel a shoal is present. Varying the tidal prism, the width of the tidal inlet, the wave height and the bed-slope coefficient in the sediment transport formulation within the range of observed values, leaves these patterns qualitatively unchanged. However, the exact extent and shape of the modeled deltas are affected by these parameters. Compared to observations, the modeled ebb-tidal delta is smaller and the ebb-dominated channel is shorter. The observed exponent in the power-law relation between sand volume of the delta and the tidal prism is recovered and explained with the model.

### 3.1 Introduction

Ebb-tidal deltas are complex, highly dynamic, morphologic structures situated at the seaward side of tidal inlets. They are observed in many parts of the world (*Ehlers*, 1988; *Sha*, 1989a; *Oost and de Boer*, 1994; *FitzGerald*, 1996). The deltas are located at the seaward end of the main ebb-dominated channel (i.e., a channel with stronger peak currents during the ebb-phase than during the flood-phase) and are flanked by two adjacent flood-dominated channels (*Hayes*, 1975). The typical horizontal extent of the ebb-tidal delta ranges from a minimum of  $\sim 200$  m (inlets along the Florida coast, (*Davis*, 1997; *FitzGerald*, 1996)) to a maximum of  $\sim 5$  km (Texel delta, Dutch Wadden Sea (*Oost and de Boer*, 1994)). Field data reveal an almost linear relationship between the tidal prism (i.e., the volume of water entering the tidal inlet during one tidal cycle) and the volume of sand stored in the delta (*Walton and Adams*, 1976; *Sha*, 1989a). Necessary conditions for the emergence of ebb-tidal deltas are a sandy bottom and the presence of strong tidal currents. Apart from tidal currents, waves are often an important constituent of the water motion in the region of the ebb-tidal delta (*Ranasinghe and Pattiaratchi*, 2003). Analysis of field data has resulted in three major classes of deltas (*Gibeaut and Davis Jr.*, 1993): tide-dominated, mixed-energy and wave-dominated deltas.

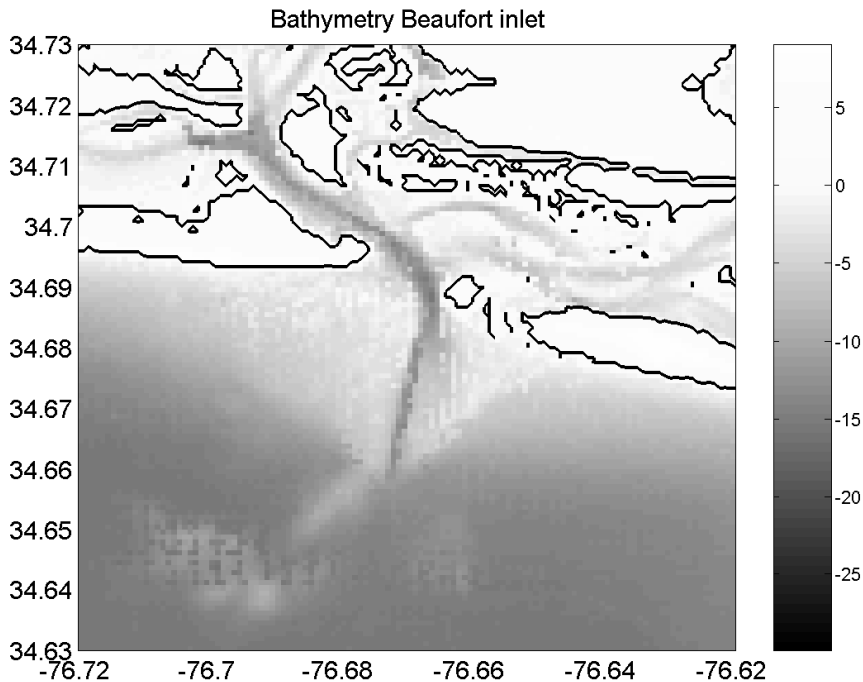


Figure 3.1: The bathymetry of Beaufort Inlet, North Carolina, USA. The depth is in meters. The black line denotes the zero contour line. The width of the inlet is  $B = 1$  km. The data are taken from NOAA's Coastal Relief Model (<http://www.ngdc.noaa.gov/mgg/gdas>).

The aim of the present study is to gain fundamental knowledge about the physical mechanisms that cause the presence of ebb-tidal deltas. To limit the scope of the study the focus is on tide-dominated ebb-tidal deltas characterized by small alongshore tidal

currents compared to the cross-shore currents. Such deltas have an almost symmetric shape with respect to the mid-axis of the inlet and therefore are the simplest features that can be studied. Prototypes of such inlets are found along the US east coast, for example in North and South Carolina, Georgia and Florida (*FitzGerald*, 1996; *Davis*, 1997).

Field data of velocity profiles over an inlet reveal maximum currents in the middle and vanishing currents near the sides (*Chadwick and Largier* (1999), for San Diego Inlet). Furthermore, laboratory experiments show that the flow patterns during ebb and flood are quite different (*Wells and Van Heyst*, 2003). During ebb the outflow from inlet to sea is jet-like, while during flood the inflow is radial.

In only a few studies process-based models have been used to study the dynamics of ebb-tidal deltas. Most of these studies focus on the hydrodynamics (*Stommel and Farmer*, 1952; *Awaji et al.*, 1980; *van Leeuwen and de Swart*, 2002; *Hench and Luettich*, 2003). These studies identified and explained the observed asymmetry in flow patterns seaward of tide-dominated inlets during flood and ebb. They also demonstrated the existence of residual circulation cells at the seaward side of the tidal inlet.

The morphodynamics of ebb-tidal deltas have been studied less extensively. Symmetric deltas are believed to form when the ebb-jet removes sediment from the entrance of the inlet and deposits it on the seaward side (*Oertel*, 1972; *FitzGerald*, 1996). State-of-the-art process-based models have been used to study the morphodynamic evolution of asymmetric ebb-tidal deltas under various forcing conditions (*Wang et al.*, 1995; *Ranasinghe and Pattiaratchi*, 2003; *van Leeuwen et al.*, 2003; *Siegle et al.*, 2004). However, in these studies the concepts as discussed by *Oertel* (1972); *FitzGerald* (1996) were not reproduced and the exact mechanisms that cause and maintain ebb-tidal deltas were not identified.

In view of the aim of the present study, the results of *van Leeuwen et al.* (2003) are of special interest, since they suggest that ebb-tidal deltas can be interpreted as morphodynamic equilibrium solutions (no evolution in time of the bottom), even in the absence of waves. They simulated the temporal evolution of the bathymetry of a tidal inlet system, starting from a state without a delta. During the simulation an asymmetric ebb-tidal delta developed and after a long time ( $\sim 500$  years) the bathymetric changes decreased. Due to numerical resolution problems a true morphodynamic equilibrium was not reached.

Motivated by these results, the specific objectives of the present paper are twofold. The first is to develop a morphodynamic model that contains only the physical processes that are essential for the existence of an equilibrium bathymetry that resembles an ebb-tidal delta. The bottom pattern together with the corresponding hydrodynamics and sediment transport patterns comprises a so-called a morphodynamic equilibrium. The second objective is to investigate the characteristics of the modeled bottom patterns (e.g. channel-shoal pattern, sand volume, ...) and compare them with field data of ebb-tidal deltas. Since the focus of this study is on gaining fundamental knowledge rather than a detailed simulation of the features, an idealized model will be developed and analyzed. The idealized model describes explicit feedbacks between the water motion and the sandy bottom in case of symmetric tide-dominated inlets. All processes that cause asymmetry (Coriolis force, obliquely incident waves, large-scale pressure gradients in alongshore direction) are ignored.

To obtain equilibrium solutions of the model a continuation technique is used. This technique is often used in dynamical systems theory to explore the dependence of solutions on parameter values (*Manneville, 1990*). It was successfully applied in *Schuttelaars and de Swart (2000)* and *Schramkowski et al. (2004)* to compute morphodynamic equilibria in sheltered tidal embayments.

The results of the idealized morphodynamic model are compared with both the observations and the results of a hydrodynamic modeling study of the Beaufort Inlet (North Carolina, USA, *Hench and Luettich (2003)*). The bathymetry of Beaufort Inlet is shown in Figure 3.1. The inlet has a width of  $B = 1$  km. The ebb-tidal delta is almost symmetric with respect to the mid-axis through the inlet. The ebb-channel is maintained at a depth of 10 m. The region of the ebb-tidal delta is shallow with typical depth of 2 – 10 m. Maximum  $M_2$  cross-shore currents are in the order of  $1 \text{ ms}^{-1}$ .

The paper is organized as follows. In section 3.2 the physical model is described. The methods that are used to calculate the morphodynamic equilibria are introduced in section 3.3. In section 3.4 the results are presented. The sensitivity of results to model parameters is studied in both section 3.4 and 3.5. The physical mechanisms are studied in section 3.6. Section 3.7 contains the discussion and the conclusions.

## 3.2 Model

### 3.2.1 Domain

The model domain consists of a coastal sea that is bounded by a straight coast bisected by one inlet with width  $B$ . A Cartesian coordinate system is chosen, with the  $x, y, z$ -axes pointing in the cross-shore, alongshore and vertical direction, respectively. The coastline is located at  $x = 0$ , while the center of the inlet is located at  $(x, y) = (0, 0)$  (Figure 3.2(a)). The location of the bottom is denoted by  $z = -H$ , where  $H$  is the water depth with respect to  $z = 0$ . In the regions far away from the inlet the water depth is assumed to be alongshore uniform with a constant depth  $H_0$  at the coast and increasing exponentially to  $H_s > H_0$  at the shelf break (Figure 3.2(b)). Figure 3.3 shows three cross-shore profiles taken along stretches of the eastern US-coast that are relatively far away from any tidal inlet. The profiles can be approximated by

$$H_R(x) = H_0 + (H_s - H_0)(1 - e^{-x/L_s}) \quad (3.1)$$

Equation (3.1) is fitted to the three profiles, which yields values of  $H_0 \sim \mathcal{O}(1 - 10)$  m,  $H_s \sim \mathcal{O}(15 - 25)$  m and  $L_s \sim \mathcal{O}(10 - 25)$  km.

### 3.2.2 Hydrodynamics

#### Waves

Waves stir sediment and thereby contribute to the net (tidally averaged) transport of sediment. Furthermore, the wave-orbital motion at the bed causes an increase of the bottom friction experienced by the tidal currents. To describe these processes the magnitude of the wave-orbital motion near the bottom is needed. It is assumed that the waves are in

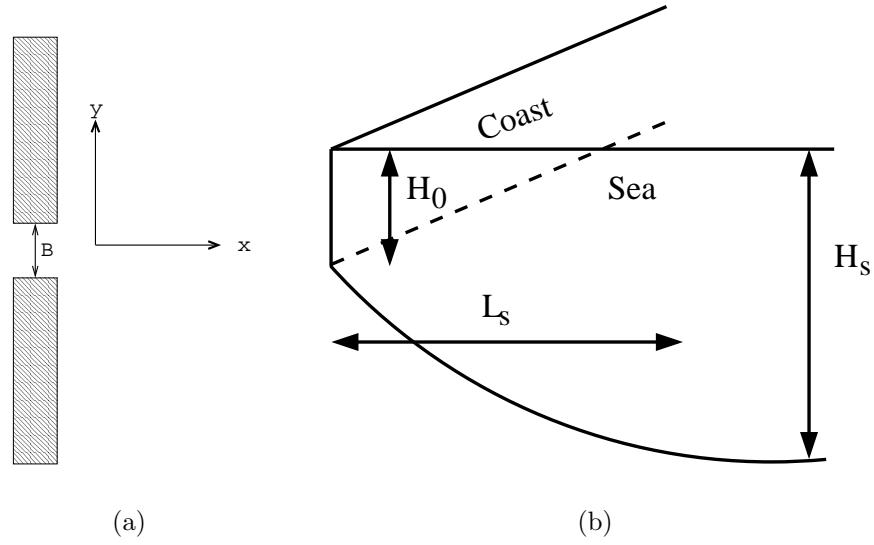


Figure 3.2: Top view (a) and side view (b) of model geometry.

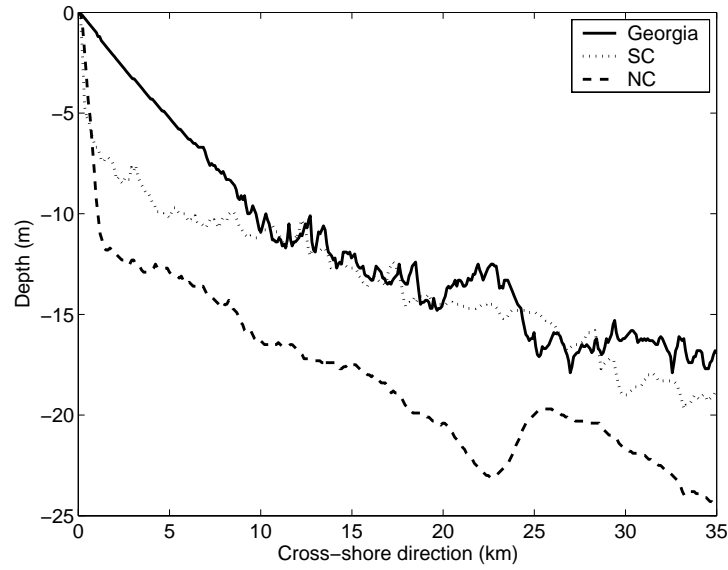


Figure 3.3: Various cross-shore profiles along the east coast of the USA. These are obtained via NOAA's Coastal Relief Model (<http://www.ngdc.noaa.gov/mgg/gdas>). Profile for Georgia started at ( $31.6^\circ$  N,  $81.1^\circ$  W), for SC at ( $33.6^\circ$  N,  $78.9^\circ$  W) and for NC at ( $34.4^\circ$  N,  $77.6^\circ$  W). The profiles are taken perpendicular to the coast.

shallow water, nearly linear and monochromatic. The waves enter shore-normal with a given period and amplitude. While they travel inside the domain they neither refract nor break. The wave orbital motion  $\vec{u}_w$  is modeled as

$$\vec{u}_w = v_w \vec{e}_x \cos(kx - \sigma_w t) + \text{small nonlinear corrections} \quad (3.2)$$

where  $v_w$  is the amplitude of the near-bed orbital velocity, given by

$$v_w = \sqrt{\frac{g}{H}} A \quad (3.3)$$

Here  $A$  is the amplitude of the wave, which is assumed to be constant in the domain. Furthermore, in Equation (3.2) is  $\vec{e}_x$  the unit-vector in the  $x$ -direction,  $k$  is the wave number and  $\sigma_w$  the wave frequency.

### Tidal currents

The tidal currents are described by the depth-averaged shallow water equations. The water motion is forced by the semi-diurnal lunar ( $M_2$ ) tide, which has frequency  $\sigma \sim 1.4 \times 10^{-4} \text{ s}^{-1}$ . The characteristic wave length is  $L_g \sim 2\pi\sqrt{gH}/\sigma \sim 300 \text{ km}$  for  $H = 5 \text{ m}$ . It is assumed that the spatial scales of the ebb-tidal delta are small compared to the wavelength of the tidal wave. The square Froude number is very small ( $\text{Fr}^2 = U^2/(gH) = 0.02$  for a typical velocity  $U = 1 \text{ ms}^{-1}$  and typical depth of 5 m). This allows for a rigid lid approximation: The sea-level variations themselves are not important, but the spatial gradients result in pressure gradients in the momentum equations (see e.g., *Huthnance (1982); Calvete et al. (2001)*). Furthermore, because the focus is on symmetric deltas, it is assumed that the alongshore pressure gradient at the seaward side of the tidal inlet is small (alongshore currents cause asymmetry (*Sha, 1989a*)). The water motion through the inlet is forced by prescribed cross-shore tidal currents in the inlet, which oscillate with frequency  $\sigma$ . A further simplification of the hydrodynamics is introduced by assuming that the bed shear-stress depends linearly on the current. In this formulation a friction coefficient  $r$  is chosen such that the dissipation of kinetic energy during one tidal cycle is equal to the dissipation that would be obtained with a standard quadratic bottom friction law. This typically results in  $r = \frac{8}{3\pi} C_d U$  (*Lorentz (1922)* and *Zimmerman (1992)*), where  $C_d$  ( $\sim 0.0025$ ) is a drag coefficient and  $U$  the characteristic velocity scale in the domain. The velocity scale is related to the intensity of the tidal currents and the wave orbital motion and will be defined later in this section. Because the local Rossby number is large ( $Ro = U/fL \sim 10$ , with  $L$  the width of the inlet and  $f$  the Coriolis parameter) the Coriolis force can be neglected. With these assumptions, the hydrodynamic equations become

$$\frac{\partial u}{\partial t} + u \frac{\partial u}{\partial x} + v \frac{\partial u}{\partial y} = -g \frac{\partial \zeta}{\partial x} - \frac{ru}{H} + A_h \left( \frac{\partial^2 u}{\partial x^2} + \frac{\partial^2 u}{\partial y^2} \right) \quad (3.4a)$$

$$\frac{\partial v}{\partial t} + u \frac{\partial v}{\partial x} + v \frac{\partial v}{\partial y} = -g \frac{\partial \zeta}{\partial y} - \frac{rv}{H} + A_h \left( \frac{\partial^2 v}{\partial x^2} + \frac{\partial^2 v}{\partial y^2} \right) \quad (3.4b)$$

$$\frac{\partial(uH)}{\partial x} + \frac{\partial(vH)}{\partial y} = 0 \quad (3.4c)$$

Here,  $u$  is the cross-shore velocity,  $v$  the alongshore velocity,  $H$  the water depth,  $\zeta$  the surface elevation,  $g$  the acceleration due to gravity,  $r$  the friction parameter and  $A_h$  the horizontal eddy viscosity coefficient (typical value of  $10 \text{ m}^2\text{s}^{-1}$  for  $1 \text{ ms}^{-1}$  tidal currents). The eddy viscosity coefficient depends on the amplitude of the tidal currents and is modeled as  $A_h = lU_t$ , with ( $l \sim 10 \text{ m}$ ) a mixing length scale and  $U_t$  a characteristic velocity



scale related to tidal currents and is chosen as the maximum current amplitude in the center of the tidal inlet. This formulation accounts for both mixing by small scale turbulent eddies and vertical shear dispersion (*Zimmerman, 1986*).

The rigid-lid approximation allows for a convenient way to solve the system. Taking the derivative of Equation (3.4b) with respect to  $x$  and subtracting the derivative of Equation (3.4a) with respect to  $y$  results in an equation for the vorticity  $\omega = \partial v/\partial x - \partial u/\partial y$ ,

$$\frac{\partial \omega}{\partial t} + u \frac{\partial \omega}{\partial x} + v \frac{\partial \omega}{\partial y} = -\omega \left( \frac{\partial u}{\partial x} + \frac{\partial v}{\partial y} \right) - \frac{r\omega}{H} + \frac{r}{H^2} \left( v \frac{\partial H}{\partial x} - u \frac{\partial H}{\partial y} \right) + A_h \left( \frac{\partial^2 \omega}{\partial x^2} + \frac{\partial^2 \omega}{\partial y^2} \right) \quad (3.5)$$

Together with Equation (3.4c) this system of equations is solved. The sea surface gradient can be calculated afterwards. Equation (3.5) states that the total change of vorticity is caused by the four terms on the right-hand side. They represent vortex stretching, dissipation of vorticity due to friction, generation of vorticity by frictional torques due to bottom gradients and dissipation by diffusion of vorticity, respectively. The imposed hydrodynamic boundary conditions are

$$u = 0, \quad \partial v/\partial x = 0 \qquad x = 0, \quad |y| > B/2 \qquad (3.6a)$$

$$u = \hat{U}(y) \cos(\sigma t), \quad \partial v/\partial x = 0 \qquad x = 0, \quad |y| < B/2 \qquad (3.6b)$$

$$u, v \rightarrow 0 \qquad (x^2 + y^2) \rightarrow \infty \qquad (3.6c)$$

Here  $\hat{U}(y)$  is a given cross-shore tidal current profile in the inlet, which is assumed to be symmetric with respect to  $y = 0$ . Furthermore, at  $x = 0$  no interaction between the nearshore zone and the inner shelf is allowed. Therefore, a free-slip condition is applied.

With the present current and wave model the magnitude of  $U$  is taken as the typical velocity scale in the center of the tidal inlet

$$U = \sqrt{\hat{U}(0)^2 + v_w(0)^2} \qquad (3.7)$$

where  $\hat{U}(0)$  is the maximum tidal velocity and  $v_w(0)$  is the amplitude of the wave orbital motion at the coast.

### 3.2.3 Sediment transport

For most ebb-tidal deltas the sediment is relatively coarse (typical grain size of  $\sim 0.3$  mm). In these situations suspended load sediment transport is not important. Previous modeling studies show that it is possible to model the evolution of a tide-dominated ebb-tidal delta with the assumption that most sediment is transported as bedload (*van Leeuwen et al., 2003*). Therefore only bedload transport is considered. A Bagnold-Bailard sediment transport formulation is used (*Bagnold, 1966*) and (*Bailard, 1981*). It is easier to transport the sediment in the down-slope direction than in the up-slope direction. This is accounted for in a very simple way by imposing a sediment transport component in

the direction of the bottom slope. The instantaneous bedload sediment transport on the intra-wave timescale is modeled as

$$\vec{q}_{\text{inst}} = \alpha(|\vec{u} + \vec{u}_w|^2(\vec{u} + \vec{u}_w) + \hat{\gamma}|\vec{u} + \vec{u}_w|^p \vec{\nabla} H) \quad (3.8)$$

The constant  $\alpha$  depends on sediment characteristics and for a grain size of  $\sim 0.3$  mm has a value of  $\alpha = 10^{-5} \text{ s}^2\text{m}^{-1}$ . The bed-slope coefficient  $\hat{\gamma} \sim 1(\frac{m}{s})^{3-p}$  in this model. The value of the constant is  $p = 2$ , (*Struiksmas et al.*, 1985), or  $p = 3$ , as in *Bailard* (1981) and *Sekine and Parker* (1992). Next, the wave-averaged sediment transport  $\vec{q}$  is calculated, assuming that the wave-averaged value of  $\hat{\gamma}|\vec{u} + \vec{u}_w|^p$  is  $\hat{\gamma}U^p$ . Here  $\hat{\gamma}$  is a constant and  $U$  is the characteristic velocity scale inside the domain (Equation (3.7)). Substituting (3.2) in (3.8) and averaging over the wave period yields the wave-averaged sediment transport

$$\vec{q} = \vec{q}_{\text{asym}} + \alpha(|\vec{u}|^2\vec{u} + \frac{1}{2}v_w^2\vec{u} + v_w^2(\vec{u} \cdot \vec{e}_x)\vec{e}_x + \hat{\gamma}U^p\vec{\nabla} H) \quad (3.9)$$

The term  $\vec{q}_{\text{asym}}$  is caused by the asymmetry of the wave orbital velocity due to nonlinear processes and will be specified later.

### 3.2.4 Sediment mass balance

Lastly, the sediment mass conservation is prescribed. When the sediment transport is convergent the water depth will decrease because the sediment is deposited at the bed. For divergent sediment transport the total water depth will increase. Furthermore, the time scale on which bottom patterns evolve is much larger than the time scale of the hydrodynamics (period of the  $M_2$  tide). This allows us to calculate the hydrodynamics with a constant bathymetry while the evolution of the bed is driven by the convergence of the residual sediment transport (for mathematical details about this tidal averaging method, see *Sanders and Verhulst* (1985)). The bed evolution equation is therefore given by

$$\frac{\partial H}{\partial t} - \vec{\nabla} \cdot \langle \vec{q} \rangle = 0 \quad (3.10)$$

Here, the brackets  $\langle . \rangle$  denote an average over the tidal period. The boundary conditions for the sediment mass balance are

$$\langle q_x \rangle = 0 \quad x = 0, |y| > \frac{B}{2} \quad (3.11a)$$

$$H \text{ is finite} \quad x = 0, |y| < \frac{B}{2} \quad (3.11b)$$

$$H \rightarrow H_R(x) \quad (x^2 + y^2) \rightarrow \infty : \quad (3.11c)$$

where  $q_x$  is the cross-shore component of  $\vec{q}$ . At the coastline no cross-shore sediment transport is allowed and  $H_R(x)$  is defined in Equation (3.1). In the tidal inlet the regularity condition is imposed.

### 3.2.5 Morphodynamic equilibrium condition

As explained in the introduction, the aim of this paper is to study morphodynamic equilibrium solutions of the model. They obey the condition

$$\frac{\partial H}{\partial t} = 0 \quad (3.12)$$

which implies, according to Equation (3.10), that the sediment transport should have zero divergence. Henceforth we assume that  $H(x, y)$  represents an equilibrium.

### 3.2.6 Reference equilibrium

Note that the equations still contain the unknown sediment transport  $\vec{q}_{\text{asym}}$ . This transport is determined by defining a so-called reference equilibrium solution for the case of no tidal currents (hence, no delta). In that case, combining Equations (3.9), (3.10) and (3.12) yields

$$\vec{\nabla} \cdot \langle \vec{q}_{\text{asym}} \rangle + \vec{\nabla} \cdot \langle \alpha \hat{\gamma} U^p \vec{\nabla} H_{\text{R}} \rangle = 0 \quad (3.13)$$

where  $H_{\text{R}}$  is the reference bathymetry. Since the waves are assumed to be alongshore uniform,  $H_{\text{R}}$  is alongshore uniform as well and is equal to the bathymetry prescribed in the regions far away from the inlet (Equation (3.1)). Substituting this bottom profile in Equation (3.13) determines  $\vec{\nabla} \cdot \langle \vec{q}_{\text{asym}} \rangle$ . It is assumed that when tidal currents through the tidal inlet are nonzero, balance (3.13) still holds, and the reference bathymetry is unchanged.

## 3.3 Methods

### 3.3.1 Finding morphodynamic equilibria

We now discuss a method to find morphodynamic equilibria of the model for arbitrary flow conditions. From Equations (3.9), (3.10), (3.12) and (3.13) it follows that

$$\vec{\nabla} \cdot \alpha \hat{\gamma} U^p \vec{\nabla} H' = -\vec{\nabla} \cdot \vec{q}_f \quad (3.14)$$

where  $H' = H - H_{\text{R}}$  and

$$\vec{q}_f = \alpha \langle |\vec{u}|^2 \vec{u} + \frac{1}{2} v_w^2 \vec{u} + v_w^2 (\vec{u} \cdot \vec{e}_x) \vec{e}_x \rangle \quad (3.15)$$

Equation (3.14) is a nonlinear equation for  $H'(x, y)$ . Because the cross-shore component of  $\vec{q}_f$  vanishes at  $x = 0$  for  $|y| > B/2$ , Equations (3.9), (3.11a) and (3.13) imply that at these locations  $\frac{\partial H'}{\partial x} = 0$ . In the inlet the cross-shore component of  $\vec{q}_f$  is nonzero, and the boundary condition on  $H'$  does not require that  $\langle q_x \rangle$  is locally zero. Hence, a net local flux of sediment is allowed in the inlet. However, integrated over the whole inlet the total cross-shore sediment transport is zero. This follows from integrating Equation (3.14) over the whole domain and applying the theorem of Gauss.

Morphodynamic equilibria in the model are obtained by using a continuation method (see *Manneville* (1990) for a discussion). Starting point is a known equilibrium solution of the model (for example, the reference morphodynamic equilibrium). The corresponding bottom pattern is denoted by  $H = H(x, y; \mu)$ , where  $\mu$  represents a parameter (e.g., the magnitude of  $\hat{U}(0)$ ). Next, the value of  $\mu$  is changed by a small increment  $\Delta\mu$  and the tidal currents are computed using the 'old' bathymetry  $H = H(x, y; \mu)$ . From this, the sediment flux vector  $\vec{q}_f$  is computed from Equation (3.15). Because the right-hand side of Equation (3.14) can be calculated, this nonlinear equation for  $H'$  has become a Poisson equation. This equation is solved and a first guess for the 'new' equilibrium bottom  $H = H(x, y; \mu + \Delta\mu)$  is obtained. This is not yet the 'true' bottom, because  $\vec{q}_f$  was computed with a previous guess of the bottom pattern. So, an iteration procedure is adopted which involves recomputation of the tidal currents with the new guess of the bottom and finding subsequent updates for  $\vec{q}_f$  and  $H = H(x, y; \mu + \Delta\mu)$  until convergence is established. After this, the parameter  $\mu$  can be changed again, resulting in a continuum of equilibrium solutions obtained for different parameter values. The success of this method was already demonstrated in the context of one-dimensional models for tidal embayments by *Schuttelaars and de Swart* (2000) and *Schramkowski et al.* (2004).

### 3.3.2 Numerical method to solve the hydrodynamic equations

#### Expansion of the variables

Equations (3.4c) and (3.5) are solved using a pseudospectral method. The spatial variables are expanded in Chebyshev polynomials (see *Boyd* (2001) for details). In previous morphodynamic modeling studies these Chebyshev polynomials have been successfully used in resolving spatial patterns (*Falqués et al.*, 1996), especially when boundary layers have to be resolved. For the time dependent part, a Galerkin approach is adopted. The velocity components  $u$  and  $v$  are expanded in their harmonic agents  $M_0$ ,  $M_2$ ,  $M_4$  and so on. In this study the series is truncated after the  $M_2$  components, so nonlinear tides are not accounted for. Hence, the variables are expanded as

$$u(x, y, t) = \sum_{i=1}^{N_x} \sum_{j=1}^{N_y} \left[ U_{ij}^0 + U_{ij}^s \sin(\sigma t) + U_{ij}^c \cos(\sigma t) \right] T_i(\tilde{x}) T_j(\tilde{y}) \quad (3.16a)$$

$$v(x, y, t) = \sum_{i=1}^{N_x} \sum_{j=1}^{N_y} \left[ V_{ij}^0 + V_{ij}^s \sin(\sigma t) + V_{ij}^c \cos(\sigma t) \right] T_i(\tilde{x}) T_j(\tilde{y}) \quad (3.16b)$$

$$H(x, y) = \sum_{i=1}^{N_x} \sum_{j=1}^{N_y} H_{ij} T_i(\tilde{x}) T_j(\tilde{y}) \quad (3.16c)$$

Herein  $N_x$  and  $N_y$  are truncation numbers in the  $x$  and  $y$ -direction,  $T_i$  and  $T_j$  are the Chebyshev polynomials and  $U_{ij}^0, \dots, V_{ij}^c, H_{ij}$  are coefficients. The subscripts  $i$  and  $j$  refer to Chebyshev polynomials in the  $x$  and  $y$ -direction, while the superscripts denote the Fourier components. This means that  $U_{ij}^s$  represent coefficients of the cross-shore velocity component which behaves as  $\sim \sin(\sigma t)$ . The transformation of the Chebyshev domain to

the physical domain is  $x = L_x \frac{1+\tilde{x}}{1-\tilde{x}}$  in the cross-shore direction and  $y = L_y \tilde{y} / \sqrt{1-\tilde{y}^2}$  in the alongshore direction, where  $L_x$  and  $L_y$  are stretching parameters.

### Solving the hydrodynamic equations

The expansions of Equation (3.16) are substituted into Equations (3.4c) and (3.5) and evaluated at the  $N_x N_y$  collocation points. This results in a system of  $6N_x N_y$  nonlinear algebraic equations with  $6N_x N_y$  unknown variables  $U_{ij}^0, U_{ij}^s, \dots, V_{ij}^c$ . For given  $H_{ij}$  and model parameters  $\mu$ , this describes the Flow Over Topography (FOT) problem. Using a previous solution of this system of equations for given  $H_{ij}$  and  $\mu$ , a new solution can be found for different  $H_{ij}$  or  $\mu$  by using the Newton-Raphson method.

#### 3.3.3 Method to solve the Poisson problem

Because the domain is infinite it is difficult to solve the Poisson Equation (3.14) in Cartesian coordinates. Therefore, elliptic-cylindrical coordinates  $(r, \theta)$  are introduced. This coordinate system is similar to the cylindrical coordinate system, except that  $r = 0$  is not a point but a line. Close to the origin the lines of constant radius are ellipses, while far from the origin the coordinate system is close to the cylindrical coordinate system. It is relatively easy to apply the boundary conditions in the elliptic-cylindrical coordinates.

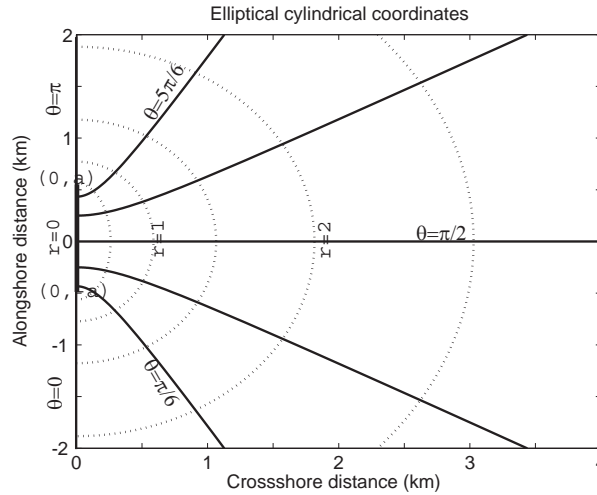


Figure 3.4: The elliptical cylindrical coordinates. The dotted lines represent contour lines of constant  $r$ . The solid lines represent the contour lines of constant  $\theta$ . Note that  $r = 0$  is a line from  $(0, -a)$  to  $(0, a)$  instead of a point  $(0, 0)$  in cylindrical coordinates. Close to  $r = 0$  the curves of constant  $r$  (dashed lines) are ellipses, while for large  $r$  the elliptic-cylindrical coordinate system resembles cylindrical coordinates. The line  $\theta = 0$  is the line for  $x = 0$  and  $y < a$  and  $\theta = \pi$  is the line  $x = 0$  and  $y > a$ .

Figure 3.4 shows the contour lines of constant angle and radius for the elliptic-cylindrical coordinate system. The transformation from elliptic-cylindrical coordinates to Cartesian coordinate reads

$$x = a \sinh(r) \sin(\theta); \quad y = -a \cosh(r) \cos(\theta) \quad (3.17)$$

Here,  $y = a$  and  $y = -a$  for  $x = 0$  denotes the outermost positions of the line  $r = 0$ . Equation (3.14) in elliptic-cylindrical coordinates reads

$$\left[ \frac{\partial^2}{\partial r^2} + \frac{\partial^2}{\partial \theta^2} \right] H' = -a^2 (\sinh^2 r + \sin^2 \theta) F(r, \theta) = G(r, \theta) \quad (3.18)$$

$F(r, \theta)$  is the divergence of the sediment transport (Equation (3.15)) in elliptic-cylindrical coordinates. This differential equation is solved by expanding the solutions and the non-homogeneous part in a multipole series,

$$h(r, \theta) = h_0(r) + \sum_{n=1}^N h_n^s(r) \sin(n\theta) + h_n^c(r) \cos(n\theta) \quad (3.19a)$$

$$G(r, \theta) = G_0(r) + \sum_{n=1}^N G_n^s(r) \sin(n\theta) + G_n^c(r) \cos(n\theta) \quad (3.19b)$$

Substituting these expansions into Equation (3.18) yields differential equations in  $r$  for  $h_0(r)$ ,  $h_n^s(r)$  and  $h_n^c(r)$  which are subsequently solved. The boundary condition at the coastline is that  $\frac{\partial H'}{\partial x} = 0$  (section 3.3.1) and therefore  $h_n^s(r) = 0$ . Furthermore, the application of the regularity condition in  $r = 0$  is quite straightforward. Details of the solution procedure are given in Appendix 3.7. The Poisson equation is solved and this yields  $H'$  for a given  $\vec{\nabla} \cdot \vec{q}_f$ .

## 3.4 Results

### 3.4.1 Default case

In the first experiment values of parameters are chosen that are representative for a typical inlet along the US-coast. The width of the inlet is 1 km. The reference equilibrium bathymetry is characterized by a depth of  $H_0 = 5$  m at the coastline, an offshore depth of  $H_s = 25$  m and an  $e$ -folding length scale of  $L_s = 10$  km (Equation (3.1)). This is within the range of observed values along the east coast of the USA (section 3.2.1). Furthermore, the profile of the cross-shore  $M_2$  tidal currents over the inlet is

$$\hat{U}(y) = \hat{U}(0) \left[ \left( 2 \frac{y}{B} - 1 \right)^3 \left( 2 \frac{y}{B} + 1 \right)^3 \right] \quad (3.20)$$

Here is  $\hat{U}(0)$  the maximum current amplitude in the center of the inlet. As can be seen from Equation (3.6) this models an time-oscillating vorticity dipole in the inlet. The profile has been chosen such that both velocity and vorticity vanishes at the boundaries  $y = \pm B/2$ . This is consistent with observations which show that the velocity in the center of the tidal inlet is larger than at both sides of the tidal inlet (*Chadwick and Largier, 1999*).

No waves are considered in this reference experiment ( $v_w = 0$ ). The drag coefficient  $C_d = 0.0025$ , the mixing length scale  $l = 10$  m,  $p = 2$  and the bed-slope parameter  $\hat{\gamma} = 1$  ms<sup>-1</sup>. Note that Equations (3.14) and (3.15) imply that the magnitude of the bottom patterns does not depend on the value of  $\alpha$ . The number of collocation points is  $N_x = 40$  and  $N_y = 60$  and the stretching parameters are  $L_x = 5$  km and  $L_y = 2$  km. These choices were based on extensive convergence tests.

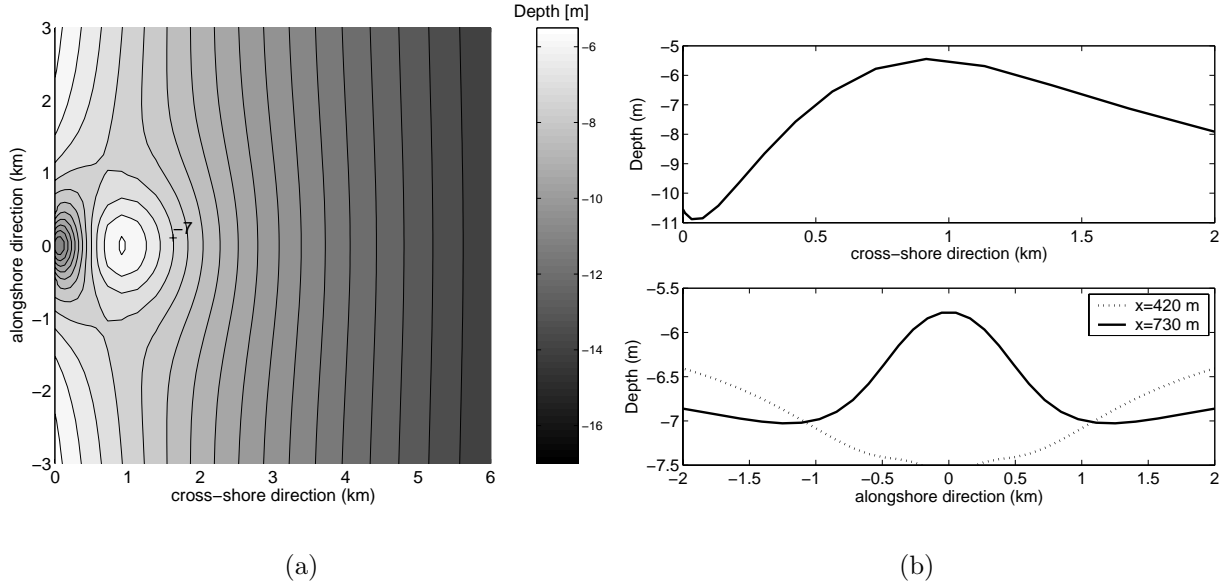


Figure 3.5: (a) Equilibrium bathymetry for an inlet of 1 km width. Maximum  $M_2$  current through the inlet is  $1.0$  ms<sup>-1</sup>. Other parameter values are specified in the text. The black lines are the contour lines and are drawn every  $0.5$  m. (b) Cross-section of equilibrium bathymetry through the center of the tidal inlet (top) and alongshore transects at two different cross-shore positions (bottom).

The maximum tidal current amplitude,  $\hat{U}(0)$ , was gradually increased from  $0$  to  $1$  ms<sup>-1</sup>. The calculated equilibrium bathymetry for a maximum outflow of  $1$  ms<sup>-1</sup> is shown in Figure 3.5(a). The contour lines are drawn every  $0.5$  m. Clearly, an ebb-tidal delta can be seen, which is located at the end of a deep channel that originates from the middle of the inlet. The delta is  $\sim 1.5$  m higher than its surroundings and the minimum water depth is  $6$  m. It extends from about  $1$  km to  $2$  km offshore. At  $4$  km off-shore the contour lines are still curved due to the presence of the tidal inlet. In the center of the inlet a deep channel is present. The depth of the channel increases in the cross-shore direction (Figure 3.5(b) top). The channel branches into two channels protruding in the seaward direction along both sides of the ebb-shoal (Figure 3.5(b) bottom). In the center of the inlet the maximum depth is  $10$  m, while along both sides of the ebb-shoal the depth is about  $7$  m. For smaller tidal current amplitudes bottom patterns with similar but less pronounced characteristics are found. The modeled bottom patterns are robust for different profiles of  $H_R(x)$ . Changing the magnitudes of  $H_0$ ,  $H_S$  and  $L_S$  between the values that are observed along the east coast of the USA, resulted in deltas with the same qualitative characteristics as the one shown in Figure 3.5(a). Furthermore, the results are

robust for the prescribed outflow profile  $\hat{U}(y)$ , provided that the currents are maximum in the center of the inlet and vanish at both sides.

The channel in the center can be identified as an ebb-channel, i.e., with ebb-dominated currents. At both sides the channels are flood-dominated. This can be traced back from Figure 3.6(a) which shows the residual current pattern for  $\hat{U}(0) = 1 \text{ ms}^{-1}$ . Two residual circulation cells are present. During the ebb-phase these residual currents enhance the cross-shore current in the center of the inlet and reduce the cross-shore flow at both sides of the inlet. As a result, during maximum ebb an ebb-jet is clearly seen (Figure 3.6(b)) while during the flood phase the inflow is radial (Figure 3.6(c)). The presence of the ebb-jet and radial inflow is consistent with the theory of tidal flushing described by *Stommel and Farmer (1952)* (see also *Wells and Van Heyst (2003)*).

### 3.4.2 Sensitivity to width of the inlet

The width of tidal inlets along the US-coast varies between  $\sim 100 \text{ m}$  and  $\sim 5 \text{ km}$  (*FitzGerald, 1996*). Therefore, in this section the influence of the width on the characteristics of the equilibrium bathymetry is studied. The results of inlets with  $B = 500 \text{ m}$  and  $B = 2000 \text{ m}$  are compared, keeping the tidal prism approximately fixed. For the experiment with  $B = 500 \text{ m}$ ,  $\hat{U}(0) = 0.8 \text{ ms}^{-1}$  and for  $B = 2000 \text{ m}$ ,  $\hat{U}(0) = 0.2 \text{ ms}^{-1}$ . The width of the inlet has no influence on the modeled equilibrium channel shoal pattern, but does influence the spatial scales of the ebb-tidal delta (Figure 3.7). For  $B = 500 \text{ m}$  the spatial scales of the ebb-tidal delta are much smaller than for  $B = 2000 \text{ m}$ .

### 3.4.3 Influence of waves

In this section the sensitivity of the equilibrium bathymetry to monochromatic, linear, shore-normal waves is studied. Due to the wave-orbital motion, sediment is stirred and subsequently transported by the currents. Hence,  $v_w \neq 0$  in Equation (3.9). It is assumed that the wave orbital velocity amplitude does not change when  $H' \neq 0$ . In Figures 3.8(a) and 3.8(b) the equilibrium bathymetry for  $\hat{U}(0) = 1.0 \text{ ms}^{-1}$  and  $v_w(0) = 0.25 \text{ ms}^{-1}$  and  $v_w(0) = 1.0 \text{ ms}^{-1}$  are shown. Again, a large ebb-shoal is present. This ebb-shoal is larger than in the case without waves and protrudes further seaward. In the center of the inlet a channel is present, similar as in the experiment without waves. The two flood channels are more pronounced than in the experiment without waves. The areas at both sides of the inlet are shallower compared to those found in the reference experiment.

## 3.5 Comparison of model results with observations

### 3.5.1 Beaufort Inlet

An experiment is performed with settings based on the observations of the Beaufort tidal inlet. The reference bathymetry is taken from *Hench and Luettich (2003)*. It has a depth  $H_0 \sim 5 \text{ m}$  at  $x = 0$  and a depth  $H_s \sim 14 \text{ m}$  at  $20 \text{ km}$  offshore. From thereon a flat bottom is used. All other parameter values were as in the default case. For  $\hat{U}(0) = 1 \text{ ms}^{-1}$  two residual circulation cells are found and residual currents have a typical magnitude of  $0.1$



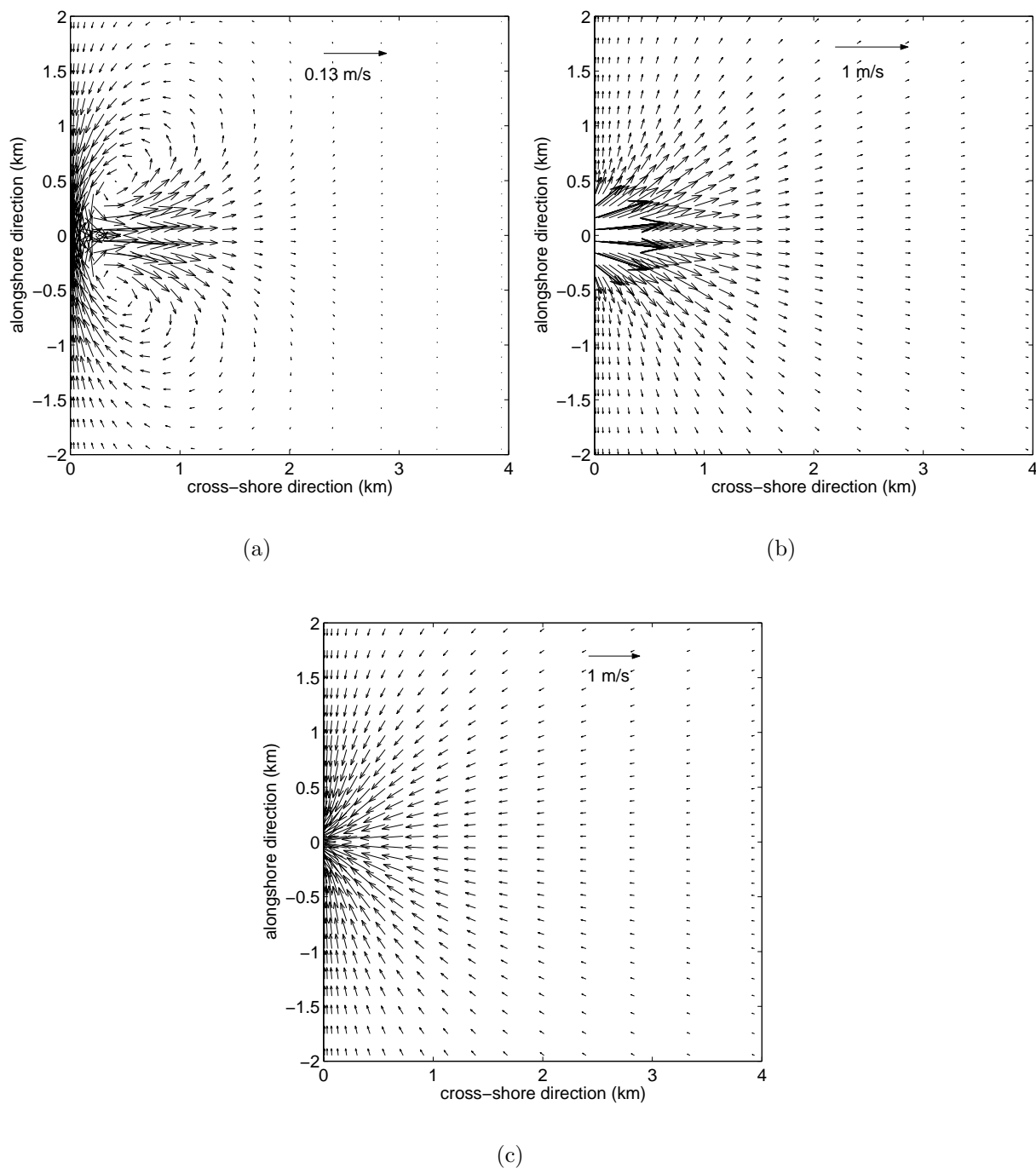


Figure 3.6: (a) Residual flow pattern for  $\hat{U}(0) = 1 \text{ ms}^{-1}$ . The width of the tidal inlet is 1 km. Other parameter values are specified in the text. Two residual circulation cells can be seen with maximum currents in the order of  $0.13 \text{ ms}^{-1}$ . (b) Ebb-jet outflow pattern during maximum ebb. (c) Radial inflow pattern during maximum flood.

$\text{ms}^{-1}$ . Consequently, during ebb there is an ebb-jet and during flood the water flows radial into the basin. Similar residual current patterns and magnitudes are obtained by *Hench*

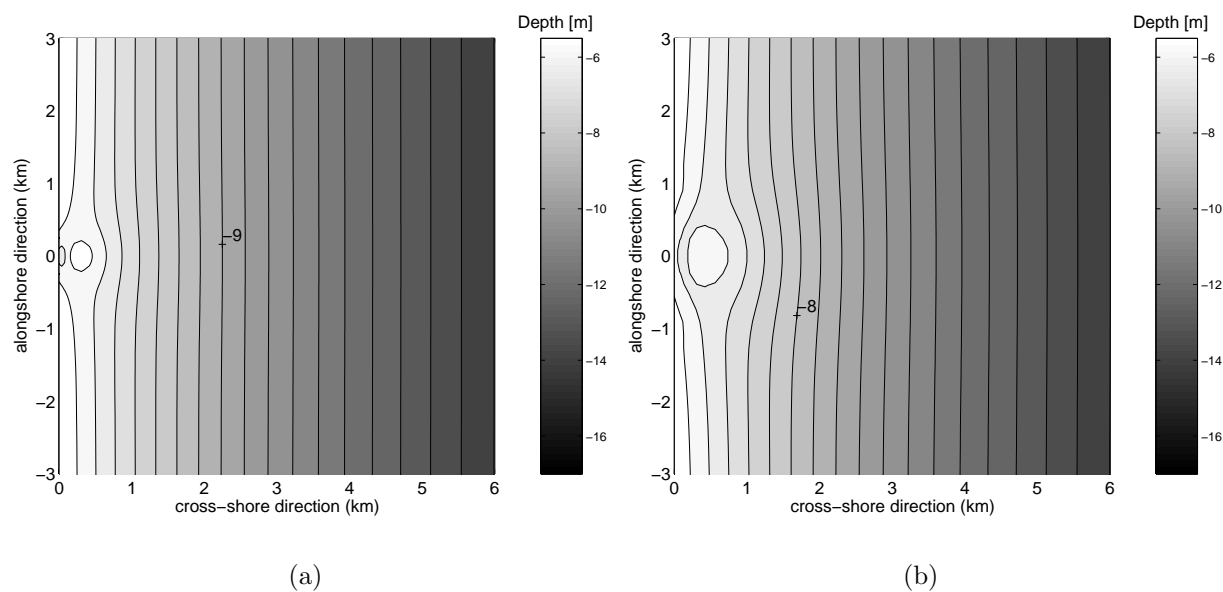


Figure 3.7: Both panels show the equilibrium bottom pattern for approximately the same values of the tidal prism. Contour lines are drawn every  $\sim 0.5$  m. (a)  $B = 500$  m and  $\hat{U}(0) = 0.8$   $\text{ms}^{-1}$ . (b)  $B = 2000$  m and  $\hat{U}(0) = 0.2$   $\text{ms}^{-1}$ . Other parameter values are specified in Ssection 3.4.2.

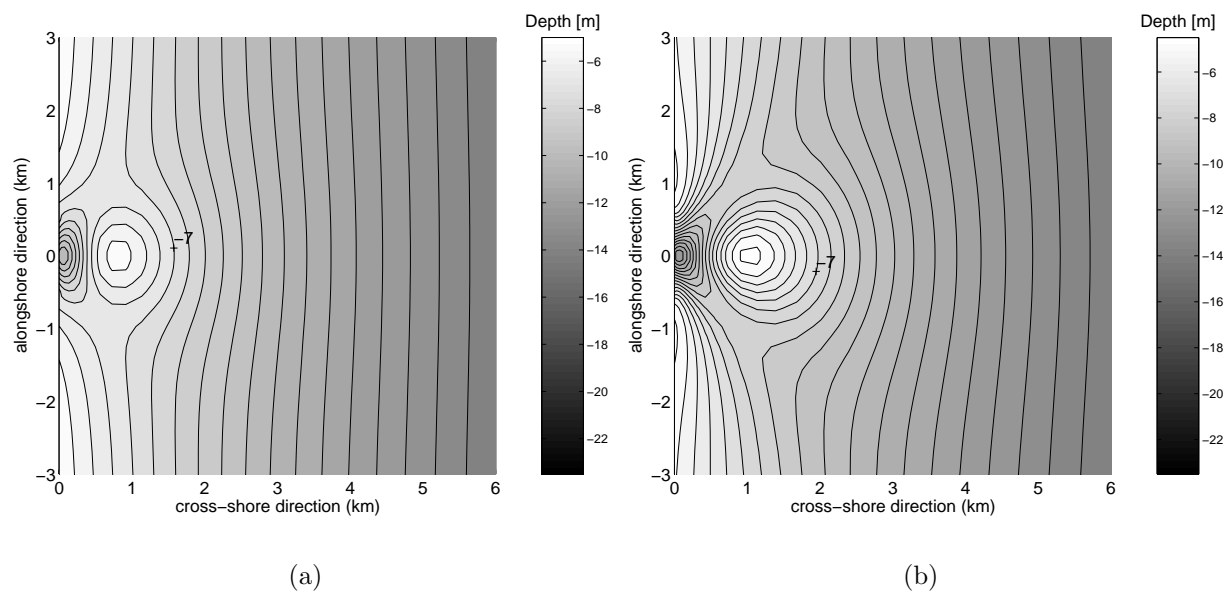


Figure 3.8: Equilibrium bathymetry for  $B = 1$  km with shore-normal waves. Contour lines are drawn every  $\sim 0.5$  m. (a)  $v_w(0) = 0.25$   $\text{ms}^{-1}$  and  $\hat{U}(0) = 1.0$   $\text{ms}^{-1}$ . (b)  $v_w(0) = 1.0$   $\text{ms}^{-1}$  and  $\hat{U}(0) = 1.0$   $\text{ms}^{-1}$ .

and Luettich (2003).

The modeled equilibrium bathymetry for  $\hat{U}(0) = 1.0$   $\text{ms}^{-1}$  is shown in Figure 3.9. A qualitative comparison is made with the observed bathymetry of Beaufort inlet (see

Figure 3.1). The model predicts the presence of an ebb-tidal delta with a spatial extent of about 2 km and an minimum depth of 5 m. The observed delta that is located seaward of Beaufort Inlet has a similar size, but the minimum depth is a bit smaller (2 m). The maximum depth of the ebb-dominated channel obtained with the model is 9 m, while the observed channel has a depth of 10 m. At both sides of the ebb-delta the model predicts the presence of two flood channels. These features seem to be absent in the observations (Figure 3.1), but are believed to be an essential part of the ebb-tidal delta (*Hayes, 1975*). The seaward extent of the ebb-channel is much shorter in the modeled Beaufort inlet as it is in observations. This is partly due to the dredging of the main channel in this area. This dredging might also explain the absence of the flood-dominated channels. The modeled tidal prism is  $5.2 \cdot 10^7 \text{ m}^3$  and the modeled ebb-tidal sand volume is  $3.9 \cdot 10^6 \text{ m}^3$ , while from observations  $\text{TP}=2.8 \cdot 10^7 \text{ m}^3$  and  $\text{ESV}=3.5 \cdot 10^6 \text{ m}^3$  (data from the US Army Corps of Engineers, <http://cirp.wes.army.mil/cirp/structdb/>). In the next section the definitions of TP and ESV can be found.

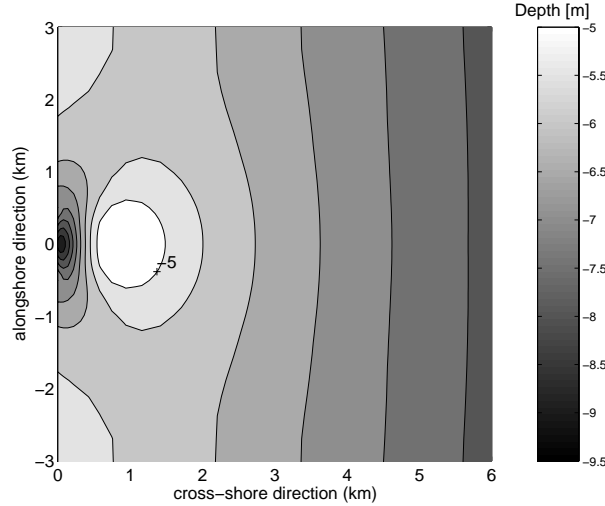


Figure 3.9: Modeled equilibrium bathymetry for parameter setting that represents the idealized Beaufort Inlet of *Hench and Luettich (2003)*. Contour lines are drawn every  $\sim 0.5 \text{ m}$ . The maximum  $M_2$  tidal current amplitude in the inlet is  $\hat{U}(0) = 1.0 \text{ ms}^{-1}$ .

### 3.5.2 Observed and modeled sand volumes

Field data of ebb-tidal deltas discussed in *Walton and Adams (1976)* and *Sha (1989a)* suggest an almost linear relation between ebb-tidal delta sand volume (ESV) and tidal prism (TP). Within the model that is used in this study, the tidal prism is defined as the amount of water that flows in and out the tidal inlet during one tidal cycle, i.e.

$$\text{TP} = \int_0^T \int_{-B/2}^{B/2} |u(0, y, t)| H(0, y) dy dt \quad (3.21)$$

where  $T$  is the tidal period. The ebb-tidal delta sand volume is defined as the amount of sand that is above the reference bathymetry. In terms of the model description adopted

here it is defined as

$$ESV = - \int_{\Omega} (H(x, y) - H_R(x)) \Theta(H_R(x) - H(x, y)) d\Omega \quad (3.22)$$

where  $\Theta$  is the Heaviside function and  $\Omega$  the model area. So, only areas where the depth is smaller than  $H_R$  contribute to the sand volume of the ebb-tidal delta.

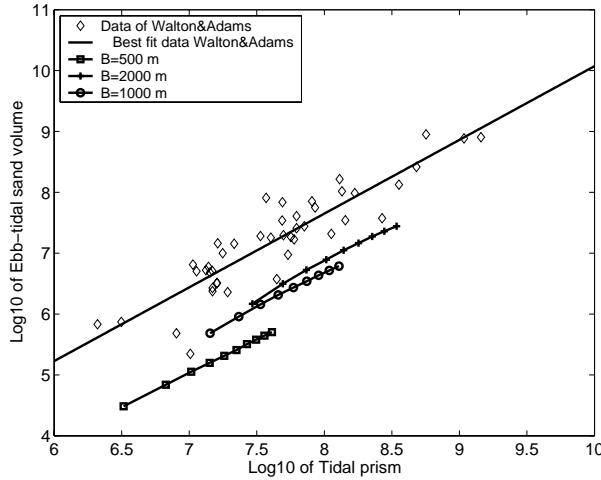


Figure 3.10: Modeled ebb-tidal sand volume as function of tidal prism for  $B = 500$  m,  $1000$  m and  $2000$  m. Diamonds indicate field data of ESV and TP from *Walton and Adams* (1976).

Figure 3.10 shows the modeled ESV as a function of TP for  $B = 500$  m,  $1000$  m and  $2000$  m. In addition, the field data of *Walton and Adams* (1976) of observed ESV and TP are shown (diamonds). *Walton and Adams* (1976) fitted a power-law relation between ESV and TP:

$$ESV = c_1 TP^{c_2} \quad (3.23)$$

This fit is also shown in Figure 3.10. The tidal prism and ebb-tidal sand volume have been made dimensionless and  $c_1$  and  $c_2$  have been determined. The fitted parameters for the field data are  $c_1 = 0.0066$  and  $c_2 = 1.23$ . The modeled relation between ESV and TP is similar as observed. However, the modeled sand volumes are smaller than observed ones. The best fit for  $B = 500$  m is  $c_1 = 0.0018$  and  $c_2 = 1.11$ . For  $B = 1000$  m it is  $c_1 = 0.00095$  and  $c_2 = 1.22$  and for  $B = 2000$  m it is  $c_1 = 0.0024$  and  $c_2 = 1.18$ . This yields that for  $B = 1000$  m the modeled sand volumes are about a factor 10 smaller than observed ones.

The behavior of ESV as a function of TP will be further discussed in section 3.6.3. For approximately the same TP the ESV of a narrower inlet is smaller compared to that of a broader inlet (Figure 3.10). In *Walton and Adams* (1976) no differentiation in width has been made.

## 3.6 Physical interpretation

In this section a physical interpretation of the model results is presented. First, the presence of two residual circulation cells is explained with vorticity concepts. Next, the physics behind the presence of the ebb-tidal delta is studied. Lastly, the physics behind the almost linear relation between ESV and TP is studied.

### 3.6.1 Hydrodynamics

Noticeable hydrodynamic features in the region seaward of the tidal inlet are the two residual circulation cells. Their presence explains the different flow patterns during maximum ebb and maximum flood. In a study by *Zimmerman* (1981), vorticity concepts have been used to explain the generation of residual circulation cells. Therefore, to understand the physics behind the presence of the two residual circulation cells, the tidally averaged vorticity balance is analyzed. The velocity components  $u$ ,  $v$  and the vorticity  $\omega$  are split into a tidally averaged part (denoted by  $\langle \rangle$ ) and a part that is varying on the tidal ( $M_2$ ) time scale (denoted by primes). These variables are substituted in Equation (3.5) and next averaged over the tidal cycle. This yields the tidally averaged vorticity balance

$$\begin{aligned}
 & \overbrace{\frac{\partial}{\partial x} \langle u' \omega' \rangle}^{(a)} + \overbrace{\frac{\partial}{\partial y} \langle v' \omega' \rangle}^{(b)} + \overbrace{\frac{\partial}{\partial x} [\langle u \rangle \langle \omega \rangle]}^{(c)} + \overbrace{\frac{\partial}{\partial y} [\langle v \rangle \langle \omega \rangle]}^{(d)} \\
 & - \underbrace{\frac{r}{H^2} \left( \langle u \rangle \frac{\partial H}{\partial y} - \langle v \rangle \frac{\partial H}{\partial x} \right)}_{(e)} + \underbrace{\frac{r \langle \omega \rangle}{H}}_{(f)} - \underbrace{A_h \left( \frac{\partial^2 \langle \omega \rangle}{\partial x^2} + \frac{\partial^2 \langle \omega \rangle}{\partial y^2} \right)}_g = 0
 \end{aligned} \tag{3.24}$$

Here, (a)-(d) represent the divergence of the mean vorticity flux. The vorticity flux is the transport of vorticity by the velocity. Furthermore, (e) represents the frictional torque, (f) models the dissipation of mean vorticity by friction and (g) models the diffusion of mean vorticity. The mean vorticity flux has components due to the transfer of tidal vorticity by the tidal velocity ((a) and (b)) and components due to the transfer of tidally averaged vorticity by the tidally averaged velocity ((c) and (d)). Because both tidally averaged vorticity and velocity are one order of magnitude smaller than the tidal vorticity and velocity, the tidally averaged vorticity flux is mainly determined by (a) and (b). Another production term of tidally averaged vorticity is the frictional torque (e), but this term is much smaller than (a) and (b) because the residual currents are small. In conclusion, the main tidally averaged vorticity balance is between (a), (b), (f) and (g).

Generation of residual circulation cells can be explained as follows. Starting point is the situation that no ebb-tidal delta is present and only  $M_2$  tidal currents are present. During the ebb, the tidal vorticity in the tidal inlet is transported seaward (term (a) and (b) in Equation (3.24)). The tidal vorticity in the tidal inlet is prescribed by the velocity profile over the inlet,  $\omega' = -\partial \hat{U} / \partial y$ . In the area  $y > 0$  ( $y < 0$ ) the tidal vorticity is positive (negative). Because the magnitude of tidal velocity and vorticity are decreasing in the seaward direction, positive (negative) residual vorticity is generated in the region

$y > 0$  ( $y < 0$ ). During flood, the water flows from the sea to the tidal inlet and both tidal vorticity and tidal velocity change sign. Hence, the resulting residual vorticity flux has the same sign as during the ebb phase. In conclusion, in the area where  $y > 0$  positive residual vorticity is created and in the region  $y < 0$  negative residual vorticity. This results in two residual eddies. These residual circulation cells in their turn affect the  $M_2$  tidal currents. This leads to small modifications of the residual and  $M_2$  tidal currents.

### 3.6.2 Equilibrium bathymetry

According to Equation (3.14), the convergence of the flow-induced sediment transport,  $\vec{q}_f$ , in morphodynamic equilibrium is balanced by the convergence of the slope-induced sediment transport. Consider the default experiment for  $\hat{U}(0) = 0.1 \text{ ms}^{-1}$  and  $H_R(x)$  as the first estimate for the equilibrium bathymetry. After solving the hydrodynamic equations,  $\vec{q}_f$  and  $\vec{\nabla} \cdot \vec{q}_f$  are known. In Figure 3.11(a) a vector plot of  $\vec{q}_f$  is shown. Sediment is transported onshore from the sides to the center of the inlet. From the center of the tidal inlet it is transported offshore. A contour plot of  $\vec{\nabla} \cdot \vec{q}_f$  is shown in Figure 3.11(b). Close to the inlet  $\vec{\nabla} \cdot \vec{q}_f$  is positive, whilst further seaward it is negative.

Splitting the currents in a time-dependent part  $\vec{u}'$  and a time-independent part  $\langle \vec{u} \rangle$ ,  $\vec{q}_f$  can be written as

$$\begin{aligned} \vec{q}_f &= \vec{q}_{f1} + \vec{q}_{f2} \\ \vec{q}_{f1} &= \alpha [\langle |\vec{u}'|^2 \rangle + \langle \vec{u} \rangle^2] \langle \vec{u} \rangle, \quad \vec{q}_{f2} = 2\alpha \langle (\vec{u}' \cdot \langle \vec{u} \rangle) \vec{u}' \rangle \end{aligned} \quad (3.25)$$

The first term describes tidally averaged stirring of sediment by the tidal and residual currents and its transport by the residual current. Contrary to  $\vec{q}_{f1}$ , the transport  $\vec{q}_{f2}$  is generally not in the direction of the residual current. The negative values for  $\vec{\nabla} \cdot \vec{q}_f$  further seaward is mainly caused by  $\vec{\nabla} \cdot \vec{q}_{f1}$  (Figure 3.11(c)), the positive values close the center of the tidal inlet results from the divergence of  $\vec{q}_{f2}$  (Figure 3.11(d)).

According to equilibrium condition (3.14),  $\nabla^2 H'$  is positive (negative) in areas where  $\vec{\nabla} \cdot \vec{q}_f$  is negative (positive). Using the boundary condition that  $H'$  must vanish at large distance from the inlet, the bottom pattern that balances  $\vec{\nabla} \cdot \vec{q}_f$  has a channel near the inlet and a shoal at some distance from the inlet. From this it can also be concluded that the presence of the shoal is mainly explained by the divergence of  $\vec{q}_{f1}$ , whilst the presence of a deep ebb-channel can only be explained by the divergence of  $\vec{q}_{f2}$ .

Comparing the hydrodynamics of the morphodynamic equilibrium state with the hydrodynamics at the first iteration step, shows that the presence of the ebb-tidal delta results in a slight enhancement of the two residual circulation cells. Furthermore, the difference between  $\vec{q}_f$  in morphodynamic equilibrium and at the first iteration step are small. The same holds for  $\vec{\nabla} \cdot \vec{q}_f$  and  $H'$ . Hence, analyzing  $\vec{\nabla} \cdot \vec{q}_f$  for  $H' = 0$  yields a clear clue of the final equilibrium bottom pattern that will be found.

Waves influence the pattern of  $\vec{q}_f$ ,  $\vec{\nabla} \cdot \vec{q}_f$  and  $H'$ . Instead of  $v_w(0) = 0 \text{ ms}^{-1}$  in the previous case, now the case  $v_w(0) = 1.0 \text{ ms}^{-1}$  and  $\hat{U}(0) = 0.1 \text{ ms}^{-1}$  is considered. A vector plot of  $\vec{q}_f$  is shown in Figure 3.12(a). The sediment transport is much larger than in the case that waves were absent (Figure 3.11(a)). The transport is organized in two

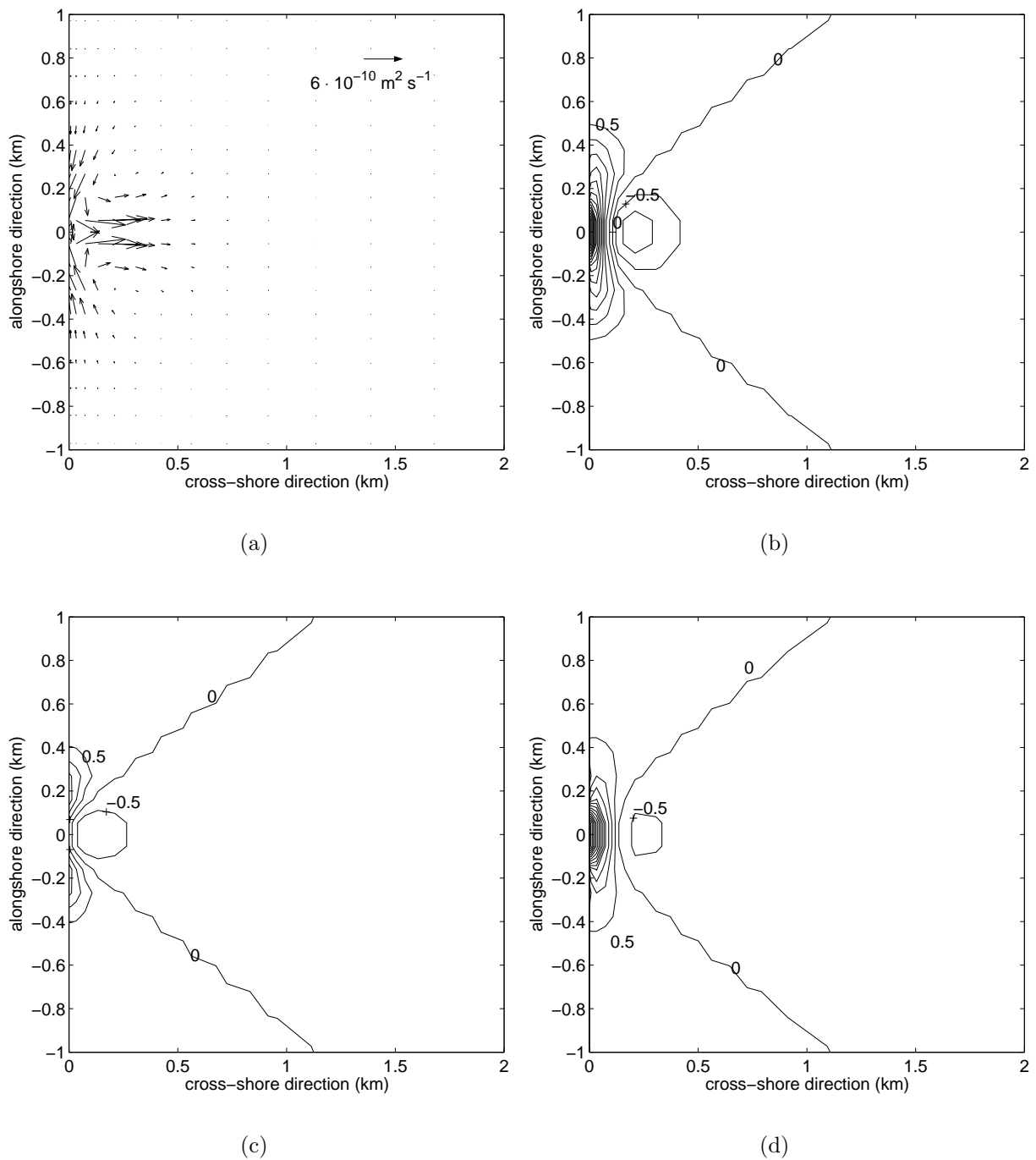


Figure 3.11: (a) Tidally averaged sediment flux  $\vec{q}_f$  in first iteration step for  $\hat{U}(0) = 0.1 \text{ ms}^{-1}$ . A value of  $\alpha = 10^{-5} \text{ s}^2\text{m}^{-1}$  is used. Other parameter values as in the default case (section 3.4.1). (b) Contour plot of  $\vec{\nabla} \cdot \vec{q}_f$  at first iteration step for  $\hat{U}(0) = 0.1 \text{ ms}^{-1}$ . Negative values indicate deposition and positive values indicate erosion. Multiply values with  $10^{-12}$  to obtain erosion deposition rate in  $\text{ms}^{-1}$ . (c) Same as (b), but now contour plot of  $\vec{\nabla} \cdot \vec{q}_{f1}$ , as defined in Equation (3.25). (d) Same as (c), but now  $\vec{\nabla} \cdot \vec{q}_{f2}$ .

cells. The divergence of  $\vec{q}_f$  is shown in Figure 3.12(b). There is one area where its values are positive. This area extends to the sides. There are three areas where  $\vec{\nabla} \cdot \vec{q}_f$  has positive values. In the case without waves there was only one area with negative values. In morphodynamic equilibrium the presence of two extra areas with negative values of  $\vec{\nabla} \cdot \vec{q}_f$  results in a bottom which is shallower at both sides of the inlet. Furthermore, the two flood channels are more pronounced because in these areas  $\vec{\nabla} \cdot \vec{q}_f$  is positive, whereas it is negative in the case that no waves are taken into account.

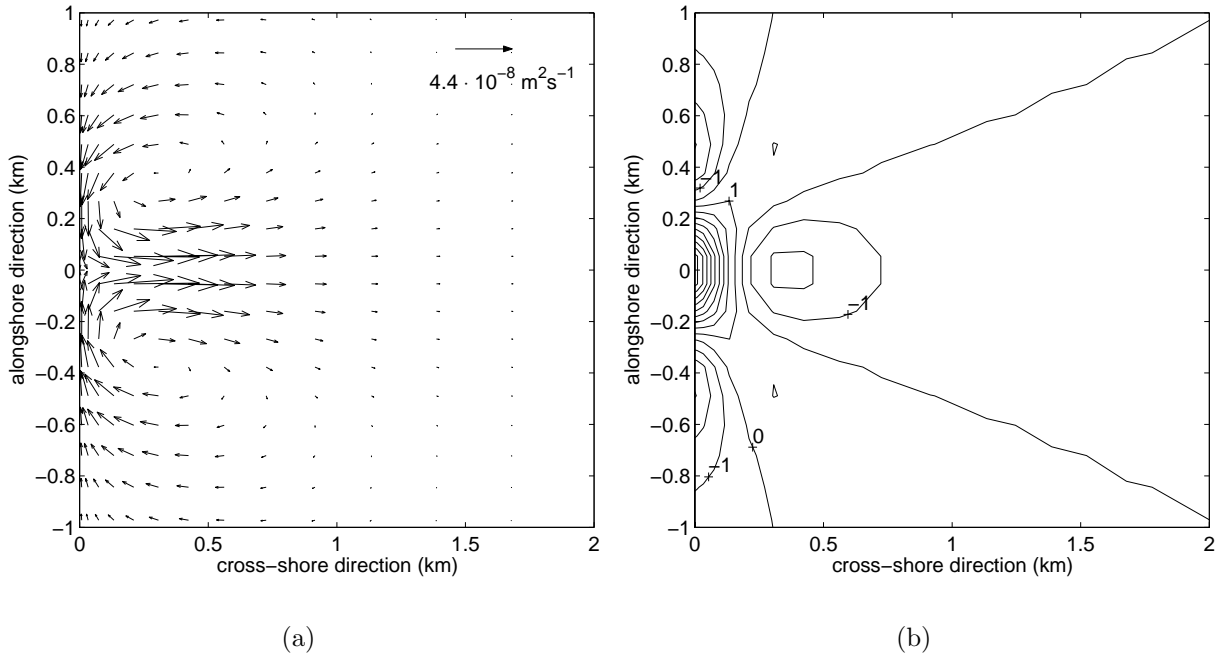


Figure 3.12: (a) Vector plot of  $\vec{q}_f$  at first iteration step for  $\hat{U}(0) = 0.1 \text{ ms}^{-1}$  and  $v_w(0) = 1.0 \text{ ms}^{-1}$ . A value of  $\alpha = 10^{-5} \text{ s}^2\text{m}^{-1}$  has been used. (b) Contour plot  $\vec{\nabla} \cdot \vec{q}_f$ . Negative values indicate deposition and positive values indicate erosion. Multiply values with  $10^{-11}$  to obtain erosion deposition rate in  $\text{ms}^{-1}$ .

### 3.6.3 Relation between ESV and TP

The modeled relation between the ebb tidal sand volume and tidal prism is almost linear if  $p = 2$ . This relation is explained in two steps. In the first step the behavior of  $H'$  as a function of the prescribed outflow amplitude is explained for the default case. In the second step the first step is used to explain the behavior of ESV and TP as a function of  $\hat{U}(0)$  and thereby the relation between ESV and TP. First of all,  $\vec{\nabla} \cdot \vec{q}_f$  is cubic in the prescribed outflow amplitude  $\hat{U}(0)$ . This can be seen from Equation (3.15). Furthermore,  $\vec{\nabla} \cdot \vec{q}_f$  is in morphodynamic equilibrium balanced by  $\hat{\gamma}U^2\nabla^2 H'$  (Equation (3.14)). Because  $U$  scales linearly in  $\hat{U}(0)$  the magnitude of  $H'$  has to scale linearly in  $\hat{U}(0)$ .

Secondly, because the depth in the inlet is increasing for increasing  $\hat{U}(0)$ , the tidal prism will increase more than linearly (Equation (3.21)). Also the ebb-tidal sand volume



increases more than linearly with linearly increasing  $\hat{U}(0)$  because the spatial scales of the ebb-tidal delta increase with increasing  $\hat{U}(0)$ . Figure 3.13 shows the  $\log_{10}$  of ESV and TP as function of the  $\log_{10}$  of  $\hat{U}(0)$  for  $B = 1000$  m. From this figure it can be concluded that ESV increases at a greater rate with increasing  $\hat{U}(0)$  than TP does. In conclusion, the relation between ESV and TP must be slightly more than linear.

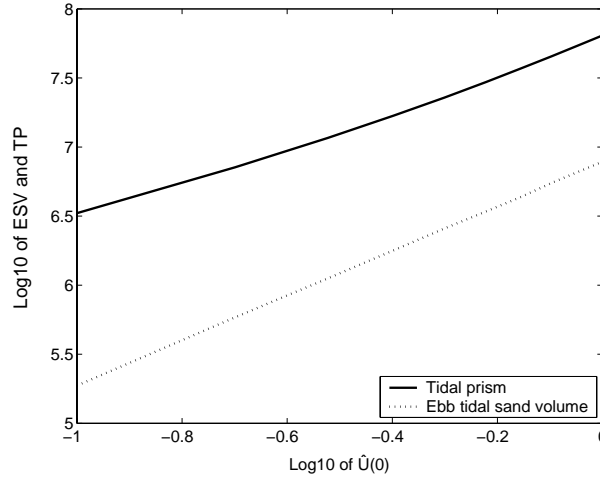


Figure 3.13: Ebb tidal sand volume (dotted line) and tidal prism (solid line) as a function of  $\hat{U}(0)$ .

Experiments showed that for  $p = 3$  the relation between ESV and TP tends to a constant and for  $p = 0$  the modeled ESV depends cubically on TP (results not shown).

### 3.7 Discussion and conclusions

In this paper an idealized process-based model has been developed and analyzed which describes the interactions between tidal currents, waves and the sandy bottom in the area located seaward of an inlet. A summary of all the restrictions and approximations can be found in Table 3.1. Forcing of the system is due to a prescribed tidal current profile in the inlet (symmetric with respect to the mid-axis of the inlet) and due to incoming shore-normal waves. The model allows for so-called morphodynamic equilibrium solutions that have a steady bottom pattern. This pattern consists of a shallow delta located at the seaward end of an ebb channel that originates near the inlet. Two shallower flood-dominated channels flank this ebb channel. The pattern resembles that of observed, nearly symmetric, ebb-tidal deltas as found for example along the coasts of the US (*FitzGerald, 1996; Davis, 1997*). The modeled hydrodynamics is in close agreement with observations (*Wells and Van Heyst, 2003*) and previous modeling studies (*Hench and Luettich, 2003*). This includes an ebb-jet during outflow and a radial inflow pattern during flood. In addition, two residual circulation cells are modeled. The model also yields an explicit relationship between the volume of sand stored in the delta and the tidal prism of the inlet. It appears that, using well-accepted formulations for sand transport, this relationship is almost linear, in agreement with empirical relationships deduced from field data (*Walton and Adams, 1976*).

<b>Assumptions and restrictions</b>
Rigid lid approximation
Linearized shear-stress formulation
Only bedload sediment transport
Symmetric tidal current profile at inlet
Shallow water waves
Shore-normal incident waves
No wave refraction
No wave breaking
No radiation stresses
Effects of waves on mean shear-stress is parameterized
No large-scale shore-parallel currents
No littoral drift
No Coriolis force

Table 3.1: A list of the assumptions used to derive the model that is analyzed in the present study.

A physical analysis of the model has revealed that the equilibrium bottom pattern is the result of a local balance between the divergence of two types of sand transport. The first is caused by the joint action of waves and tides, which stir sand from the bottom and transport it. The second transport type is that induced by local bedslopes, where its magnitude depends on the intensity of both tidal currents and wave orbital motion. The presence of the delta is caused by the tidally averaged stirring of sediment by waves and tides and the transport by the residual currents. The channels are caused by the part of the sediment transport which is not in the direction the residual currents.

There are also noticeable differences between the modeled and observed ebb-tidal deltas. Observed ebb-channels are much deeper than modeled ones. In addition, the delta only has a weak tendency to fold around the ebb channel, as is commonly observed. The modeled ESV is a factor 5-10 smaller than the observed values. Probably, these discrepancies result from negligence in the model of a number of processes that might affect the results. First, the tidal currents in the model are described by depth-averaged shallow water equations that include a linearized bed shear stress. Only residual currents and the semi-diurnal tidal currents are explicitly solved. This might affect the generation of nonlinear tides and residual currents, with possible consequences for the sand transport and morphologic patterns.

Second, in the formulation for  $A_h = lU_t$  and in  $r = 8/3\pi C_d U$  and  $\hat{\gamma}U^p$ ,  $U_t$  and  $U$  are constants. However,  $U_t$  and  $U$  are related to the intensity of tidal currents and can therefore vary one order of magnitude in the region of the tidal inlet. The velocity scale  $U_t$  and  $U$  was such that it represents the maximum velocity in the inlet. Consequently, away from the inlet damping and diffusion of vorticity and the bed-slope induced sediment transport are overestimated. This results in bottom patterns with relatively small amplitudes and in much smaller values of the modeled ESV. A first test has been performed which used a spatial dependent  $U$ . This resulted in an increase by a factor 5 of the modeled ESV. However, the modeled channel shoal pattern did not change significantly.

Third, the model uses a fixed velocity profile in the inlet with no residual currents. There is no dynamic interaction between the tidal basin and the ebb-tidal delta. The way to investigate this is to extend the model with a tidal basin.

Fourth, the wave module in the present model is highly simplified. It describes only the shoaling of normally incident waves and ignores processes like refraction of waves, breaking of waves and no spatial variations in the radiation stresses are taken into account. Although these processes are not expected to be crucial in the present system, because the minimum depths obtained are quite large (more than 4 m), in reality waves break near the delta and generate alongshore currents due to spatial variations of radiation stresses.

Fifth, a bedload formulation is used with only one grain size. In reality, grains have different shapes and sizes and many of them will be in suspension.

## Appendix

### 3.A Solving the Poisson problem

The solution for  $n = 0$  is the monopole, the solution for  $n = 1$  is the dipole, and so on. Equation (3.18) for the monopole becomes

$$\frac{d^2 h_0(r)}{dr^2} = G_0(r) \quad (3.A-1)$$

Applying the method of variation of constant yields the general solution

$$h_0(r) = a_1 + a_2 r + \int_0^r r' G_0(r') dr' - r \int_0^r G_0(r') dr' \quad (3.A-2)$$

The constants  $a_1, a_2$  are determined with the boundary conditions. For  $r \rightarrow \infty$  the total solution (Equation (3.A-2)) must vanish while for  $r = 0$  the solution has to be finite. This determines the two unknown constants

$$a_1 = - \int_0^\infty r' G_0(r') dr' \quad a_2 = \int_0^\infty G_0(r') dr' \quad (3.A-3)$$

A similar solution procedure holds for the other poles except that these poles have a dependency on the angle. The Poisson equations for all other poles for both sine and cosine components are given by

$$\left[ \frac{d^2}{dr^2} - n^2 \right] h_n^s(r) = G_n^s(r); \quad \left[ \frac{d^2}{dr^2} - n^2 \right] h_n^c(r) = G_n^c(r) \quad (3.A-4)$$

Because the solutions have to satisfy boundary conditions (3.11),  $h_n^s(r) = 0$ . Again, the solution for the cosine part of every pole is obtained using the method of variation of constants, and the results are

$$h_n^c(r) = c_{n,1} e^{-nr} + c_{n,2} e^{nr} + \frac{e^{-nr}}{2n} \int_0^r e^{nr'} G_n^c(r') dr' - \frac{e^{nr}}{2n} \int_0^r e^{-nr'} G_n^c(r') dr' \quad (3.A-5)$$

The boundary condition is used that for  $r \rightarrow \infty$  the solution must vanish and for  $r = 0$  the solution has to be finite. Applying these conditions yields that  $c_{n,1} = 0$  and

$$c_{n,2}(r) = \frac{1}{2n} \int_0^\infty e^{-nr'} G_n^c(r') dr' \quad (3.A-6)$$

The solution of Equation (3.18) is the sum over all poles.

# Chapter 4

## Physical processes causing asymmetry of tide-dominated ebb-tidal deltas

### Abstract

In Chapter 3 an idealized model was developed to study physical processes that maintain the spatially symmetric ebb-tidal delta. In this chapter the idealized model of Chapter 3 is extended with physical processes that lead to asymmetric ebb-tidal deltas. The focus is on tide-dominated systems. The following tide-related processes are added: Coriolis force, large-scale shore-parallel tidal currents and large-scale shore-parallel residual currents. Including the Coriolis force results in a small asymmetry of the ebb-tidal delta. For the Northern Hemisphere the model predicts that the area with ebb-dominated currents is located at the right-hand side of the tidal inlet (when viewing from the inlet in the seaward direction). The ebb-tidal delta is located at the seaward end of the area with ebb-dominated currents. No ebb-dominated channel is modeled. The delta is called right-oriented. On the left-hand side of the mid-axis of the inlet a channel is modeled, which has flood-dominated currents. Shore-parallel tidal currents have a strong influence on the asymmetry of ebb-tidal deltas. For a parameter setting that is representative for the Dutch Wadden coast, the area with ebb-dominated currents is located at the left-hand side of the mid-axis of the inlet. An increase of the phase difference between shore-parallel and cross-shore tidal currents results in a less asymmetric delta and ultimately its orientation changes. Increasing the magnitude of the shore-parallel currents while keeping the cross-shore tidal currents constant, leads to an increase of the asymmetry of the deltas. The influence of the residual shore-parallel currents on the characteristics of the deltas is also large. A residual current from left to right (when viewing in seaward direction) leads to a right-oriented delta. A residual current from right to left leads to a left-oriented delta. Model results are compared with observations of the ebb-tidal deltas of the tidal inlet systems of the Dutch Wadden Sea. The modeled current patterns agree well with observed ones. The modeled bottom patterns are consistent with the bottom patterns as found in Chapters 3 and 5. Furthermore, the position of the ebb-tidal delta corresponds with observed ones. However, the model is not able to reproduce the observed ebb-dominated channel.

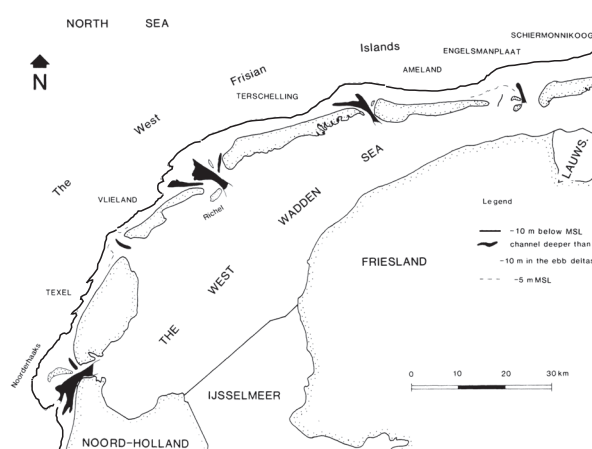
## 4.1 Introduction

Ebb-tidal deltas are shallow sandy structures situated at the seaward side of tidal inlets. They are observed in many parts of the world (*Ehlers*, 1988; *Sha*, 1989a; *FitzGerald*, 1996; *Davis*, 1997; *Hicks et al.*, 1999). The center of the deltas are located at the seaward end of an area with ebb-dominated currents (i.e., stronger peak currents during the ebb-phase than during the flood-phase). The delta folds around the ebb-dominated channel. Close to the coast two flood-dominated channels are found (*Hayes*, 1975). Necessary conditions for the emergence of ebb-tidal deltas are a sandy bottom and the presence of strong tidal currents. Apart from tidal currents, waves are often an important constituent of the water motion in the region of the ebb-tidal delta (*Sha*, 1989a; *FitzGerald*, 1996). Since the strength of the tidal currents and wave influence varies orders of magnitude for the ebb-tidal deltas around the world, *Gibeaut and Davis Jr.* (1993) identified three major classes of deltas, i.e., tide-dominated, mixed-energy and wave-dominated deltas. These different classes of deltas have different characteristics. This makes it inevitable to limit the scope of this study. Here, only tide-dominated deltas are studied.

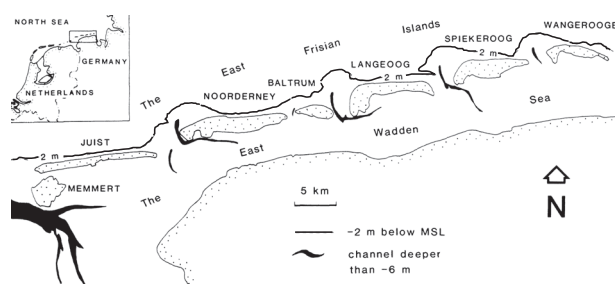
In Chapter 3 the tide-dominated ebb-tidal deltas along the eastern US-coast (Georgia, South Carolina) were discussed. It was noticed that they are almost symmetric with respect to reflections about the mid-axis through the center of the inlet. The ebb-dominated channels have a shore-normal orientation. The shore-parallel currents along the east US-coast are small compared to the cross-shore tidal currents through the inlets. A barrier coast where shore-parallel currents have the same order of magnitude as the cross-shore tidal currents is found along the Dutch and German Wadden coast. Also in this area tide-dominated ebb-tidal deltas are found, but they are not spatially symmetric (*Ehlers*, 1988; *Sha*, 1989a; *FitzGerald*, 1996). Here, we introduce the convention that left-hand (right-hand) side is always defined as left (right) when viewing from the inlet in the seaward direction. If the ebb-dominated channel is oriented to the left the ebb-tidal delta is called left-oriented. When the area with ebb-dominated currents is found on the right-hand side the delta is called right-oriented. In Figure 4.1(a) the channels and deltas along the Dutch Wadden Sea are shown. The black contour line represents the outlines of the ebb-tidal deltas. The dark shaded parts represent the channels. Most of them are ebb-dominated and are oriented to the left. In addition, also most sediment of the delta seems to be located at the left-hand side of mid-axis of the inlet. In Figure 4.1(b) the deltas and ebb-dominated channels along the German Wadden Sea are shown. The position of the ebb-tidal deltas is represented by the black contour line and the position of the channels by the dark shaded parts. In this area most ebb-dominated channels are right-oriented.

The observed variation in the orientation of the ebb-dominated channels raises the question which physical process can lead to the oblique orientation of the ebb-dominated channel. In the conceptual model of *Sha* (1989a,b) it is argued that the asymmetry is caused by the interaction between the shore-parallel and cross-shore tidal currents. This interaction causes weaker and more rotary currents at the right-hand side of the tidal inlet. On the left-hand side the tidal currents are stronger and sediment is eroded from the bed. Hence, the ebb-dominated channel is oriented to the left (see Figure 4.2). Furthermore, most sand of the ebb-tidal delta is found on the left-hand side. In contrast, obliquely

incident waves can cause the ebb-dominated channel to be oriented to the right (see *Oertel* (1975); *FitzGerald* (1996) and references therein). Obliquely incident waves refract and break in the surf zone and this results in a wave-driven current. Assume that far away from the tidal inlet the wave-drive currents are from left to right and transport sediment. The presence of the tidal inlet causes an interruption of the wave-driven currents, because the waves do not break in the inlet where the depths are large. This interruption causes deposition at the left-hand side of the tidal inlet and erosion of sediment at the right-hand side. Hence, the main channel will be right-oriented. This effect becomes more important when wave influence becomes more important.



(a)



(b)

Figure 4.1: (a) Channels and deltas along the Dutch Wadden Sea. Dark contour line represents the 10 meter depth contour line and shows the presence of the ebb-tidal deltas. The dark shaded parts represent the channels with more than 10 meter depth. (b) Channels and shoals along the German Wadden Sea. The 2 meter depth contour line shows the presence of the ebb-tidal deltas. Dark shaded parts are channels with more than 6 meter depth. Both figures after *Sha* (1989a).

Process-based models are needed to validate the conceptual models of *Oertel* (1975); *Sha* (1989a); *FitzGerald* (1996). State-of-the-art process-based models have been used to study the initial response (*van Leeuwen and de Swart*, 2002; *Schuttelaars et al.*, 2003;

*Siegle et al.*, 2004) and the long-term evolution (*Cayocca*, 2001; *van Leeuwen et al.*, 2003) of asymmetric ebb-tidal deltas under various forcing conditions. In view of the aim of the present study, the results of *van Leeuwen et al.* (2003) are of specific interest. They simulated the temporal evolution of the bathymetry of the Frisian Inlet (located between the islands of Ameland and Schiermonnikoog, see Figure 4.1(a)), starting from a state without a delta and with a backbarrier basin having a constant depth of 2 m. During the simulation an asymmetric ebb-tidal delta developed and after a long time ( $\sim 500$  years) the bathymetric changes decreased. Due to numerical resolution problems a true morphodynamic equilibrium was not reached. In addition, their results suggest that the mechanism proposed by *Sha* (1989a) can not completely explain the asymmetric shape of ebb-tidal deltas. They found that the currents on the left-hand side of the inlet are indeed bidirectional and ebb-dominated as argued by *Sha* (1989b), but this did not result in a preferred erosion of sediment.

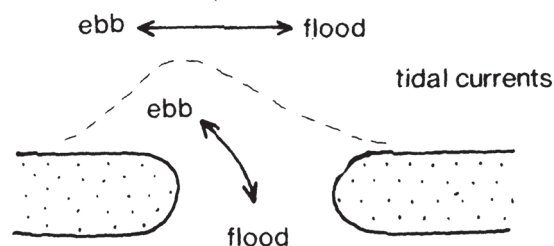


Figure 4.2: Sketch presented by *Sha* (1989a) to explain the asymmetry of tide-dominated deltas along the Dutch Wadden Sea. Due to interaction of shore-parallel tidal currents and cross-shore tidal currents are maximum ebb-currents oriented to the left of the inlet.

The results of *van Leeuwen et al.* (2003) motivated *van der Veegt et al.* (2005) to develop and analyze an idealized morphodynamic model to answer the question whether ebb-tidal deltas can be modeled as morphodynamic equilibria. Rather than calculating the temporal evolution of a tidal inlet system, they developed a direct method to calculate the equilibrium solutions (characterized by a steady bottom pattern) of such a system. They found morphodynamic equilibria that resemble observed ebb-tidal deltas. The focus of their study was on symmetric deltas such as those found along the US-coast. Therefore, they ignored the Coriolis force, prescribed a symmetric velocity profile over the inlet, did not allow for large-scale alongshore pressure gradients related to propagation of the tide along the coast, did not allow for large-scale alongshore residual currents and only accounted for shore-normal incident waves.

A fundamental process-based understanding of the processes that cause asymmetry of tide-dominated deltas is still missing. Therefore the main aim of this study is to investigate the physical processes related to tides which cause such deltas to be asymmetric. This is done by extending the model of *van der Veegt et al.* (2005) with processes that can lead to asymmetry. The influence of the following processes on the (a)symmetry of ebb-tidal deltas are studied:

- Coriolis force;
- Large scale alongshore pressure gradients at sea;
- Residual alongshore currents at sea;



This study proceeds as follows. In Section 4.2 the model is described, followed by an analysis of the equations of motion in Section 4.3. In Section 4.4 the method to calculate morphodynamic equilibrium solutions is shortly explained. A detailed explanation can be found in *van der Vegt et al. (2005)*. Then the three agents causing asymmetry of the ebb-tidal delta are studied in Section 4.5. Section 4.6 contains a discussion and ends with suggestions for further research.

## 4.2 Model description

### 4.2.1 Domain

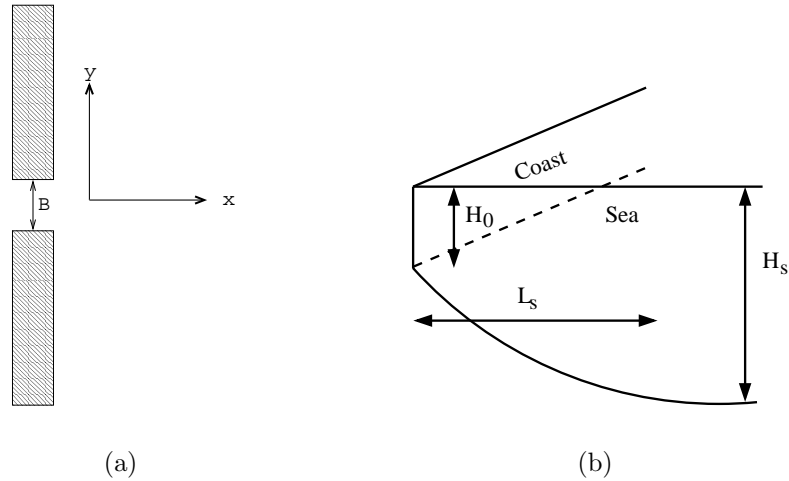


Figure 4.3: (a) Inlet of width  $B$  is centered around  $(x, y) = (-x_s, 0)$ . (b) Side view of model. For more information see text.

The model domain consists of a coastal sea that is bounded by a straight coast. The latter is interrupted by one inlet (having a width  $B$ ). A Cartesian coordinate system is used, with the  $x, y, z$ -axes pointing in the cross-shore, alongshore and upward direction, respectively. The coastline is located at  $x = -x_s$ , while the center of the interruption of the coast is at  $(x, y) = (-x_s, 0)$ , as is sketched in Figure 4.3(a). The transition from the nearshore zone to the inner shelf is located at  $x = 0$ . In the nearshore zone the dynamics is mainly determined by complex wave-driven processes. At the inner shelf the tide is the dominant constituent of the water motion. It is assumed that there is no interaction between the nearshore zone and the inner shelf. The domain on which the calculations are performed is  $x \in [0, \infty)$  and  $y \in (-\infty, +\infty)$ .

The position of the bottom is denoted by  $z = -H$ , with  $H$  the undisturbed water depth. In the regions far away from the inlet the bathymetry is given by  $H = H_R(x)$ , where

$$H_R(x) = H_0 + (H_s - H_0)(1 - e^{-x/L_s}) \quad (4.1)$$

Here,  $H_0$  is the undisturbed water depth at  $x = 0$ . This water depth increases exponentially to a value  $H_s > H_0$  in the cross-shore direction (Figure 4.3(b)). Typical values for

the Dutch coast are  $H_0 = 5$  m,  $H_s = 25$  m and an  $e$ -folding length scale  $L_s = 10$  km (see Chapter 2).

## 4.2.2 Currents

The hydrodynamics is described by the depth-averaged shallow water equations. A semi-diurnal lunar ( $M_2$ ) tide is considered (frequency  $\sigma \sim 1.4 \times 10^{-4} \text{ s}^{-1}$ ) and the tidal wave has a characteristic wavelength  $L_g = 2\pi\sqrt{gH}/\sigma \sim 300$  km in water with a depth of 5 meter. It is assumed that the spatial scales of interest (spatial scale of the ebb-tidal delta, width of the tidal inlet) are small compared to the wavelength of the tidal wave. This allows for a rigid lid approximation: The sea level variations itself are not important, but the spatial gradients result in pressure gradients in the momentum equations (see e.g., *Huthnance (1982); Calvete et al. (2001)*). The hydrodynamic equations become

$$\frac{\partial u}{\partial t} + u\frac{\partial u}{\partial x} + v\frac{\partial u}{\partial y} - fv = -g\frac{\partial \zeta}{\partial x} - \frac{\tau_x}{\rho H} + A_h\left(\frac{\partial^2 u}{\partial x^2} + \frac{\partial^2 u}{\partial y^2}\right) \quad (4.2a)$$

$$\frac{\partial v}{\partial t} + u\frac{\partial v}{\partial x} + v\frac{\partial v}{\partial y} + fu = -g\frac{\partial \zeta}{\partial y} - \frac{\tau_y}{\rho H} + A_h\left(\frac{\partial^2 v}{\partial x^2} + \frac{\partial^2 v}{\partial y^2}\right) \quad (4.2b)$$

$$\frac{\partial(uH)}{\partial x} + \frac{\partial(vH)}{\partial y} = 0 \quad (4.2c)$$

Here,  $u$  is the cross-shore component and  $v$  the alongshore component of the velocity vector  $\vec{u}$ ,  $t$  is time,  $f$  is the Coriolis parameter,  $H$  the water depth,  $\zeta$  the surface elevation,  $\tau_x, \tau_y$  are the cross-shore and alongshore component of the bed shear-stress vector  $\vec{\tau}$ ,  $g$  the acceleration due to gravity,  $\rho$  the density of water and  $A_h$  the horizontal eddy viscosity coefficient. The latter depends on the amplitude of the tidal currents and is modeled as  $A_h = lU$ , with  $l \sim 10$  m a mixing length scale and  $U \sim 1 \text{ ms}^{-1}$  a characteristic velocity scale related to the strength of the tidal currents. This  $U$  will be defined in Section 4.3.2. This formulation accounts for both mixing by small-scale turbulent eddies and vertical shear dispersion (*Zimmerman, 1986*).

A formulation for the bed shear-stress is used that is linear in the current

$$\vec{\tau} = \rho r \vec{u} \quad (4.3)$$

In this study a spatially uniform friction coefficient  $r$  is chosen, which is defined as

$$r = \frac{8}{3\pi} C_d U \quad (4.4)$$

Here,  $C_d (\sim 0.0025)$  is a drag coefficient and  $U$  is a characteristic flow amplitude of the domain and is related to the intensity of the tidal currents. The water motion in the domain is forced by prescribed cross-shore tidal currents in the inlet and by large-scale alongshore pressure gradients induced by the tidal wave. The boundary conditions are that the tidal currents in the inlet are prescribed. Far away from the inlet the tidal currents have their magnitude due to the prescribed large-scale alongshore pressure gradient.

### 4.2.3 Sediment transport

It is assumed that the sediment is relatively coarse and that its transport takes place as bedload (see *van Leeuwen et al. (2003)* and *van der Vegt et al. (2005)*). A Bagnold-Bailard sediment transport formulation is used, which is based on concepts discussed by *Bagnold (1966)* and *Bailard (1981)*. This formulation requires information of the currents at about 5 cm from the bed. Therefore, the depth-averaged currents (denoted by  $\vec{u}$ , having component  $u$  and  $v$ ) have to be transformed to the magnitude of the currents at that specific position ( $\vec{u}_{bl}$ ). This is done by assuming a logarithmic profile of the horizontal current and choosing a specific roughness height (here, the grain size of  $\sim 0.3$  mm). Thus, Coriolis effects (causing veering of the currents over the vertical) are neglected. This yields  $\vec{u}_{bl} = \beta\vec{u}$ , with  $\beta \approx 0.35$  a constant factor. Note that in the model of Chapter 3 it was implicitly assumed that  $\beta = 1$ .

The sediment transport is split into two different contributions. The first is the sediment transport induced by the tidal currents and the second is the sediment transport induced by the presence of the bed-slopes. The bedload transport averaged over the tidal period reads

$$\vec{q} = \vec{q}_f + \vec{q}_{bot} \quad (4.5)$$

with

$$\vec{q}_f = \alpha\beta^3 \langle |\vec{u}|^2 \vec{u} \rangle \quad (4.6)$$

$$\vec{q}_{bot} = \alpha\gamma\beta^p U^p \vec{\nabla} \tilde{H} \quad (4.7)$$

Here, the brackets  $\langle . \rangle$  denote an averaging over the tidal period. The constant  $\alpha$  depends on sediment characteristics and has for a grain size of  $\sim 0.3$  mm a value of  $\alpha = 10^{-5} \text{ s}^2\text{m}^{-1}$ . The bed-slope coefficient  $\gamma$  is  $\sim 1 \left(\frac{m}{s}\right)^{3-p}$  with  $p$  a constant. It has been argued that its value should be  $\sim 2$ , *Struiksmas et al. (1985)*, or  $\sim 3$  in *Bailard (1981)* and *Sekine and Parker (1992)*. Here, a value of  $p = 2$  will be used. Furthermore,  $U$  is the characteristic velocity scale which will be defined in Section 4.3.2. The variable  $\tilde{H}$  in Equation (4.7) is the deviation of the bathymetry from the reference bathymetry,  $\tilde{H} = H - H_R$ . Note that Equation (4.7) implies that only deviations of the reference bathymetry cause bed-slope induced sediment transport. This is allowed since the spatial scales of the ebb-tidal delta (the width  $B$ ) are much smaller than the typical scale of the reference bathymetry (the e-folding length scale  $L_s$ ) and therefore the typical magnitude of  $\vec{\nabla} H_R$  is much smaller than that of  $\vec{\nabla} \tilde{H}$ .

### 4.2.4 Sediment mass conservation and morphodynamic equilibrium

When the sediment transport is convergent the water depth will decrease because the sediment is deposited at the bed. In case of a divergent sediment transport the total water depth will increase. Furthermore, the time scale on which bottom patterns evolve is much larger than the time scale of the hydrodynamics (period of the  $M_2$  tide). This allows for calculating the hydrodynamics with a constant bathymetry while the evolution of the bed

is driven by the convergence of the residual sediment transport (for mathematical details about this tidal averaging method see *Sanders and Verhulst* (1985)). The bed evolution equation reads

$$\frac{\partial H}{\partial t} - \vec{\nabla} \cdot \vec{q} = 0 \quad (4.8)$$

The aim of this study is to calculate morphodynamic equilibrium solutions of the model. They obey the condition

$$\frac{\partial H}{\partial t} = 0 \quad (4.9)$$

which implies, according to Equation (4.8), that the sediment flux should have zero divergence. Henceforth we assume that  $H(x, y)$  represents an equilibrium. The boundary conditions are that far away from the inlet the bathymetry is given by the reference bathymetry, as given in Equation (4.1). In the tidal inlet a regularity conditions is applied which states that the depth is finite. Outside the inlet it is required that the cross-component of  $\vec{q}$  vanishes.

### 4.3 Reference state and inlet state

The model allows for a morphodynamic equilibrium which is alongshore uniform. This so-called reference state is obtained by considering the case without tidal currents through the tidal inlet. The water motion is only forced by the large-scale pressure gradient. In case an inlet is present this reference state is obviously modified. Hence, the state variables are split into a part which is due to the prescribed large-scale pressure gradient and a part which is due to the prescribed cross-shore tidal currents through the tidal inlet (denoted by a tilde):

$$\begin{aligned} \vec{u} &= \vec{U} + \vec{\tilde{u}}; & u &= U + \tilde{u}; & v &= V + \tilde{v}; & \vec{\nabla} \zeta &= \vec{\nabla} Z + \vec{\nabla} \tilde{\zeta}; \\ \vec{q} &= \vec{Q} + \vec{\tilde{q}}; & \vec{q}_f &= \vec{Q}_f + \vec{\tilde{q}}_f; & \vec{q}_{\text{bot}} &= \vec{Q}_{\text{bot}} + \vec{\tilde{q}}_{\text{bot}}; & H &= H_R + \tilde{H} \end{aligned} \quad (4.10)$$

In the next section the reference state morphodynamic equilibrium is described. This section is followed by a section in which the morphodynamic equilibrium due to the presence of the tidal inlet is described.

#### 4.3.1 Reference state morphodynamic equilibrium

##### Hydrodynamics

In the present model the gradient of  $Z$  is spatially uniform and it forces shore-parallel currents which are alongshore uniform. In the reference state the cross-shore velocity is zero ( $U = 0$ ) and the bathymetry is taken alongshore uniform. Substituting Equation (4.10) into Equations (4.2a)-(4.2c) and assuming that all variables due to the presence of the tidal inlet are zero leads to the equations that describe the hydrodynamics of the reference

state. The momentum balance in the alongshore direction comprises a balance between local inertia, the pressure gradient due to the alongshore sea surface gradient, friction and diffusive terms. However, diffusive terms are only important in the nearshore zone  $x \in (-x_s, 0)$  due to the boundary condition at  $x = -x_s$ . The boundary layer thickness ( $\sim \sqrt{A_h/\sigma}$ ) is small compared to the width of the nearshore zone ( $x_s$ ). In the region  $x > 0$  a scaling analysis reveals that the diffusive terms are small compared to the other terms in the reference state alongshore momentum equation. Because we are only interested in the region outside the nearshore zone, it can be used that  $A_h \frac{\partial^2 V}{\partial x^2}$  is small compared to the other terms in the alongshore momentum balance. Consequently, Equations (4.2a) and (4.2b) for the reference state become

$$fV = g \frac{\partial Z}{\partial x} \quad (4.11a)$$

$$\frac{\partial V}{\partial t} = -g \frac{\partial Z}{\partial y} - \frac{rV}{H_R} \quad (4.11b)$$

Note that Equation (4.11a) describes geostrophic balance. Following the description of the basic state in Chapter 2, the large-scale alongshore pressure gradient due to the tidal wave is written as

$$-g \frac{\partial Z}{\partial y} = S_0 + S_2 \cos(\sigma t + \phi_a) \quad (4.12)$$

with  $S_0$  a residual component and  $S_2$  the magnitude of the tidal ( $M_2$ ) component. Furthermore,  $\phi_a$  is an arbitrary phase to control the phase difference between the prescribed currents in the tidal inlet and the alongshore tidal currents at sea induced by the large-scale pressure gradient. The solution of Equation (4.11b) can be found in *Calvete et al.* (2001) and reads

$$V(x) = V_0(x) + V_2(x) \cos(\sigma t - \Phi(x)) \quad (4.13)$$

where

$$V_0 = \frac{S_0 H_R}{r}; \quad V_2(x) = \frac{H_R(x) S_2}{\sqrt{H_R(x)^2 + (r/\sigma)^2}}; \quad \Phi(x) = \arctan\left(\frac{r}{\sigma H_R(x)}\right) + \phi_a \quad (4.14)$$

### Net sediment transport

The net sediment transport in the reference state is obtained by substituting Equation (4.10) into Equations (4.6)- (4.7). This yields

$$\vec{Q}_f = \alpha \beta^3 \langle |\vec{U}|^2 \vec{U} \rangle \quad (4.15)$$

$$\vec{Q}_{\text{bot}} = 0 \quad (4.16)$$

Note that  $\vec{Q}_f$  is only nonzero when  $V_0$  is nonzero. In that case  $\vec{Q}_f$  only has an alongshore component, which is alongshore uniform.

## Morphodynamic equilibrium

In the reference state the sediment mass balance becomes

$$\vec{\nabla} \cdot \vec{Q}_f = 0 \quad (4.17)$$

Note that  $\vec{\nabla} \cdot \vec{Q}_f = 0$ , because  $\vec{Q}_f$  is alongshore uniform.

### 4.3.2 Morphodynamic equilibrium due to presence of tidal inlet

#### Hydrodynamics

The equations that describe the hydrodynamics due to the presence of a tidal inlet are obtained by substituting Equation (4.10) into Equations (4.2a)-(4.2c), subtracting Equations (4.11a)-(4.11b) that describe the reference state and finally using that  $A_h \frac{\partial^2 V}{\partial x^2} = 0$ . The results are

$$\frac{\partial \tilde{u}}{\partial t} + \tilde{u} \frac{\partial \tilde{u}}{\partial x} + (V + \tilde{v}) \frac{\partial \tilde{u}}{\partial y} - f \tilde{v} = -g \frac{\partial \tilde{\zeta}}{\partial x} - \frac{r \tilde{u}}{H_R + \tilde{H}} + A_h \left( \frac{\partial^2 \tilde{u}}{\partial x^2} + \frac{\partial^2 \tilde{u}}{\partial y^2} \right) \quad (4.18a)$$

$$\frac{\partial \tilde{v}}{\partial t} + \tilde{u} \frac{\partial (V + \tilde{v})}{\partial x} + (V + \tilde{v}) \frac{\partial (V + \tilde{v})}{\partial y} + f \tilde{u} = -g \frac{\partial \tilde{\zeta}}{\partial y} - \frac{r(V + \tilde{v})}{H_R + \tilde{H}} + \frac{rV}{H_R} + A_h \left( \frac{\partial^2 \tilde{v}}{\partial x^2} + \frac{\partial^2 \tilde{v}}{\partial y^2} \right) \quad (4.18b)$$

$$\frac{\partial}{\partial x} [\tilde{u}(H_R + \tilde{H})] + \frac{\partial}{\partial y} [(V + \tilde{v})(H_R + \tilde{H})] = 0 \quad (4.18c)$$

The rigid lid approximation allows for a convenient way to solve the hydrodynamic equations by constructing an equation for the vorticity. The vorticity is defined as  $\omega = \partial v / \partial x - \partial u / \partial y$ . Following the splitting of the variables as in Equation (4.10), we define  $\omega = \Omega + \tilde{\omega}$  with  $\Omega = \partial V / \partial x$  and  $\tilde{\omega} = \partial \tilde{v} / \partial x - \partial \tilde{u} / \partial y$ . Taking the derivative of Equation (4.18b) with respect to  $x$  and subtracting the derivative of Equation (4.18a) with respect to  $y$  results in an equation for the vorticity,

$$\begin{aligned} \frac{\partial \tilde{\omega}}{\partial t} + \tilde{u} \frac{\partial (\Omega + \tilde{\omega})}{\partial x} + (V + \tilde{v}) \frac{\partial \tilde{\omega}}{\partial y} &= -(\Omega + \tilde{\omega} + f) \left( \frac{\partial \tilde{u}}{\partial x} + \frac{\partial \tilde{v}}{\partial y} \right) - \frac{r(H_R \tilde{\omega} - \tilde{H} \Omega)}{H_R(H_R + \tilde{H})} \\ &+ \frac{r}{(H_R + \tilde{H})^2} \left[ (V + \tilde{v}) \frac{\partial (H_R + \tilde{H})}{\partial x} - \tilde{u} \frac{\partial \tilde{H}}{\partial y} \right] \\ &- \frac{rV}{H_R^2} \frac{dH_R}{dx} + A_h \left( \frac{\partial^2 \tilde{\omega}}{\partial x^2} + \frac{\partial^2 \tilde{\omega}}{\partial y^2} \right) \end{aligned} \quad (4.19)$$

The vorticity equation (4.19) and the continuity equation (4.18c) are solved in the model with boundary conditions

$$x = 0, \quad |y| > B/2 : \quad \tilde{u} = 0, \quad \frac{\partial \tilde{v}}{\partial x} = 0 \quad (4.20a)$$

$$x = 0, \quad |y| < B/2 : \quad \tilde{u} = \hat{U}(y) \cos(\sigma t), \quad \frac{\partial \tilde{v}}{\partial x} = 0 \quad (4.20b)$$

$$(x^2 + y^2) \rightarrow \infty : \quad \tilde{u} \rightarrow 0, \quad \tilde{v} \rightarrow 0 \quad (4.20c)$$

At  $x = 0$  a free-slip condition for the alongshore velocity component is applied. Furthermore,  $\hat{U}(y)$  is a given cross-shore tidal current profile in the inlet,

$$\hat{U}(y) = \hat{U}(0) \left[ \left(2\frac{y}{B} - 1\right)^3 \left(2\frac{y}{B} + 1\right)^3 \right] \quad (4.21)$$

where  $\hat{U}(0)$  is the maximum current amplitude in the center of the inlet. This models an oscillating vorticity dipole in the inlet. The profile has been chosen such that both velocity and vorticity vanish at the boundaries  $y = \pm B/2$ . This is consistent with observations, which show that the velocity in the center of the tidal inlet is larger than at both sides of the tidal inlet (*Chadwick and Largier, 1999*). This velocity profile was also used in Chapter 3 of this thesis.

The typical scale of the velocity through the inlet and the typical scale of the shore-parallel tidal currents are known. From these two velocity scales the typical velocity scale of the domain ( $U$ ) is determined. It is chosen as

$$U = \sqrt{\hat{U}(0)^2 + V_2(0)^2} \quad (4.22)$$

### Sediment transport

The sediment transport due to the prescribed cross-shore tidal currents over the inlet is obtained by subtracting the reference state sediment transport from equations (4.6)-(4.7)

$$\vec{q}_f = \alpha \beta^3 \left( \langle |\vec{U} + \vec{u}|^2 (\vec{U} + \vec{u}) \rangle - \langle |\vec{U}|^2 \vec{U} \rangle \right) \quad (4.23)$$

$$\vec{q}_{\text{bot}} = \alpha \gamma \beta^2 U^2 \vec{\nabla} \tilde{H} \quad (4.24)$$

### Morphodynamic equilibrium

The sediment mass balance in morphodynamic equilibrium due to the presence of the tidal inlet is obtained by substituting Equations (4.23) and (4.24) into the morphodynamic equilibrium condition ( $\vec{\nabla} \cdot \vec{q} = 0$ ) and subtracting the reference state equilibrium condition (4.15)- (4.17). The result is

$$\vec{\nabla} \cdot \vec{q}_f + \vec{\nabla} \cdot \vec{q}_{\text{bot}} = \vec{\nabla} \cdot \vec{q}_f + \alpha \gamma \beta^2 U^2 \nabla^2 \tilde{H} = 0 \quad (4.25)$$

The boundary conditions are

$$x = 0, |y| > \frac{B}{2} : \quad \partial \tilde{H} / \partial x = 0 \quad (4.26a)$$

$$x = 0, |y| < \frac{B}{2} : \quad \tilde{H} = \text{finite} \quad (4.26b)$$

$$(x^2 + y^2) \rightarrow \infty : \quad \tilde{H} \rightarrow 0 \quad (4.26c)$$

Outside the inlet at  $x = 0$  no exchange of sediment between the nearshore zone and the inner shelf is allowed. This implies that the cross-shore component of  $\vec{q}$  is zero. From Equation (4.23) it follows that the cross-shore component of  $\vec{q}_f$  is zero and therefore outside the inlet at  $x = 0$  it is required that  $\partial \tilde{H} / \partial x = 0$ . In the inlet a regularity condition for the water depth is required. Far from the inlet the bathymetry tends to the reference bathymetry  $H_R(x)$ .

## 4.4 Methods

### 4.4.1 Finding morphodynamic equilibria

Morphodynamic equilibria in the model are obtained as follows. The starting point is a known equilibrium of the model (e.g., the reference equilibrium). The corresponding bathymetry is denoted by  $H = H(x, y; \mu)$ , where  $\mu$  represents a parameter (e.g.,  $\hat{U}(0)$ ). Next, the value of  $\mu$  is changed by a small increment  $\Delta\mu$  and the tidal currents are computed using the 'old' bathymetry  $H = H(x, y; \mu)$ . From this, the sediment flux vector  $\vec{q}_f$  is calculated from Equation (4.23) and next Equation (4.25) is solved to obtain a first guess for the 'new' equilibrium bottom  $H = H(x, y; \mu + \Delta\mu)$ . This boils down to finding the solution of a Poisson equation. This is not yet the 'true' bottom, because  $\vec{q}_f$  was computed with a previous guess of the bottom pattern. So, an iteration procedure is applied which involves recomputation of the tidal currents with the new guess of the bottom and finding subsequent updates for  $\vec{q}_f$  and  $H = H(x, y; \mu + \Delta\mu)$  until convergence is established. After this, parameter  $\mu$  can be changed again, resulting in a continuum of equilibrium solutions obtained for different parameter values. The success of this method was already demonstrated in Chapter 3.

### 4.4.2 Method to solve hydrodynamic equations

To numerically solve Equations (4.18c), (4.19) with boundary conditions (4.20), a pseudospectral method is used in the spatial coordinates (*Boyd, 2001*). For the time-dependent part a Galerkin method is used. The velocity components  $u$  and  $v$  are expanded in their harmonic constituents  $M_0$  (residual current),  $M_2$  (principal tide),  $M_4$  (first overtide) and so on. In this study the series is truncated after the  $M_2$  components, so nonlinear tides are not accounted for. In *van Leeuwen et al. (2003)* it was shown that at the seaward side of the tidal inlet the dominant transport mechanism was the transport of sediment by the residual currents, while inside the tidal basin higher harmonics of the tide were important. Therefore it is sufficient to calculate the sediment flux by only considering



the  $M_0$  and  $M_2$  components of the velocity field. The validity of this assumption will be discussed in the next chapter. The numerical details of the solution procedure are equal to that described in Chapter 3.

### 4.4.3 Numerical Method to Solve the Poisson Problem

Each iteration step Equation (4.25) has to be solved for given  $\vec{q}_f$ . The method employed consists of transforming this Poisson equation into elliptic-cylindrical coordinates. This allows for construction of solutions as multipole series. The results are integral equation for each pole, which are subsequently solved. For more details, see Chapter 3 and *van der Vegt et al.* (2005). In Chapter 3 the symmetric delta was studied. Therefore, it was sufficient to only consider the symmetric poles. Furthermore, the boundary condition that  $\partial\tilde{H}/\partial x = 0$  yields that all sine poles are zero. Hence, the bottom pattern is described by the sum of even cosine poles. In this study the bottom patterns can be asymmetric. Therefore the bottom patterns are described by the sum of both odd and even cosine poles.

## 4.5 Results

The number of collocation points used in this study is  $N_x = 40$  for the  $x$ -direction and  $N_y = 60$  for the  $y$ -direction. This is based on several sensitivity experiments and the values have been chosen such that calculations are fast and reasonably accurate. To solve Equation (4.25) every iteration step 150 poles have been used. An overview of the parameter values which are the same for all experiment is given in Table 4.1. The factor  $\gamma$  has been chosen such that  $\gamma/\beta = 2$ . This factor can be changed, but this will only result in a change of the amplitude of the modeled bottom patterns but does not influence the patterns itself. An overview of the performed experiments and the magnitude of the other parameters is presented in Table 4.2.

The phase of the shore-parallel currents at sea is determined by Equation (4.14). The phase difference between the shore-parallel tidal currents and the cross-shore currents through the tidal inlet is given by  $\Phi(0)$ . A negative value of  $\Phi(0)$  means that the cross-shore currents through the tidal inlet are lagging the shore-parallel tidal currents, which is quite often observed for tidal inlet systems (*Sha and van den Berg, 1993*). A value of  $\Phi(0) = 0^\circ$  is representative for tidal inlet systems along the Dutch Wadden Sea, while  $\Phi(0) = -90^\circ$  is observed for the Western Scheldt estuary (*Sha and van den Berg, 1993*).

### 4.5.1 Coriolis force

In the first experiments the influence of the Coriolis force on the asymmetry of the ebb-tidal deltas is studied. The large-scale pressure gradient at sea is zero,  $S_0, S_2 = 0$ . The only symmetry-breaking mechanism in this experiment is related to the Coriolis force. The Coriolis parameter is  $f = 1.11 \cdot 10^{-4} \text{ s}^{-1}$  for a latitude of  $50^\circ$ . The relative influence of the Coriolis force compared with local acceleration due to inertia is measured by the inverse Rossby number,  $Ro^{-1} = fL/U$ . Here,  $L$  is the typical length scale, which is the width of

Parameter	Value
$N_x$	40
$N_y$	60
$N_{\text{poles}}$	150
$C_d$	$2.5 \cdot 10^{-3}$
$A_h$	$l * U \text{ m}^2\text{s}^{-1}$
$l$	14 m
$U$	Eq. (4.22)
$\gamma$	$0.7 \text{ ms}^{-1}$
$\beta$	0.35

Table 4.1: Parameter values used in the experiments.

section	$B$ (km)	$\hat{U}(0)$ ( $\text{ms}^{-1}$ )	$f$ ( $\text{s}^{-1}$ )	$V_2$ ( $\text{ms}^{-1}$ )	$\Phi(0)$ ( $^\circ$ )	$V_0$ ( $\text{ms}^{-1}$ )
4.5.1	5	0.3	$1.11 \cdot 10^{-4}$	0	0	0
4.5.2	2	0.5	0	0.15	0	0
4.5.2	2	0.2-0.5	0	0.15	0	0
4.5.2	2	0.5	0	0.025-0.15	0	0
4.5.2	2	0.5	0	0.15	-100-0	0
4.5.2	5 and 7	0.5	0	0.15	0	0
4.5.3	2	0.5	0	0	0	0.01

Table 4.2: Overview of experiments performed for this study.

the inlet. For  $\hat{U}(0) = 1 \text{ ms}^{-1}$  and  $B = 2 \text{ km}$  the inverse Rossby number is  $Ro^{-1} = 0.2$  and its effect is small. To show the influence of the Coriolis force on the asymmetry of the equilibrium bathymetry, results are presented for a relatively broad inlet ( $B = 5 \text{ km}$ ) with small cross-shore tidal currents ( $\hat{U}(0) = 0.3 \text{ ms}^{-1}$ ). In this situation  $Ro^{-1} = 1.8$  and the influence of Coriolis force is of the same order of magnitude as inertia.

The modeled equilibrium bathymetry is shown in Figure 4.4(a). It is slightly asymmetric with respect to the mid-axis through the tidal inlet. The deepest channel is oriented to the left. The channel on the right-hand side of the inlet is a little shallower than the channel on the left-hand side. There is not a clear channel in the center of the inlet. Most sediment of the delta is located at the right-hand side of the mid-axis through the inlet. The ebb-tidal delta is shifted a little to the right. Figure 4.4(b) shows the residual current pattern. Two residual circulation cells can be recognized as was the case with symmetrical ebb-tidal deltas described in Chapter 3, but they are slightly asymmetric. The residual currents in the right-hand cell are slightly smaller than the currents in the left-hand cell. The ebb-tidal delta is located at the end of the ebb-dominated currents.

Experiments have been performed for smaller inlets and with larger magnitude of  $\hat{U}(0)$  (smaller inverse Rossby number). The equilibrium bottom patterns are less asymmetric. For typical configurations as found along the Dutch and German Wadden Sea the influence of the Coriolis is negligible because the inlets have strong magnitudes of the outflow ( $\sim 1 \text{ ms}^{-1}$ ) and are relatively small (between 2 and 10 km). For tidal inlets which are relatively wide and have relatively small cross-shore tidal currents (inverse Rossby number

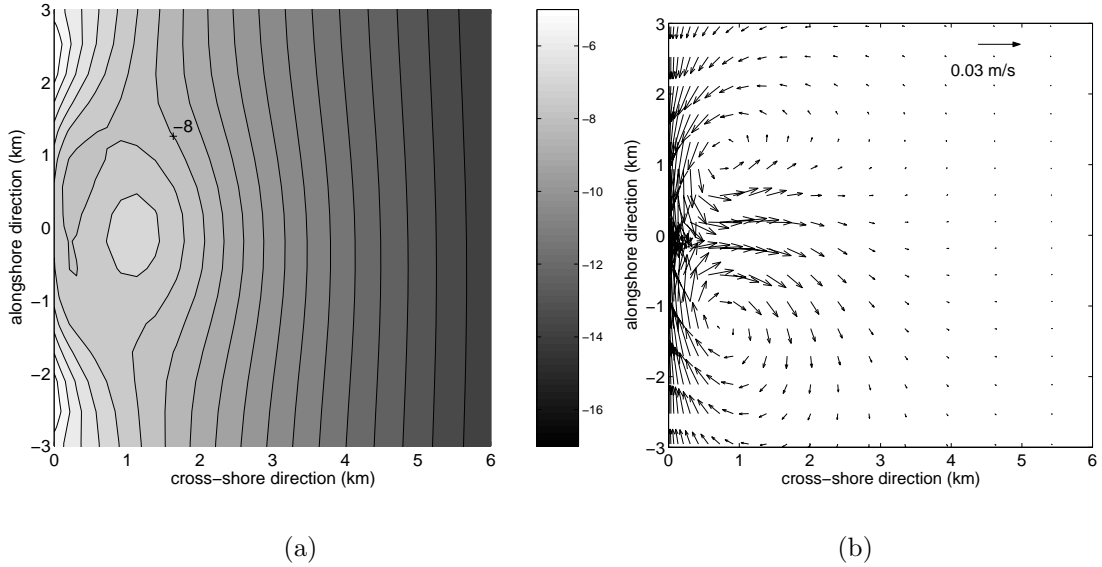


Figure 4.4: (a) Equilibrium bathymetry for  $\hat{U}(0) = 0.3 \text{ ms}^{-1}$ ,  $B = 5 \text{ km}$  and no large-scale shore-parallel currents. The Coriolis parameter is set for a latitude of  $50^\circ$  north. Contour lines are drawn every 0.5 meter. (b) Residual currents in morphodynamic equilibrium.

is large) the Coriolis force can be important.

On the Southern Hemisphere the Coriolis parameter is negative. In that case the asymmetry changes from right-oriented to left-oriented.

## 4.5.2 Shore-parallel currents

In this subsection the influence of the interaction between the shore-parallel and cross-shore tidal currents on the (a)symmetry properties of ebb-tidal deltas is studied. It is assumed that the deltas are located at the Northern Hemisphere. Similar results for the Southern Hemisphere can be obtained by increasing  $\Phi(0)$  with  $180^\circ$ .

### Default case

In the first series of experiments the width of the inlet is  $B = 2 \text{ km}$ . The maximum tidal currents at  $x = 0$  induced by the alongshore pressure gradient in the reference state is  $V_2(0) = 0.15 \text{ ms}^{-1}$ . The magnitude of  $\hat{U}(0)$  is varied between  $\hat{U}(0) = 0$  and  $\hat{U}(0) = 0.5 \text{ ms}^{-1}$ . For increasing magnitude of  $\hat{U}(0)$  also the typical velocity scale  $U$  increases (see Equation (4.22)). Therefore, also the magnitude of the friction coefficient  $r$  and the magnitude of the diffusion parameter  $A_h$  increase. As a consequence, for increasing magnitudes of the outflow in principle both the reference state velocity profile and phase would change (Equations (4.14)). However, in the experiments presented in this section it is chosen to study the influence of a change in  $\hat{U}(0)$  while keeping the phase  $\Phi$  and the magnitude  $V_2$  of the reference state velocity fixed. This profile is calculated with a friction parameter  $r = (8/3\pi)C_d V_2(0)$ . The pressure gradient is such that  $V_2(0) = 0.15$

$\text{ms}^{-1}$ . To calculate  $\tilde{u}$  and  $\tilde{v}$  it is used that  $r = 8/3\pi C_d U$ , and  $U$  is given by Equation (4.22).

The residual currents in morphodynamic equilibrium for  $\hat{U}(0) = 0.5 \text{ ms}^{-1}$  are shown in Figure 4.5(a). Two cells are present, with the residual currents in the right-hand cell being larger than those in the left-hand cell. Figure 4.5(b) shows the tidal ellipses of the  $M_2$  tidal currents. From this figure it is concluded that the  $M_2$  tidal currents are large and bidirectional at the left-hand side of the inlet and weak and more rotary at the right-hand side. Furthermore, the area with ebb-dominated currents is located at the left-hand side of the mid-axis through the tidal inlet. A vector plot of the residual sediment transport  $\vec{q}_f$  is shown in Figure 4.5(c). Sediment is transported from the right-hand side of the inlet to the center of the inlet. From there it is transported seaward to the left-hand side of the inlet. The equilibrium bathymetry is shown in Figure 4.5(d). Most sediment of the ebb-tidal delta is positioned at the left-hand side. There is not a clear isolated ebb-shoal (no closed contour lines) as was obtained in the case of the symmetric deltas (Chapter 3) or in the experiment with Coriolis force (previous section). Instead, the delta starts at the left-hand side of the inlet and protrudes seaward until approximately  $x = 1 \text{ km}$  and  $y = 0$ . The main channel is oriented to the right. It has a maximum depth of 8 meter and has flood-dominant currents. Although the currents are strong, bidirectional and ebb-dominated at the left-hand side of the inlet, there is no clear channel in that area. The strong bidirectional tidal currents at the left-hand side of the inlet transport sediment, but this sediment transport is convergent and is balanced by the convergence of the bed-slope induced sediment transport. This results in the presence of an ebb-tidal delta without a clear ebb-dominated channel.

It has been studied whether the profile of  $V_2$  has a strong influence on the results. In the calculation of  $V_2$  it was used that the friction coefficient was  $r = (8/3\pi)C_d V_2(0)$  and  $V_2(0) = 0.15 \text{ ms}^{-1}$ . An experiment has been performed in which  $V_2$  was calculated with a friction coefficient  $r = 8/3\pi C_d U$ , and  $U$  as given by Equation (4.22). From the results it is concluded that it has only a small influence on the final equilibrium (Figure 4.6).

### Sensitivity of the results to magnitude of the tidal currents through the inlet

To obtain the results described in the previous section, the magnitude of  $\hat{U}(0)$  was increased with steps of  $0.1 \text{ ms}^{-1}$ . To quantify the "amount of asymmetry", an objective parameter is introduced. Because the maximum of the shoal or the minimum of the channel does not exist in all experiments that have been performed, the alongshore position of the maximum of  $\tilde{H}$  is used as a measure for the asymmetry of the ebb-tidal delta. This parameter is called  $y_p$ . When  $y_p$  has a negative value, most sediment is on the right-hand side of the inlet. The ebb-delta is always located seaward of the area where currents are ebb-dominated. This implies that when most sediment is located at the right-hand side of the inlet, also the area with ebb-dominated currents is located at the right-hand side. Hence, the delta is called right-oriented. A positive value of  $y_p$  implies that the delta is left-oriented.

In Figure 4.7(a)  $y_p$  is shown as a function of  $\hat{U}(0)$ . For  $\hat{U}(0) = 0.2 \text{ ms}^{-1}$  the delta is right-oriented. For larger values the delta is left-oriented. Increasing  $\hat{U}(0)$  results in an increase of  $y_p$ . The increase in  $y_p$  becomes smaller for larger values of  $\hat{U}(0)$ .

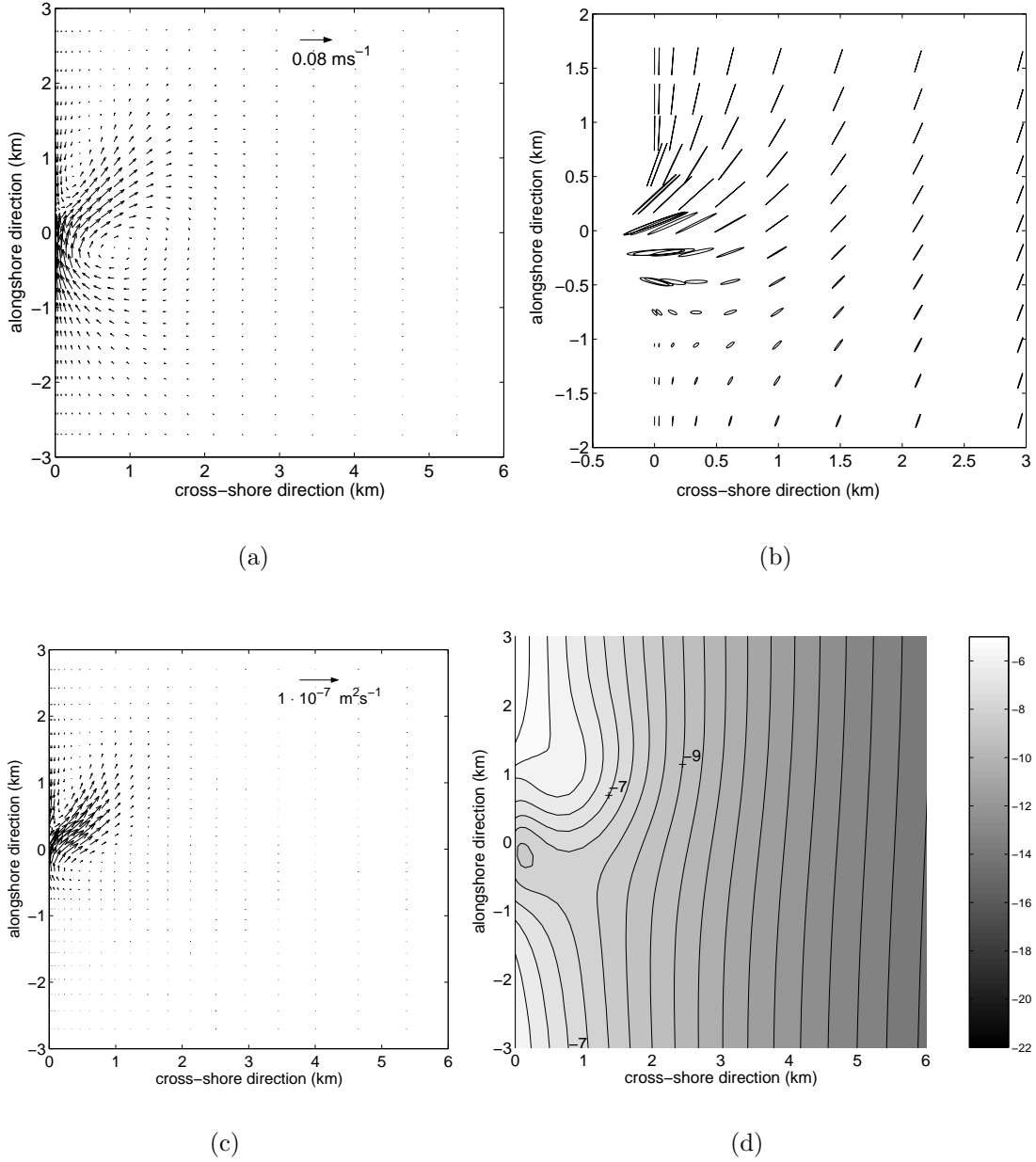


Figure 4.5: (a) Residual currents for  $\hat{U}(0) = 0.5 \text{ ms}^{-1}$ ,  $V_2(0) = 0.15 \text{ ms}^{-1}$ ,  $\Phi(0) = 0^\circ$ ,  $f = 0$  and  $B = 2 \text{ km}$ . (b) Same as (a), but now the current ellipses of the  $M_2$  tide. (c) Same as (a), but now residual sediment transport in morphodynamic equilibrium is shown for  $\alpha = 10^{-5} \text{ s}^2 \text{ m}^{-1}$ . (d) Same as (a), but now the equilibrium bathymetry is shown. Contour lines are drawn every 0.5 meter.

### Sensitivity of the results to magnitude of the shore-parallel tidal currents

In the experiments described in this subsection  $\hat{U}(0) = 0.5 \text{ ms}^{-1}$ ,  $\Phi(0) = 0^\circ$  and  $V_2(0)$  is increased from zero to  $0.15 \text{ ms}^{-1}$ . The reference velocity profile is calculated as in the previous sections. This means that  $V_2$  and  $\Phi$  are calculated with  $r = (8/3\pi)C_d V_2(0)$ . For the

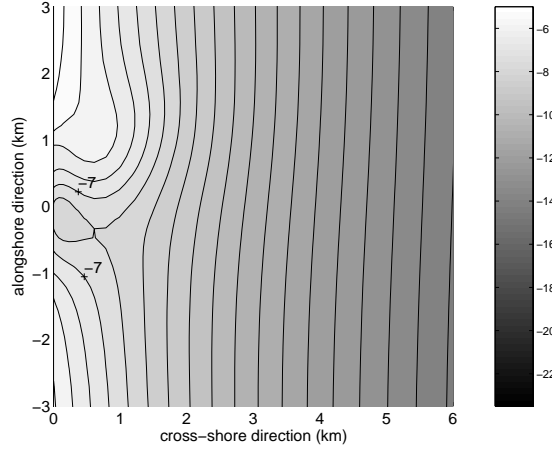


Figure 4.6: Same as Figure 4.5(d), but now  $V_2$  has been determined with  $r = 8C_dU/(3\pi)$ , so  $U$  given by Equation (4.22) instead of  $U = V_2(0)$ .

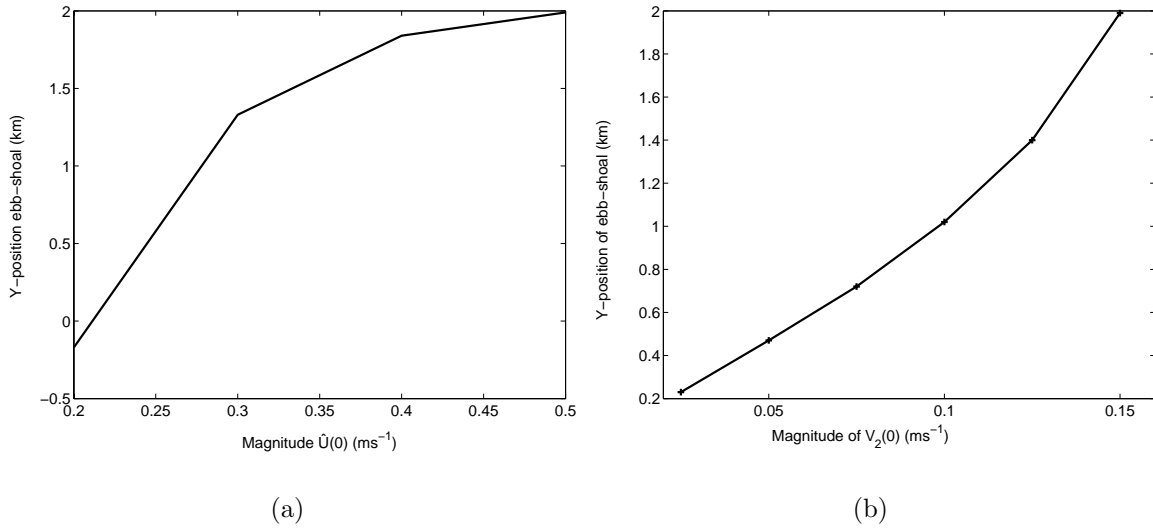


Figure 4.7: (a) The  $y$ -coordinate of the position of the ebb-shoal for  $B = 2$  km,  $V_2(0) = 0.15$   $\text{ms}^{-1}$ ,  $\Phi(0) = 0^\circ$  and  $f = 0$  as a function of  $\hat{U}(0)$ . (b) The  $y$ -coordinate of the position of the ebb-shoal for  $B = 2$  km,  $\hat{U}(0) = 0.5$   $\text{ms}^{-1}$ ,  $\Phi(0) = 0^\circ$  and  $f = 0$  as a function of  $V_2(0)$ .

calculations of  $\tilde{u}$  and  $\tilde{v}$  it is used that  $r = 8/(3\pi)C_dU$ , with  $U$  as given in Equation (4.22).

Again, the value of  $y_p$  has been determined for each experiment. In this parameter setting for each value of  $V_2(0)$  the value of  $y_p$  is positive. This means that the area with ebb-dominated currents and the area where most sediment of the ebb-tidal delta is located, is found on the left-hand side of the tidal inlet. Increasing the magnitude of  $V_2(0)$  causes a faster than linear increase of  $y_p$  (Figure 4.7(b)).

### Sensitivity of the results to $\Phi(0)$

According to *Sha and van den Berg* (1993), the phase difference between the cross-shore and shore-parallel currents is an important factor for the asymmetry properties of ebb-tidal deltas. Therefore, in the next experiment the sensitivity of the results to the phase  $\Phi(0)$  is studied. The width of the inlet is  $B = 2$  km,  $\hat{U}(0) = 0.5$  ms<sup>-1</sup> and  $V_2(0) = 0.15$  ms<sup>-1</sup>. The phase is changed from  $\Phi(0) = -100^\circ$  to  $\Phi(0) = 0^\circ$ .

A vector plot of the residual currents for  $\Phi(0) = -100^\circ$  is shown in Figure 4.8(a). The residual currents are organized in two cells and magnitudes of the currents in the two cells are of the same order. Compared to the case that  $\Phi(0) = 0^\circ$  (Figure 4.5(a)), the magnitudes of the residual currents are smaller and the two cells are less asymmetric. Furthermore, the area with ebb-dominated currents is now found on the right-hand side of the inlet. The tidal current ellipses of the  $M_2$  tide are strongly polarized on both sides of the tidal inlet (Figure 4.8(b)). The residual sediment transport  $\vec{q}_f$  is shown in Figure 4.8(c) and is organized in two cells. Compared to the case that  $\Phi(0) = 0^\circ$ , the sediment is transported less far seaward and it is transported to the right-hand side of the inlet instead of being transported to the left-hand side. Figure 4.8(d) shows the equilibrium bottom pattern. The flood-dominated channel is oriented to the left and most sediment is found on the right-hand side of the tidal inlet. The delta has now become right-oriented. The bottom pattern is less pronounced than that obtained for  $\Phi(0) = 0^\circ$ .

The equilibrium bathymetry has been calculated for  $\Phi(0) = -100^\circ, -75^\circ, -50^\circ, -25^\circ$  and for  $\Phi(0) = 0^\circ$ . The value of  $y_p$  as a function of  $\Phi(0)$  is shown in Figure 4.9. For  $B = 2$  km  $y_p$  is positive for most values of  $\Phi(0)$ . However, for  $\Phi(0) \approx -80^\circ$  the delta changes orientation. In that case the area with ebb-dominated currents and the area where most sediment of the ebb-tidal delta is found is located at the right-hand side.

### Sensitivity of the results to width of the tidal inlet

The width of the inlets along the Dutch coast ranges between approximately two kilometers and ten kilometers. Therefore, in the following experiment the width of the inlet has been varied between these extremes. The flow profile was not changed. This is done to facilitate the comparison between the results, although it is realized that the prescribed velocity profile (4.21) is a reasonable approximation for relatively small inlets (up to 1-2 kilometers), but it is not very realistic for an inlet with  $B = 10$  km.

The parameters used in the experiments are  $\hat{U}(0) = 0.5$  ms<sup>-1</sup>,  $V_2(0) = 0.15$  ms<sup>-1</sup> and  $\Phi(0) = 0$ . The equilibrium bathymetry for  $B = 2$  km was already presented in Figure 4.5(d). The equilibrium bathymetry for  $B = 5$  km and  $B = 7$  km are shown in Figure 4.10(a) and 4.10(b), respectively. For  $B = 10$  km no equilibrium bathymetry was obtained for this setting. Interestingly, for  $B = 7$  km a second channel appears on the left-hand side. This channel is not present for  $B = 2$  km and has approximately the same depth as the channel on the right-hand side. The currents in this channel are flood-dominated. The presence of the channel on the left-hand side is already noticeable in the equilibrium bathymetry for  $B = 5$  km. For both  $B = 5$  km and  $B = 7$  km the area with ebb-dominated currents is found on the left-hand side. Increasing the width of the tidal inlet causes a change in the asymmetry properties. This is also confirmed by the results

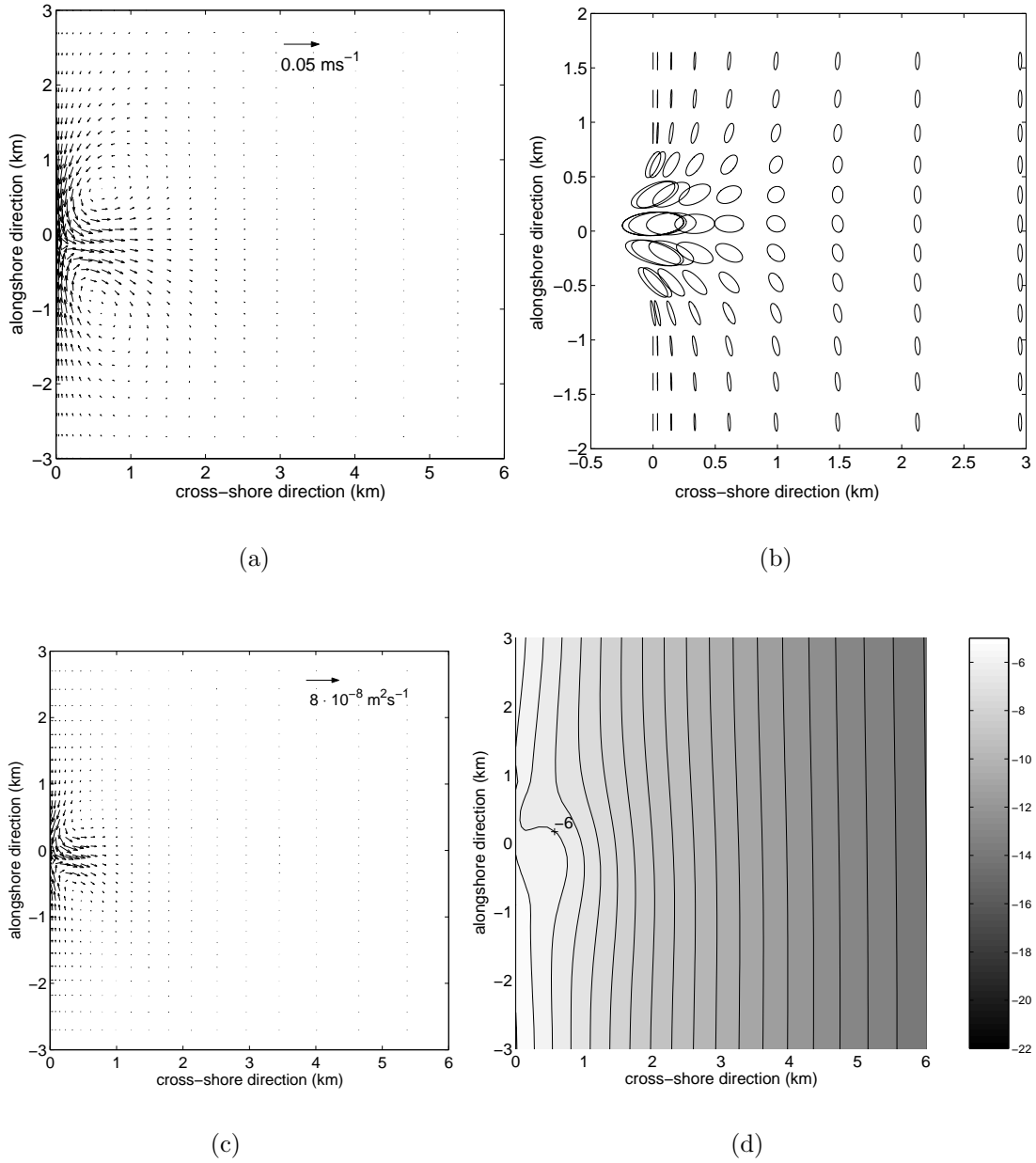


Figure 4.8: As Figure 4.5, except that in this experiment  $\Phi(0) = -100^\circ$ .

presented in Figure 4.9. The solid line shows  $y_p$  as a function of  $\Phi(0)$  for  $B = 7 \text{ km}$ ,  $V_2 = 0.15 \text{ ms}^{-1}$  and  $\hat{U}(0) = 0.5 \text{ ms}^{-1}$ . While for  $B = 2 \text{ km}$  the delta changes orientation for  $\Phi(0) \approx -80^\circ$ , for  $B = 7 \text{ km}$  the delta changes orientation for  $\Phi(0) \approx -60^\circ$ .

### 4.5.3 Residual currents at sea

In this section the influence of a prescribed residual shore-parallel current on the asymmetry of the ebb-tidal delta is studied. The width is  $B = 2 \text{ km}$ , the Coriolis force is absent,



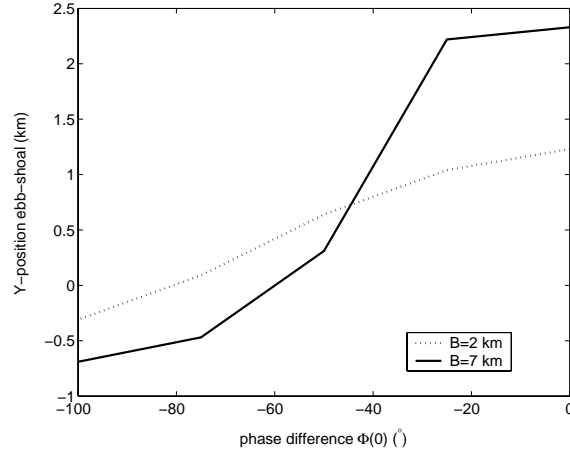


Figure 4.9: The  $y$ -coordinate of the position of the ebb-shoal for  $\hat{U}(0) = 0.5 \text{ ms}^{-1}$ ,  $V_2(0) = 0.15 \text{ ms}^{-1}$ ,  $f = 0$  and  $B = 2 \text{ km}$  and  $B = 7 \text{ km}$  as a function of the phase difference  $\Phi(0)$  between alongshore tidal currents and currents through the tidal inlet.

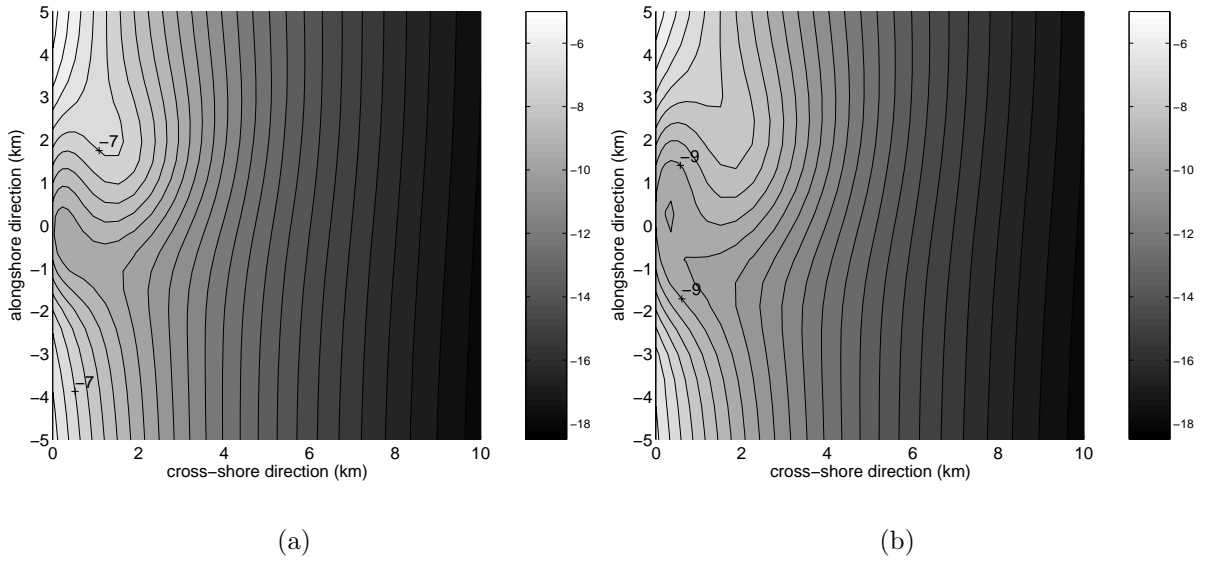


Figure 4.10: (a) Equilibrium bathymetry for  $\hat{U}(0) = 0.5 \text{ ms}^{-1}$ ,  $V_2(0) = 0.15 \text{ ms}^{-1}$ ,  $\Phi(0) = 0^\circ$ ,  $f = 0$  and  $B = 5 \text{ km}$ . Contour lines are drawn every 0.5 meter. (b) Same as (a), but now for  $B = 7 \text{ km}$ .

$\hat{U}(0) = 0.5 \text{ ms}^{-1}$  and the large-scale alongshore current only has a mean component,  $S_2 = 0$  and  $S_0 \neq 0$ . A value for  $S_0$  is chosen such that  $V_0(0) = -0.01 \text{ ms}^{-1}$  and for  $x \rightarrow \infty$   $V_0$  is  $-0.05 \text{ ms}^{-1}$ . The residual currents are in the negative  $y$ -direction. In Figure 4.11(a) the equilibrium bathymetry is shown. The ebb-tidal delta is located at the right-hand side of the tidal inlet. The deepest channel is oriented against the direction of the residual currents. A vector plot of the residual currents is shown in Figure 4.11(b). The residual circulation pattern is also asymmetric. Changing the direction of the large-scale residual currents changes the orientation of the delta.

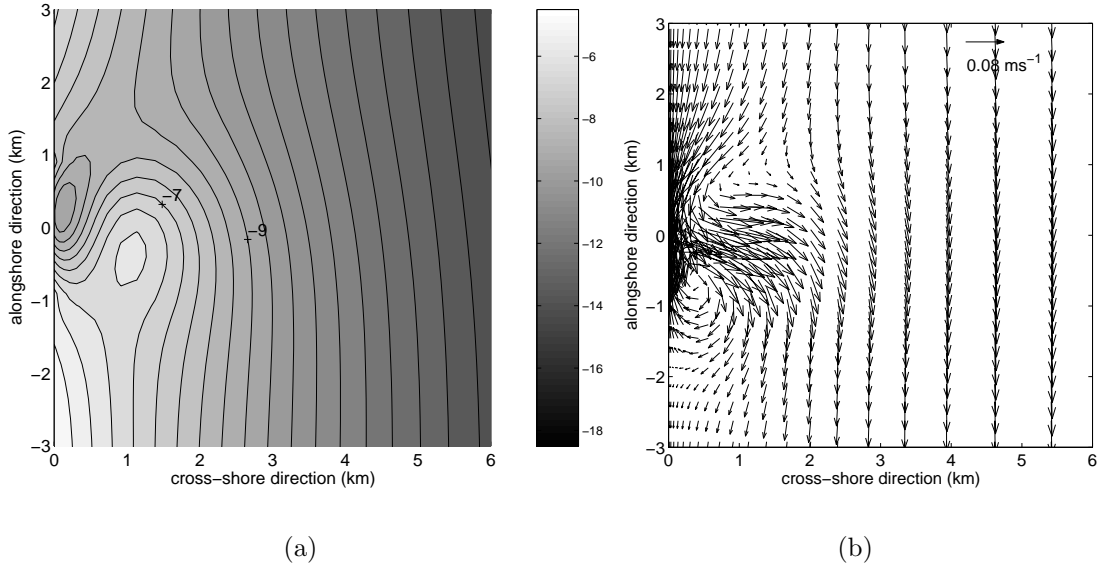


Figure 4.11: (a) Equilibrium bathymetry for large-scale alongshore mean current from left to right.  $\hat{U}(0) = 0.5 \text{ ms}^{-1}$ ,  $V_0(0) = -0.01 \text{ ms}^{-1}$ ,  $f = 0$  and  $B = 2 \text{ km}$ . Contour lines are drawn every 0.5 meter. (b) Mean currents in morphodynamic equilibrium.

In a last experiment the influence of both residual and tidal shore-parallel tidal currents is studied. The Ameland Inlet (see figure 1.7) is characterized by residual currents which are directed in the negative  $y$ -direction and by shore-parallel tidal currents with a small phase difference  $\Phi(0)$  (Ridderinkhof, 1989; Sha, 1989a; Israel and Dunsbergen, 1999). The effects of the residual currents and the shore-parallel tidal currents are counteracting, as they cause the delta to become right-oriented and left-oriented respectively. In the following experiment  $B = 2 \text{ km}$ ,  $\hat{U}(0) = 0.5 \text{ ms}^{-1}$ ,  $V_2(0) = 0.15 \text{ ms}^{-1}$ ,  $\Phi(0) = 0^\circ$  and the magnitude of  $V_0(0)$  is gradually increased from  $-0.01 \text{ ms}^{-1}$  to  $-0.03 \text{ ms}^{-1}$ . The equilibrium bathymetry for  $V_0(0) = -0.01 \text{ ms}^{-1}$  is shown in Figure 4.12(a) and for  $V_0(0) = -0.03 \text{ ms}^{-1}$  it is shown in Figure 4.12(b). For  $V_0(0) = -0.01 \text{ ms}^{-1}$  the delta is left-oriented, while for  $V_0(0) = -0.03 \text{ ms}^{-1}$  the delta is right-oriented. In both cases the main channel is flood-dominated and the ebb-tidal delta is found at the seaward end of the area with ebb-dominated currents.

## 4.6 Discussion and conclusions

The main aim of this study was to investigate the influence of several tide-related processes on the (a)symmetry properties of ebb-tidal deltas. If the area with ebb-dominated currents is located at the left-hand side of the tidal inlet the delta is called left-oriented, if the area with ebb-dominated currents is located at the right-hand side the delta is called right-oriented. In this section both the modeled hydrodynamics and the modeled bottom pattern are discussed and compared with both field observations and with results of previous studies. The several processes that were included in the model and that lead to

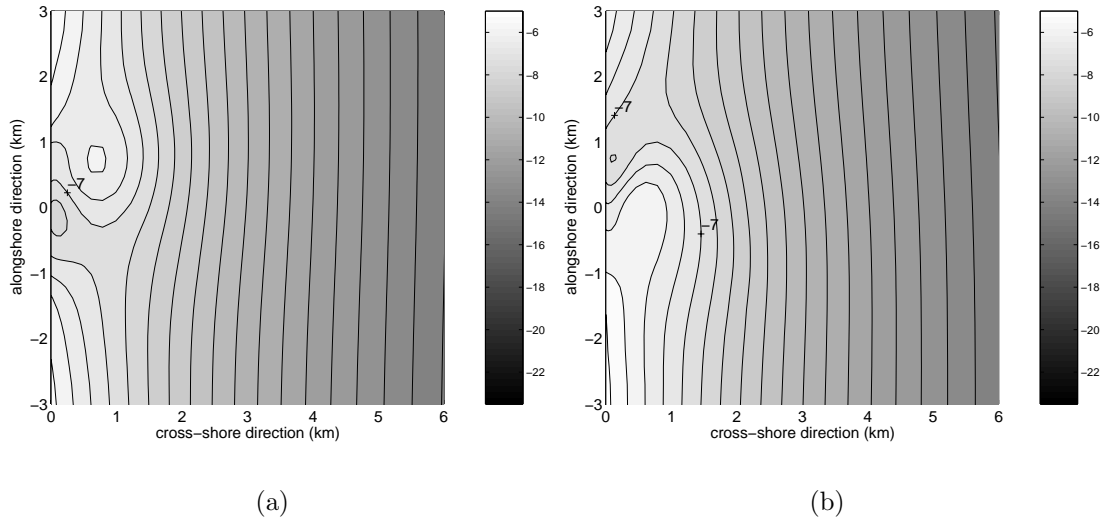


Figure 4.12: (a) Equilibrium bathymetry for  $B = 2$  km,  $\hat{U}(0) = 0.5$  ms $^{-1}$ ,  $V_2(0) = 0.15$  ms $^{-1}$ ,  $\Phi(0) = 0^\circ$ ,  $f = 0$  and  $V_0(0) = -0.01$  ms $^{-1}$ . Contour lines are drawn every 0.5 meter. (b) Same as (a), but now  $V_0(0) = -0.03$  ms $^{-1}$ .

asymmetric ebb-tidal deltas are subsequently discussed. A brief physical interpretation of the results obtained is presented. This section ends with suggestion for further research.

#### 4.6.1 Coriolis force

The influence of the Coriolis force on the asymmetry of the ebb-tidal delta is only small. Only for wide inlets with small magnitudes of the cross-shore tidal currents its influence becomes noticeable. In these situations delta is right-oriented. However, it is hard to compare these results with existing studies or with observed asymmetric ebb-tidal deltas. The effect is too small to be measured and other processes turn out to be more important for the asymmetry of ebb-tidal deltas.

The mechanisms that lead to asymmetry of the ebb-tidal delta can be explained by vorticity concepts (*Zimmerman*, 1981). Because the delta is always found at the seaward end of the area where currents are ebb-dominated, the main clue is to explain the mechanisms that cause the asymmetry in the two residual circulation cells. In the symmetric case the transfer of tidal vorticity (generated by the shear in the prescribed velocity profile over the inlet) by the tidal currents is such that positive residual vorticity is generated at the left-hand side of the tidal inlet and negative residual vorticity at the right-hand side (for a detailed discussion, see Chapter 3).

The torque induced by the Coriolis force is an additional source of tidal vorticity. During ebb the tidal currents transport the planetary vorticity seaward. Because the water depth is increasing, positive tidal vorticity is generated due to vortex stretching. This additional tidal vorticity enhances the magnitude of the tidal vorticity at the left-hand side (where the vorticity becomes more positive) and reduces the magnitude at the right-hand side of the mid-axis of the inlet (where the vorticity becomes less negative).

This vorticity is transferred by the tidal currents. Because this transport is convergent, large positive residual vorticity is generated at the left-hand side (the area  $x > 0$  and  $y > 0$ ) and small negative residual vorticity at the right-hand side of the inlet (the area  $x > 0$  and  $y < 0$ ). During flood the vortex stretching related to the planetary vorticity transport enhances the magnitude of the vorticity at the left-hand side (where the vorticity becomes more negative) and diminishes the magnitude at the right-hand side of the mid-axis of the inlet (where the vorticity becomes less positive). Hence, the vorticity fluxes have the same sign and magnitude as during ebb and therefore also during flood large positive residual vorticity is generated at the left-hand side and small negative residual vorticity at the right-hand side of the inlet. As a consequence, there is large positive mean vorticity at the left-hand side and small negative mean vorticity at the right-hand side of the inlet. This results in the residual circulation cells as modeled in Section 4.5.1.

#### 4.6.2 Shore-parallel tidal currents

In the experiment described in Section 4.5.2 the width of the inlet is 2 km,  $\hat{U}(0) = 0.5 \text{ ms}^{-1}$ ,  $f = 0 \text{ s}^{-1}$ ,  $V_2(0) = 0.15 \text{ ms}^{-1}$  and  $\Phi(0) = 0^\circ$ . The modeled tidal currents on the left-hand side of the tidal inlet are strong and bidirectional, while on the right-hand side they are weaker and more rotary. The modeled residual currents results in an area with ebb-dominated currents which is located at the left-hand side of the mid-axis through the inlet. At the right-hand side the currents are flood-dominated. These modeled hydrodynamics are in agreement with observations in the Texel Inlet (*Sha*, 1989b). Furthermore, they are consistent with the conceptual model of *Sha* (1989a). The model results are also consistent with the modeled hydrodynamics of the Ameland Inlet by *Ridderinkhof* (1989). The residual circulation patterns are quite similar.

The model results of Section 4.5.2 show that the sediment is transported seaward from the center of the inlet to the left-hand side. At the right-hand side of the inlet the sediment is transported from the sea to the inlet. This mean sediment transport  $\vec{q}_f$  is in gross agreement with observed sediment transport patterns in the Texel Inlet (*Sha*, 1989b).

The model results show that the seaward transport of sediment at the left-hand side of the inlet is convergent and causes the presence of an ebb-tidal delta. No ebb-dominated channel is modeled. On the right-hand side of the mid-axis through the inlet a flood-dominated channel is modeled. This modeled bottom pattern is consistent with those obtained in Chapter 3 and 5. There it was also found that the ebb-tidal delta is located in the area where the strength of the ebb-dominated currents is decreasing. Furthermore, the model results are consistent with the findings of *Schuttelaars et al.* (2003). They performed experiments that represent the hydrodynamic setting of the Dutch Wadden Sea by modeling a traveling wave along the coast. This coast was interrupted by a tidal inlet. They took into account the dynamic interaction between the backbarrier basin and the sea and used a local formulation of the sediment transport (the formulation of *Engelund and Hansen* (1967)). The modeled initial erosion-deposition rates showed that the channel was oriented in the direction of propagation of the tidal wave, that is to the right in the convention adopted in this study. The delta was found on the left.

Although the modeled bottom patterns are consistent with previous studies, they are

not in complete agreement with observed bottom patterns of ebb-tidal deltas along the Dutch Wadden Sea. The model results predict that most sediment of the delta is located at the left-hand side. This is in gross agreement with the predictions of *Sha* (1989a), which is based on observations of the ebb-tidal deltas of the Dutch Wadden Sea. However, the model predicts the presence of a channel on the right-hand side of the mid-axis through the inlet. This deep channel is not found in observations. Furthermore, no ebb-dominated channel is modeled. Observations show the presence of deep ebb-dominated channels which are oriented to the left. In addition, the observations suggest the presence of an almost shore-parallel flood-dominated current at the left-hand side. This is not recovered with the model.

The model results are sensitive to several parameters. However, the delta is always located at the seaward end of the area with ebb-dominated currents. The modeled channel has flood-dominated currents and is always located at the opposite side of where the ebb-tidal delta is found. The results show that increasing the magnitude of  $V_2(0)$  while keeping the other parameters constant, results in an increase of the asymmetry of the ebb-tidal delta. Increasing the magnitude of  $\hat{U}(0)$  while keeping other parameters constant, also results in an increase of the asymmetry of the delta. Furthermore, when the tidal currents in the inlet are significantly lagging the shore-parallel tidal currents at sea, the delta can change orientation. For  $B = 2$  km this occurs for  $\Phi(0) \approx -80^\circ$ , while for  $B = 7$  km this occurs for  $\Phi(0) \approx -60^\circ$ . Hence, increasing the width of the inlet causes the delta to be less asymmetric.

The residual circulation patterns obtained with the model can again be understood by analyzing the vorticity balance. However, this analysis is quite elaborate and is therefore not presented in detail. In Chapter 2 the growth or decay of coastline perturbations was determined by the relative strength of the alongshore gradient of the vorticity fluxes in the alongshore direction and the cross-shore gradient of the vorticity fluxes in the cross-shore direction. An analysis revealed that for the locations of the centers of the residual circulation cells with respect to the mid-axis through the inlet a similar competition is important. The locations and magnitudes of these residual circulation cells determine the area where the currents are ebb-dominated. The total mean vorticity flux partly involves terms that describe the transfer of vorticity generated at the tidal inlet ( $\tilde{\omega}$ ) by the velocity components  $\tilde{u}$  and  $\tilde{v}$ . This is the vorticity flux that causes the two residual circulation cells in the symmetric case (see Chapter 3). The other part of the mean vorticity flux is due to the joint presence of externally forced shore-parallel tidal currents and the tidal currents which are due to the presence of the tidal inlet. The tidal velocity components  $\tilde{u}$  and  $\tilde{v}$  transfer the vorticity of the reference state  $\Omega$  and the shore-parallel tidal currents  $V$  transfer the vorticity due to the presence of the inlet  $\tilde{\omega}$ . The alongshore gradient of this 'interaction' vorticity flux in the alongshore direction ( $\partial/\partial y[V\tilde{\omega} + \tilde{v}\Omega]$ ) results in residual circulation cells that cause the area with ebb-dominated currents to be located at the left-hand side, while the cross-shore gradient of the vorticity fluxes in the cross-shore direction ( $\partial/\partial x[\tilde{u}\Omega]$ ) results in residual circulation cells that cause the area with ebb-dominated currents to be located at the right-hand side of the mid-axis through the inlet. In most cases the alongshore convergence is dominant and the area with ebb-dominated currents is located at the left-hand side. For broader inlets the convergence of the cross-shore 'interaction' vorticity flux can be dominant and the orientation of the delta changes.

### 4.6.3 Residual currents at sea

In Section 4.5.3 the influence of residual currents at sea was studied. These currents are caused by a large-scale residual pressure gradient along the Dutch coast. In the case that these currents are in the negative  $y$ -direction, the area with ebb-dominated currents is located at the right-hand side of the mid-axis through the inlet. Also the sediment is transported seaward from the center of the inlet to the right. The modeled ebb-tidal delta is located at the right. No ebb-dominated channel is modeled. The modeled channel is located at the left-hand side of the inlet and has flood-dominated currents.

It is hard to compare the results with observations. Most observations concern the case that the residual currents at sea are forced by the waves. These wave-driven currents are very strong and confined to a small area near the coast. The currents modeled in this study are driven by the tide. However, the model results are consistent with the findings of *Schuttelaars et al.* (2003). They also found that the delta is located at the right-hand side of the inlet when the mean currents at sea are from left to right.

The asymmetry of the flow and bottom pattern caused by the large-scale mean flow is mainly due to the superposition of the currents induced by the dipole of the symmetric case and the currents induced by the large-scale mean flow (Figure 4.13). This causes a dipole which is asymmetric. The circulation cell at the left-hand side is enhanced. The right-hand circulation cell is weakened. The mean sediment transport is such that sediment is removed from the tidal inlet and is transported offshore to the right-hand side of the inlet. This causes a delta at the right-hand side and the ebb-tidal delta is right-oriented.

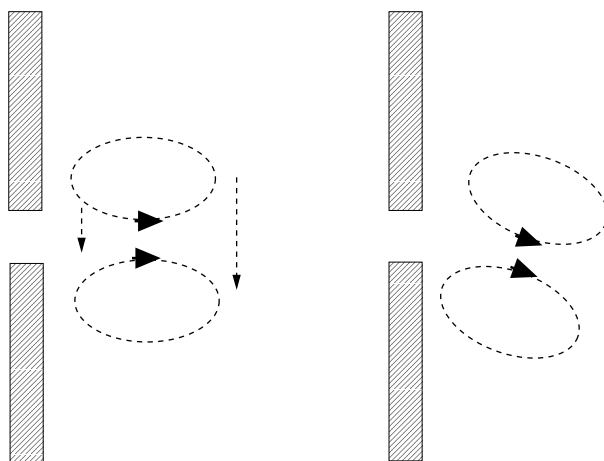


Figure 4.13: Influence of adding a large scale residual flow to a situation when two residual circulation cells are present (as calculated in the symmetric case). Two residual circulation cells are represented by the two dashed ellipses. Large scale mean current is represented by dashed arrow. Adding these two residual currents results in an asymmetric residual current pattern as shown in the right panel.

#### 4.6.4 Suggestions for further research

The modeled hydrodynamics seem to be consistent with field data. However, the modeled bottom patterns do not agree with observations. We will discuss possible reasons that cause the discrepancy between modeled bottom patterns and observed ones. This also motivates the suggestions for further research.

First, in the idealized model no backbarrier basin is present. The prescribed velocity profile over the inlet is fixed and does not follow from physical laws. In reality the velocity profile will change when the depth in the inlet changes. When it becomes deeper the effect of friction decreases and the velocity will increase. Furthermore, in contrast to the backbarrier basins observed along the east US-coast (Georgia, South Carolina), the backbarrier basins of the Dutch Wadden Sea are very shallow. In shallow water the tide has a traveling wave character. In a traveling wave, water is transported in the direction of the wave, the so-called Stokes drift. In *van Leeuwen et al. (2003)* the Frisian Inlet was modeled. They took into account the backbarrier basin. This basin was shallow (uniform depth of 2 m). Their results suggest the importance of Stokes drift in the generation of the ebb-tidal delta. Because equilibrium was never reached, their results can not be used to determine whether Stokes drift is also important for the maintenance of the asymmetric ebb-tidal delta. Furthermore, the results of *Schuttelaars et al. (2003)* suggest that Stokes drift is not important for the dynamics of asymmetric ebb-tidal deltas. However, it should be noted that their backbarrier basin was relatively deep (10 m) and is therefore more representative for a backbarrier basin observed along the east US-coast. It is expected that for such deep backbarrier basin Stokes drift is not important. In the idealized model Stokes drift is not modeled because the rigid lid approximation was applied. Therefore, to study the possible influence of such a Stokes drift a relatively shallow backbarrier basin should be added to the model geometry. Furthermore, no rigid lid approximation should be used. In view of many other simplifying assumptions in the hydrodynamics (e.g., the linearized bed shear-stress formulation), it would be very interesting to use a state-of-the-art morphodynamic model (like Delft3D) and to adapt it such that morphodynamic equilibria can be calculated.

Second, the sediment transport only includes effects of tidal currents and has a local character. No time-lag effects were taken into account. To study such an effect, a suspended-load sediment transport formulation should be used instead of a bedload sediment transport formulation. Previous studies suggest that this may be important. *Murray (2004)* showed that neglecting such effects prevented the formation of channels in his morphodynamic model of the nearshore zone. Furthermore, no effects of waves or wind were accounted for in this study. Observations show that wave influence is considerable for the Dutch Wadden Sea *Sha (1989a)*. In addition, the effect of a critical velocity for erosion was not taken into account. For coarse sediment this critical velocity for erosion might be up to  $0.3 \text{ ms}^{-1}$ .

Third, no 3D effects have been modeled with the idealized model. In the case that the channels are bending, curvature effects may become very important.

The last aspect that should be mentioned here is that  $U$  was taken as a constant. However, the magnitude of the tidal currents changes one order of magnitude in the region of the tidal inlet. This also implies that  $U$  should change one order of magnitude

and calculations should be performed with a spatially dependent  $U$ . Hence, the friction coefficient  $r$  will become spatially dependent. This might influence the asymmetry of the residual circulation cells. Furthermore,  $\vec{q}_{\text{bot}}$  will also vary due to spatial variations in  $U$  instead of variations in  $\vec{\nabla}\tilde{H}$  only.



# Chapter 5

## Numerical modeling of ebb-tidal deltas

### Abstract

Results are presented of experiments performed with a numerical morphodynamic model in order to gain more fundamental knowledge about ebb-tidal deltas. The model simulates waves (SWAN code), tides (Delft3D-flow code), sand transport and sand balance in a coastal sea bounded by a straight coast that is interrupted by one inlet. The model has first been used to confirm conclusions of an earlier study (Chapter 3 of this thesis), which was based on a much more idealized model, that ebb-tidal deltas can be modeled as equilibrium solutions (steady bottom pattern). These deltas resemble observed ebb-tidal deltas, but they do not fold around the deep ebb-dominant channel and their sand volume is a factor 5 smaller than observed sand volumes. Therefore, the dependence of characteristics of modeled ebb-tidal deltas has been investigated on processes that were not accounted for in the idealized model, viz. tidal asymmetry, dissipation of momentum due to a quadratic bottom stress and wave height variations due to shoaling and refraction. It is found that internally generated nonlinear tides hardly affect the characteristics of the deltas. In contrast, prescribing ebb(flood)-dominant tidal currents in the inlet leads to more (less) pronounced delta. Including a quadratic (rather than a linear) bottom stress leads to ebb-tidal deltas of which both the spatial pattern and the sand volume are in reasonable agreement with observed ebb-tidal deltas. This resemblance becomes even more satisfactory if shoaling and refraction of waves are accounted for.

## 5.1 Introduction

Ebb-tidal deltas are morphologic structures situated at the seaward side of tidal inlets. They are observed in many parts of the world (*Ehlers*, 1988; *Davis*, 1997; *Hicks et al.*, 1999; *FitzGerald*, 1996). The ebb-tidal delta is located at the end of the ebb-dominant channel (i.e., stronger peak ebb currents than peak flood currents) and is relatively shallow. It is flanked by two adjacent flood-dominant channels. Analysis of field observations (*Walton and Adams*, 1976; *Hayes*, 1975; *Sha*, 1989a) indicate that the characteristics of ebb-tidal deltas strongly depend on the magnitudes of tidal currents (both the cross-shore and the alongshore component) and on the characteristics of the incoming waves. Because of the large variation in strength of tides and waves, the deltas have been classified in accordance with their external forcing (*Gibeaut and Davis Jr.*, 1993). The aim of this study is to improve our understanding of the physical mechanisms that maintain ebb-tidal deltas. To limit the scope of this study the focus is on tide-dominated ebb-tidal deltas which are characterized by small shore-parallel tidal currents with respect to the cross-shore tidal currents. Such deltas are almost symmetrical with respect to the mid-axis of the inlet and are the simplest features that can be studied. Prototypes of these deltas can be found along the US east coast, see Chapter 1 and 3.

In Chapter 3 an idealized model was developed and used to show that TD and METD ebb-tidal deltas can be modeled as morphodynamic equilibria (i.e., the bottom patterns do not evolve). The model calculates the feedback between a sandy bottom, tidal currents and waves. Instead of performing time integrations to study the time evolution of ebb-tidal deltas, a continuation technique was used to directly calculate morphodynamic equilibria. The modeled channel-shoal patterns compared reasonably well with those of observed symmetric, tide-dominated deltas. In the center of the tidal inlet an ebb-dominant channel is found and at its seaward end the delta is located. This delta is flanked by two flood-dominant channels. In addition, the observed (almost linear) relation between the tidal prism and ebb-tidal sand volume was recovered with the model. However, differences were noticed as well. First, the modeled ebb-dominant channel was less deep and did not protrude as far seaward as observed ones. Second, observations show that the delta is folded around the ebb channel (see Figure 1.2). This was not recovered with the idealized model. Third, the modeled ebb tidal sand volumes were a factor  $\sim 5$  smaller than observed volumes. These differences might be caused by the assumptions and limitations in the wave and current model and in the sediment transport model. The currents were modeled by using a rigid lid approximation and a linearized bottom shear-stress formulation. The enhanced bottom friction experienced by currents due to the presence of waves was modeled in a heuristic manner. Furthermore, higher harmonics of the tide were not accounted for. The wave model does not allow for spatial variations in the wave height due to shoaling and refraction of the waves. Furthermore, it was assumed that the waves are in shallow water.

To verify the conclusions obtained with the idealized model, numerical morphodynamic process-based models are needed. They include processes that were not accounted for by the idealized model. Previous studies show that the numerical morphodynamic models have become accurate enough to simulate the evolution of ebb-tidal deltas (*Cayocca*, 2001; *van Leeuwen et al.*, 2003; *Siegle et al.*, 2004). Although the study of *van Leeuwen et al.*

(2003) suggests the evolution of the ebb-tidal delta towards morphodynamic equilibrium, the existence of such equilibria have never been convincingly demonstrated with such numerical morphodynamic models. This might be caused by the fact that they perform time integrations to study the temporal evolution of the bed under influence of waves and currents. The results of the idealized models show that a continuation method is a successful technique to calculate morphodynamic equilibria. The continuation method has never been used within numerical process-based morphodynamic models.

The objectives of this study are therefore twofold. The first one is to verify the conclusions obtained with the idealized model. An equilibrium solution of an ebb-tidal delta is calculated by using a numerical morphodynamic model. The characteristic of the ebb-tidal delta are compared with those of the idealized model and with observations. The second objective is to study the sensitivity of the characteristics of the equilibrium to processes which were not accounted for in the idealized model: tidal asymmetry, dissipation of momentum due to a quadratic bottom shear-stress and effects of waves obtained from a wave model which accounts for refraction and shoaling of waves.

This chapter proceeds along the following lines. In Section 5.2 the mathematical formulations of water motion, sediment transport, sediment mass balance and morphodynamic equilibrium are discussed. In Section 5.3 a description of the solution procedure and the numerical tools is given. The results of the experiments performed are presented in Section 5.4. In Section 5.5 the results are compared with observations and with the results of the idealized model. Section 5.7 contains a discussion and the conclusions.

## 5.2 Model formulation

The morphodynamic model consists of several modules, each accounting for different processes (water motion, sediment transport and bottom changes). A sketch of the model structure is given in Figure 5.1. Starting point is a domain with an erodible bottom. Next, the waves and currents are calculated. The currents and waves transport the sediment. Spatial differences in this sediment transport give rise to bottom changes. Since the currents and waves are altered by this new bottom, the loop starts again. In this section the various modules of the morphodynamic model are discussed.

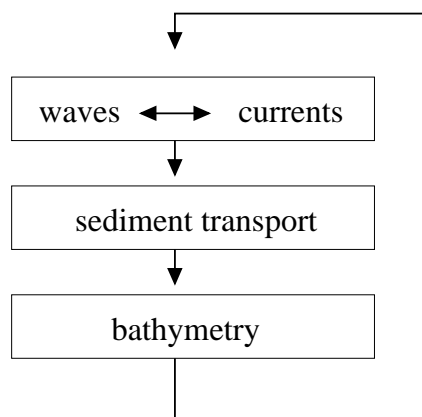


Figure 5.1: Schematic representation of the numerical morphodynamic model.

### 5.2.1 Domain

The domain represents an idealized version of the geometry that is commonly observed seaward of an inlet, see Figure 5.2. A Cartesian coordinate system is adopted where the  $x$ -axis points seaward, the  $y$ -axis alongshore and the  $z$ -axis points upward. The position of the coastline is at  $x = -x_s$ . The coastline is interrupted by one inlet having a width  $B$ , typically in the order of 2 kilometers. At  $x = 0$  the transition line from the surf zone to the inner shelf is located. It is assumed that there is hardly any interaction between the inner shelf and the surf zone. To avoid calculations in the surf zone, where the dynamics are very complicated and mainly driven by processes related to waves, the computational domain is at  $x \in [0, \infty)$  and  $y \in (-\infty, +\infty)$ . In the regions far away from the inlet the water depth is assumed to be alongshore uniform with a constant depth  $H_0$  at the coast and increasing exponentially to  $H_s > H_0$  at the shelf break, i.e.

$$H_R(x) = H_0 + (H_s - H_0)(1 - e^{-x/L}) \quad (5.1)$$

This depth profile was also used and motivated in Chapter 3 and in *van der Veegt et al.* (2005). Typical values for the depth parameters are  $H_0 \sim 5$  m near the coast,  $H_s \sim 25$  m far away from the inlet and an e-folding length scale of  $L \sim 10$  km.

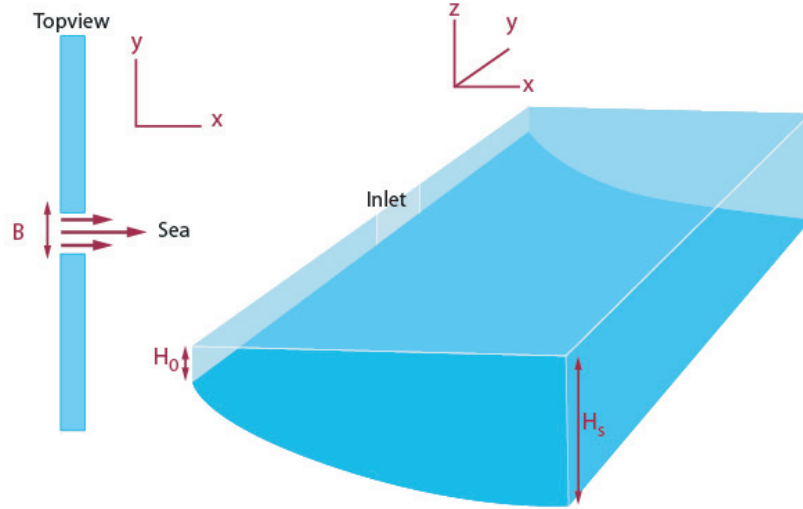


Figure 5.2: Schematic representation of the domain.

### 5.2.2 Hydrodynamics

#### Waves

The evolution and propagation of waves through the domain is described by the spectral action density balance (*Holthuijsen et al.*, 1989; *Booij et al.*, 1999, and references therein)

$$\frac{\partial N}{\partial t} + \frac{\partial(Nc_x)}{\partial x} + \frac{\partial(Nc_y)}{\partial y} + \frac{\partial(Nc_\omega)}{\partial \omega} + \frac{\partial(Nc_\theta)}{\partial \theta} = \frac{S}{\omega_*} \quad (5.2)$$

where  $N$  is the spectral action density, defined as

$$N = \frac{E}{\omega_*} \quad \omega_* = \omega - \vec{u} \cdot \vec{k} \quad (5.3)$$

Here,  $E$  (in  $\text{m}^2/\text{Hz}$ ) is the variance per wave frequency and depends on the absolute frequency  $\omega$  and wave direction  $\theta$ , as slowly varying functions of  $x, y$  and time  $t$ . Furthermore,  $\omega_*$  is the relative frequency of the waves,  $\vec{u} = (u, v)$  is the depth-averaged current vector with components  $u$  and  $v$  in the  $x$ - and  $y$ -direction, respectively, and  $\vec{k} = (k_x, k_y)$  is the wave vector with components  $k_x$  and  $k_y$  in the  $x$ - and  $y$ -direction, respectively. The relative frequency  $\omega_*$  is the frequency observed while moving with the currents and the absolute frequency  $\omega$  is the frequency of the wave observed by a stationary observer. The last term on the r.h.s. of Expression (5.3) represents the Doppler frequency shift. Here, weakly nonlinear waves are assumed. To a good approximation, they obey the dispersion relation

$$\omega_*^2 = gk \tanh(kD); \quad k = |\vec{k}| \quad (5.4)$$

where  $g = 9.81 \text{ m}^2\text{s}^{-1}$  is the acceleration due to gravity and  $D = H + \langle \zeta \rangle$  is the total water depth. The water depth is composed of component  $H$ , which represents the position of the bottom with respect to  $z = 0$ , and of component  $\langle \zeta \rangle$ , which represent the wave-averaged position of the sea level (due to tides and wave-induced set-up).

Furthermore, in Equation (5.2) the variables  $c_x$  and  $c_y$  are components of the vector  $\vec{c} = \vec{c}_g + \vec{u}$ , which is the propagation velocity of action density, with  $\vec{c}_g = (\partial\omega_*/\partial k_x, \partial\omega_*/\partial k_y)$  is the intrinsic group velocity vector. The other variables in Equation (5.2) are defined as

$$c_\omega = \frac{\partial\omega_*}{\partial D} \frac{\partial D}{\partial t} + \vec{k} \cdot \frac{\partial \vec{u}}{\partial t} \quad c_\theta = -\frac{1}{k} \frac{\partial\omega_*}{\partial D} \frac{\partial D}{\partial n} + \vec{k} \cdot \frac{\partial \vec{u}}{\partial n} \quad (5.5)$$

with  $n$  a coordinate in the direction normal to the wave propagation.

The first term at the left-hand side of Equation (5.2) describes the time variation of the spectral energy density, the second and third term describe the divergence in the transport of action density by the group velocity and the currents. The fourth term describes the change in action density while moving in  $\omega$ -space and models the shift of the relative frequency due to variations in depth and currents. The fifth term describes a shift in action density while moving in  $\theta$ -space and models the effect of wave refraction by the bottom and the currents. The term on the right-hand side of Equation (5.2) includes the effects of generation of waves by wind, dissipation by white-capping, depth-induced breaking and bottom friction, and triad and quadruplet wave-wave interactions (Holthuijsen *et al.*, 1989; Booij *et al.*, 1999).

At the boundaries the spectral action is prescribed. A JONSWAP spectrum (Hasselmann *et al.*, 1973) is used and the characteristics of the incoming waves are characterized by four parameters: The significant wave height  $h_{\text{sig}}$ , the peak period  $T_p$ , the peak direction and the directional spreading. At the two other open boundaries the spectral action density is zero. At  $x = 0$  it is required that wave energy leaves the domain (no reflection).

Interesting variables that come out of the model and are needed for the calculations of the currents and the sediment transport, are the amplitude of the near-bed wave orbital velocity  $u_{\text{orb}}$ , the wave-induced radiation stress tensor  $\underline{S}$  and the mean peak value of the

bed-shear stress  $\tau_w$  induced by the waves. Using results from linear wave theory it is found that

$$u_{orb} = \sqrt{\int \int \frac{2\omega^2}{\sinh^2(kD)} E(\omega, \theta) d\omega d\theta} \quad (5.6)$$

The time dependent near-bed wave-orbital vector is

$$\vec{u}_{wave} = \vec{u}_w \sin(\bar{\omega}t) \quad (5.7)$$

where  $\bar{\omega}$  is the mean wave frequency and  $\vec{u}_w$  is the magnitude and direction of the near-bed wave orbital motion:

$$\vec{u}_w = u_{orb} \begin{pmatrix} -\cos \bar{\theta} \\ \sin \bar{\theta} \end{pmatrix} \quad (5.8)$$

with  $\bar{\theta}$  the mean direction of the waves with respect to the  $y$ -axis. The radiation stresses for random waves are defined as

$$\underline{S} = \begin{pmatrix} S_{xx} & S_{xy} \\ S_{yx} & S_{yy} \end{pmatrix}$$

with components

$$S_{xx} = \rho g \int \int [m \cos^2 \theta + m - \frac{1}{2}] E(\omega, \theta) d\omega d\theta \quad (5.9a)$$

$$S_{xy} = S_{yx} = \rho g \int \int m \sin \theta \cos \theta E(\omega, \theta) d\omega d\theta \quad (5.9b)$$

$$S_{yy} = \rho g \int \int [m \sin^2 \theta + m - \frac{1}{2}] E(\omega, \theta) d\omega d\theta \quad (5.9c)$$

where  $m$  is the ratio of the group velocity and the phase velocity and  $\rho$  the density of water. The peak value of the bed shear-stress due to waves ( $\tau_w$ ) is defined as

$$\tau_w = \frac{1}{2} \rho f_w u_{orb}^2 \quad (5.10)$$

where

$$f_w = \begin{cases} 0.00251 e^{5.21 (\frac{u_{orb}}{k_s \bar{\omega}})^{-0.19}} & ; \quad \frac{u_{orb}}{k_s \bar{\omega}} > \frac{\pi}{2} \\ 0.3 & ; \quad \frac{u_{orb}}{k_s \bar{\omega}} < \frac{\pi}{2} \end{cases} \quad (5.11)$$

is the wave-induced friction stress factor that depends on the Nikuradse roughness length  $k_s$  (typical value 1 mm) (see e.g. *Soulsby* (1997)).

## Currents

It is assumed that the currents have horizontal scales that are much larger than the vertical scale (typically kilometers versus meters) and that the vertical structure of the currents is not essential for the modeling of ebb-tidal deltas. The currents can therefore be described by the depth-averaged shallow water equations,

$$\frac{\partial \vec{u}}{\partial t} + (\vec{u} \cdot \vec{\nabla}) \vec{u} = -g \vec{\nabla} \zeta - \frac{\vec{\tau}_b}{\rho D} - \frac{\vec{\nabla} \cdot \underline{S}}{\rho D} + A_h \nabla^2 \vec{u} \quad (5.12)$$

$$\frac{\partial \zeta}{\partial t} + \vec{\nabla} \cdot [D \vec{u}] = 0 \quad (5.13)$$

which express the momentum and mass balance, respectively. In Equations (5.12) and (5.13) is  $\vec{\nabla} = (\partial/\partial x, \partial/\partial y)$  the horizontal gradient vector,  $\nabla^2$  the horizontal Laplace operator,  $\zeta$  the sea surface elevation relative to the undisturbed water level  $z = 0$ ,  $\vec{\tau}_b$  the wave-averaged bed shear-stress vector and  $A_h$  is the horizontal eddy viscosity coefficient.

The eddy viscosity coefficient is modeled as  $A_h = l U_t$ , with  $l \sim 10$  m a mixing length scale and  $U_t (\sim 1 \text{ ms}^{-1})$  a characteristic velocity scale related to the magnitude of the tidal currents. This formulation takes both small-scale turbulent eddies and vertical shear dispersion into account (*Zimmerman, 1986*). Following the model formulation of the idealized model described in Chapter 3,  $U_t$  is defined as the maximum current amplitude in the tidal inlet,

$$U_t = \text{MAX} |\vec{u}(0, 0, t)| \quad (5.14)$$

The radiation stresses  $\underline{S}$  are output of the wave model (see Equation (5.2.2)) and may induce changes in mean sea level and wave-driven currents. The formulation of  $\vec{\tau}_b$  is discussed in the next subsection.

To solve equations (5.12) and (5.13) boundary conditions are needed. At  $x = 0$  outside the tidal inlet the shore-normal velocity is zero and a free slip condition is applied to have no exchange of momentum across the transition line. In the tidal inlet also a free slip condition is applied and the cross-shore velocity is prescribed as  $u = \hat{U}(y, t)$ , where  $\hat{U}(y, t)$  is the given tidal velocity field in the inlet. The oscillating tidal flow in the inlet generates water motion in the entire domain. Far from the inlet the currents vanish.

## Bottom shear-stress formulations

In this study several formulations of the bottom shear-stress experienced by the currents are used. In experiments where waves are absent, two different formulations for  $\vec{\tau}_b$  are considered. The first is

$$\vec{\tau}_b = \rho \frac{g}{C_z^2} |\vec{u}| \vec{u} \quad (5.15)$$

where  $C_z$  is the Chézy coefficient and is set to its commonly used value  $C_z = 65 \text{ m}^{1/2} \text{ s}^{-1}$ . This is the quadratic friction law. The second formulation reads

$$\vec{\tau}_b = \rho \frac{g}{C_z^2} \frac{8}{3\pi} U_t \vec{u} \quad (5.16)$$

Note that the stress in (5.16) is linear in the current. For this reason it will be referred to as the linearized bottom stress formulation. Using Equation (5.14) implies that in the center of the inlet the tidally averaged energy dissipation induced by the linearized bottom shear-stress (5.16) equals that of the full nonlinear stress (5.15) (*Lorentz, 1922*).

The third formulation for the bed shear-stress considers the case that both currents and waves are important constituents of the water motion. As is reviewed in *Soulsby et al. (1993)*, all studies that deal with the wave-averaged bed shear-stress show that its magnitude increases when waves become stronger. This stress has a magnitude  $\tau_b$  and is a function of two variables,  $\tau_c$  and  $\tau_w$ . Here,  $\tau_c$  is the magnitude of the current-induced bed shear-stress, of which the components are given in (5.15), and  $\tau_w$  is the magnitude of the bed shear-stress induced by waves, as given by Equation (5.10). Both are quadratic in the velocity. The direction of the stress,  $\beta$ , is in general different from that of the waves and the currents. In the present model the formulations for  $\tau_b$  and direction  $\beta$  as proposed by *Fredsøe (1984)* are used.

### 5.2.3 Sediment transport

For the sediment transport the formulation of *van der Veegt et al. (2005)*, as described in Section 3.2.3, is used. This is a generalized Bagnold-Bailard formulation (*Bagnold, 1966; Bailard, 1981*). The sediment is transported as bedload. A correction for the direction of the sediment transport is introduced that accounts for the influence of the bed slope. Furthermore, the bedload transport is averaged over the wave and tidal period. This yields

$$\vec{q} = \vec{q}_f + \vec{q}_{\text{bot}} + \vec{q}_{\text{asym}} \quad (5.17)$$

where  $\langle \cdot \rangle$  denotes an averaging over the tidal period of the variable within the brackets. In Equation (5.17) is  $\vec{q}_f$  the tidally averaged sediment transport induced by the waves and currents,  $\vec{q}_{\text{bot}}$  induced by bed slope effects and  $\vec{q}_{\text{asym}}$  induced by nonlinear effects of waves. The sediment transport relation is defined at the top of the wave boundary layer. Because the tidal currents are depth-averaged, the depth-averaged currents are transformed to their magnitudes at the top of the wave boundary layer by assuming a logarithmic velocity profile. The sediment transport due to waves and currents is expressed as

$$\vec{q}_f = \alpha\beta^3 \left\langle |\vec{u}|^2 \vec{u} + \frac{1}{2} \frac{|\vec{u}_w|^2}{\beta^2} \vec{u} + \left( \vec{u} \cdot \frac{\vec{u}_w}{\beta} \right) \frac{\vec{u}_w}{\beta} \right\rangle \quad (5.18)$$

with  $\alpha$  a grain size dependent constant (typical value of  $10^{-5} \text{ s}^2\text{m}^{-1}$ ) and  $\beta \sim 0.35$  a factor that relates the tidal currents at the top of the wave boundary layer to the depth-averaged tidal currents. Here,  $\beta$  is assumed to be constant in the domain while in reality it will be a weakly varying function of the local water depth. Note that  $\vec{q}_f = 0$  in the absence of tidal currents. The mean sediment transport due to the presence of bed slopes reads

$$\vec{q}_{\text{bot}} = \alpha\beta^p \gamma U^p \vec{\nabla} H \quad (5.19)$$

In this expression  $U$  is the magnitude of the flow due to waves and currents and is defined as



$$U = \sqrt{U_t^2 + (u_{orb}/\beta)^2} \quad (5.20)$$

Furthermore, in Equation (5.19) is  $\gamma$  the bed-slope coefficient (with a typical value of  $1(\frac{m}{s})^{3-p}$ ). The constant  $p$  is determined from observations and is found to be  $p = 2$  (*Struikisma et al.*, 1985) or  $p = 3$  (*Bailard*, 1981; *Sekine and Parker*, 1992). In this study  $p = 2$ . The last term of Equation (5.17) is the sediment transport due to nonlinear effects of waves (wave asymmetry). It reads

$$\vec{q}_{\text{asym}} = -\alpha\gamma\beta^2 U^2 \vec{\nabla} H_R \quad (5.21)$$

where  $H_R$  is defined in Equation (5.1). The sediment transport  $\vec{q}_{\text{asym}}$  is chosen such that it balances the off-shore sediment transport induced by the bed slopes when tidal currents through the inlet are zero. For further details, see Chapter 3.

For further use,  $\vec{q}_f$  is considered in more detail. Assume that  $\vec{u} = \langle \vec{u} \rangle + \vec{u}'$ , i.e., the currents are composed of a residual and a time-varying (tidal) component. In that case  $\vec{q}_f$  can be split into

$$\vec{q}_f = \vec{q}_{\text{res}} + \vec{q}_a + \vec{q}_{\text{wave}} \quad (5.22)$$

where  $\vec{q}_{\text{res}}$  is that part of the flow-induced sediment transport that involves residual and tidal currents,  $\vec{q}_a$  only depends on  $\vec{u}'$  and is related to tidal asymmetry (*van de Kreeke and Robaczewska*, 1993) and  $\vec{q}_{\text{wave}}$  involves sediment transport due to waves and residual currents. The components read

$$\vec{q}_{\text{res}} = \alpha\beta^3 [(\langle |\vec{u}|^2 \rangle + \langle |\vec{u}'|^2 \rangle) \langle \vec{u} \rangle + \langle (\vec{u}' \cdot \langle \vec{u} \rangle) \vec{u}' \rangle] \quad (5.23a)$$

$$\vec{q}_a = \alpha\beta^3 \langle |\vec{u}'|^2 \vec{u}' \rangle \quad (5.23b)$$

$$\vec{q}_{\text{wave}} = \alpha\beta^3 \left[ \frac{|\vec{u}_w|^2}{2\beta^2} \langle \vec{u} \rangle + \frac{\vec{u}_w \cdot \langle \vec{u} \rangle}{\beta^2} \vec{u}_w \right] \quad (5.23c)$$

#### 5.2.4 Sediment mass balance

At locations where the sediment transport is divergent (convergent) the water depth will increase (decrease). The behavior of the water depth in time is governed by the bed evolution equation

$$\frac{\partial H}{\partial t} - \vec{\nabla} \cdot \vec{q} = 0 \quad (5.24)$$

The bottom only changes due to divergences and convergences in the tidally averaged sediment transport. This can be used because the time scale on which bottom patterns evolve (typically in the order of years) is much larger than the time scale of the currents ( $M_2$  period). This implies that the bottom hardly changes during the calculation of the currents and waves and can be taken as a constant (*Sanders and Verhulst*, 1985). The boundary conditions for the sediment mass balance are that far from the inlet the mean sediment transport vanishes. At  $x = 0$  outside the inlet the mean cross-shore sediment flux is zero. In the tidal inlet a regularity condition for the depth is imposed ( $H$ =finite).

## 5.2.5 Morphodynamic equilibrium

In this study the focus is on morphodynamic equilibria. These are defined as states which involve a bottom that does not change in time,

$$\frac{\partial H}{\partial t} = 0 \quad (5.25)$$

Henceforth  $H$  will represent an equilibrium bathymetry. In morphodynamic equilibrium currents and waves are still present and transport sediment. Note that Equations (5.25) and (5.24) imply that in equilibrium the net sand transport is non-divergent

$$\vec{\nabla} \cdot \vec{q} = 0 \quad (5.26)$$

## 5.3 Methods

### 5.3.1 Domain

The model equations have to be solved on a finite domain. This domain is designed such that it represents the infinite domain as described in Section 5.2.1. A finite rectangular domain is chosen which is centered around the tidal inlet and has a length  $2L_y$  in the alongshore direction and  $L_x$  in the cross-shore direction. The domain is chosen large enough to have vanishing velocities at the seaward boundaries.

### 5.3.2 Hydrodynamics

#### Waves

To solve the wave model as described in Section 5.2.2 a state-of-the-art numerical model is used, called SWAN. The model variables are calculated on a numerical grid. The domain is divided into  $N_y^w$  and  $N_x^w$  grid points in the  $y$ - and  $x$ -direction, respectively. At one seaward boundary (at  $x = L_x$ ) the wave characteristics are prescribed. At the other boundaries full absorption of wave energy is assumed. A detailed description of SWAN and the numerical details can be found in *Booij et al. (1999)*.

#### Currents

To solve the shallow water equations the hydrodynamic module of Delft3D is used. Delft3D is a process-oriented numerical model developed by WL-Delft Hydraulics. In this study the 2D (depth-averaged) version is used. The domain that is used in the calculations is the same as the domain that is used for the calculations of the waves. The number of grid points ( $N_x^c, N_y^c$ ), however, is larger than in the wave model. At  $x = 0$  a closed wall is used, except for one region with width  $B$  that models the tidal inlet. At the closed boundary the cross-shore velocity is zero and a free slip condition is applied. In the inlet a discharge boundary is used in which the cross-shore velocity is prescribed. By using this discharge boundary no free-slip condition in the inlet can be applied. Instead, during ebb (outflow) the tangential advection is neglected ( $v\partial u/\partial y = 0, v\partial v/\partial y = 0$ ).

During flood no extra boundary condition is required. For numerical details on Delft3D, see *Stelling and Leendertse (1992); Roelwink and van Banning (1994)*.

### 5.3.3 Sediment transport

In the idealized model higher harmonics of the tide were not accounted for. Since the first goal is to validate and compare the results of the idealized model with the results that are obtained with the numerical model, two cases are considered in this study. In the first case the time series of  $\vec{u}$  is decomposed into a Fourier series. This series is truncated after the  $M_2$  component. With this truncated series of the velocity the sediment transport due to tides ( $\vec{q}_f$ ) is calculated. This equals the formulation of  $\vec{q}_f$  as is used in the idealized model (Equation (3.15) of Chapter 3). It will be referred to as  $\vec{q}_{fM_0M_2}$ . Note that  $\vec{q}_a = 0$  in this case. In the second case the complete time series of  $\vec{u}$  is used to calculate  $\vec{q}_f$ .

### 5.3.4 Morphodynamic equilibria

#### Mathematical description

A continuation method is used to obtain morphodynamic equilibria. This method requires a known equilibrium solution to start from. In the present model the latter corresponds to the situation that there are no tidal currents and  $H = H_R(x)$ . In that case the divergence of the sediment transport due to bed slopes balances the divergence of the sediment transport due to wave asymmetry. When currents through the tidal inlet are nonzero the following balance holds:

$$\alpha\beta^2\gamma U^2 \nabla^2 H' = -\vec{\nabla} \cdot \vec{q}_f \quad (5.27)$$

where  $H' = H - H_R$ . This balance is obtained by substituting Equation (5.17) and Equation (5.19) into Equation (5.26) and using the sediment mass balance in case that tidal currents through the inlet are zero. Because  $\vec{q}_f$  is an implicit function of  $H'$ , Equation (5.27) describes a nonlinear differential equation for  $H'$ . The boundary conditions are that at the seaward boundaries the mean sediment transport vanishes. At  $x = 0$  outside the inlet the cross-shore component of the sediment transport is zero. Using the definition of  $\vec{q}_{\text{asym}}$  (Equation (5.21)) and that the cross-shore component of  $\vec{q}_f$  is zero, this yields that  $\partial H' / \partial x = 0$ . Inside the inlet a regularity condition for  $H'$  is applied.

#### Continuation method and iteration procedure

A schematic representation of the method to calculate morphodynamic equilibria is shown in Figure 5.3. Starting point is a known equilibrium solution of the model. The corresponding bottom pattern is denoted by  $H = H(x, y; \mu)$ , where  $\mu$  represents a parameter (e.g., the typical velocity scale in the center of the inlet  $U$ ). Next, the parameter  $\mu$  is changed by a small increment  $\Delta\mu$ . As long as the increment is small enough, it can be assumed that  $H = H(x, y; \mu + \Delta\mu)$  does not differ much from  $H = H(x, y; \mu)$ . To solve

Equation (5.27) an iterative procedure is used. The previous estimate of the morphodynamic equilibrium is used to calculate the waves and currents. From this,  $\vec{q}_f$  and  $\vec{\nabla} \cdot \vec{q}_f$  are calculated and the right-hand side of Equation (5.27) is known. This equation has now become a Poisson equation which is subsequently solved by using a multipole expansion in the elliptic-cylindrical coordinates. A detailed description of this coordinate system and how the Poisson problem is solved can be found in Chapter 3. If the new bathymetry differs much from the previous estimate, a new iteration is performed. This procedure is repeated until convergence is established and the morphodynamic equilibrium for the parameter setting is obtained. From this, the parameter  $\mu$  can be changed again.

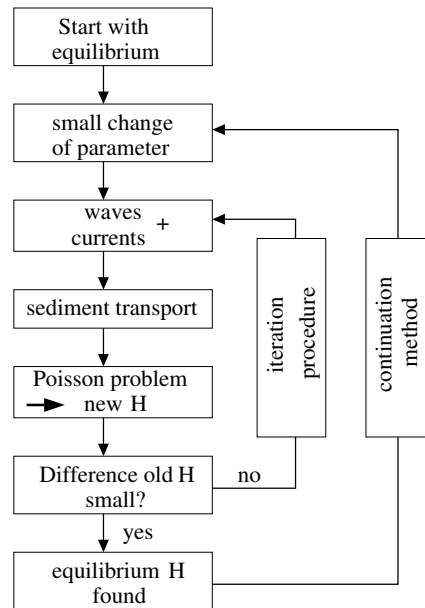


Figure 5.3: Schematic representation of the iteration procedure and continuation method. Further details are given in the text.

## 5.4 Results

### 5.4.1 Set-up of the experiments

The default model set-up is chosen such that it is as close as possible to that of the idealized model. This means that a linearized bed shear-stress formulation is used, no waves are considered and  $\vec{q}_f = \vec{q}_{fM_0M_2}$ . Next, the sensitivity of the results to extensions of the model formulation are studied. An overview of all the experiments and in which section the results are presented is given in Table 5.1.

The numerical parameters that are used for the experiments are shown in Table 5.2. The domain covers the area from  $x \in [0, 15]$  km and  $y \in [-15, 15]$  km. Test experiments showed that this choice of the domain obeys the condition of vanishing velocity far away from the inlet. The total area spanned is 15 x 30 km and is divided into  $N_x^c = 150$  and  $N_y^c = 300$  grid points in  $x$ - and  $y$ -direction, respectively. The grid distance  $\Delta x = 100$

Section	Bed shear-stress	Higher harmonics	Sediment transport	Waves
4.2 + 4.3	Linear	No	$\vec{q}_f = \vec{q}_{fM_0M_2}$	No
4.4.1	Linear	Internal	$\vec{q}_f = \vec{q}_{\text{res}} + \vec{q}_a$	No
4.4.2	Linear	Internal + External	$\vec{q}_f = \vec{q}_{\text{res}} + \vec{q}_a$	No
4.5	Quadratic	Internal	$\vec{q}_f = \vec{q}_{\text{res}} + \vec{q}_a$	No
4.6	<i>Fredsøe</i> (1984)	Internal	$\vec{q}_f = \vec{q}_{\text{res}} + \vec{q}_a + \vec{q}_{\text{wave}}$	Yes

Table 5.1: Overview of the experiments performed in this study.

m and  $\Delta y = 100$  m is found from convergence tests as the optimum choice when both considering accuracy and calculation time. The numerical time-step used is  $\Delta t = 2$  minutes and the total simulation time is four tidal periods. Only the fourth tidal period is used for the sediment transport calculations. Test experiments showed that the transients were damped after three periods. To solve the wave model a coarser grid is used. The grid distance is 300 m and  $N_x^w = 50$  and  $N_y^w = 100$ . The wave parameters that are calculated on the grid for the waves are linearly interpolated to the grid of the currents. The number of poles that are used to solve the Poisson problem is 150.

Parameter	Delft3D	SWAN
$L_x$	15 km	15 km
$L_y$	15 km	15 km
$\Delta x$	100 m	300 m
$N_x$	150	50
$\Delta y$	100 m	300 m
$N_y$	300	100
$\Delta t$	120 s	

Table 5.2: Numerical parameters of SWAN and Delft3D as used in the calculations.

### 5.4.2 Results for default case

In the default case  $B = 2$  km. The cross-shore bottom profile is described by Equation (5.1), with  $H_0 = 5$  m at the coast,  $H_s = 25$  m and an e-folding length scale of  $L = 10$  km. These values are characteristic for the reference bathymetry observed along the barrier coast of the US (see Chapter 3). The forcing of the water motion is due to the tidal current in the inlet (no waves). The current profile over the inlet is equal to the one used in Chapter 3 and only an  $M_2$  tidal component is prescribed:

$$\hat{U}(y, t) = U_{M_2} \left[ \left( 2 \frac{y}{B} - 1 \right)^3 \left( 2 \frac{y}{B} + 1 \right)^3 \right] \cos(\sigma t) \quad (5.28)$$

Here,  $\sigma = 1.4 \cdot 10^{-4} \text{ s}^{-1}$  denotes the frequency of the  $M_2$  tide. The profile is symmetric with respect to the mid-axis of the inlet and the velocity amplitude increases from zero on both sides ( $y = \pm B/2$ ) to a maximum value in the middle ( $y = 0$ ). The typical velocity

scale  $U$ , needed to calculate the linearized bottom stress and the sediment transport, and the velocity scale  $U_t$  to calculate the eddy viscosity coefficient  $A_h$ , become  $U = U_t = U_{M_2}$ . In this experiment  $U_{M_2} = 0.2 \text{ ms}^{-1}$ . In Table 5.3 the values of the model parameters for this default experiment are given.

Parameter	Choice
$B$	2 km
$H_0$	5 m
$H_s$	25 m
$L$	10 km
$\hat{U}$	Eq. (5.28)
$U$	$U_{M_2}$
$U_t$	$U_{M_2}$
$U_{M_2}$	$0.2 \text{ ms}^{-1}$
$C_z$	$65 \text{ m}^{1/2}\text{s}^{-1}$
$A_h$	$2.8 \text{ m}^2\text{s}^{-1}$
$\alpha$	$10^{-5} \text{ s}^2\text{m}^{-1}$
$\gamma/\beta$	$1(\frac{\text{m}}{\text{s}})$
$p$	2

Table 5.3: Parameter values for the default experiment.

Within the iteration procedure the first estimate of the equilibrium bathymetry for  $U_{M_2} = 0.2 \text{ ms}^{-1}$  is  $H = H_R(x)$ . The velocity pattern at two phases of the tide and the residual current pattern are shown in Figure 5.4; Figure 5.4(a) shows the currents at maximum ebb and Figure 5.4(b) at maximum flood. During ebb the water mainly flows in the cross-shore direction. The alongshore velocity components are small. This resembles an ebb-jet. During the flood phase the water flows from all sides towards the inlet. The alongshore component of the velocity almost has the same magnitude as its cross-shore component. The residual velocity pattern is shown in Figure 5.4(c). It reveals the presence of two counter-rotating residual circulation cells at some distance from the inlet. The maximum of the residual currents is  $0.03 \text{ ms}^{-1}$ .

The net sediment transport  $\bar{q}_{fM_0M_2}$  is shown in Figure 5.5(a). The sediment is transported from the sides towards the inlet. From the inlet the sediment is transported seaward. The convergence of the net sediment transport is shown in Figure 5.5(b). It yields negative values near the inlet and positive values further seaward.

From this convergence the new estimate for  $H$  is calculated and is shown in Figure 5.6(a). It reveals a channel-shoal pattern. In the center of the inlet a channel is found and at its end a shoal is located, the ebb-tidal delta. This shoal is flanked by two smaller channels. Because this bathymetry differs much ( $\sim 1.5 \text{ m}$ ) from the old bathymetry, a next iteration is needed. The new bathymetry gives rise to changes in the currents and net sediment transport and repetition of the procedure results in a new guess for the bathymetry, etc. The bottom changes appear to be gradual with decreasing differences between the successive estimates of  $H$ . After 7 iterations the maximum difference with the previous estimate is less than 4 cm and equilibrium is reached. This bathymetry is shown in Figure

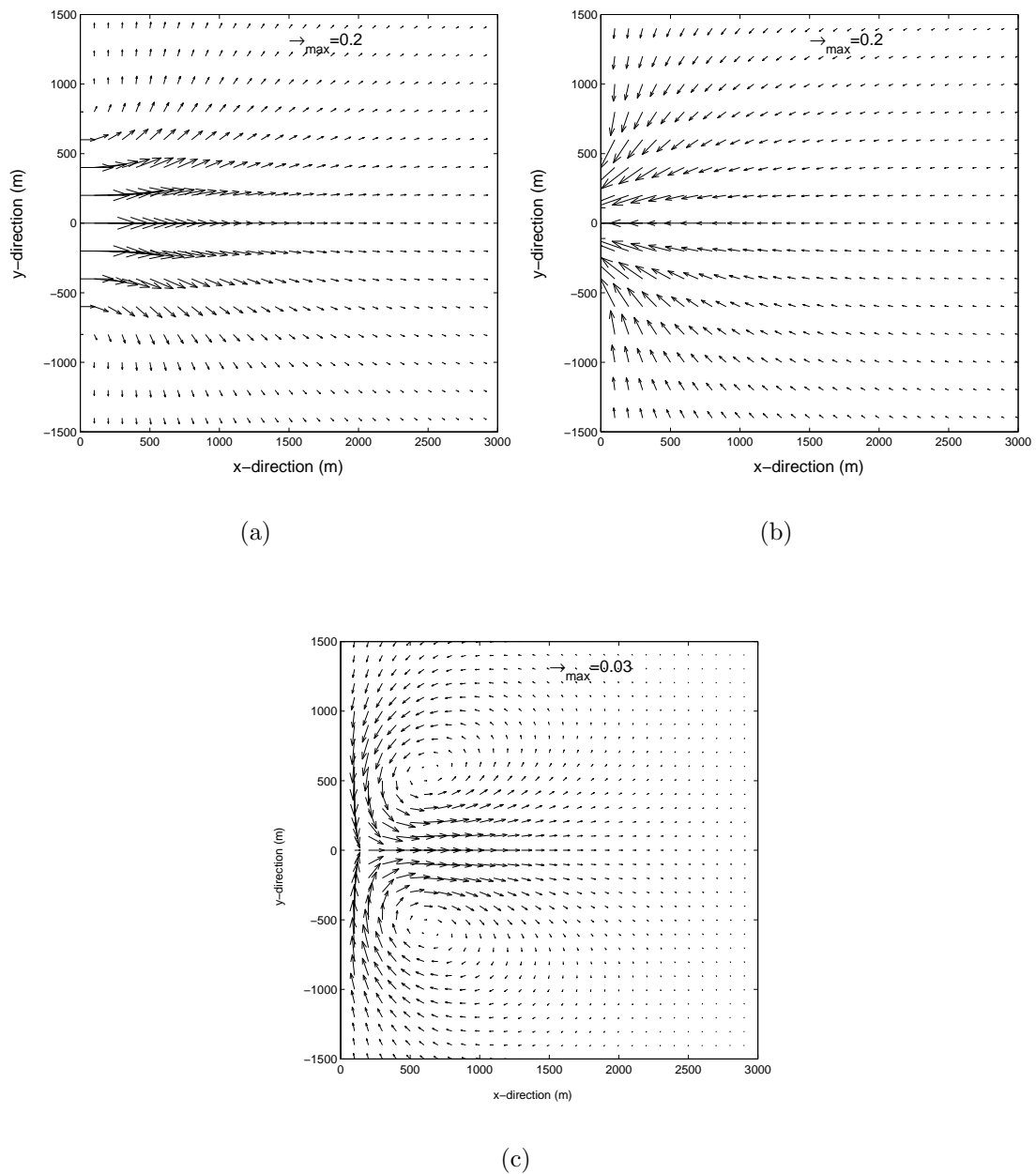


Figure 5.4: (a) The velocity field during ebb in the default experiment, first iteration step. For model setting and parameter values, see Tables 5.1-5.3. The inlet is located at  $(x, y) = (0, 0)$  and has a width  $B = 2$  km. (b) Same as (a), but now during flood. (c) Vector plot of the residual currents

5.6(b). Clearly, a shoal is found seaward of the inlet with its center around  $x = 1000$  m. This shoal resembles an ebb-tidal delta. The depth above the shoal is 1 m smaller than the depth of the reference bathymetry at that position. Furthermore, a channel in the inlet is modeled which is about 1.5 m deeper than the reference bathymetry at this position. It is an ebb-dominated channel. The two channels that flank the delta are flood-dominated

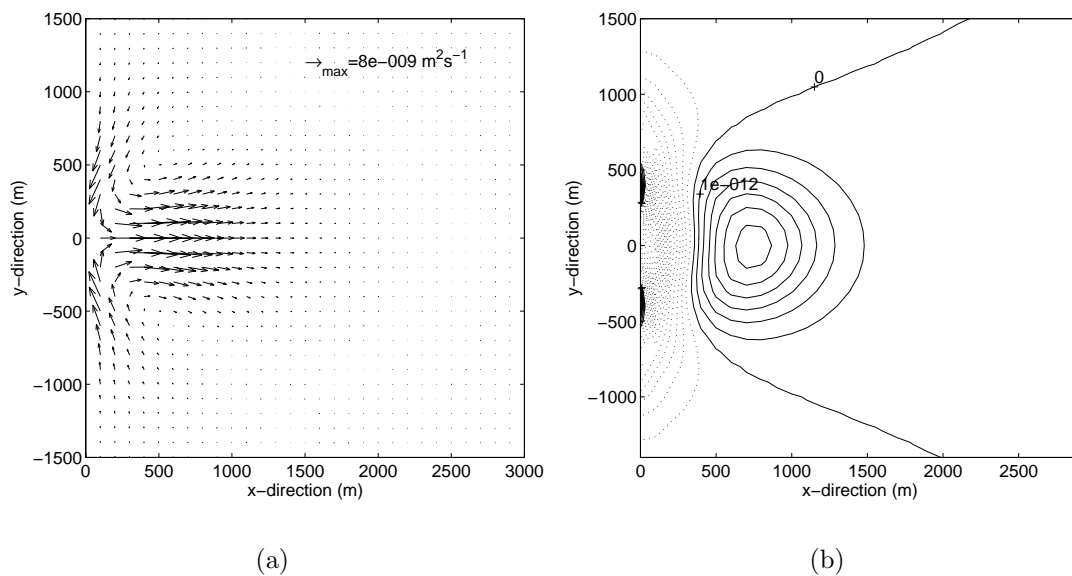


Figure 5.5: Variables at the first iteration step in the default experiment when  $H = H_R(x)$ . (a) Mean sediment transport  $\vec{q}_{fM_0M_2}$ . (b) Convergence of mean sediment transport,  $-\vec{\nabla} \cdot \vec{q}_{fM_0M_2}$ . Contour intervals are  $1 \cdot 10^{-12} \text{ ms}^{-1}$ .

channels. The presence of the inlet is still noticeable at 3 km away from the inlet by the curving of the isobaths.

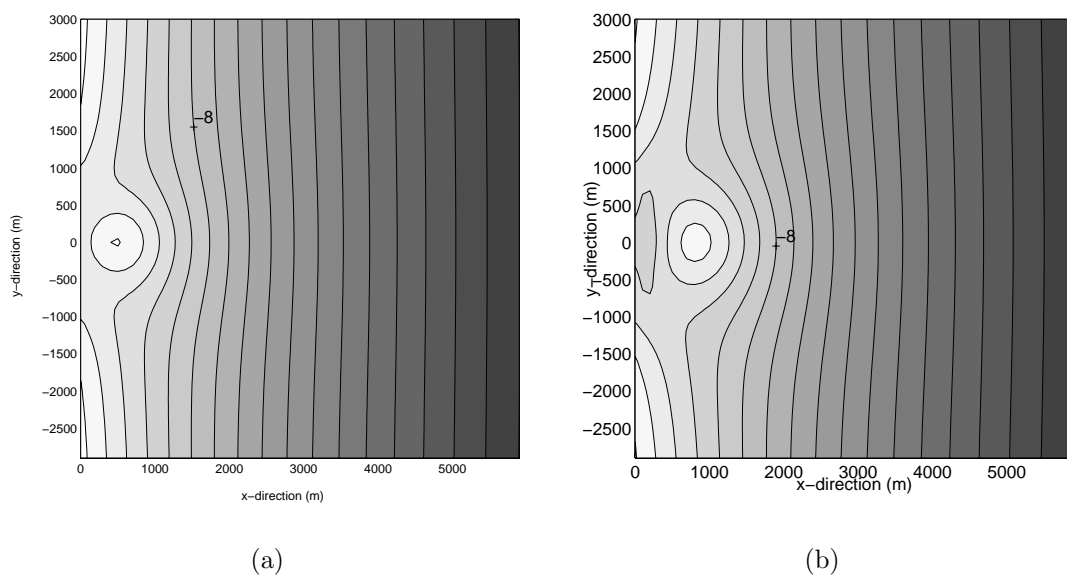


Figure 5.6: (a) Estimate of equilibrium bathymetry after first iteration step. Contour intervals are 0.5 meter. (b) Equilibrium bathymetry for the default experiment. For model setting and parameter values, see Tables 5.1-5.3. Contour lines are drawn every 0.5 m.



### 5.4.3 Sensitivity of model results to tidal velocity amplitude in the inlet

A series of experiments has been performed for different values of  $U_{M_2}$ . Other parameter values were identical to those used in the default experiment. Because the procedure to obtain morphodynamic equilibrium and the resulting patterns for currents and sediment transport are similar to those of the default experiment, only the equilibrium bathymetries are presented. They are shown in Figure 5.7.

With increasing amplitude of the tidal current the channel-shoal pattern becomes more pronounced. An increase of  $U_{M_2}$  results in an increase of the depth of the channels and a shift of the delta in the seaward direction. For  $U_{M_2} = 0.10 \text{ ms}^{-1}$  the shoal is 0.4 m above the reference bathymetry  $H_R$ , for  $U_{M_2} = 0.30 \text{ ms}^{-1}$  this is  $\sim 2$  m. For  $U_{M_2} = 0.10 \text{ ms}^{-1}$  the depth in the channel is 0.5 m beneath the reference bathymetry, for  $U_{M_2} = 0.30 \text{ ms}^{-1}$  this is  $\sim 3$  m. For  $U_{M_2} > 0.30 \text{ ms}^{-1}$  no equilibrium solutions are found. This will be discussed in Section 5.7.

### 5.4.4 Sensitivity of results to tidal asymmetry

In the previous experiments the sediment transport is calculated with only the  $M_0$  and  $M_2$  components of the tide. Although being the dominant constituents, higher harmonics of the tide are present as well. The effect of these higher harmonics on the results is studied by a series of experiments in which  $\vec{q}_f = \vec{q}_{\text{res}} + \vec{q}_a$  instead of  $\vec{q}_f = \vec{q}_{fM_0M_2}$ . So,  $\vec{q}_a$  is nonzero and  $\vec{q}_{\text{res}}$  also includes effects of the higher harmonics of the tide, see Equations (5.23a) and (5.23b). Two cases are considered. In the first case, only the internally generated higher harmonics of the tide are considered, i.e., higher harmonics that are generated by nonlinear processes. In the second case, also externally generated higher harmonics are considered by imposing an  $M_4$  component on the prescribed cross-shore tidal currents in the inlet.

#### Internally generated higher harmonics

The same parameter setting as in the default experiment is used. At the first iteration the current patterns during maximum ebb and flood and the residual current pattern are identical to the default experiment. After decomposing the velocity components into its Fourier components it is found that the maximum magnitude of long axis of the  $M_4$  tidal current ellipse is  $0.013 \text{ ms}^{-1}$ , or about 6 % of the  $M_2$  tidal current amplitude. The tidal current ellipses of the  $M_4$  tide are shown in Figure 5.8(a). The pattern consists of two cells. In the center of the inlet the  $M_4$  current ellipses are bidirectional, while at the sides there is stronger ellipticity. The magnitude of the  $M_6$  tidal currents is much smaller than the  $M_4$  tidal currents, with a maximum magnitude of the long axis of the  $M_6$  tide of  $0.002 \text{ ms}^{-1}$ . The residual sediment transport  $\vec{q}_{\text{res}}$  is almost equal to  $\vec{q}_{fM_0M_2}$  in the default case and is therefore not shown. In Figure 5.8(b)  $\vec{q}_a$  is shown and its convergence is shown in Figure 5.9(a). The sediment transport due to the higher harmonics of the tide has a similar pattern as  $\vec{q}_{\text{res}}$ . However, the magnitudes of  $\vec{q}_a$  are 10 times smaller than those of  $\vec{q}_{\text{res}}$ . The convergence of  $\vec{q}_a$  has a similar pattern as the convergence of  $\vec{q}_{\text{res}}$ , but they are a

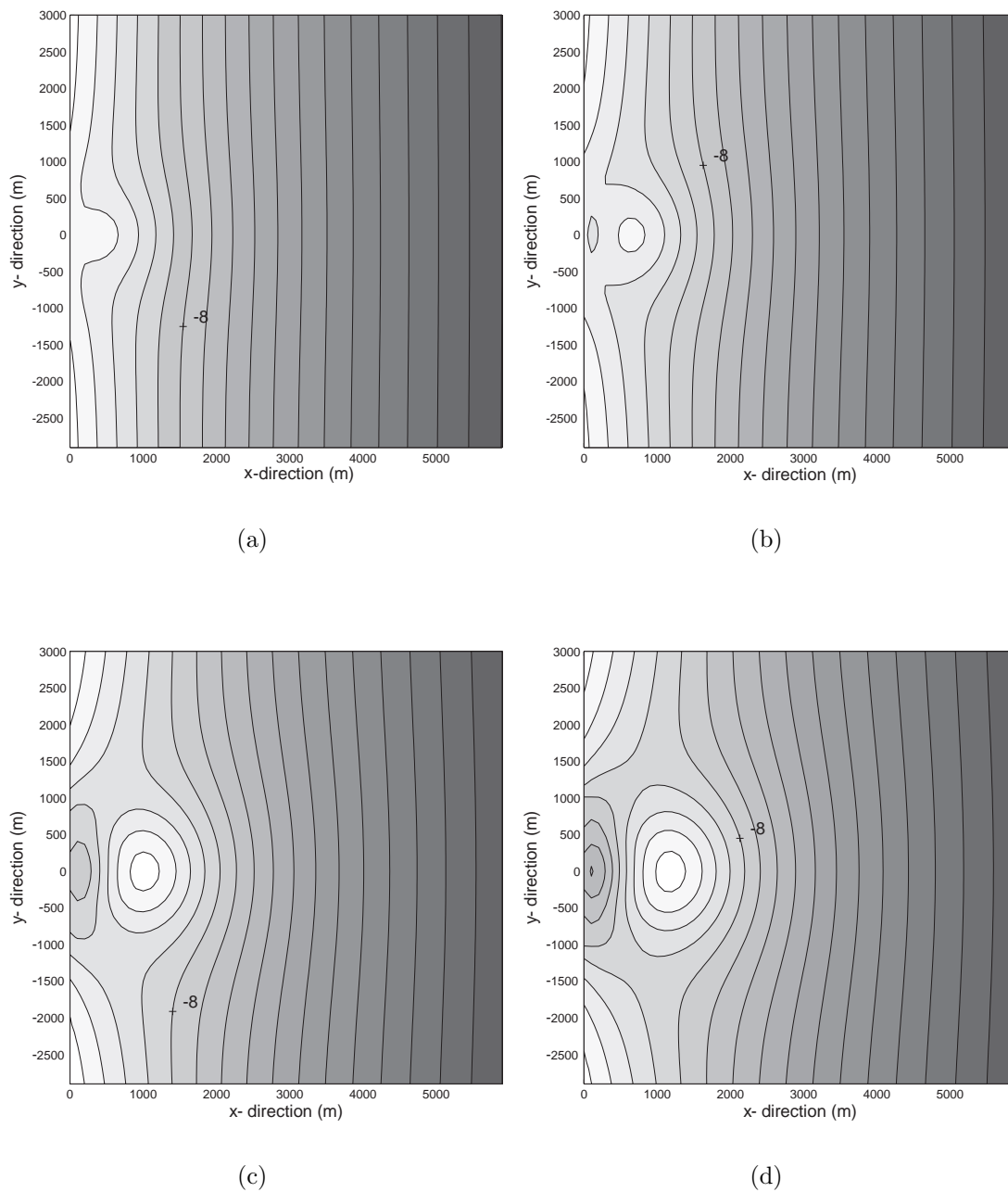


Figure 5.7: Equilibrium bathymetries for different values of  $U_{M_2}$ . Contour lines every 0.5 meter. For model setting and parameter values, see Tables 5.1-5.3. Note that  $A_h$  and  $U$  increase if  $U_{M_2}$  increases. (a)  $U_{M_2} = 0.1 \text{ ms}^{-1}$ ; (b)  $U_{M_2} = 0.15 \text{ ms}^{-1}$ ; (c)  $U_{M_2} = 0.25 \text{ ms}^{-1}$ ; (d)  $U_{M_2} = 0.30 \text{ ms}^{-1}$ .

factor 10 smaller. The initial erosion-deposition rate is increased by about 10 % compared to the default experiment. From the convergence in the sediment transport a new estimate of the equilibrium bathymetry is calculated. After a few iterations equilibrium is reached. The modeled equilibrium bathymetry is shown in Figure 5.9(b). It only differs slightly

from that of the default experiment (Figure 5.6(b)). It is characterized by a slightly deeper channel near the inlet and a shoal that extends a bit further in the alongshore direction. These results indicate that internally generated nonlinear overtides hardly affect the main characteristics of the ebb-tidal delta.

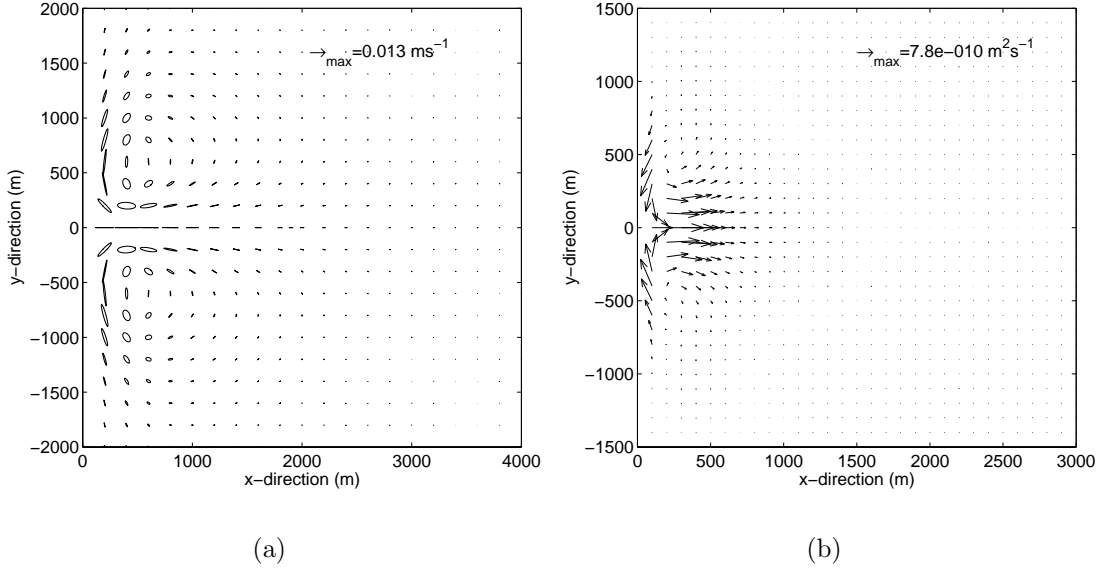


Figure 5.8: (a) Current ellipses of  $M_4$  tide at the first iteration step in the experiment with internally generated higher harmonics. For model setting and parameter values, see Tables 5.1-5.3. (b)  $\bar{q}_a$  at the first iteration step.

### Externally prescribed higher harmonics

In the experiments described in this section an external higher harmonic constituent is prescribed in the inlet. The cross-shore velocity component in the tidal inlet is specified as

$$\hat{U}(y, t) = U_{M_2} \left[ \left( 2 \frac{y}{B} - 1 \right)^3 \left( 2 \frac{y}{B} + 1 \right)^3 \right] \left[ \cos(\sigma t) + \frac{U_{M_4}}{U_{M_2}} \cos(2\sigma t - \phi) \right] \quad (5.29)$$

with  $U_{M_4}$  the magnitude of the  $M_4$  tidal currents and  $\phi$  the relative phase between the  $M_2$  and  $M_4$  tidal currents. For  $\phi = 0^\circ$  the current in the inlet is ebb-dominated, for  $\phi = 90^\circ$  there is no dominance (peak flood currents equals peak ebb currents) and for  $\phi = 180^\circ$  the current in the inlet is flood-dominated. Observations show that the velocity in the inlet can have a large  $M_4$  component. For instance, Price Inlet in South Carolina is ebb-dominated and  $U_{M_4}/U_{M_2} = 0.16$  (FitzGerald and Nummedal, 1983). Here, results are presented of experiment in which a relatively strong external  $M_4$  is prescribed with  $U_{M_4} = 0.0375 \text{ ms}^{-1}$ ,  $U_{M_2} = 0.15 \text{ ms}^{-1}$  and  $\phi = 0^\circ, 90^\circ$  or  $180^\circ$ . Note that the value of  $U$ , which is defined in Equation (5.14), now depends on  $\phi$ . For  $\phi = 0^\circ$  and  $\phi = 180^\circ$   $U = 0.1875 \text{ ms}^{-1}$ , while for  $\phi = 90^\circ$   $U = 0.165 \text{ ms}^{-1}$ . All other parameters have their

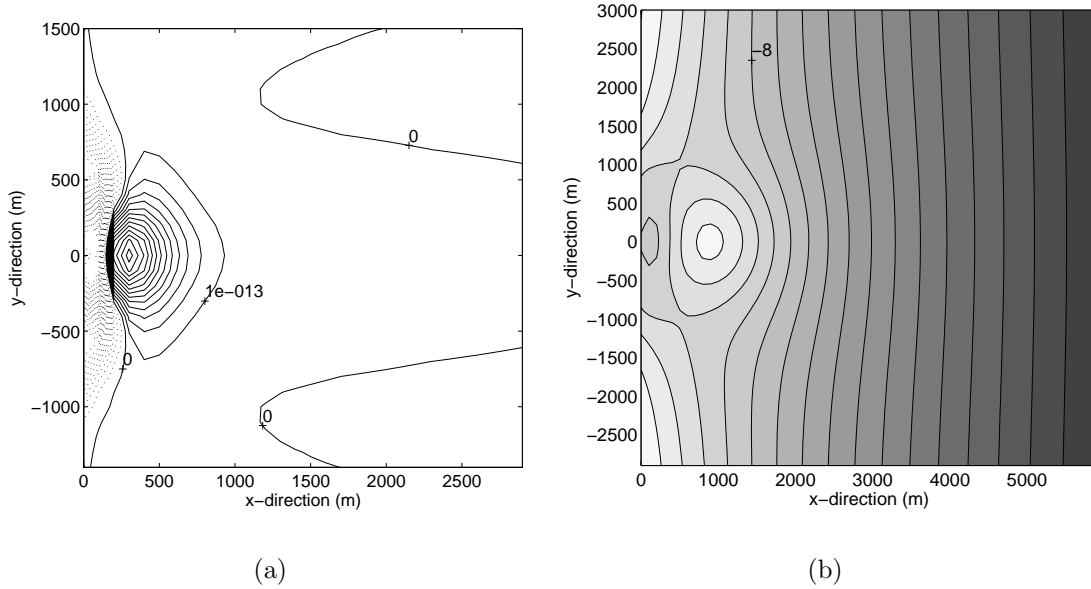


Figure 5.9: (a) Convergence of  $\vec{q}_a$  at the first iteration step. Contour lines are drawn every  $10^{-13} \text{ ms}^{-1}$ . (b) The equilibrium bathymetry in the experiment with internally generated higher harmonics. Contour lines every 0.5 meter.

default values. Furthermore,  $\vec{q}_f = \vec{q}_{\text{res}} + \vec{q}_a$  and is calculated with Equations (5.23a) and (5.23b).

For these three cases morphodynamic equilibrium has been calculated. The tidal current pattern during maximum ebb in morphodynamic equilibrium are almost similar for the three cases. For  $\phi = 0^\circ$ ,  $\phi = 90^\circ$  and  $\phi = 180^\circ$  the flow pattern during maximum ebb resembles an ebb-jet. However, the maximum magnitudes of the currents are relatively large for  $\phi = 0^\circ$  ( $0.19 \text{ ms}^{-1}$ ), moderate for  $\phi = 90^\circ$  ( $0.165 \text{ ms}^{-1}$ ) and relatively weak for  $\phi = 180^\circ$  ( $0.11 \text{ ms}^{-1}$ ). The magnitudes of the residual currents in equilibrium are different for the various phases. In case of ebb-dominated currents, the residual currents are largest. When the inlet is flood-dominated the residual currents are weakest. The tidal current ellipses of the  $M_4$  tide are similar for various phases  $\phi$ . The ellipses are mainly bidirectional.

In the case that  $\phi = 0^\circ$  the presence of higher harmonics of the tide results in a nonzero  $\vec{q}_a$ . The sediment is removed from the center of the inlet and transported in the seaward direction. The convergence of  $\vec{q}_a$  results in positive values (deposition) in the whole domain and the magnitudes are much larger than those obtained in the experiment with internally generated higher harmonics. In morphodynamic equilibrium the divergence of the flow-induced sediment transport is balanced by  $\vec{\nabla} \cdot \vec{q}_{\text{bot}}$ . The equilibrium bathymetry is shown in Figure 5.10(a). The channel-shoal pattern is more pronounced than in the default experiment (compare with Figure 5.6(b)). The channel is more extended in the alongshore direction.

In the case that  $\phi = 90^\circ$  the sediment transport  $\vec{q}_s$  has an almost similar pattern as in the experiment with internally generated higher harmonics (Figure 5.8(b)). However, the

magnitudes are larger. The convergence of the sediment transport has a similar pattern as the pattern of  $-\vec{\nabla} \cdot \vec{q}_{\text{res}}$ . The channel-shoal pattern of the equilibrium bathymetry is similar to the situation that no external  $M_4$  is prescribed in the inlet as is shown in Figure 5.10(b).

In the case that  $\phi = 180^\circ$  the currents in the inlet are flood-dominated. The sediment transport due to the higher harmonics of the tide ( $\vec{q}_a$ ) results in a transport of sediment from all sides towards the inlet. The convergence of  $\vec{q}_a$  causes a strong erosion in the entire domain and dominates the erosion and deposition pattern induced by  $\vec{\nabla} \cdot \vec{q}_{\text{res}}$ . The equilibrium bathymetry is shown in Figure 5.10(c). It has a completely different channel-shoal pattern compared to the previous experiments. The equilibrium bathymetry for  $\phi = 180^\circ$  is characterized by a channel near the center of the inlet and on both sides a delta.

### 5.4.5 Sensitivity of results to quadratic bottom stress

In the experiments described in this section a quadratic bottom stress formulation is used instead of the linearized one. No waves are considered. The sediment transport calculations include the effect of the higher harmonics of the tide and is calculated with Equations (5.23a) and (5.23b), where  $\vec{u}$  contains all tidal harmonics. All other parameters have their default values (Table 5.3).

Figure 5.11(a) shows the residual currents and sediment transport at the first iteration step. The residual currents are stronger than those obtained in the default experiment (compare with Figure 5.5), typically  $0.05 \text{ ms}^{-1}$  versus  $0.03 \text{ ms}^{-1}$ . In addition, the spatial extensions of the residual circulation cells in Figure 5.11(a) are larger than those of the default experiment. The center of the cells is at  $(x, y) = (1000, \pm 800)$ , where in the default experiment they are at  $(x, y) = (600, \pm 600)$ . A vector plot of the sediment transport  $\vec{q}_f$  is shown in Figure 5.11(b). The sediment is transported from the sides of the inlet towards the center. From the center of the inlet the sediment is transported in the seaward direction. The convergence of  $\vec{q}_f$  in equilibrium is shown in Figure 5.12(a). Interestingly, the convergence of the sediment transport shows a first indication that the delta tends to fold around the channel. The area with positive values folds around the area with negative values. The equilibrium bathymetry is shown in Figure 5.12(b). The modeled channel-shoal pattern is more pronounced compared to that of the default experiment (Figure 5.6(b)). The delta protrudes about 2 km into the sea and extends further in the alongshore direction. The height of the delta is almost the same as the delta in the default experiment. The channel in the center of the tidal inlet is deeper than in the default case.

Additional experiments were performed in which  $U_{M_2}$  is varied. For each experiment the position of the shoal has been determined. Increasing the tidal current amplitude results in a seaward shift of the position of the shoal (Figure 5.13). The maximum depth of the channel increases with increasing  $U_{M_2}$ .

### 5.4.6 Sensitivity of results to waves

In the experiment described in this section the water motion is forced by both cross-shore tidal currents in the inlet and by waves of which the characteristics are imposed at the

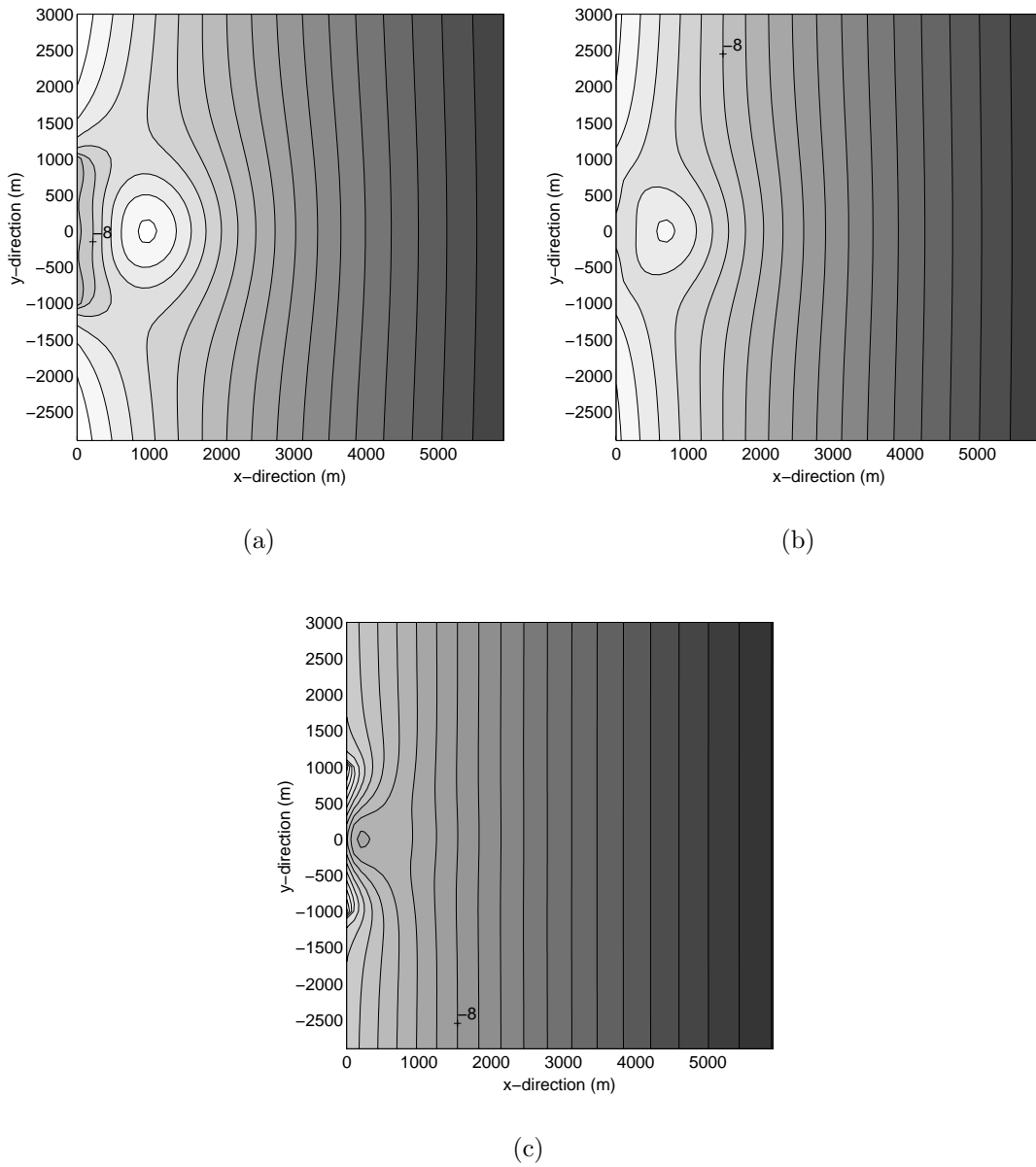


Figure 5.10: (a) Equilibrium bathymetry for experiment with zero phase difference between  $M_2$  and  $M_4$  tidal currents,  $\phi = 0^\circ$  (ebb-dominated case). Furthermore, in this experiment  $U_{M_2} = 0.15 \text{ ms}^{-1}$  and  $U_{M_4} = 0.0375 \text{ ms}^{-1}$  and velocity at the tidal inlet is prescribed according to Equation (5.29). For model setting and parameter values, see Tables 5.1-5.3. Contour lines are drawn every 0.5 m. (b) Same as (a), but now  $\phi = 90^\circ$  (no dominance). (c) Same as (a), but now  $\phi = 180^\circ$  (flood-dominated case).

offshore boundary. The values of the wave parameters are specified in Table 5.4. Other parameters are similar to the default parameter setting (Table 5.3), except for the value of  $U_{M_2}$ ,  $U_t$  and  $U$ . The typical velocity scales are:  $U_t = U_{M_2}$ ,  $U = \sqrt{U_t^2 + (u_{orb}/\beta)^2}$  and  $U_{M_2} = 0.1 \text{ ms}^{-1}$ . The offshore wave parameters have been chosen such that  $u_{orb}$  is near the inlet comparable to  $U_{M_2}$ . At the seaside boundary the waves have a significant wave

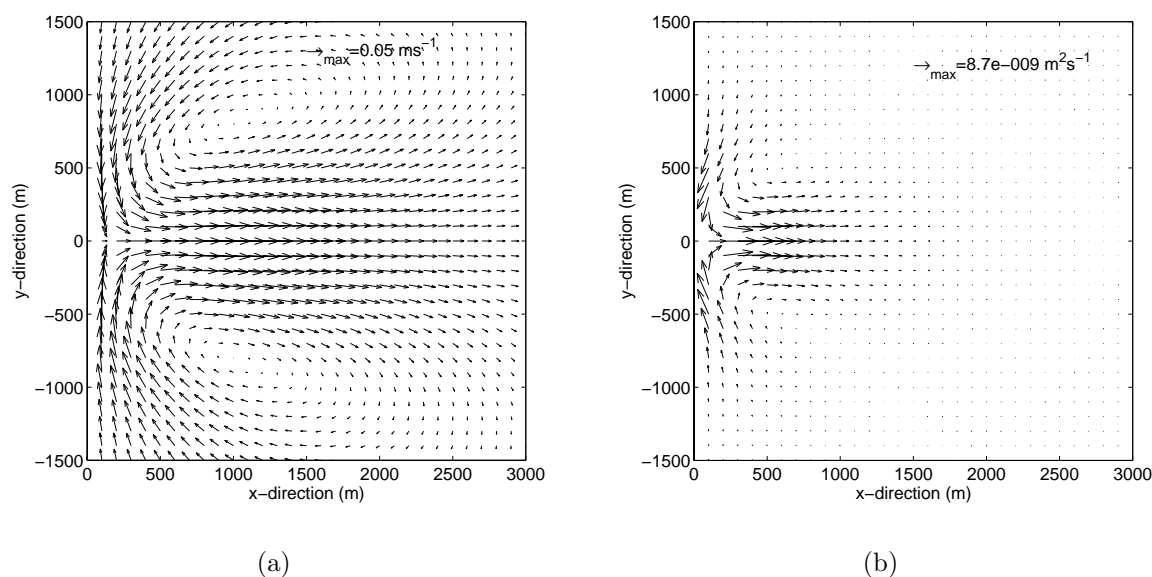


Figure 5.11: Residual currents (a) and mean sediment transport  $\vec{q}_f$  (b) for quadratic bottom stress at the first iteration step.  $U_{M_2} = 0.2 \text{ ms}^{-1}$ . For model setting and parameter values, see Tables 5.1-5.3.

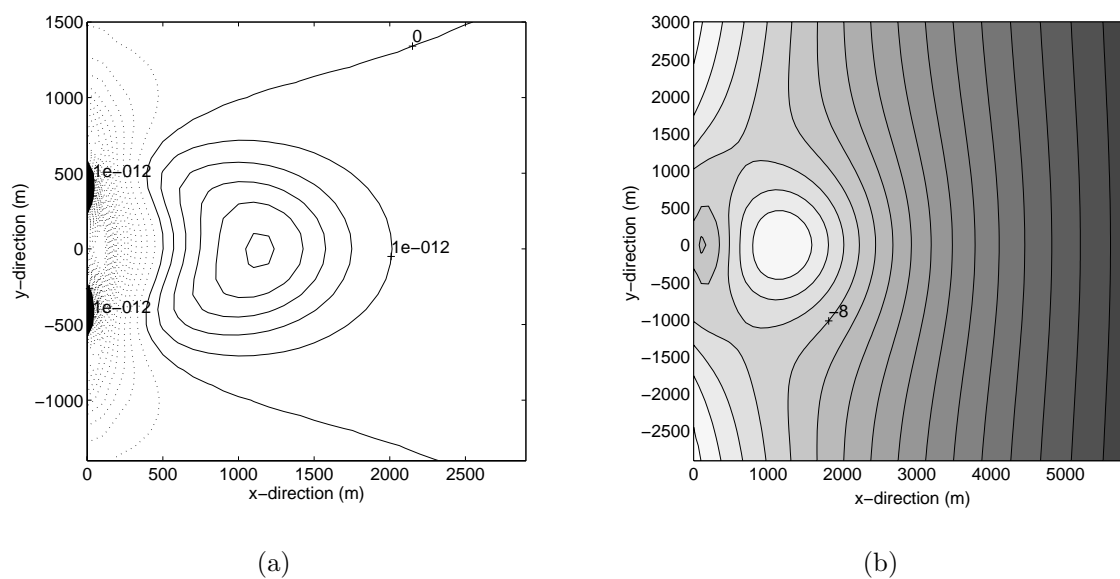


Figure 5.12: Experiment with quadratic bottom stress formulation,  $U_{M_2} = 0.2 \text{ ms}^{-1}$ . For model setting and parameter values, see Tables 5.1-5.3. (a) Convergence of the sediment transport in equilibrium,  $-\vec{\nabla} \cdot \vec{q}_f$ . Contour lines are drawn every  $10^{-12} \text{ ms}^{-1}$ . (b) Equilibrium bathymetry. Contour lines are drawn every 0.5 meter.

height of 0.21 m and a period of 7 s. The waves have shore-normal incidence and the directional spreading is  $2^\circ$ . The influence of the currents on the waves is not included in the calculations. The wave parameters are used to calculate the bottom shear-stress

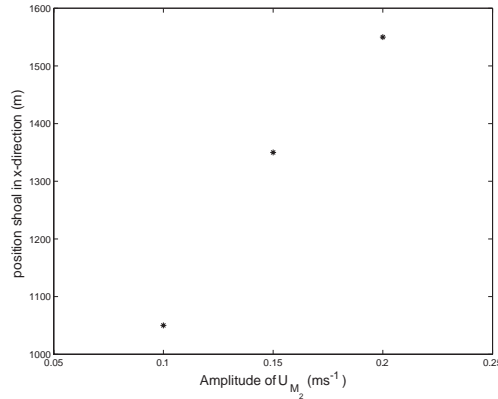


Figure 5.13: The cross-shore position of the shoal against the amplitude of the prescribed cross-shore current in the experiment with quadratic bottom shear-stress.

experienced by the currents as described in Section 5.2.2. The sediment transport includes the effect of waves and is calculated using Equations (5.23a)-(5.23c).

Variable	Choice
$H_{sig}$	0.21 m
$T_p$	7 s
dir	90°
directional spreading	2°
$U$	$\sqrt{U_{M_2}^2 +  u_{orb}/\beta ^2}$
$U_{M_2}$	0.1 $\text{ms}^{-1}$

Table 5.4: Parameters for experiment with waves.

The wave parameters at the first iteration step are plotted in Figure 5.14. In this stage the bathymetry is  $H = H_R(x)$ . The top panel shows the bathymetry along the line  $y = 0$ . In the middle panels the significant wave height and the wave number  $k$  are plotted. The wave height increases and the wave length decreases (so  $k$  increases) when the water depth decreases. The lowest figure shows  $u_{orb}$ . It increases in shallower water. The radiation stresses, the dissipation of energy due to breaking and due to whitecapping is found to be very small.

The sediment transport pattern of  $\vec{q}_{res}$  and  $\vec{q}_a$  and the corresponding sediment erosion-deposition pattern are similar to those found in the previous experiments where waves were absent. There are differences, but these are small. A vector plot of the sediment transport  $\vec{q}_{wave}$  is shown in Figure 5.15(a). The transport is clearly organized in two cells. Also far from the inlet ( $\sim 1500$  m) the sediment transport rate is large. The convergence of  $\vec{q}_{wave}$  is shown in Figure 5.15(b). In the center of the inlet sand is eroded. This area of erosion stretches diagonally out to the sides of the inlet. There are three distinct areas where sediment is deposited. One of them is located at 500-1500 m seaward of the tidal



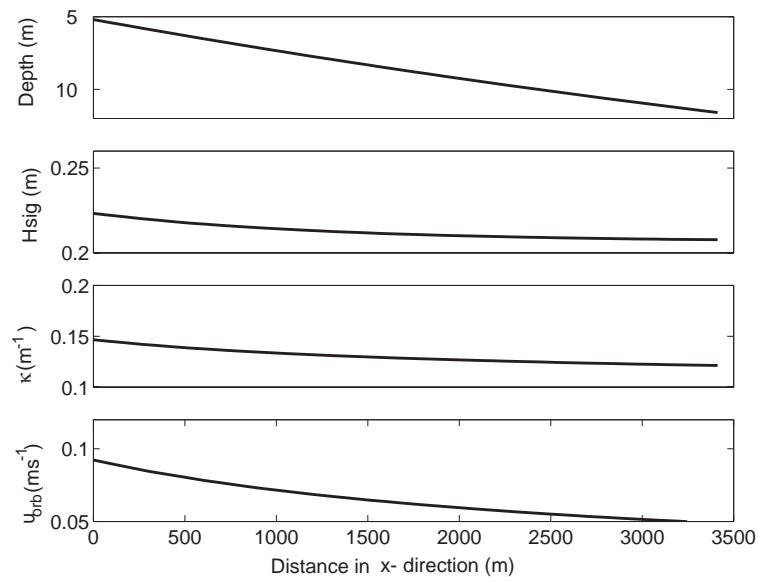


Figure 5.14: Wave parameters for the initial iteration step ( $H = H_R$ ). The top panel shows the bathymetry along the line  $y = 0$ . The second panel shows the significant wave height. The third shows the magnitude of the mean wave number  $|\vec{k}|$  and in the lowest panel  $u_{orb}$  is plotted.

inlet, as was always found in the previous experiment. In addition, there are two areas with wave-induced sediment deposition at both sides of the inlet.

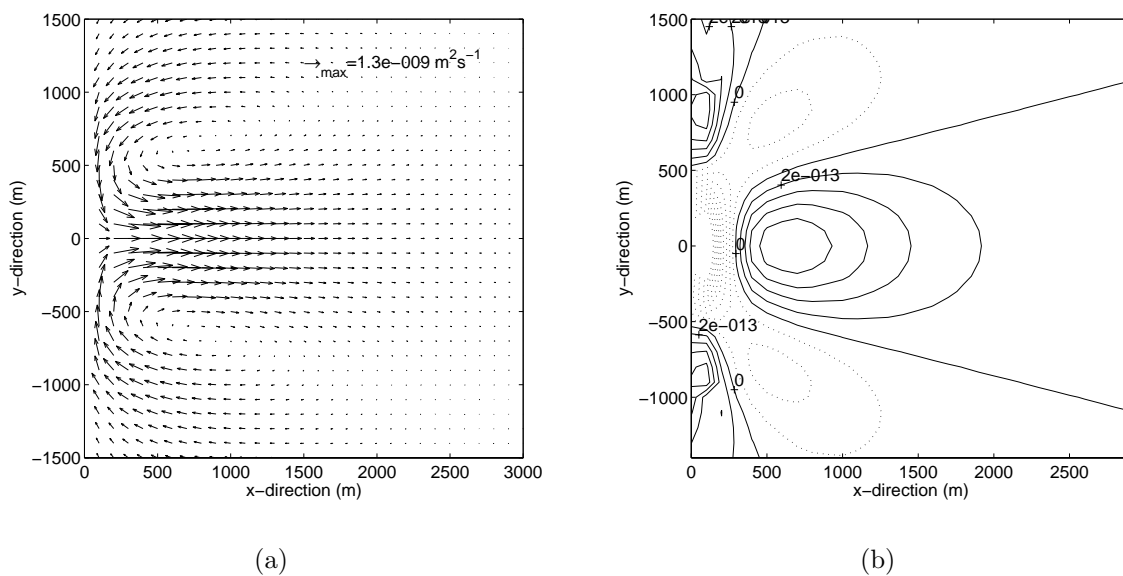


Figure 5.15: (a) Sediment transport due to waves ( $\vec{q}_{wave}$ ) in first iteration step. (b) Convergence  $\vec{q}_{wave}$ . Contour lines are drawn every  $2 \cdot 10^{-13} \text{ ms}^{-1}$ .

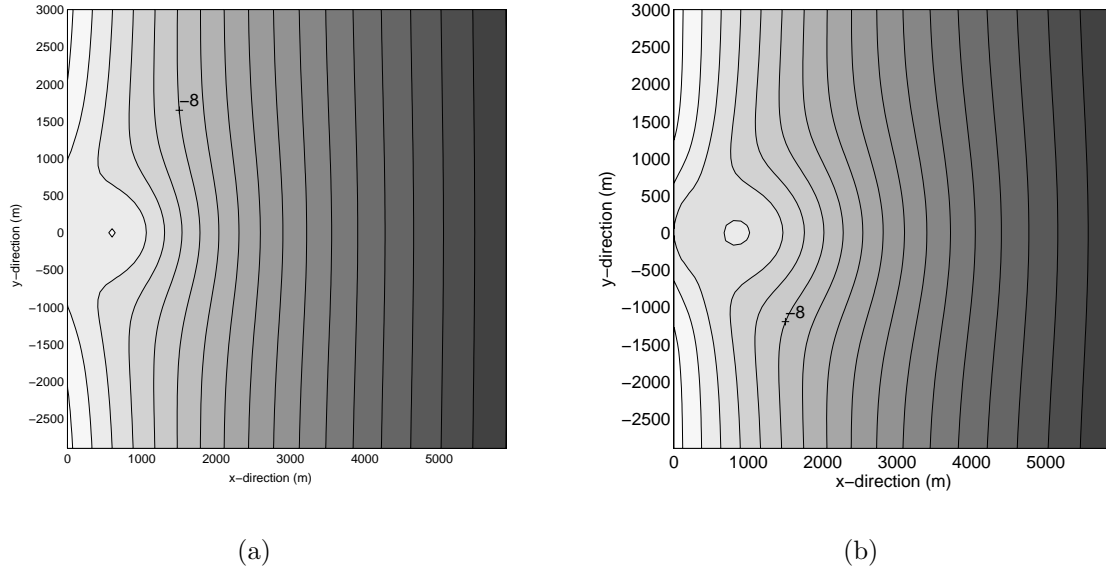


Figure 5.16: (a) Equilibrium bathymetry for quadratic bottom stress and  $U_{M_2} = 0.1 \text{ ms}^{-1}$ ; no waves. (b) same as (a), but now with waves and parameters as defined in Table 5.4.

After 11 iterations morphodynamic equilibrium is reached. The equilibrium bathymetry is compared with that which is closest in parameter setting:  $U_{M_2} = 0.1 \text{ ms}^{-1}$ , quadratic shear-stress and  $\vec{q}_f$  calculated without the contribution of  $\vec{q}_{\text{wave}}$ . The two equilibrium bathymetries are shown in Figure 5.16. The modeled shoal of the experiment with waves protrudes further into the sea (Figure 5.16(b)) compared to the experiment without waves (Figure 5.16(a)). Furthermore, the two flood-dominated channels are more pronounced.

At the first iteration step the wave parameters did not have alongshore variations and only were a function of the cross-shore coordinate. In equilibrium the wave parameters are influenced by the presence of the channels and the shoals. In Figure 5.17(a) a contour plot of the significant wave height  $H_{sig}$  is shown. Above the shoal its value has increased more than 10 percent compared to its value at the first iteration. Note that  $H_{sig}$  has decreased on the sides of the inlet compared to its values at the first iteration. In Figure 5.17(b) a contour plot of the magnitude of the wave orbital motion is shown. It has increased above the shoal and decreased again in the ebb-channel. A vector plot of  $\vec{u}_w$  (defined in Equation (5.8)) is shown in Figure 5.17(c). The contour lines represent the equilibrium bathymetry. The alongshore components of  $\vec{u}_w$  have been magnified by a factor 16. This is done to show that the waves refract towards the shallower delta. At the first iteration step the waves had a shore-normal direction. In equilibrium the waves can have an angle of  $5^\circ$  with respect to the normal of the coast.

Because the refraction of the waves is quite small and waves do not break (the ratio of wave height and water depth is very small), it is found that the divergence in the radiation stress tensor is small and no wave-driven currents are generated in this experiment.

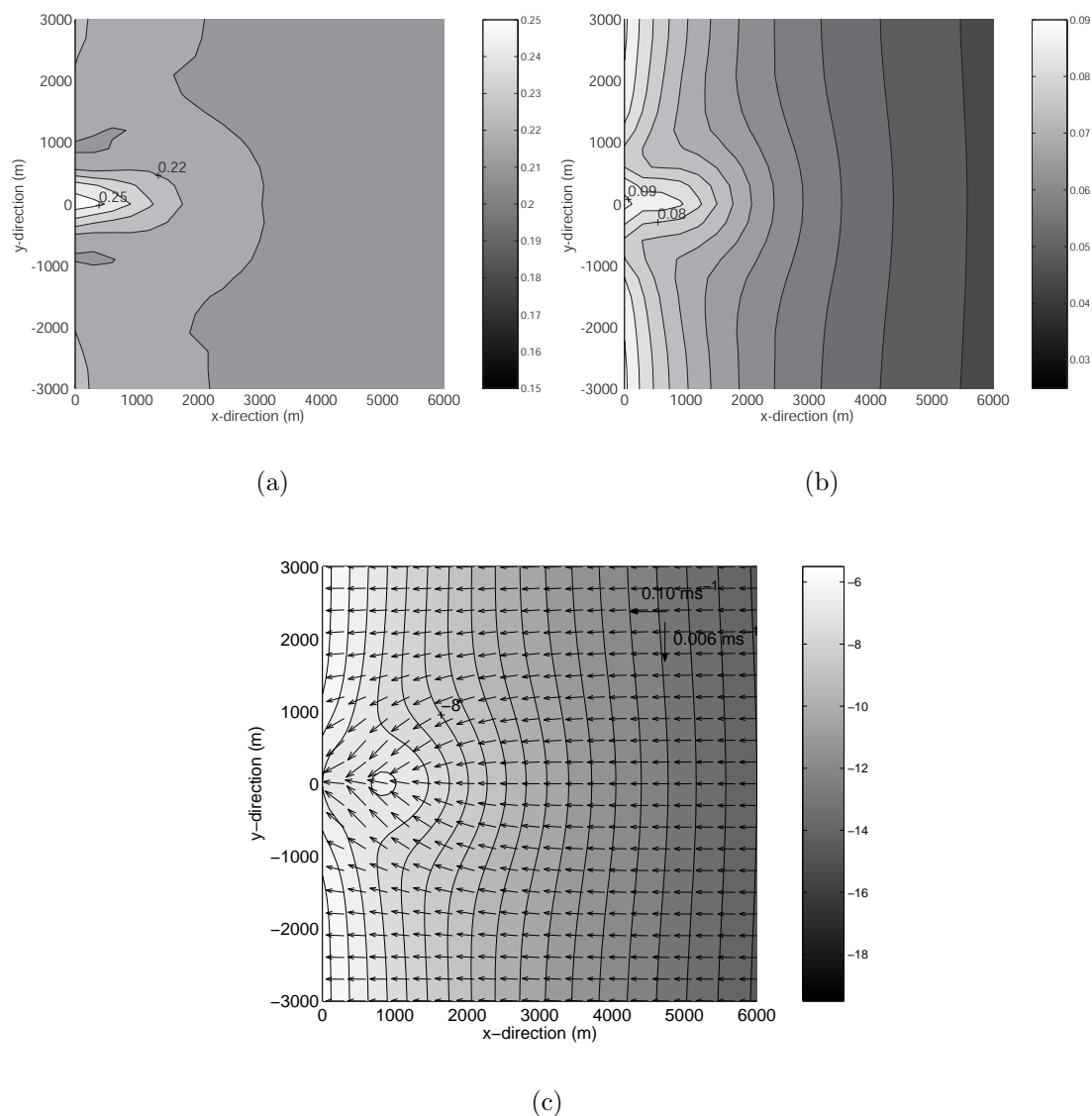


Figure 5.17: Wave parameters in equilibrium. (a)  $H_{sig}$  (m). Light parts (dark parts) indicate large (small) significant wave height. Contour lines are drawn every 0.01 m. (b) Magnitude of the near-bed wave-orbital motion  $u_{orb}$  ( $\text{ms}^{-1}$ ). Light parts (dark parts) indicate large (small) values of  $u_{orb}$ . Contour interval is 0.01  $\text{ms}^{-1}$ . (c) Vector plot of  $\vec{u}_w$  (defined in Equation (5.8)). Its alongshore component is amplified by a factor 16. Furthermore, grey values indicate the depth. Dark is deep, light is shallow. Contour lines of depth are drawn every 0.5 meter.

## 5.5 Comparison of model results with observations and idealized model

### 5.5.1 Comparison with field data

In this section the characteristics of the modeled equilibrium bathymetries and water motion are compared with field data. In all the experiments the tidal flow during ebb

and flood has the same pattern, i.e. a jet-like flow during ebb and radial inflow during flood. This is consistent with the picture presented by *Stommel and Farmer (1952)* and *Oertel (1975)*. *Wells and Van Heyst (2003)* observed similar behavior of water motion in a laboratory set-up. Quantitative comparison of the results with field data is difficult, since observed amplitudes of the tidal currents are much higher ( $1 \text{ ms}^{-1}$ ) than those used in the model. No reliable model solutions could be obtained for amplitudes of the tidal current larger than  $0.3 \text{ ms}^{-1}$ . This will be discussed in Section 5.6.

Except for the experiment with externally prescribed flood-dominated currents in the inlet, all modeled equilibrium bathymetries have a delta that is flanked by two flood-dominated channels. In the center of the tidal inlet a ebb-dominated channel is present. These findings are consistent with field observations (*Hayes, 1975*). There are, however, differences between the model results and the observations. In particular, the ebb-channel does not protrude as far seaward as observed in nature and the shoal does not bend around it. Adding higher harmonics of the tide to the sediment transport calculations and extending the model with a realistic description of the waves does not change the general picture of the equilibrium bathymetry. However, adding the quadratic bottom stress formulation results in a more seaward extension of the ebb-dominated channel and a first indication of the folding of the delta around it (Figure 5.12). For larger magnitudes of  $U_{M_2}$  no morphodynamic equilibria are found and it can not be studied whether this effect becomes more pronounced.

The most quantitative comparison with observations possible is the comparison between the observed and modeled relation between the amount of sand stored in the ebb-tidal delta and the tidal prism. The tidal prism (TP) is defined as the total amount of water that flows through the inlet during one tidal cycle,

$$\text{TP} = \int_0^T \int_{-B/2}^{B/2} |\hat{U}(y, t)| H(0, y) dy dt. \quad (5.30)$$

The ebb-tidal sand volume (ESV) is defined as the total volume of sand above the reference bathymetry  $H_R$

$$\text{ESV} = - \int \int_A [H(x, y) - H_R(x)] \Theta(H_R(x) - H(x, y)) dx dy, \quad (5.31)$$

where  $\Theta$  is the Heaviside function and  $A$  the model area. This means that only those areas with depths smaller than  $H_R$  will contribute to ESV. The values of ESV and TP are made dimensionless by dividing the volumes by a control volume of  $1 \text{ m}^3$ . In Figure 5.18 some of the inlets presented by *Walton and Adams (1976)* are plotted (stars). They found a relation between ESV and TP using the data of more than 40 inlets at the US coast. This relation is

$$\text{ESV} = c_1 \text{TP}^{c_2} \quad (5.32)$$

with  $c_1$  in the order of  $10^{-2}$  and  $c_2 = 1.23$ . This empirical fit is shown in Figure 5.18 by the solid line. The power-like behavior is best seen when the logarithm is plotted of both TP and ESV. The modeled ESV as function of the modeled TP for the default parameter setting is shown by the black dotted line. The relation between ESV and TP

has the same slope as the observed slope, which implies that the power is close to that as found by *Walton and Adams* (1976). However, the modeled magnitudes of ESV are about a factor 3.5 smaller than observed. The fit of the model results yields  $c_1 = 3 \cdot 10^{-3}$  and  $c_2 = 1.23$ . The modeled relation between ESV and TP for the experiment with quadratic bottom stress (dashed line in Figure 5.18) is even closer to the observations and the magnitude of the modeled sand volume is only a factor 2 smaller than observed. In this case the fit of the model results yields  $c_1 = 1.1 \cdot 10^{-3}$  and  $c_2 = 1.32$ . The modeled sand volume with waves is larger than in the experiment without waves. It is denoted by an asterisk in Figure 5.18. The ebb-tidal sand volume in the experiment with waves is  $7.5 \cdot 10^6 \text{ m}^3$  and the tidal prism is  $1.7 \cdot 10^7 \text{ m}^3$ . That result appears to agree quite well with the field data.

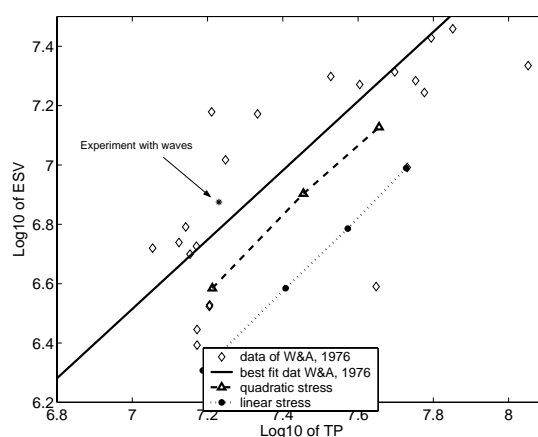


Figure 5.18: Ebb-tidal sand volume as a function of the tidal prism. Diamonds denote a part of the field data from *Walton and Adams* (1976). The solid line is the best fit of field data. The results of the quadratic stress experiments are denoted by the dashed line and those with the linear stress by the dotted line. The result of the experiment with waves is included as well.

### 5.5.2 Comparison with idealized model

The default experiment has been designed such that it is as close as possible to the idealized model as described in Chapter 3. In this section the results of the default case are compared with the results of the idealized model. In Figure 5.19(a) the flow patterns during ebb are shown. The black vectors show the currents calculated with the idealized model and the grey vectors denote the currents calculated with the numerical model. Both the numerical and idealized model generate an ebb-jet. The differences between the currents calculated with the numerical and with the idealized model are small. The largest differences are found in the region of the tidal inlet. The alongshore velocity components are smaller in the numerical model than in the idealized model. The ebb-jet is more pronounced in the numerical model than it is in the idealized model. During flood (Figure 5.19(b)) the modeled current patterns of the two models are almost similar. The differences are very small. The calculated residual currents are shown in Figure 5.19(c). Both models calculate two residual circulation cells of which the centers are located at

$(x, y) = (600, \pm 600)$ . However, there are differences as well. The differences are largest in the region of the tidal inlet. The magnitudes of the residual currents are larger in the numerical model than in the idealized model. Close to the inlet the residual currents also have different direction.

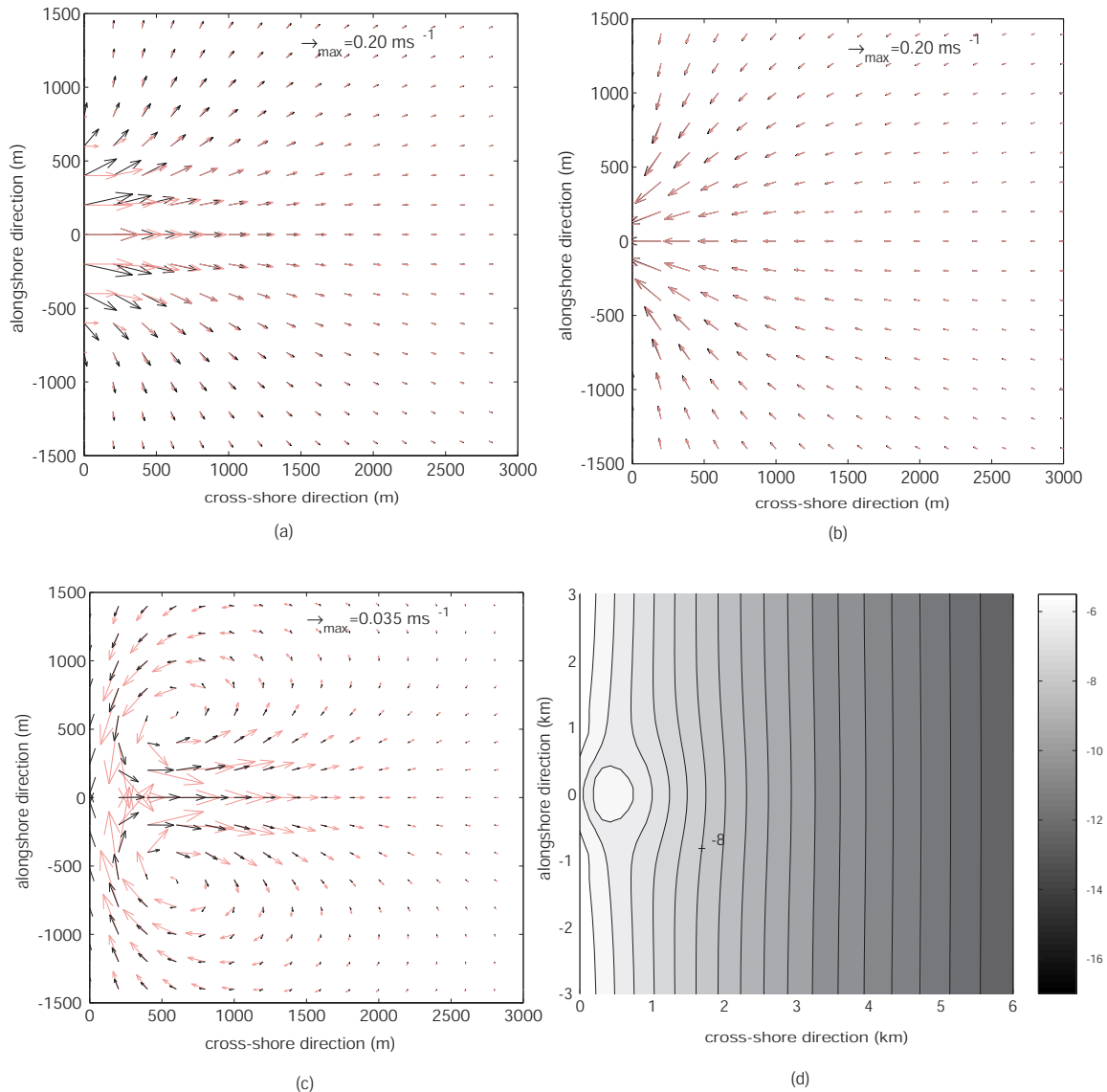


Figure 5.19: Comparison of flow patterns in morphodynamic equilibrium obtained with idealized (black vectors) and with numerical model (grey vectors). (a) Maximum ebb. (b) Maximum flood. (c) Residual currents. (d) Equilibrium bathymetry for maximum tidal currents through the inlet of  $0.2 \text{ ms}^{-1}$  and  $B=2\text{km}$  obtained with the idealized model.

Qualitatively, the differences between the modeled currents of the numerical and the idealized model are small. There are quantitative differences, however. Therefore, it can be expected that the modeled equilibrium bathymetries will differ quantitatively. The equilibrium bathymetry obtained with the idealized model is shown in Figure 5.19(d) and the one obtained with the numerical model in Figure 5.6(b). The results are very similar.

Both models reproduce the ebb-tidal delta at the end of the ebb-dominated channel. This delta is flanked by two flood-dominated channels. Quantitatively, there are differences. The minimum depth above the shoal in the idealized model is  $\sim 6$  m at a cross-shore distance of 500 m. In the numerical model it is also  $\sim 6$  m, but the shoal is located 1000 m from the center of the tidal inlets. The bottom patterns are more pronounced, compared to the results of the idealized model.

### Model formulation

Idealized model	Numerical model
Rigid lid approximation	$\zeta$ can be dynamically important
BC: In inlet $\partial v / \partial x = 0$	Inflow: no tangential advection of momentum outflow: no extra BC
Infinite domain	Finite domain

### Numerical method

Idealized model	Numerical model
Space: Pseudospectral method	Finite differences
Time: Expansion in Fourier components	Standard time integrations
Truncation after $M_2$ harmonic component	"All" harmonic components included

Table 5.5: Main differences between "idealized" model and "realistic" model

To understand why these differences in model results occur it should be realized that, although both models were as close as possible in model formulation and parameter setting, there are still differences. These are summarized in Table 5.5. They concern the model formulation and the numerical methods to solve the equations. The first difference between both models is the use of a rigid lid approximation in the idealized model. This implies that in the idealized model only the pressure gradients due to the sea surface elevation are dynamically important. This is justified as long as the square of the Froude number ( $Fr^2 = U^2/gH = \zeta/H$ ) is small. In Delft3D-FLOW this rigid lid approximation is not made. The results show that in the experiments the maximum sea surface elevation never exceeds 10 cm. Since the water depth is always more than 5 meter, this implies that  $Fr^2 \sim 10^{-2}$ . Therefore, the use of a rigid lid approximation in the idealized model is justified and it does not explain the differences between both models.

The second difference concerns the boundary conditions in the tidal inlet. In both models the cross-shore currents are prescribed, but the second condition is different: In the idealized model a free-slip condition is applied while in the numerical model during ebb the advection in the tangential direction is neglected and during flood no additional boundary condition is required. Neglecting the tangential advection is equivalent to assuming that the alongshore velocity is zero. This boundary condition forces a jet-like outflow during ebb. This is clearly visible in Figure 5.19(a). The numerical model has no alongshore component in the tidal inlet during ebb. During flood the numerical model computes a strong alongshore velocity component near the inlet. The residual currents calculated with the numerical model are larger than those obtained with the idealized model. Furthermore, the residual sediment transport and its convergence calculated with the numerical model are larger than those obtained with the idealized model. The con-

sequence is that the equilibrium bathymetry obtained with the numerical model is more pronounced than the one obtained with the idealized model.

The third difference is that the idealized model uses an infinite domain, while the numerical model uses a finite domain. This hardly influences the results, because the domain that is used in the numerical model is large enough to have vanishing currents and sediment transport at the seaward boundaries.

The fourth to sixth item listed in Table 5.5 concern the numerical method used to solve the models. In the idealized model a pseudospectral method is used, see Chapter 3. In the numerical model finite differences have been used. In the numerical model the free-slip condition at  $x = 0$  is not well resolved. In the default experiment  $A_h = 2.8 \text{ m}^2\text{s}^{-1}$ , resulting in a typical thickness of the boundary layer of  $\sqrt{A_h/\sigma} \approx 140 \text{ m}$ . The grid size is 100 m. This might be too coarse to resolve the boundary layer. The idealized model does not suffer from this problem, because with the pseudospectral method the grid can be refined near  $x = 0$ . However, because the differences between flow pattern during flood calculated with the idealized model and calculated with the numerical model hardly differ, it is believed that this difference is not important.

The last difference between both models is introduced by the numerical method to solve the time-dependent part of the variables (fifth and sixth difference). In the idealized model a Galerkin method is used. The variables are expanded into a Fourier series. This series is truncated after the  $M_2$  component. In the numerical model standard techniques are used and all components of the tide are calculated. The results obtained with the numerical mode show that there is only a very small generation of higher harmonics of the tide. Its relative magnitude is about 5% of the magnitude of the  $M_2$  components. Therefore, the harmonic truncation is not likely to be responsible for large differences between the results obtained with both models.

The most important difference between the models seems to be the formulation of the boundary conditions in the inlet. This has been tested by performing an experiment in which the idealized model was forced by new boundary conditions at  $x = 0$ . The velocity field at  $x = 0$  was prescribed with velocity components as calculated with the numerical model, retaining only the residual and  $M_2$  components.

The current pattern during maximum ebb, maximum flood and the residual currents calculated with the adapted idealized model and the numerical model are shown in Figure 5.20. Black vectors are calculated with the adapted idealized model and grey vectors with the numerical model. The differences between the results obtained with the two model are much smaller than in the previous experiment. Especially during ebb the results have come much closer, while during flood the changed boundary conditions in the adapted idealized model hardly influences the calculated flow pattern. Furthermore, the residual currents calculated with the adapted idealized model and with the numerical model are in good agreement (Figure 5.20(c)). However, especially near the tidal inlet the vectors still do not have the same magnitude and direction. The equilibrium bathymetry calculated with the adapted idealized model is shown in Figure 5.20(d). The channels calculated with the numerical model are still a little deeper and the position of the shoal is further seaward, but the differences between the idealized and the numerical are much smaller than in the previous experiment (see Figure 5.19(d)).



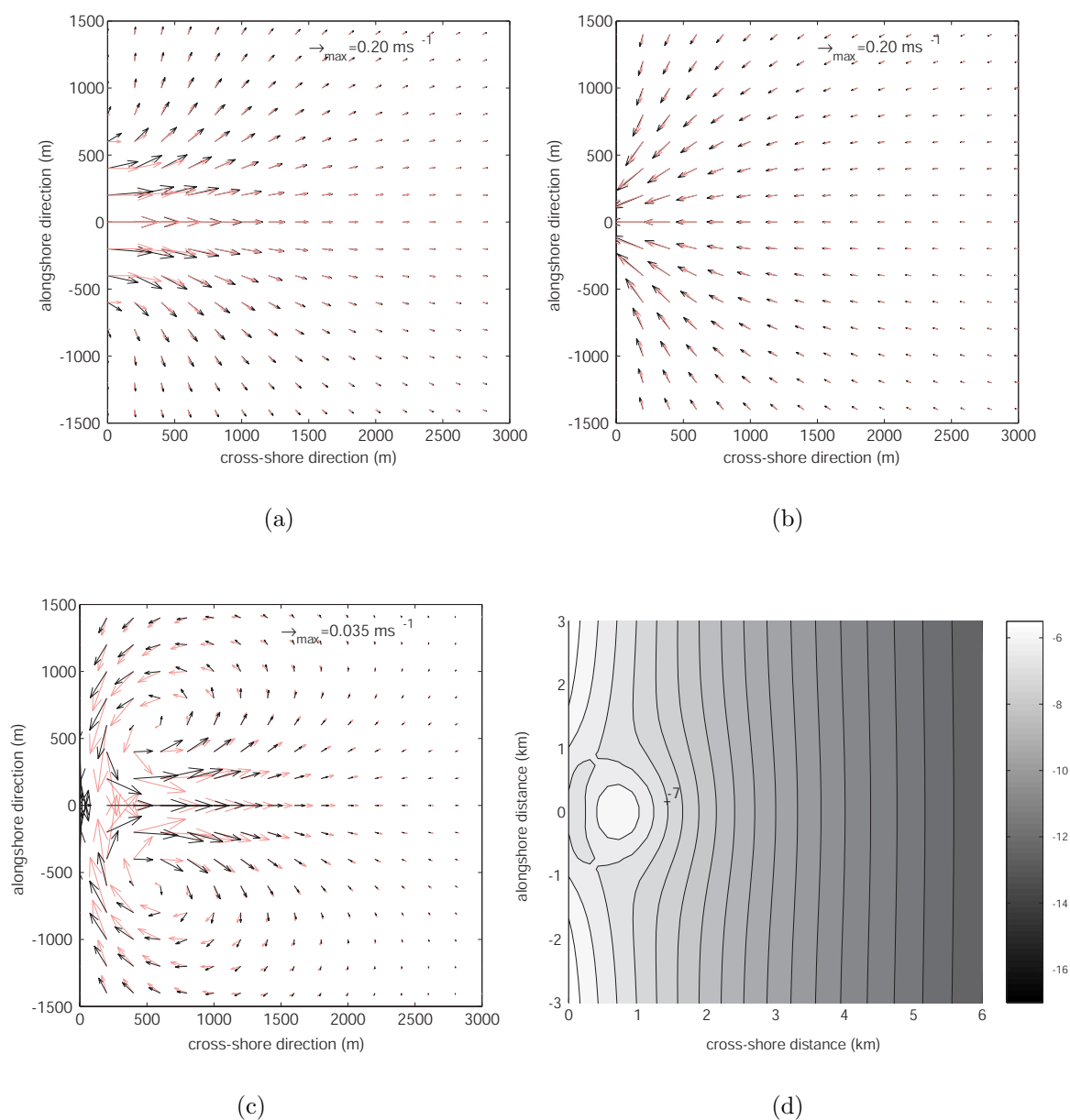


Figure 5.20: Comparison of model results in morphodynamic equilibrium obtained with the adapted idealized model and with numerical model. The velocity field obtained with the numerical model in the default case has been used as a boundary condition at the coastline for the adapted idealized model. (a) Currents during maximum ebb (black vectors represent idealized model, grey vector numerical model). (b) As (a), but now during maximum flood. (c) As (a), but now the residual currents. (d) Equilibrium bathymetry calculated with the adapted idealized model. Contour lines every 0.5 m.

## 5.6 Discussion

The objectives for the study described in this chapter were twofold. The first was to develop a numerical morphodynamic model which allows for equilibrium solutions. The

results of this model were compared with observations and with the results obtained with the idealized model described by *van der Vegt et al. (2005)*. The second was to study the sensitivity to processes that could not be accounted for in the idealized model. A detailed comparison of model results with observations and with the idealized model was presented in the previous section. Here, the sensitivity of the results to extensions in the model formulation are discussed. After this, it is discussed why for  $U_{M_2} > 0.3 \text{ ms}^{-1}$  no morphodynamic equilibria were found.

### Sensitivity to tidal asymmetry

The influence of internally generated higher harmonics on the morphodynamic equilibrium turns out to be small. The additional sediment transport due to higher harmonics of the tide,  $\vec{q}_a$ , is in the order of 10 %. In *van de Kreeke and Robaczewska (1993)* it was shown that in the one-dimensional case the magnitude and direction of  $\vec{q}_a$  depends on the magnitude of the  $M_4$  and  $M_2$  tidal currents and on their relative phase difference. In the two-dimensional case the expressions for  $\vec{q}_a$  become more elaborate (*van der Molen, 2000*). But also in that analysis  $\vec{q}_a$  is a function of the magnitude of the  $M_4$  and  $M_2$  tidal currents. The magnitude of the  $M_4$  currents is measured by the long axis of the  $M_4$  tidal current ellipse. Its maximum in the domain is  $0.013 \text{ ms}^{-1}$ , which is about a factor 3 smaller than the maximum residual currents ( $0.035 \text{ ms}^{-1}$ ). Moreover, there is an approximate phase difference of  $90^\circ$  between the  $M_2$  and  $M_4$  tidal currents. This results in only a small contribution of  $\vec{q}_a$  to  $\vec{q}_f$ .

The influence of an externally prescribed  $M_4$ -component on the calculated morphodynamic equilibria is much stronger. Depending on the phase difference  $\phi$  between the  $M_2$  and  $M_4$  tidal current, the equilibrium bathymetry has no shoal or a larger shoal compared to the situation without externally forced  $M_4$  current. When  $\phi = 0^\circ$  the ebb-dominated channel is deeper and the shoal is larger and is located further seaward. This is caused by the additional sediment transport due to the higher harmonics of the tide. In the case that  $\phi = 90^\circ$ , the tidal currents during ebb have the same magnitude as during flood and the net sediment transport  $\vec{q}_a$  is very small. For  $\phi = 180^\circ$  the currents in the inlet are flood-dominated. The convergence of  $\vec{q}_a$  causes erosion in the whole domain. This erosion is larger than the deposition of sediment induced by the convergence of  $\vec{q}_{\text{res}}$ . This results in the absence of an ebb-tidal delta. This prediction seems to be in correspondence with observations. It is found that inlets with strong flood-dominated currents only have poorly developed ebb-tidal deltas, whereas deltas with ebb-dominated currents have large ebb-tidal deltas (*Walton, 2002*).

### Sensitivity to quadratic bottom shear-stress

The results obtained with the numerical model are sensitive to the use of the quadratic bed shear-stress formulation instead of the linearized one. The magnitude of the residual currents obtained with the quadratic bottom stress formulation are larger than in the default case. Furthermore, the spatial extensions of the two residual circulation cells are increased compared to the default experiment. The linearized bottom stress formulation is normally motivated by an energy consideration: The dissipation of kinetic energy per

tidal period obtained with the linearized bottom stress formulations should equal the dissipation as obtained with a quadratic formulation. Therefore, the tidally averaged dissipation of kinetic energy is calculated for both the linearized and the quadratic bottom shear-stress formulation. This is done for the first iteration step in the case that  $U_{M_2} = 0.2 \text{ ms}^{-1}$ . The tidally averaged energy dissipation  $D_{\text{lin}}$  obtained with the linearized stress is

$$D_{\text{lin}}(x, y) = \frac{8}{3\pi} \frac{gU}{C_z^2 T} \int_{t=0}^{t=T} |\vec{u}(x, y, t)|^2 dt \quad (5.33)$$

The energy dissipation  $D_{\text{qua}}$  obtained with the quadratic bottom shear-stress is

$$D_{\text{qua}}(x, y) = \frac{g}{C_z^2 T} \int_{t=0}^{t=T} |\vec{u}(x, y, t)|^3 dt \quad (5.34)$$

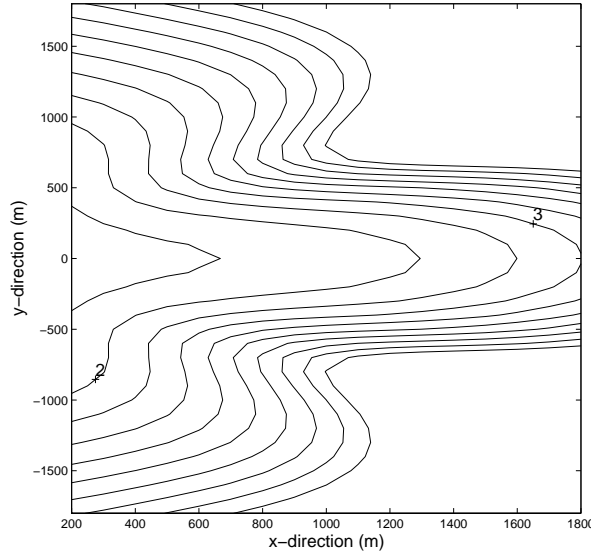


Figure 5.21: Comparison between the tidally averaged dissipation of energy obtained with linear and with quadratic bottom shear-stress,  $D_{\text{lin}}/D_{\text{qua}}$ . Contour lines indicate the factor of overestimation in the linear bottom stress. Contour lines every 0.5.

In Figure 5.6 a contour plot of the ratio of  $D_{\text{lin}}$  and  $D_{\text{qua}}$  is shown. Only in the middle of the inlet the energy dissipation due to the linearized bottom shear-stress equals that of the quadratic stress. In the rest of the domain the dissipation due to the linearized stress is substantially larger. This has importance consequences for the residual velocity. In *Zimmerman* (1981) it is shown that residual circulation cells are strongly related to tidally averaged vorticity. In *van der Veegt et al.* (2005) it was shown that the main balance in the tidally averaged vorticity balance is between the convergence in the vorticity flux (which generates residual vorticity) and the dissipation of residual vorticity by friction. When the energy dissipation by friction is overestimated, the residual vorticity will be underestimated. This results in smaller residual currents, smaller sediment transport and a smaller convergence of it. As a consequence, the modeled equilibrium bathymetry is

smaller. In conclusion, the estimate of  $U$  in Equation (5.14) leads to a strong overestimation of the energy dissipation due to linearized bottom friction and an underestimation of the magnitude of the residual currents. A better estimate is needed. Since the magnitudes of the tidal currents strongly vary in the region of the tidal inlet, it is recommended to apply the Lorentz linearization procedure at each position in the domain. This will result in a spatially dependent  $U$ . This is in principle possible with the idealized model.

### Sensitivity to waves

The last extension of the model is the incorporation of a realistic description of the waves. This leads to flood channels which are more pronounced (deeper) and to a shoal which lies further seaward compared to the experiment without waves. The depth above the shoal is still relatively deep and the waves are small. Therefore the waves do not break and no wave-driven currents are generated. However, the refracting of the waves towards the shoal is visible (Figure 5.17(c)). In the case that the depth above the shoal decreases or the wave height increases it is expected that these kind of effects will become more important. The waves will refract to and ultimately break above the shoal. This will result in wave-driven currents that will affect the modeled equilibrium bathymetry. For realistic scenarios the numerical model yields more accurate results than the idealized model.

### Why no convergent solutions for $U_{M_2} > 0.3 \text{ ms}^{-1}$ ?

In this study convergent solutions are found for  $U_{M_2}$  up to a maximum of  $0.30 \text{ ms}^{-1}$ . Interestingly, with the idealized model morphodynamic equilibria were found for much higher velocity amplitudes. This raises the question why the numerical model does not allow for equilibrium solutions for  $U_{M_2} > 0.3 \text{ ms}^{-1}$ .

There are two possible explanations. The first is related to the numerical methods to solve the model. As was already discussed in Section 5.5.2, the grid size of 100 meter might be too coarse to calculate the patterns in the convergence of the sediment transport in the region of the tidal inlet. Furthermore, the free-slip condition at  $x = 0$  is not well resolved. The input of tidal vorticity is a very important parameter for the generation of residual circulation cells (*van der Vegt et al., 2005*). In turn, the residual currents are important for the residual sediment transport and its convergence. In the idealized model the boundary conditions in the inlet are such that the input of vorticity into the domain is determined by the shear in the velocity profile prescribed in the inlet. In the numerical model this is not the case because  $\partial v / \partial x$  is to be determined by the model. If the coupling between the bottom and vorticity input is very nonlinear, a small change in the magnitude of the bottom patterns can result in a large change of the vorticity input and a large change of the current patterns. The iterative solution procedure fails to calculate the morphodynamic equilibria. However, with the idealized model also above a certain magnitude of the cross-shore tidal currents no equilibria were found. Therefore, another explanation should be considered as well.

The second explanation concerns the possible existence of bifurcations in parameter space. These bifurcations have been found in previous studies for tidal basins (*Schuttelaars*

*and de Swart, 2000; Schramkowski et al., 2004*). Although in these studies other problems have been studied, the system studied in this chapter has strong similarities in model formulation. When bifurcations exist, it might be that equilibria exist for  $U_{M_2} > 0.3 \text{ ms}^{-1}$ , but the differences with the equilibrium of a slightly smaller parameter are so large, that the continuation method fails to find the equilibrium for this parameter setting. A stability analysis has to be performed to obtain insight in the existence of these bifurcations or more sophisticated continuation techniques should be used.

## 5.7 Conclusions

In the previous section the main results already have been discussed. In this section a short summary of the main findings is given. The section ends with suggestions for further research.

The first objective of this study was to validate the results of the idealized model by calculating morphodynamic equilibria with a numerical model. The results presented in Section 5.4.2 and the discussion of Section 5.5.2 show that both models yield similar results. The main (quantitative) differences are caused by the boundary conditions at the tidal inlet which could not be made equivalent. It is concluded that the rigid-lid approximation, as used in the idealized model, is valid.

The second objective of this study was to investigate the sensitivity of the results to higher harmonics of the tide, quadratic bottom shear-stress and to waves of which the properties are obtained with a realistic wave model. The results presented in Section 5.4.4 showed that the influence of internally generated higher harmonics is small. However, externally prescribed higher harmonics can have a large influence on the calculated morphodynamic equilibria. In the case that the currents in the inlet were ebb-dominated the bottom patterns were more pronounced. In the case of flood-dominated currents the ebb-tidal delta can be absent. In Section 5.4.5 it was shown that using a quadratic bottom shear-stress formulation instead of a linearized one results in a larger ebb-tidal delta. Furthermore, the cross-shore length of the ebb-dominated channel was larger and a first indication was seen that the ebb-tidal delta folds around the ebb-dominated channel. In addition, the modeled ESV was closer to observed values than when a linearized bottom shear-stress formulation is used. The analysis presented in Section 5.6 showed that the linearized bottom shear stress formulation as used in the idealized model overestimates the dissipation of momentum due to friction. It was concluded that the linearized stress formulation can only be used if at each position in the domain a linearization procedure is applied, which will result a spatially dependent magnitude of  $U_t$ . The results presented in Section 5.2.2 showed that already for small waves processes like refraction become noticeable. From these results it is expected that for realistic scenarios a state-of-the-art wave model should be used, instead of the highly idealized version that is used in the idealized model.

Although the numerical model uses a realistic description for the waves and currents, other aspects of the model are still idealized. In the inlet the velocity was prescribed. This velocity did not change when the bathymetry changed. Hence, the interaction between the inner basin and the ebb-tidal delta is not modeled. A more realistic set-up can be

achieved when a strait connects the sea with a tidal basin. In that case the sea and basin can dynamically interact and the velocity in the strait would follow from physical laws.

Another important simplification of the model is the use of a spatially independent  $U$  and  $U_t$ . Therefore,  $\vec{q}_{\text{bot}}$  only has spatial variations due to spatial variations in  $H'$ . The analysis of the results obtained with the quadratic bottom shear-stress formulation show that a constant  $U_t$  is not a very good approximation. It would be better to use a spatially dependent  $U_t$ . If also a spatially dependent  $U$  is used, this will strongly affect the calculation of  $\vec{q}_{\text{bot}}$  and the calculation of the equilibria, as was already shown in Chapter 3. Moreover, in this study only one (bedload) sediment transport formulation has been studied. There are many other formulations for the sediment transport, which also include suspended-load sediment transport formulations. These need to be considered as well.

The last aspect that has to be mentioned here is that the processes that lead to asymmetry have been excluded. A thorough study of these processes is needed because many observed deltas are asymmetric. The morphodynamic model discussed in this chapter leaves many possibilities to systematically study the mechanisms that lead to asymmetry of ebb-tidal deltas. Moreover, the numerical model can in principle also be used to calculate morphodynamic equilibria for other areas such as tidal basins.

# Chapter 6

## Discussion and conclusions

This study focused on the dynamics of tide-dominated barrier coasts and ebb-tidal deltas. The main aim was to gain more fundamental physical understanding of their dynamics. Three questions were formulated in Chapter 1, which formed the starting point of subsequent research.

1. Which physical mechanisms control the length scale of barrier islands?
2. Which physical processes are essential to model the symmetric ebb-tidal delta as morphodynamic equilibrium?
3. Which physical processes cause the ebb-tidal delta to be asymmetric?

The detailed results and the discussions can be found in Chapter 2 to 5. In this chapter the main findings are summarized and put into perspective. This chapter ends with suggestions for further research.

### 6.1 Length scale of barrier islands

It was found by *FitzGerald* (1996) and *Oost and de Boer* (1994) that the length scale of barrier islands in both the Georgia Bight (USA) and in the Wadden Sea is inversely related to the tidal range and linearly related to the wave influence. In Chapter 1 and 2 it was noted that a process-based physical explanation for this behavior is missing. Previous process-based modeling studies mainly focused on the influence of waves on the position of the coastline (*Komar*, 1998; *Ashton et al.*, 2001; *Falqués and Calvete*, 2005). The influence of tidal currents on the stability of the coastline was never studied.

Therefore, in Chapter 2 a 1-line model was developed that describes the feedback between the position of the coastline and both tidal currents and waves. The hypothesis was that an initially straight coastline can become unstable for perturbations with a length scale between zero and tens of kilometers. At locations where the coastline has retreated, the coast is more vulnerable to breaching during storms. These are locations where inlets may potentially form.

The parameter setting was chosen such that it resembled the conditions as observed along the Dutch and German Wadden coast. In the case that only the influence of the net sediment flux due to the joint action of tidal currents and waves on the evolution of the

coastline was taken into account, it was found that the coastline is stable for perturbations with wavelengths larger than 8 km. For wavelengths smaller than 8 km the coastline perturbations grow. Perturbations with the smallest wavelengths grow fastest. No fastest growing mode (FGM) was obtained. The typical time scale on which perturbations grow is  $\sim 100$  years. The perturbations migrate with a typical phase speed of  $\sim 10$  m/year to the east.

The mechanism that causes the growth and decay of the coastline perturbations was explained in terms of vorticity dynamics following the method of *Zimmerman* (1981). The alongshore gradient of the alongshore component of the vorticity flux causes residual circulation cells that transport the sediment from the locations where the coastline is retreated to the locations where the coastline is protruded. This enhances the initial perturbation of the coastline. In contrast, the cross-shore gradient of the cross-shore component of the vorticity flux results in residual circulation cells that cause a decay of the coastline perturbation. The growth or decay of the coastline perturbations depends on which of the two effects dominates.

Adding the sediment flux that is solely due to waves by using the formulation of *Komar* (1998), resulted in the existence of a FGM. Varying the values of the model parameters between their extremes observed along the Dutch and German coast revealed preferred wavelengths between 0 and 15 kilometers. The model predicts that for increasing magnitude of the shore-parallel tidal currents and constant wave influence, the length scale of the barrier islands decreases. This has been tested by using the results of a large-scale model that was designed to predict the depth-averaged tidal currents and sea surface elevations in the region of the southern North Sea, the so-called ZUNO model (*Roelwink et al.*, 2001). The model results show that the long axis of the  $M_2$  tidal current ellipse is increasing from the Island of Texel towards the German Bight. Hence, the length of the barrier islands is also inversely related to the magnitude of the alongshore tidal currents, as predicted by the model. The model results also predict that for larger wave influence the length scales of the barrier islands increase. The waves cause a diffusion of the coastline perturbations. This effect is largest for smallest wavelengths. Increasing the wave influence results in an increase of the diffusivity of the coast. Consequently, the FGM is obtained for larger wavelengths.

Model results agree well with field data, but not all observed characteristics are reproduced with the model. Observations show that barrier islands can have lengths up to tens of kilometers. The maximum wavelength of the fastest growing mode obtained with the model is 14 km.

## 6.2 Symmetric tide-dominated ebb-tidal deltas

Data indicate that the large-scale patterns of tide-dominated ebb-tidal deltas are quasi steady. The ebb-tidal delta is found at the end of an ebb-dominated channel. The delta is flanked by two flood-dominated channels (*Hayes*, 1975). In addition, there is a relation between the volume of sand stored in the ebb-tidal delta (ESV) and the total amount of water that enters and leaves the tidal basin during one tidal cycle, the tidal prism TP (*Walton and Adams*, 1976). Some tide-dominated deltas are (almost) symmetric



with respect to the mid-axis through the inlet. These deltas occur in coastal areas where shore-parallel currents are small compared to cross-shore tidal currents. Typical examples can be found along the east US coast. The main question that was addressed in Chapter 3 and 5 was which physical mechanisms cause and maintain the symmetric ebb-tidal delta in morphodynamic equilibrium (no evolving bathymetry). It has been noted by *Stommel and Farmer* (1952) that the flow during ebb has a jet-like structure while during flood there is radial inflow. In the conceptual model of *Oertel* (1972) it is argued that the jet during the ebb-phase removes the sand from the inlet and deposits it further seaward. This results in the formation of a deep ebb-dominated channel and an ebb-tidal delta. The process-based numerical modeling study of *van Leeuwen et al.* (2003) suggested that the ebb-tidal delta might be a morphodynamic equilibrium, although true equilibrium was never reached in their simulation.

In Chapter 3 an idealized process-based morphodynamic model was developed and analyzed. It uses simplified formulations for currents, waves, sediment transport and considers the dynamics for an idealized geometry. The main assumption of the model was that the symmetric ebb-tidal delta can be modeled as a 2D morphodynamic equilibrium. Therefore, instead of performing time integrations, a continuation technique was applied to calculate the morphodynamic equilibrium solutions.

The parameter setting was chosen such that it represented the conditions as observed along the east US coast. The modeled current patterns consist of a jet-like pattern during ebb and a radial inflow during flood. This is linked to the presence of two residual circulation cells. This is consistent with field observations. The equilibrium bathymetry consists of an ebb-dominated channel in the center of the inlet. At the end of this channel the ebb-tidal delta is found. This delta is flanked by two flood-dominated channels. This is consistent with the conceptual picture of the ebb-tidal delta presented by *Hayes* (1975). Furthermore, the observed almost linear relation between ESV and TP is recovered with the model.

An analysis of the results showed that in equilibrium the ebb-tidal delta and the channels are maintained due to a balance between the net (i.e., tidally averaged) convergence of sediment transport induced by the currents and waves and the net sediment transport induced by the bed slopes. The ebb-dominated channel is formed by the sediment transport due to currents and waves which is not in the direction of the residual currents. The ebb-tidal delta is mainly caused by the stirring of sediment by waves and tides and the transport by the residual currents.

However, differences between model results and observations were noticed as well. First, the cross-shore length of the ebb-dominated channel obtained with the model is considerably smaller than observed ones. Second, the model does not recover the folding of the ebb-tidal delta around the ebb-dominated channel. The ebb-dominated channel does not protrude into the ebb-tidal delta, which is commonly observed. Third, the modeled sand volumes are a factor  $\sim 5$  smaller than observed ones.

Therefore, in Chapter 5 it was studied whether these discrepancies between observations and model results are caused by the formulation of the waves and currents used in the idealized model. Furthermore, new aspects were studied such as the net transport of sediment due to tidal asymmetry (joint action of  $M_2$  tidal currents and its overtides), the use of a quadratic bottom stress formulation and a more realistic wave model (in-

cluding wave refraction). Experiments were performed with a numerical model based on the Delft3D software. This model was adapted such that it allowed for the calculation of morphodynamic equilibria.

In a first series of experiments the set-up of the numerical model was such that it is as close as possible to the idealized model. The idealized model and numerical model give qualitatively similar results. Main (quantitative) differences are due to the boundary condition in the tidal inlet, which could not be made equivalent. From these experiments it was concluded that the rigid lid approximation, as was applied in the idealized model, is valid. After these experiments the sensitivity of the results to extensions of the model was studied. The results show that internally generated higher harmonics are not important and only lead to quantitative (order of 10%) differences in magnitude of the bottom patterns. However, externally prescribed higher harmonics at the tidal inlet can lead to different bottom patterns. Prescribed ebb-dominated currents lead to more pronounced bottom patterns while flood-dominated currents prevent the presence of an ebb-tidal delta. Experiments performed with a quadratic bottom stress formulation showed that the linearized bottom stress formulation, as was used in the idealized model, leads to an overestimation of the dissipation of momentum in the entire domain. Therefore, the modeled residual currents are too small. Furthermore, using the quadratic bottom stress formulation results in a first indication that the ebb-tidal delta folds around the ebb-dominated channel and that this channel becomes more elongated in the cross-shore direction. In addition, the modeled sand volumes are considerably closer to the observed ones if a quadratic bottom stress formulation is used instead of linearized version. From the results obtained with the quadratic bottom stress formulation it was concluded that a bed shear-stress formulation can be used which is linear in the current, but in that case a spatially varying friction coefficient should be used (instead of the constant friction coefficient that was used in the idealized model). The use of the realistic wave model yields that already for small waves and a small delta the refraction of the waves around the delta becomes noticeable. This effect can be important if larger waves are modeled. The presence of waves causes a larger delta.

Still, several features of observed ebb-tidal deltas are not recovered with the numerical model. First, the seaward extent of the ebb-dominated channel is still smaller than those of observed ebb-dominated channels. Second, field data suggest that larger wave influence results in a smaller sand volume of the ebb-tidal delta. The model predicts that larger wave influence results in a larger sand volume of the delta.

### 6.3 Asymmetric tide-dominated ebb-tidal deltas

In Chapter 3 and 5 the focus was on the dynamics of symmetric tide-dominated ebb-tidal deltas. However, observations show that many tide-dominated ebb-tidal deltas are asymmetric with respect to reflection about the mid-axis through the inlet. Typical examples are found along the Dutch and German Wadden coast (*Ehlers, 1988; Sha and van den Berg, 1993*). In this region the strength of the shore-parallel tidal currents is of the same order of magnitude as the cross-shore tidal currents. The ebb-dominated channels have an orientation with respect to the mid-axis through the tidal inlet. Some

channels are oriented to the left (Dutch Wadden Sea) and others to the right (German Wadden Sea). The main objective of Chapter 4 was therefore to study which physical mechanisms are responsible for the asymmetry properties of ebb-tidal deltas.

In previous studies two important agents were identified that render deltas asymmetric. Processes related to waves cause the ebb-dominated channel to be oriented with the direction of the wave-driven currents (*Oertel, 1975; FitzGerald, 1996*). Processes related to the presence of strong shore-parallel tidal currents cause the ebb-dominated channel to be oriented to the left (*Sha, 1989a*). However, the explanations rely on the use of conceptual models. So far, no process-based modeling studies were able to reproduce asymmetric ebb-tidal deltas as morphodynamic equilibrium solutions.

Therefore, in Chapter 4 the idealized model of Chapter 3 was generalized to the case that shore-parallel currents are also important. Furthermore, the effects of the Coriolis force and of large-scale residual currents at sea were included. The set-up of the model was such that it represented the situation as observed along the Dutch and German Wadden coast. The results show that the Coriolis force causes only a weak asymmetry of the ebb-tidal delta. An ebb-tidal delta located on the Northern Hemisphere will have its center of mass slightly shifted to the right (when viewing along the mid-axis of the inlet in the seaward direction). The area with ebb-dominated currents is also located at the right-hand side of the mid-axis of the inlet. The ebb-tidal delta is called right-oriented. An ebb-tidal delta located at the Southern Hemisphere will be left-oriented. The influence of the shore-parallel tidal currents on the asymmetry of the delta is much larger. In a first experiment the phase difference between the shore-parallel and cross-shore tidal currents was approximately zero. The modeled currents on the left-hand side of the inlet are ebb-dominated and are bidirectional. The tidal currents at the right-hand side are weaker, more rotary and are flood-dominated. This is consistent with observations (*Sha, 1989b*). At the end of the area with ebb-dominated currents the ebb-tidal delta is located. However, no ebb-dominated channel is modeled. Changing the phase difference between the tidal currents through the inlet and the shore-parallel currents such that the tidal currents through the straight are significantly lagging the shore-parallel currents (around 90 degrees), results in a change of the orientation of the delta. The area with ebb-dominated currents is now located at the right-hand side of the mid-axis of the inlet and the delta is right-oriented. Increasing the width of the inlet also results in a change of the orientation of the delta. Broader inlets have a stronger tendency to have ebb-dominated currents which are oriented to the right. Lastly, in Chapter 4 the influence of large-scale shore-parallel residual currents at sea on the asymmetry properties of the delta was studied. In the case of residual currents from the left-hand side of the tidal inlet to the right-hand side, the area with ebb-dominated currents is located at the right-hand side of the mid-axis of the inlet. The delta is again located at the right-hand side and no ebb-dominated channel is modeled. Changing the direction of the currents leads to a change in the orientation of the delta from right-oriented to left-oriented.

The modeled hydrodynamics compare well with observations. However, the modeled equilibrium bottom patterns differ in several aspects from observed patterns. The modeled ebb-tidal delta is always located at the seaward end of the area with ebb-dominated currents. This is consistent with the conceptual picture of *Hayes (1975)*. However, no ebb-dominated channel is modeled. The only channel that is modeled is located at the side

with flood-dominated currents. In Chapter 4 it was suggested that these discrepancies between observed bottom patterns and modeled ones are caused by the absence of a shallow backbarrier basin, by the absence of wind or wave influence, by the absence of modeling of 3D processes or by the absence of settling lag effects in the specific choice of the sediment transport formulation.

## 6.4 Suggestions for further research

In this section some suggestions for further research with respect to the modeling of the dynamics of barrier coasts and of ebb-tidal deltas are made. This is split up into suggestions concerning the physical processes that were included/excluded in the models, into suggestions with respect to the methodological approaches that have been used to answer the research questions and into suggestions that concern the numerical methods that were used.

### 6.4.1 Modeling the dynamics of barrier coasts

In the 1-line model that was developed in Chapter 2 many assumptions were made. It was assumed that the nearshore zone has a constant width, that the diffusive terms in the momentum balances can be ignored, that a linearized bottom stress formulation can be used and that the sediment transport due to the tides can be approximated by a formulation which only includes the effect of stirring of sediment by waves and transport by the residual currents. The sensitivity of the results to these processes can be studied by using a complex process-based model.

Concerning the methods that have been used, it should be noted that only the evolution of small perturbations were studied in Chapter 2. No nonlinear analysis has been performed, so nothing can be said about the temporal evolution of the coastline perturbations. However, performing this nonlinear evolution is not straightforward. For instance, the evolution equation that was derived, Equation (2.27), should be revised, because it is explicitly based on the assumption that perturbations are small. A last aspect that should be mentioned here, is that the evolution of the coastline is described by a 1-line model while in reality it is the result of complex three-dimensional processes. It would be interesting to extend the model formulations to 2D or even 3D formulations.

Concerning the numerical method it should be noted that the 1-line model of Chapter 2 only includes the effect of residual and  $M_2$  tidal currents. Higher harmonics of the tide were not taken into account. The Fourier expansions of the variables were truncated after the  $M_2$  component. However, the comparison of the results described in Chapter 3 and 5 showed that internally generated higher harmonics of the tide only lead to order 10% changes. Therefore, it is expected that using the full Fourier expansions of the variables will not lead to qualitatively different results.

### 6.4.2 Modeling the dynamics of ebb-tidal deltas

A main shortcoming of the models that were used in Chapter 3, 4 and 5 was that the tidal currents through the tidal inlet had to be prescribed. This aspect can be improved

by adding a tidal basin to the model geometry. This tidal basin is connected to the sea by a strait. A big advantage is that in that case the tidal currents in the inlet follow from physical laws and do not have to be imposed anymore. However, this approach is not straightforward. One has to take into account that the sediment in the area of the ebb-tidal delta is much coarser than the sediment in the tidal basin. This would imply that one has to calculate with non-uniform sediment distributions. Furthermore, considering a geometry that includes the coastal sea, the strait and the tidal basin implies that the morphodynamic equilibrium of the inner basin and the strait has to be calculated as well. This might cause problems if the typical time-scales in the tidal basin are much smaller than the typical time scale of the ebb-tidal delta. Other problems might occur if bifurcations in parameter space exist related to process that are only important in the tidal basin (they exist, see *Schuttelaars and de Swart (2000)*; *Schramkowski et al. (2004)*) or in the region of the ebb-tidal delta. Nevertheless, it is tempting to connect the tidal basin with the ebb-tidal delta, since both the models that describe the dynamics of the tidal basin (*Schuttelaars and de Swart, 2000*; *Hibma et al., 2003*) and the models described in this thesis suffer from the same problem: the boundary conditions in the tidal inlet. Other improvements of the physics can be achieved by including 3D effects such as curvature and the veering of the velocity due to Ekman processes. Furthermore, the imposed sediment transport formulation can be improved. In Chapter 4 no ebb-dominated channel was modeled. This might be caused by the fact that only bedload sediment transport is taken into account. No suspended load formulation has been studied. *Murray (2004)* showed that neglecting such effects prevented the formation of channels in his morphodynamic model of the nearshore zone. The influence of different sediment transport formulations on the morphodynamic equilibria should be studied. Furthermore, no critical velocity for erosion was included. For coarse sediment this critical velocity can be in the order of  $0.2 - 0.3 \text{ ms}^{-1}$ . When the maximum tidal currents in the inlet are in the order of  $0.5 \text{ ms}^{-1}$  it might be very important to add this effect, especially in the case of asymmetric deltas. For a hydrodynamic setting that is typical for the Dutch Wadden Sea it was found that the tidal currents on the left-hand side of the inlet are much stronger than the tidal currents on the right-hand side.

From a methodological point of view, it should be noted that, although morphodynamic equilibria have been calculated, the question whether these equilibria are stable with respect to small 2D perturbations of the bed, has not been studied. In addition, if the maximum tidal current magnitude exceeds a critical value, no equilibria could be found. This might be caused by the way the continuation method is applied. At present, after calculating a morphodynamic equilibrium a parameter is changed with certain fixed magnitude. If a fold bifurcation exists, it might be that the change in the parameter is too large and the old equilibrium is not a good estimate for the morphodynamic equilibrium for the new parameter. An arc-length method (cf. *Seydel (1994)*) might give better results since with this method the magnitude of the parameter change is calculated. The possible existence of bifurcations sets another motivation to perform a 2D stability analysis of the 2D morphodynamic equilibria. The existence of bifurcations is related to the eigenvalues that follow from the stability analysis. A first set-up of a model that calculates the eigenvalues and eigenvectors of the generalized eigenvalue problem that follows from the 2D stability analysis has been developed, but no satisfactory results were obtained due to

numerical problems (see next paragraph). Another possible way to calculate the stability of the ebb-tidal deltas would be to perturb the morphodynamic equilibrium and calculate the initial erosion deposition rate. With various techniques an estimation of the eigenfunction and growth rate with largest real part can be obtained (*Deigaard et al.*, 1999; *Klein and Schuttelaars*, 2005). A last method to gain insight in the stability characteristics of the modeled ebb-tidal deltas that is mentioned here is to perform time-integrations. The calculated equilibria are never in "true" equilibrium. Instead, a condition is applied that states that if the relative change of the new bottom is less than 1% with respect to the old estimate of the equilibrium bottom, equilibrium is reached. If the evolution of the ebb-tidal delta is immediately slowing down the equilibrium is stable. If the evolution of the delta is increasing when time evolves, the equilibrium is unstable.

The fact that no satisfactory results were obtained for the 2D stability analysis is caused by numerical problems. In the models of Chapter 3 and 4 a pseudospectral method is used. The stability of the morphodynamic equilibria is described by a generalized eigenvalue problem. The dimensions of the matrices are large and the condition number is very large. The numerical approximations are inaccurate and it is not possible to calculate the eigenvalues and eigenvectors. It is probably better to use a different numerical schematization of the spatial part of the variables. For instance, finite elements or finite differences can be used. This results in matrices with banded structures and many mathematical techniques are known which can solve the resulting generalized eigenvalue problem.

# Bibliography

- Ashton, A., A. B. Murray, and O. Arnault (2001), Formation of coastline features by large-scale instabilities induced by high-angle waves, *Nature*, *414*, 296–300.
- Ashton, A., A. B. Murray, and G. Ruessink (2003), Initial tests of a possible explanation for alongshore sandwaves along the Dutch coast, in *Proceedings 3rd IAHR symposium*, edited by T. Yanagi, pp. 265–285, Terra Scientific Publishing Company, Tokyo.
- Awaji, T., N. Imasato, and H. Kunishi (1980), Tidal exchange through a strait: A numerical experiment using a simple model basin, *Journal of Physical Oceanography*, *10*, 1499–1508.
- Bagnold, R. A. (1966), An approach to the sediment transport problem from general physics, *Geological Survey Professional Papers*, *422-I*.
- Bailard, J. (1981), An energetics total load sediment transport model for a plane sloping beach, *Journal of Geophysical Research C*, *86*, 10,938–10,954.
- Blanton, B. O., F. E. Werner, H. E. Seim, R. A. Luettich, D. R. Lynch, K. W. Smith, G. Voulgaris, F. M. Bingham, and F. Way (2004), Barotropic tides in the South Atlantic Bight, *Journal of Geophysical Research*, *109*, doi:10.1029/2004JC002455.
- Booij, N., R. C. Ris, and L. H. Holthuijsen (1999), A third-generation wave model for coastal regions 1. Model description and validation, *Journal of Geophysical Research C*, *104*, 7649–7666.
- Boyd, J. P. (2001), *Chebyshev and Fourier spectral methods*, Dover, New York, 688 pp.
- Calvete, D., M. Walgreen, H. E. de Swart, and A. Falqués (2001), A model for sand ridges on the shelf: effect of tidal and steady currents, *Journal of Geophysical Research C*, *106*, 9311–9338.
- Cayocca, F. (2001), Long-term morphological modelling of a tidal inlet: the Arcachon Basin, France, *Coastal Engineering*, *42*, 115–142.
- Chadwick, D. B., and J. L. Largier (1999), Tidal exchange at the bay-ocean boundary, *Journal of Geophysical Research C*, *104*, 29,901–29,924.
- Davis, R. A. (1997), Regional coastal morphodynamics along the United States Gulf of Mexico, *Journal of Coastal Research*, *13*, 594–604.

- Davis, R. A., and D. M. FitzGerald (2004), *Beaches and coasts*, Blackwell, 419 pp.
- de Vriend, H. J. (1996), Mathematical modelling of meso-tidal barrier island coasts. part I: Empirical and Semi-Empirical Models, in *Advances in coastal and ocean engineering*, edited by P. L. F. Liu, pp. 115–149, World Scientific.
- de Vriend, H. J., and J. S. Ribberink (1996), Mathematical modelling of meso-tidal barrier island coasts. part II: Process-Based Simulation Models, in *Advances in coastal and ocean engineering*, edited by P. L. F. Liu, pp. 151–197, World Scientific.
- Deigaard, R., N. Drønen, J. Fredsøe, J. J. Jensen, and M. P. Jørgensen (1999), A morphological stability analysis for a long straight barred coast, *Coastal Engineering*, *36*, 171–195.
- Ehlers, J. (1988), *The morphodynamics of the Wadden Sea*, Balkema, Rotterdam, 397pp.
- Engelund, F., and E. Hansen (1967), A monograph on sediment transport in alluvial streams, *Tech. rep.*, Technical Press, Copenhagen.
- Falqués, A. (2003), On the diffusivity in coastline physics, *Geophysical Research Letters*, *30*(21), 2119, doi:10.1029/2003GL017760.
- Falqués, A. (2005), Wave driven alongshore sediment transport and stability of the Dutch coastline, *Coastal Engineering*, *in press*, doi:10.1016/j.coastaleng.2005.10.012.
- Falqués, A., and D. Calvete (2005), Large scale dynamics of sandy coastlines: Diffusivity and instability, *Journal of Geophysical Research*, *110*, doi:10.1029/2004JC002587.
- Falqués, A., A. Montoto, and V. Iranzo (1996), Bed-flow instability of the longshore current, *Continental Shelf Research*, *16*, 1927–1964.
- FitzGerald, D. M. (1996), Geomorphic variability and morphologic and sedimentologic controls on tidal inlets, *Journal of Coastal Research*, *23*, 47–71.
- FitzGerald, D. M., and D. Nummedal (1983), Responce characteristics of an ebb-dominated tidal inlet channel, *Journal of Sedimentary Petrology*, *53*, 833–845.
- Fredsøe, J. (1984), Turbulent boundary layer in wave-current interaction, *Journal of Hydraulic Engineering ASCE.*, *110*, 1103–1120.
- Gibeaut, J. C., and R. A. Davis Jr. (1993), Statistical geomorphic classification of ebb-tidal deltas along the west-central Florida coast, *Journal of Coastal Research*, *18*, 165–184.
- Glaesser, D. J. (1978), Global distribution of barrier islands in terms of tectonic setting, *Journal of Geology*, *86*, 283–297.
- Grasmeijer, B. T., and M. G. Kleinans (2004), Observed and predicted bed forms and their effect on suspended sand concentrations, *Coastal Engineering*, *51*, 351–371.



- Hasselmann, K., T. P. Barnett, E. Bouws, H. Carlson, D. E. Cartwright, K. Enke, J. A. Ewing, H. Gienapp, D. E. H. P. Kruseman, A. Meerburg, P. M. D. J. Olbers, K. Richter, W. Sell, and H. Walden (1973), Measurements of wind-wave growth and swell decay during the Joint North Sea Wave Project, *Deutsche Hydrographische Zeitschrift*, 12, 95 pp.
- Hayes, M. O. (1975), Morphology of sand accumulations in estuaries, in *Estuarine Research*, vol.2, edited by L. E. Cronin, pp. 3–22, Academic Press, New York.
- Hench, J. L., and A. Luettich (2003), Transient tidal circulation and momentum balances at a shallow inlet, *Journal of Physical Oceanography*, 33, 913–932.
- Hibma, A., H. M. Schuttelaars, and Z. B. Wang (2003), Comparison of longitudinal equilibrium profiles of estuaries in idealized and process-based model, *Ocean Dynamics*, 53, 252–269.
- Hicks, M. D., T. M. Hume, A. Swales, and M. O. Green (1999), Magnitudes, spatial extent, time scales and causes of shoreline changes adjacent to an ebb-tidal delta, Katikati Inlet, New Zealand, *Journal of Coastal Research*, 15, 220–240.
- Holthuijsen, L. H., N. Booij, and T. H. C. Herbers (1989), A prediction model for stationary, short crested waves in shallow water with ambient currents, *Coastal Engineering*, 13, 23–54.
- Hulscher, S. J. M. H., H. E. De Swart, and H. J. De Vriend (1993), The generation of offshore tidal sand banks and sand waves, *Continental Shelf Research*, 13(11), 1183–1204.
- Huthnance, J. M. (1982), On one mechanism forming linear sand banks, *Estuarine, Coastal and Shelf Science*, 14, 79–99.
- Israel, C., and D. W. Dunsbergen (1999), Cyclic morphological evolution of the Ameland Inlet., in *Proceedings of the IAHR*, edited by G. Seminara, pp. 151–197, World Scientific.
- Klein, M. D., and H. M. Schuttelaars (2005), Morphodynamic instabilities of planar beaches: Sensitivity to parameter values and process formulations, *Journal of Geophysical Research F*, 111, doi:10.1029/2004JF000213.
- Komar, P. D. (1998), *Beach processes and sedimentation*, Prentice Hall, Upper Saddle River, 544 pp.
- Lorentz, H. A. (1922), Ein Rechnungsansatz für den Widerstand bei Flüssigkeitsschwindungen, *De Ingenieur*, 37, 695.
- Luck, G. (1975), Der Einfluss der Schutzwerke der Ostfriesischen Inseln auf die morphologischen Vorgänge im Bereich der Seegaten und ihrer Einzugsgebiete, *Tech. Rep. Heft 47*, Technischen Univerisät Braunschweig.
- Manneville, P. (1990), *Dissipative structures and weak turbulence*, Academic Press, Boston, 485pp.

- Murray, A. B. (2004), Rip channel development on nonbarred beaches: The importance of a lag in suspended-sediment transport, *Journal of Geophysical Research C*, 109, doi: 10.1029/2002JC001581.
- Oertel, G. F. (1972), Sediment transport on estuary entrance shoals and the formation of swash planforms, *Sedimentary Petrology*, 42, 857–863.
- Oertel, G. F. (1975), Ebb-tidal deltas of Georgia estuaries, in *Estuarine Research*, edited by L. Cronin, pp. 267–276, Academic Press, New York.
- Oertel, G. F. (1988), Processes of sediment exchange between tidal inlets, ebb deltas and barrier islands., in *Hydrodynamics and sediment dynamics of tidal inlet, cecture cotes on coastal and estuarine studies 29*, edited by D. Aubray and L. Weishar, pp. 297–318.
- Oost, A. P., and P. L. de Boer (1994), Sedimentology and development of barrier islands, ebb-tidal deltas, inlets and back-barrier areas of the Dutch Wadden Sea, *Senckenbergiana Maritima*, 24, 65–115.
- Pelnard-Considère, R. (1956), Essai de théorie de l'évolution des formes de rivages en plages de sable et de galets, in *4th Journées de l'Hydraulique, Les Energies de la Mer*, pp. 289–298, Soc. de Hydrotech. de France, Paris.
- Ranasinghe, R., and C. Pattiaratchi (2003), The seasonal closure of tidal inlets: causes and effects, *Coastal Engineering Journal*, 45, 601–627.
- Ridderinkhof, H. (1989), Tidal and residual flows in the Western Dutch Wadden Sea, iii: Vorticity balances, *Netherlands Journal of Sea Research*, 24, 9–26.
- Roelvink, J. A., and G. K. M. F. van Banning (1994), Design and development of DELFT3D and application to coastal morphodynamics, in *Proceedings of hydroinformatics conference*, edited by Babovic and Maksimovic, pp. 451–456, Balkema, Rotterdam.
- Roelvink, J. A., T. van der Kaaij, and B. G. Ruessink (2001), Calibration and verification of large-scale 2d/3d flow models phase 1. onl coast and sea studies, project 2: Hydrodynamics and mophology., *Tech. Rep. Z3029.10. 131 pp.*, WL—Delft Hydraulics.
- Roos, P. C., S. M. J. H. Hulscher, M. A. F. Knaapen, and R. M. J. van Damme (2004), The cross-sectional shape of tidal sandbanks: Modeling and observations, *Journal of Geophysical Research F*, 109, doi:10.1029/2003JF000070.
- Ruessink, B., and M. C. L. Jeuken (2002), Dunefoot dynamics along the Dutch coast, *Earth Surface Processes and Landforms*, 27, 1043–1056.
- Sanders, J. A., and F. Verhulst (1985), *Averaging methods in nonlinear dynamical systems*, Springer-Verlag, New York.
- Schramkowski, G. P., H. M. Schuttelaars, and H. E. de Swart (2004), Non-linear channel-shoal dynamics in long tidal embayments, *Ocean Dynamics*, 54, 399–407, doi: 10.1007/s10236-003-0063-6.

- Schuttelaars, H. M., and H. E. de Swart (2000), Multiple morphodynamic equilibria in tidal embayments, *Journal of Geophysical Research C*, 105, 24,105–24,118.
- Schuttelaars, H. M., J. G. Bonekamp, and J. A. Roelvink (2003), Role of tides in generating downdrift-oriented channels on ebb-tidal deltas, in *Proceedings of Coastal Sediments*, pp. 3–22, Academic Press, New York.
- Sekine, M., and G. Parker (1992), Bed-load transport on transverse slope. i, *Journal of Hydraulic Engineering*, 118, 513–535.
- Seydel, R. (1994), *Practical bifurcation and stability analysis: From equilibrium to chaos*, Springer, New York.
- Sha, L. P. (1989a), Variation in ebb-delta morphologies along the West and East Frisian Islands, The Netherlands and Germany, *Marine Geology*, 89, 11–28.
- Sha, L. P. (1989b), Cyclic morphological changes of the ebb-tidal delta, Texel Inlet, The Netherlands, *Geologie en Mijnbouw*, 68, 35–49.
- Sha, L. P. (1990), Sedimentological studies of the ebb-tidal deltas along the West Frisian Islands, the Netherlands, Ph.D. thesis, Geologica Ultraiectina, 64, Utrecht University.
- Sha, L. P., and J. H. van den Berg (1993), Variation in ebb-tidal delta geometry along the coast of the Netherlands and the German Bight, *Journal of Coastal Research*, 9, 730–746.
- Siegle, E., D. A. Huntley, and M. A. Davidson (2004), Physical controls on the dynamics of inlet sandbar systems, *Ocean Dynamics*, 54, 360–373, doi:10.1007/s10236-003-0062-7.
- Soulsby, R. L. (1997), *Dynamics of marine sands*, Thomas Telford, London, 249pp.
- Soulsby, R. L., L. Hamm, G. K. D. Myrhaug, R. R. Simons, and G. P. Thomas (1993), Wave-current interaction within and outside the bottom boundary layer, *Coastal Engineering*, 21, 41–69.
- Stelling, G. S., and I. I. Leendertse (1992), Approximation of convective processes by cyclic ADI methods, in *Proceedings Estuarine and Coastal Modelling*, edited by M. L. Spaulding, pp. 771–782, ASCE, Tampa, FL.
- Stommel, H., and H. G. Farmer (1952), On the nature of estuarine circulation, *Tech. Rep. 52-88*, WHOI.
- Struiksma, N., K. W. Olesen, and C. F. H. J. De Vriend (1985), Bed deformation in curved alluvial channels, *Journal of Hydraulic Research*, 23(1), 57–79.
- van de Kreeke, J., and K. Robaczewska (1993), Tide-induced residual transport of coarse sediment; application to the Ems Estuary, *Netherlands Journal of Sea Research*, 31(3), 209–220.

- van der Molen, J. (2000), A 2DH numerical model for tidally induced sand transport in the southern North Sea, in *Interactions between estuaries, coastal seas and shelf seas*, edited by T. Yanagi, pp. 265–285, Terra Scientific, Tokyo.
- van der Vegt, M., H. M. Schuttelaars, and H. de Swart (2005), Modeling of equilibrium tide-dominated ebb-tidal deltas, *Accepted for publication in Journal of Geophysical Research F*.
- van Leeuwen, S. M., and H. E. de Swart (2002), Intermediate modelling of tidal inlet systems: Spatial asymmetries in flow and mean sediment transport, *Continental Shelf Research*, 57, 899–907.
- van Leeuwen, S. M., M. van der Vegt, and H. E. de Swart (2003), Morphodynamics of ebb-tidal deltas: A model approach, *Estuarine, Coastal and Shelf Science*, 22, 1795–1810.
- Walton, T. (2002), Tidal velocity asymmetry at inlets, *Tech. Rep. CHETN-IV-47*, US Army Corps of Engineers.
- Walton, T. L., and W. D. Adams (1976), Capacity of inlet outer bars to store sand, in *Proceedings of the 15th ICCE*, pp. 1919–1938, ASCE, New York.
- Wang, Z. B. (1991), A morphodynamic model for a tidal inlet, in *Computer modelling in ocean engineering '91- Proceedings of the second international conference*, edited by A.S. Arcilla & others, pp. 235–245, Balkema, Rotterdam.
- Wang, Z. B., T. Louters, and H. J. de Vriend (1995), Morphodynamic modelling for a tidal inlet in the Wadden Sea, *Marine Geology*, 126, 289–300.
- Wells, M. G., and G. F. Van Heyst (2003), A model of tidal flushing of an estuary by dipole formation, *Dynamics of Atmospheres and Oceans*, 37, 223–244.
- Zimmerman, J. T. F. (1981), Dynamics, diffusion and geomorphological significance of tidal residual eddies, *Nature*, 290, 549–555.
- Zimmerman, J. T. F. (1986), The tidal whirlpool: A review of horizontal dispersion by tidal and residual currents, *Netherlands Journal of Sea Research*, 20, 133–154.
- Zimmerman, J. T. F. (1992), On the Lorentz linearization of a nonlinearly damped tidal Helmholtz oscillator, *Proceedings Koninklijke Nederlands Akademie van Wetenschappen*, pp. 127–145.

# Samenvatting

## Waddeneilanden

Langs de Nederlandse, Duitse en Deense kust ligt een lange reeks van eilanden, de zogenaamde Waddeneilanden (zie Figuur 1.6, Pag. 7). De ligging van de eilanden is niet willekeurig, maar het lijkt juist alsof de reeks eilanden een ritmisch patroon vertoont. De golflengte van dit ritmische patroon is niet constant. De eilanden Texel, Ameland en Terschelling zijn het langst, terwijl de lengte van de Waddeneilanden afneemt in de richting van Duitsland. In de Duitse Bocht zijn de eilanden zelfs afwezig. Voorbij de Duitse bocht verschijnen de eilanden weer en neemt de lengte langzamerhand weer toe. Waarnemingen suggereren dat de lengte van de Waddeneilanden omgekeerd evenredig is met de sterkte van het getij (verschil waterstand tussen eb en vloed). Bij Texel is het verschil in waterstand tussen eb en vloed het kleinst, terwijl deze maximaal is in de Duitse bocht.

Tussen twee Waddeneilanden ligt een zeegat dat de open zee met een half afgesloten bekken verbindt. Gedurende vloed wordt het bekken gevuld met water van zee dat via het zeegat naar binnen stroomt. Gedurende eb stroomt het water van het bekken naar zee en wordt het bekken gelegegd. Aan de zeewaartse (buiten) kant van het zeegat is in veel gevallen een gebied dat relatief ondiep is ten opzichte van de omgeving. Dit gebied wordt de buitendelta of eb-getijde delta genoemd. De buitendelta ligt aan het eind van een diepe geul die gekarakteriseerd wordt door ebgedomineerde stromingen (maximum stroomsnelheid tijdens eb is groter dan tijdens vloed). Aan beide zijkanten van de buitendelta liggen in veel gevallen twee vloedgedomineerde geulen. De maximum diepte van deze geulen is kleiner dan die van de ebgedomineerde geul.

Alhoewel de verschillende buitendelta's die gevonden worden langs de Waddeneilanden veel met elkaar gemeen hebben, zijn er ook onderlinge verschillen. Een belangrijk verschil tussen de verschillende delta's is de oriëntatie van de ebgedomineerde geul. Deze geul is bij de Nederlandse Waddeneilanden naar links georiënteerd (kijkend in zeewaartse richting) en bij de Duitse naar rechts (zie Figuur 4.1, pag. 75). Als de ebgedomineerde geul naar rechts wijst, is het meeste sediment van de buitendelta ook rechts van de middenas door het zeegat te vinden. De buitendelta noemen we in dit geval dan rechts georiënteerd.

## Oostkust van de Verenigde Staten

Langs de oostkust van de VS komt ook een reeks eilanden voor. De lengte van deze eilanden varieert van enkele tot vele tientallen kilometers. Net als bij de Waddeneilanden, is het verschil in waterstand tussen eb en vloed maximaal voor de kortste eilanden en minimaal voor de langste eilanden. Ook blijkt de golfvloed in de buurt van de langste eilanden maximaal te zijn en minimaal in de buurt van de kortste eilanden. Een twee overeenkomst tussen de oostkust van de VS en de Waddenkust is de aanwezigheid van

buitendelta's. Het grote verschil met die van langs de Waddenkust is dat in veel gevallen hier de ebgedomineerde geul een kustdwarse orientatie heeft en dus geen hoek heeft t.o.v. de middenas door het zeegat. In sommige gevallen is het sediment ook symmetrisch verdeeld t.o.v. de middenas door het zeegat. In dat specifieke geval is er sprake van een symmetrische buitendelta.

### **Bestaande kennis**

Er is nog geen fundamentele verklaring voor de waargenomen lengteschaal van eilanden. Er is gesuggereerd dat een groter verschil in waterstand tussen eb en vloed er voor zorgt dat gedurende vloed meer water het bekken in stroomt. Er zijn dan meer openingen nodig om de bekkens met water te vullen. Deze conceptuele verklaring is echter niet bevredigend. Zo heeft bijvoorbeeld het zeegat van Texel het grootste getijprisma (volume van het water dat gedurende vloed en eb het bekken in- en uitstroomt) terwijl de getijamplitude hier minimaal is. Bovendien wordt zand geërodeerd door schuifspanningen aan de bodem. Deze worden veroorzaakt door waterbewegingen in de buurt van de bodem. De waterbeweging zorgt ook voor het transport van het sediment van de ene plaats naar de andere. Convergenties en divergenties in het sedimenttransport zorgen voor een verandering van de bodem. Door terugkoppelingseffecten tussen waterbeweging, sedimenttransport en de bodemligging, kunnen ritmische bodemvormen ontstaan. Een fysische verklaring voor de lengte van eilanden dient expliciet danwel impliciet de stroomsnelheden aan de bodem in beschouwing te nemen. Wat dat betreft is er op dit moment nog geen bevredigende fysische verklaring voor de lengte van de eilanden in waddenkusten.

Over de waterbeweging in de buurt van buitendelta's is redelijk veel bekend. Tijdens eb stroomt het water uit het bekken naar zee. Het water stroomt vooral kustdwars en heeft slechts een kleine component in de kustlangse richting. Dit wordt de eb-jet genoemd. Tijdens vloed wordt het water als het ware het bekken ingezogen en stroomt het water van alle kanten het bekken in. Het water stroomt dan radiëel naar binnen.

Over het sedimenttransport en de uiteindelijke bodempatronen bestaat minder fundamentele kennis. Volgens conceptuele modellen wordt de symmetrische delta gevormd tijdens eb. Het sediment wordt dan van het zeegat in zeewaartse richting getransporteerd naar plaatsen waar de stromingen zwakker zijn. Tijdens vloed wordt een gedeelte van het sediment van de delta weer naar het zeegat getransporteerd, maar die hoeveelheid is kleiner dan de hoeveelheid sediment dat tijdens eb verplaatst is. Aangezien eb en vloed zich voortdurend herhalen, betekent dit dat er zich een steeds diepere geul vormt en er een delta ontstaat die steeds groter en ondieper wordt. Waarnemingen suggereren echter dat de buitendelta een morfodynamisch evenwicht is van het bekken-zee systeem. In een morfodynamisch evenwicht zijn de stromingen, het sedimenttransport en de bodem dusdanig dat er gemiddeld over meerdere getijperiodes geen verandering van de bodem is. Bovendien is het zandvolume van de buitendelta middels een machtsrelatie aan het getijprisma gerelateerd. Het conceptuele model biedt geen verklaring of en waarom er een eventueel morfodynamisch evenwicht bestaat. Bovendien verklaart het conceptuele model niet waarom langs de oostkust van de VS de buitendelta's in sommige gevallen symmetrisch zijn en de ebgedomineerde geul kustdwars georiënteerd zijn, terwijl langs de Nederlandse en Duitse kust de buitendelta's asymmetrisch zijn en de ebgedomineerde

geulen een duidelijke oriëntatie hebben.

### **Resultaten: Lengte van eilanden**

In hoofdstuk twee van dit proefschrift is onderzocht of er verklaring te vinden is voor de lengte van een eiland. Dit is gedaan middels een stabiliteitsanalyse. Met een stabiliteitsanalyse wordt de dynamica van kleine verstoringen van een evenwicht onderzocht. Als deze verstoringen groeien in de tijd, is het evenwicht instabiel. Als de verstoringen weer uitdempen, is het evenwicht stabiel. Er is onderzocht of een rechte, zandige kust stabiel is voor kleine golfvormige verstoringen van de positie van de kustlijn. De achterliggende aanname is dat op plaatsen waar de kust zich heeft teruggetrokken, de kust gedurende een storm makkelijker kan doorbreken en dat daar dan een zeegat ontstaat. Daar waar de kust is uitgebouwd zal zich een eiland vormen. Een verstoring met een golflengte die harder groeit dan verstoringen met een andere golflengte, is het meest effectief. Deze golflengte wordt de preferente lengteschaal genoemd. Bij een kust die zich net ontwikkelt van een rechte kustlijn naar een meanderende kust, zullen na verloop van tijd vooral de meanderingen met deze specifieke golflengte zichtbaar worden. Dit geeft de lengteschaal van de eilanden aan.

De waterbeweging in het model wordt veroorzaakt door zowel golven als getij. Sedi-ment wordt opgewoeld door de golven en vervolgens getransporteerd door getijstromen en golfgedreven stromingen. De centrale vraag in hoofdstuk twee is of de interactie tussen kustlangse getijstromen en golfgedreven stromingen met de positie van de kustlijn dusdanig is, dat er sediment getransporteerd wordt van de plek waar de kust is teruggetrokken naar nabijgelegen locaties waar de kust is uitgebouwd. Dit zorgt er voor dat een initiële verstoring van de kust groeit in de tijd. Het nieuwe aspect in dit onderzoek is dat ook de invloed van getijstromen op de stabiliteit van de kustlijn is meegenomen. Daarom zijn eerst experimenten gedaan waarin de golfinvloed dusdanig is dat zij noch voor groei noch voor demping van de verstoringen van de kustlijn zorgt. De resultaten laten zien dat voor parameterwaardes gebaseerd op de Nederlandse kust, verstoringen van de kustlijn met een golflengte kleiner dan 8 km, groeien. De verstoringen met de kleinste golflengte groeien het hardst. Verstoringen van de kustlijn groeien met een typische tijdschaal van 100 jaar. De verstoringen groeien niet alleen, maar migreren ook met een typische snelheid van 10 meter per jaar. In het geval van de Nederlandse kust betekent dit dat de Waddeneilanden naar het oosten bewegen. Voor verstoringen met golflengtes langer dan 8 km is de interactie tussen de verstoring van de kustlijn en de kustlangse getijstromen dusdanig dat de verstoringen uitdoven.

Hoewel golfvormige verstoringen van de kustlijn kunnen groeien, laten de resultaten zien dat wanneer het sediment alleen maar getransporteerd wordt door getijstromingen, geen verklaring gegeven kan worden voor de lengte van een eiland. Het model voorspelt geen golflengte die het hardst groeit. Er is geen mechanisme dat voor demping van de verstoringen met de kleinste lengteschaal zorgt.

Uit eerder onderzoek is bekend dat golfgedreven stromingen voor een demping van de verstoringen zorgen. Daarom is de gecombineerde invloed van golfgedreven stromingen en getijstromingen op de stabiliteit van de kustlijn onderzocht. Voor bepaalde combinaties van parameters is er dan een golflengte die het snelst groeit. De bijbehorende

lengteschaal varieert, voor verschillende parameter combinaties, tussen bijna nul en 15 kilometer. Gevoeligheidsstudies laten zien dat bij gelijkblijvende golfinvloed en toenemende magnitude van de kustlangse getijstromen de preferente lengteschaal afneemt. Bij constante magnitude van de kustlangse getijstromen en toenemende golfinvloed neemt de preferente lengteschaal juist toe. Deze theoretische voorspellingen zijn vergeleken met waarnemingen van lengtes van eilanden en de sterkte van de kustlangse getijstromen. Hieruit blijkt dat langs de Waddenkust niet alleen het verschil tussen eb en vloed toeneemt, maar ook de sterkte van de kustlangse getijstromingen. Tegelijkertijd neemt de lengte van de Waddeneilanden af. De modelresultaten zijn op dit punt in overeenstemming met de waarnemingen. Bovendien voorspellen de modelresultaten dat Terschelling op dit moment erg lang is in verhouding tot de hydrodynamische condities. De modelresultaten voorspellen dat wanneer de natuur op Terschelling de vrije hand zou krijgen dit eiland zou kunnen opsplitsen in meerdere kleine eilanden. De modelresultaten zijn ook in overeenstemming met waarnemingen langs de oostkust van de V.S.

### **Resultaten: Symmetrische buitendelta's**

In de rest van het proefschrift is de dynamica van buitendelta's bestudeerd. Een belangrijke vraag is of de buitendelta als een morfodynamisch evenwicht beschouwd kan worden. Om deze vraag te beantwoorden is gebruik gemaakt van een geïdealiseerd model. Zowel de geometrie als de beschrijving van de fysische processen zijn geïdealiseerd. De geometrie bestaat uit een zee die aan één kant begrensd wordt door een lange, gesloten kust. Deze kust is over een afstand van een paar kilometer open. Deze opening stelt het zeegat voor. De snelheden in het zeegat volgen niet uit fysische behoudswetten, maar worden als bekend verondersteld en als dusdanig voorgeschreven. Om symmetrische oplossingen te krijgen is aangenomen dat alle stromingen in het domein veroorzaakt worden door de stromingen door het zeegat, dat de invloed van de Coriolis-kracht op de dynamica verwaarloosbaar klein is, dat het uitstroomprofiel over het zeegat symmetrisch is t.o.v. de middenas door het zeegat en dat de golven loodrecht op kust invallen. Het sedimenttransport wordt met een zogenaamde bed-load formulering beschreven. Hierin zijn twee componenten van belang: een component van het sedimenttransport dat door stromingen alleen geïnduceerd wordt en een gedeelte dat veroorzaakt wordt door de aanwezigheid van bodemhellingen. Deze laatste component beschrijft in feite dat het makkelijker is om sediment met de helling mee te transporteren dan tegen de helling op. Convergenties en divergenties in het sedimenttransport zorgen voor een verandering van de bodem. In morfodynamisch evenwicht wordt de convergentie van het sedimenttransport door stromingen alleen, gecompenseerd door de divergentie van het sedimenttransport door de aanwezigheid van bodemhellingen.

Om evenwichtoplossingen van het stelsel vergelijkingen dat de dynamica beschrijft te vinden, is een zogenaamde continueringsmethode gebruikt. Uitgangspunt is dat er een bestaande evenwichtoplossing bekend is. In hoofdstuk drie beschrijft deze zogenaamde referentietoestand een kustlangs uniforme bodem. In de kustdwarse richting neemt de waterdiepte toe. Door het zeegat zijn geen stromingen. Vervolgens wordt een parameter een klein beetje veranderd, bijvoorbeeld de magnitude van de stromingen door het zeegat. Als de verandering van de parameter erg klein is, kan aangenomen worden dat het evenwicht



behorend bij de oude parameter waarde, een redelijke schatting is voor het evenwicht dat bij de nieuwe parameterwaarde hoort. Met behulp van de oude evenwichtsooplossing wordt de waterbeweging en het sedimenttransport t.g.v. de stromingen voor de nieuwe parameterwaarde berekend. Vervolgens wordt een nieuwe schatting voor de evenwichtsbodem berekend door de evenwichtsconditie toe te passen. Omdat de stromingen zelf weer afhangen van de waterdiepte, moet de waterbeweging, het sedimenttransport en de evenwichtsconditie opnieuw uitgerekend worden. Dit wordt herhaald totdat het verschil tussen twee opeenvolgende schattingen van de evenwichtsbodem kleiner is dan een vooraf bepaalde waarde. Vervolgens kan opnieuw een parameter veranderd worden.

De resultaten beschreven in hoofdstuk drie laten zien de buitendelta inderdaad beschouwd kan worden als de bodem behorend bij het morfodynamisch evenwicht door de interactie tussen de zee en het bekken. De berekende symmetrische bodempatronen lijken sterk op waargenomen bodempatronen van buitendelta's. Bovendien is de gemodelleerde relatie tussen het getijprima en het zandvolume in de delta ongeveer gelijk aan die van de waarnemingen. Ook de gemodelleerde waterbeweging komt goed overeen met waarnemingen. De modelresultaten zijn robuust. De gemodelleerde bodempatronen worden voor een grote reeks verschillende parameterwaardes gevonden. Zelfs het toevoegen van sterke golfinvloed heeft slechts een kleine invloed op de gemodelleerde bodempatronen: de delta is iets groter en de twee vloedgeulen iets dieper.

Er zijn echter ook verschillen tussen de gemodelleerde en waargenomen bodempatronen van buitendelta's. De gemodelleerde ebgeul is veel korter dan waargenomen. Bovendien lijkt het in waarnemingen haast alsof de delta om de ebgeul heengevouwen is. De ebgeul snijdt in de buitendelta. Ook dit wordt niet gereproduceerd met het model. Een ander belangrijk verschil is dat de gemodelleerde zandvolumes van de buitendelta ongeveer een factor vijf kleiner zijn dan de waargenomen zandvolumes. Waar worden deze verschillen door veroorzaakt? Zoals reeds gezegd, het geïdealiseerde model heeft zeer veel beperkingen en aannames. De gevoeligheid van de resultaten voor deze aannames kan niet met het geïdealiseerde model zelf onderzocht worden. Bovendien moet gecontroleerd worden of de aannames wel hout snijden. Hier moet een ander model voor ontwikkeld worden. Dit is gedaan in hoofdstuk vijf. De hydrodynamische modules van Delft3D (FLOW en SWAN) zijn gebruikt als state-of-the-art model om de waterbeweging te berekenen. Vervolgens is ongeveer dezelfde formulering van het sedimenttransport gebruikt (alleen wordt de invloed van hogere harmonische componenten van het getij op het residuele sedimenttransport in dit geval wel meegenomen) en dezelfde evenwichtsconditie toegepast. Ook in hoofdstuk vijf is een continueringstechniek gebruikt om evenwichtsbodems te berekenen.

Allereerst is geprobeerd om de configuratie en parameterwaardes van het numerieke model zo dicht mogelijk bij die van het geïdealiseerde model te kiezen. In dat geval lijken de resultaten van beide modellen erg op elkaar. De verschillen zijn vooral kwantitatief van aard en worden veroorzaakt door de randvoorwaarden in het zeegat die niet gelijk aan elkaar te krijgen zijn.

Gevoeligheidsexperimenten laten zien dat de resultaten niet al te gevoelig zijn voor de intern gegenereerde hogere harmonischen van het getij. Als echter een extern M4 getij wordt voorgeschreven hangen de gemodelleerde bodempatronen af van het relatieve faseverschil tussen het M4 en het M2 getij. In het geval dat het zeegat ebgedomineerd of neutraal is, zijn de bodempatronen hetzelfde, maar hebben een ze grotere amplitude

dan in het geval dat er geen extern M4 getij is. Een vloedgedomineerd zeegat leidt tot een afwezigheid van de buitendelta. Op de plaats waar in alle andere gevallen zich een buitendelta bevond, is nu een vloedgedomineerde geul.

Uit een andere serie experimenten blijkt dat de gemodelleerde bodempatronen een stuk beter met de waarnemingen te vergelijken zijn als er een kwadratische bodemwrijvingsformulering gebruikt wordt i.p.v. een gelineariseerde. De zeewaartse lengte van de ebgeul is groter en er is een eerste indicatie dat de buitendelta om de ebgeul heen buigt. Bovendien ligt het gemodelleerde zandvolume een stuk dichterbij de waargenomen waarden.

Het laatste aspect dat in Hoofdstuk 5 is onderzocht, is in hoe verre de resultaten gevoelig zijn voor golfparameters berekend met een state-of-the-art golfmodel i.p.v. berekend met een zeer geïdealiseerd golfmodel. Er blijkt een verschil te zijn: Als de buitendelta ondieper wordt en de golfhoogte toeneemt, kunnen de effecten van brekende golven belangrijk worden.

### **Resultaten: Asymmetrische delta's**

In Hoofdstuk drie en vijf stond de symmetrische buitendelta centraal. Alle processen die tot asymmetrie leiden waren niet meegenomen. Waarnemingen laten echter zien dat langs de Nederlandse Waddenkust de ebgeulen een oriëntatie hebben t.o.v. de middenas door het zeegat en dat het sediment asymmetrisch is verdeeld. Daarom is het geïdealiseerde model uit hoofdstuk drie uitgebreid met processen die tot asymmetrie kunnen leiden. De aandacht is vooral gericht op processen die gerelateerd zijn aan getij. De resultaten laten zien dat de Coriolis-kracht weinig invloed heeft op de asymmetrie van de buitendelta. Het gebied met ebgedomineerde stromingen is iets naar rechts (kijkend in zeewaartse richting) verschoven t.o.v. de symmetrische situatie. Ook de buitendelta is iets naar rechts verschoven, maar de buitendelta is amper asymmetrisch. Een tweede effect dat belangrijk kan zijn voor de asymmetrie van de buitendelta zijn de kustlangse getijstromen. Deze kustlangse getijstromen interacteren met de kustdwarse stromingen door het zeegat. Als de kustlangse en kustdwarse stromingen in fase zijn (ongeveer de situatie langs de Nederlandse Waddenkust) leidt dit tot sterke ebgedomineerde stromingen aan de linkerkant van het zeegat en zwakke vloedgedomineerde stromingen aan de rechterkant. Het systeem is links georiënteerd. De buitendelta bevindt zich links van de middenas van het zeegat. Er wordt echter geen ebgedomineerde geul gemodelleerd, wel een vloedgedomineerde geul rechts van de middenas. Een verandering van het faseverschil tussen de kustlangse en kustdwarse getijstromen zodanig dat de kustlangse getijstromen voor lopen op de kustdwarse getijstromen, leidt tot een verandering van de asymmetrie-eigenschappen. Bij toenemend faseverschil ligt het sediment steeds meer rechts van de middenas en bij een faseverschil van meer dan 80 graden bevinden zich zowel het gebied met ebgedomineerde stromingen als het meeste sediment van de buitendelta zich rechts van de middenas. Een grootschalige reststroom op zee veroorzaakt door getij heeft ook een sterke invloed op de asymmetrie. Wanneer de reststroom in het geval van de Nederlandse Waddenkust van west naar oost is gericht, liggen zowel het gebied met ebgedomineerde stromingen als het grootste deel van het sediment van de buitendelta rechts van de middenas door het zeegat. Dit kan dus mogelijk het effect van de interactie tussen de kustdwarse en kustlangse getijstromen teniet doen.

# Dankwoord

Als rechtgeaarde protestant ben ik opgevoed met de drieslag 'ellende, verlossing, dankbaarheid'. Het is zeer verleidelijk om dit concept ook op de tastbare werkelijkheid toe te passen. Zo verliepen de eerste drie jaren van mijn promotietijd vol ellende. De resultaten wilden maar niet komen. Ik ging vervolgens maar harder werken om te compenseren voor het feit dat het niet werkte. Maar dit brengt de verlossing niet dichterbij. Je wentelt jezelf steeds meer in de ellende. Zonnige zomerdagen worden gevuld met donkere dwangarbeid. En juist op het moment dat je denkt aan opgeven, komt het moment dat je vanuit een ander perspectief naar het probleem gaat kijken. Het is de laatste strohalm die je aangereikt wordt en vervolgens moet aannemen. En je bent verlost. Alles werkt. Alsof het nooit anders is geweest. Slechts een klein vreugdedansje en dan begint het vreugdevolle werken. Opeens is er perspectief en anderhalf jaar later kijk je terug en is het de tijd voor dankbaarheid.

Allereerst wil ik Huib en Henk bedanken voor hun tomeloze inzet om mij het promotieonderzoek succesvol af te laten ronden. Ik vond (en vind) het erg leuk om met jullie samen te werken. Ik kan me nog heel wat levendige discussies herinneren. Het grote whiteboard werd telkens verrassend snel volgeschreven. Henk, je werd in de loop van de tijd steeds meer bij het onderzoek betrokken. Je hebt altijd ideeën en bent bovendien in staat om lastige concepten zo uit te leggen dat ik kan doen alsof ik ze snap. Dit gaf mij het idee dat het me wel moest lukken om te promoveren. En in tijden van ongeloof hielp je me ook om frustraties weg te drinken in de kroeg of weg te slaan op de squashbaan. Huib, volgens mij komt je het best tot je recht als je een fysisch probleem voorgeschoteld krijgt. Je wordt hierdoor zo uitgedaagd dat je in bijna alle gevallen de volgende dag met oplossingen tevoorschijn komt. Dit heeft in veel gevallen tot nieuwe ideeën geleid. Ook wil ik je danken voor de vele keren (zeker H2!) dat je mijn manuscripten van commentaar hebt voorzien. Will, je was op de achtergrond betrokken bij het onderzoek. Bij het lezen van het manuscript bleek je in staat om met een paar scherpe opmerkingen de vinger op de zere plek te leggen. Daar heb ik veel aan gehad.

De volgende groep mensen die sterk bij je werk betrokken zijn en veel positieve woorden verdienen, zijn je collega's. In het bijzonder wil ik de kustengroep bedanken voor de gezellige etentjes, gedeelde kennis en voor de kritische houding in de leesclub. De kritische fase tijdens de leesclub begon meestal met een aanzwellend gegrom van George, waarna het door iemand anders overgenomen werd en uiteindelijk het verhaal tot in de meest elementaire vorm uitgekleeft werd. Jeroen, jou wil ik danken voor je inzet tijdens je afstuderen. De resultaten die je behaald hebt, vormen de basis voor hoofdstuk vijf van dit proefschrift. Bovendien bleek je gedurende een half jaar ook een erg gezellige kamergenoot. De collega's op het IMAU wil ik bedanken voor de gezelligheid tijdens koffie- en lunchpauzes. Nog leuker waren de vrijdagmiddagborrels voor de gevorderdengroep, die nooit beperkt bleven tot de vrijdagmiddag alleen.

Je omgeving van familie en vrienden vraagt zich voortdurend af wat je nu toch allemaal aan het doen bent en wat het nut hiervan is. Dat is een goede zaak. Als er welgemeende interesse is maar je kunt niet uitleggen wat je doet en waarom, dan is de kans groot dat je de zaken vanaf een ander level dient te bekijken. Dit heet relativieren. Ik wil iedereen bedanken die me geholpen heeft het werk te relativieren door met mij te praten over geloof, vertrouwen, liefde, voetbal, muziek, het enneagram en weet ik wat. Of door gewoon een gezellige tijd samen te hebben en veel te lachen.

Hoewel je misschien wel meer tijd doorbrengt met collega's dan met je eigen partner, heb ik gemerkt dat er zoiets als 'quality time' bestaat. De afgelopen drie jaar met jou, Hilde, waren fantastisch. Dat we zijn getrouwd was geen jeugdige overmoed, maar een welwillende overgave aan de lente. En elke dag word ik bevestigd in onze keuze voor elkaar. Het heeft mij en mijn leven veranderd. Je hebt me altijd gesteund, hebt het belang van werk altijd weer genuanceerd, hebt veel geduld gehad, zelfs als ik "even" iets ging afmaken. Daarvoor ben ik je dankbaar. Ook voor de keren dat je me het onmogelijk maakte om 's avonds of in het weekend te werken.

# Curriculum Vitae

Ik ben geboren op 17 september 1977 in Hattem. Het grootste gedeelte van mijn jeugd heb ik doorgebracht in een klein dorpje nabij Steenwijk, Kallenkote. In 1995 heb ik mijn VWO-diploma behaald op het Greydanuscollege in Zwolle. Tijdens mijn VWO-tijd raakte ik steeds meer geïnteresseerd in natuurkunde. Het verbaasde dan ook niemand dat ik in 1995 in Groningen aan de studie natuurkunde begon. Alhoewel ik in 1997 nog wel mijn propedeuse behaalde, bleek dat de opleiding niet geheel aan mijn verwachtingen voldeed. In de zomer van 1997 heb ik daarom ook besloten om mijn studie voort te zetten in Utrecht en aldaar meteorologie en fysische oceanografie te gaan studeren. Tijdens deze opleiding werd steeds meer de interesse voor de morfodynamica gewekt. Ik studeerde in 2001 af op een studie naar de ontwikkeling van de buitendelta van het Friesche Zeegat. Omdat het doen van onderzoek mij goed beviel, besloot ik om in te gaan op het aanbod om aan een promotieonderzoek te beginnen. Na het behalen van mijn diploma in juli 2001, begon ik in augustus 2001 als AiO aan het Instituut voor Marien en Atmosferisch onderzoek Utrecht (IMAU). De resultaten van het onderzoek kunt u vinden in dit proefschrift. Sinds 1 februari 2006 werk ik als postdoc bij de sectie waterbouwkunde aan de Technische Universiteit Delft.





